Non-Equilibrium Dynamics of Photoexcited Correlated Quantum Matter

Dissertation

for the award of the degree
“Doctor rerum naturalium” (Dr. rer. nat.)
of the Georg-August-Universität Göttingen

within the doctoral program
Physics
of the Georg-August University School of Science (GAUSS)

submitted by
Alexander Osterkorn
from Niebüll

Göttingen, 2022

Thesis Committee

Prof. Dr. Stefan Kehrein
Institute for Theoretical Physics
University of Göttingen

Prof. Dr. Stefan Mathias
I. Physical Institute
University of Göttingen

PD Dr. Salvatore R. Manmana
Institute for Theoretical Physics
University of Göttingen

Members of the Examination Board

Reviewer: Prof. Dr. Stefan Kehrein
Institute for Theoretical Physics
University of Göttingen

2nd Reviewer: PD Dr. Salvatore R. Manmana
Institute for Theoretical Physics
University of Göttingen

Further Members of the Examination Board

Prof. Dr. Stefan Mathias
I. Physical Institute
University of Göttingen

Prof. Dr. Fabian Heidrich-Meisner
Institute for Theoretical Physics
University of Göttingen

Prof. Dr. Claus Ropers
Department of Ultrafast Dynamics
Max Planck Institute for Multidisciplinary Sciences, Göttingen

Prof. Dr. Matthias Krüger
Institute for Theoretical Physics
University of Göttingen

Date of oral examination: 07.02.2023

Abstract

The interaction of time-dependent electromagnetic fields with electrons in quantum materials can give rise to many both fundamentally interesting as well as technologically relevant phenomena like transient band structure manipulations or the emergence of prethermal states of matter, which are not a result of heating. This thesis contributes theoretical insights to both these topics: We model the interference of Floquet and Volkov side bands, which are a result of the dressing of electron states by light, in a time-resolved angle-resolved photoemission spectroscopy (ARPES) experiment. Furthermore, we analyze the emergence of a band-like feature in the non-equilibrium spectral function of a one-dimensional charge-density wave insulator upon periodic driving. Secondly, we use the fermionic truncated Wigner approximation (fTWA), a phase space method for the time evolution of interacting fermions, to study the light-induced order parameter dynamics in SU(N)-symmetric fermionic lattice models. By comparison with exact analytical results for an interaction quench in the Hubbard model, we find that dephasing-induced prethermalization is correctly described by fTWA. We discuss photoinduced prethermal transitions between competing phases of matter in the large-N Hubbard-Heisenberg model and find a pronounced frequency-dependence of the transition. This work contributes to a better understanding of photoinduced order parameter dynamics from a microscopic perspective.

Author's Note

Parts of this dissertation have been published in peer-reviewed journals or are currently under review.

- *Systematic large flavor fTWA approach to interaction quenches in the Hubbard model* [1], preprint at `arXiv:2007.05063`,
  A. Osterkorn and S. Kehrein

- *Photoinduced prethermal order parameter dynamics in the two-dimensional large-N Hubbard-Heisenberg model* [2], publication Phys. Rev. B **106**, 214318 (2022),
  A. Osterkorn and S. Kehrein

- *Electromagnetic dressing of the electron energy spectrum of Au(111) at high momenta* [3], publication Phys. Rev. B **102**, 161403(R) (2020),
  M. Keunecke, M. Reutzel, D. Schmitt, **A. Osterkorn**, T. A. Mishra, Ch. Möller, W. Bennecke, G. S. M. Jansen, D. Steil, S. R. Manmana, S. Steil, S. Kehrein, S. Mathias
  Author's contribution: I contributed the modeling of the angular dependence of the side band intensities in equations (2) to (4)) . I wrote section III of the Supplemental Material.

- *In-Gap Band Formation in a Periodically Driven Charge Density Wave Insulator* [4], publication Comm. Phys. **6**, 245 (2023)
  A. Osterkorn, C. Meyer, S. R. Manmana
  Author's contribution: I contributed the A-B model and mean-field calculations. C.M. performed the MPS numerics. All authors analyzed the data and discussed the results. I wrote the manuscript together with S.R.M. and with input from C.M.

Other contributions to publications during the time of the PhD that are not explicitly included in the dissertation:

- *Detecting superconductivity out-of-equilibrium* [5],
  publication Phys. Rev. B **101**, 180507(R) (2020)
  S. Paeckel, B. Fauseweh, **A. Osterkorn**, T. Köhler, D. Manske, S. R. Manmana
  Author's contribution: I performed all DMRG/TDVP simulations for the t-J chain, analyzed the data, wrote the related section in the Supplemental Material and produced all the figures in that section.

- *Lifshitz transition in the phase diagram of two-leg t-J ladder systems at low filling*,
  publication Phys. Rev. B **108**, 155148 (2023),
  S. Bollmann, **A. Osterkorn**, E. J. König, S. R. Manmana
  Author's contribution: I calculated the exact two electron solution of the model, determined the phase boundaries at zero filling and wrote section IV. of the manuscript

Contents

Chapter 1

Introduction

Since the advent of quantum physics and quantum mechanics – almost 100 years ago [6]) – scientists have been fascinated with this powerful yet very counterintuitive theory, which so accurately describes the behavior of elementary particles at the nanoscale. Nowadays, the theory of "hard"[1] condensed matter is a major field of application of quantum physics. Many properties of materials, e.g. their electrical conductivity, can only consistently be explained within a quantum mechanical description [7]. Remarkable successes of the theory of condensed matter include the BCS theory of superconductivity [8] as well as the establishment of Fermi liquid theory [9] as a theoretical paradigm that allows to describe the properties of various, even strongly, interacting materials. A source of many interesting and technologically relevant physical phenomena like high-temperature superconductivity [10, 11] or the colossal magnetoresistance [10] are strong electronic correlations [12, 13], which are typically realized in materials with partially filled f and d electron shells [14]. Many transition metals like manganese fall in this category. A strong focus in condensed matter theory traditionally lies on the exploration and modeling of equilibrium properties of such strongly correlated materials. However, many of their characteristic effects, e.g., the formation of interaction-induced Mott insulators [15], cannot be explained within a simple band picture of electronic states, which successfully describes the electrical resistivity for many materials [7]. This led to the design and the analysis of strongly interacting lattice models like the Hubbard or the t-J model. The Hubbard lattice model [16, 17, 18] is often considered as the "drosophila" of strong correlation research [19]. Its Hamiltonian reads

$$\hat{H}_{\text{Hub}} = -t_h \sum_{\langle i,j\rangle,\sigma} \left(c^\dagger_{i\sigma} c_{j\sigma} + \text{H.c.} \right) + U \sum_i \hat{n}_{i\uparrow}\hat{n}_{i\downarrow}, \tag{1.1}$$

where $c^{(\dagger)}_{i\sigma}$ denote electronic annihilation and creation operators on sites i of a lattice and $\langle i,j\rangle$ denotes nearest neighbors. Remarkably, exact analytical solutions exist for the one-[20] and the infinite-dimensional [21] model. One great success is the observation of an interaction-induced Mott insulator phase in the Hubbard model at large interaction strength U [22, 23]. Nowadays, the phase diagram of the square lattice model is at the forefront of theoretical research [24]. Many major theoretical insights

---

[1] i.e. glued together by quantum effects, in contrast to "soft" matter for which thermal fluctuations dominate

on phase transitions in materials were due to the renormalization group machinery, pioneered by Kadanoff and Wilson [25]. Its modern children like the density matrix renormalization group [26, 27] and the functional renormalization group [28] are particularly well suited to analyze strongly correlated systems. Another important step was the development of dynamical mean-field theory [14]. Of particular interest in current research are layered two-dimensional strongly correlated materials like the transition metal dichalcogenides [29]. It turned out that stacking monolayer materials onto each other, possibly twisted by a “magic angle”, can give rise to superconducting states [30] or novel quantum Hall phases [31]. The exploration of stacked 2D materials is only at its beginning.

Next to many remaining open questions in equilibrium physics, quantum systems out-of-equilibrium have emerged as a very active field of research [32, 33, 34] that offers a lot of open fundamental questions as well as many perspectives for technological applications. One important driving force behind this interest in non-equilibrium physics are the better and better possibilities to realize quantum mechanical model systems with ultracold gas experiments [35]. Atoms or ions can be trapped in lattices created by laser light and serve as quantum simulators [36, 37] that allow to prepare quantum states and monitor their dynamics in real time. Likewise, time-resolved experimental techniques in solid state physics [38] have advanced and enable researchers to observe the dynamics of excited electrons in solids on the femtosecond scale. The interaction of quantum matter with light is one of the most active and most innovative research directions in contemporary condensed matter physics [34, 39, 40, 41]. While correlated quantum materials in equilibrium already allow for a great wealth of physically interesting and technologically relevant states of matter, light-matter interaction hosts the potential to even actively manipulate properties of such materials out-of-equilibrium. This can be used, for example, to design ultrafast switches and novel opto-electronic components [42]. In time-resolved angle-resolved photoemission spectroscopy (trARPES), one of the main experimental techniques to unravel the electronic structure of materials [41, 43, 44], one measures the electronic response to the application of a strong laser pulse. Among the many fascinating applications of this technique are a direct measurement of the collapse of long-range order in solids [45], the direct observation of quantum states dressed by light [46, 47] and the ultrafast manipulation of magnetic order [48]. A developing paradigm in the field of out-of-equilibrium quantum materials is the creation of non-thermal pathways [34] to control the properties of quantum materials. Light-induced superconductivity [49, 50] is one of the most prominent research directions in this spirit.

The great wealth of experimental techniques and research directions requires reliable theoretical simulations of such setups in order to link the experimental observations with microscopic models [51, 52]. However, theoretical simulations of the light-induced quantum dynamics in correlated systems are very challenging due to the lack of a numerical or analytical method that is valid both for a broad range of systems and over long time periods [53]. Therefore, experimental observations are often modeled in terms of coarse-grained descriptions using free energy landscapes (cf., e.g., [54, 55, 56]). Microscopic modeling of non-equilibrium correlated states is often based on non-equilibrium dynamical mean-field theory [57], which is a very powerful technique that goes beyond a simple mean-field description. However, its limited ability to include the effect of spatial correlations is currently one of its main restrictions. For one-dimensional strongly correlated electron models in- and out-of-equilibrium, matrix product state (MPS) techniques are the most versatile and powerful [27, 58]. Unfortunately, they are less efficient in the two-dimensional situation. MPS methods work reasonably well for ground state calculations of medium-sized two-dimensional lattice models (e.g. Heisenberg models on cylinders with 16×8 sites [59]). Time evolution in such system is more severely restricted due to the rapid growth of entanglement [60].

In the following, a few perspectives on current research topics, to which this thesis can contribute new insights, are presented before we close with an overview of the chapters.

1.1 Non-Equilibrium Quantum Many-Body Systems

A quote, commonly attributed to John von Neumann, states that a theory of non-equilibrium would be like a theory of non-elephants. This is to say that non-equilibrium states might have as much in common as all animals different from elephants. Indeed, the great success of the concept of thermal equilibrium is based on the observation that within statistical mechanics and in the thermodynamic limit equilibrium states are characterized by only a few macroscopic variables like temperature or magnetization. Generic non-equilibrium states can differ from this emergent simplicity in an overwhelmingly large number of ways. Nevertheless, theoretical physicists continue to identify sub-classes of non-equilibrium states that share at least some properties, e.g. the way they are prepared. A challenge for research is to identify new categories of problems that allow for a systematic treatment as well as to develop new computational methods. In the following, we give a brief overview over classes of non-equilibrium systems that are also touched upon in this thesis. More detailed summaries can be found in specialized reviews and overview articles [32, 61, 62].

Parameter Quenches While the concept of “quenching” originally refers to a sudden change of temperature, it is now used as well as a name for instantaneous modifications of model parameters like, for instance, the interaction strength. Model parameter quenches can be implemented directly in experiments with ultracold atoms in optical lattices [63, 64, 65, 66, 67]. The relevance of quench scenarios in solid state systems is a bit less obvious. Nevertheless, they can be useful as approximate descriptions of transient modifications of material properties, e.g. via renormalized phonon modes [68]. Quenched systems are particularly convenient for theoretical studies because time propagation with only one single time-independent Hamiltonian is required. Therefore, the analysis can be focused on the two relevant Hamiltonians before and after the quench. A good overview was given by Kollar et al. [69]. One can roughly distinguish three classes of systems with distinct dynamical properties: integrable Hamiltonians, near-integrable and non-integrable ones. Integrability can be defined in multiple ways [70], usually it refers to Hamiltonians with a large number of mutually commuting conserved charges (not the energy eigenstate projectors, which are trivially conserved). The most prominent analytical technique is Bethe ansatz [20]. Quenches from integrable to integrable Hamiltonians allow for a lot of exact mathematical results [61], which we do not want to review here. The great amount of additional conservation laws prohibits a relaxation to thermal states of local observables in position or momentum space; instead, they often reach non-thermal steady states [71, 72], whose expectation values are usually well described by generalized Gibbs ensembles [69]. A variation of the topic are quenches to near-integrable models, i.e. to Hamiltonians of the form $\hat{H}_0 + \epsilon \hat{H}_1$, where $\hat{H}_0$ is integrable, $\hat{H}_1$ is non-integrable and $\epsilon \ll 1$ is small. Such a situation typically leads to a separation of time scales: the early-time dynamics is still influenced by the conservation laws [73, 74], while at a later stage thermalization is possible [75]. We consider such a scenario in Chapter 4. Quenches to non-integrable models are generally expected to ultimately lead to thermal expectation values of local observables [76] except for situations in which, for instance, strong disorder can delay or even completely prohibit thermalization [77]. An interesting effect that can be observed in quenches to non-integrable models is confinement [78]. A major success in the field of quantum quenches was achieved by Calabrese and Cardy [79, 80, 81] who connected the dynamics of correlation functions after a quench to conformal field theories in a higher spatial dimension.

Periodically Driven Systems Another subclass of non-equilibrium systems with a rich existing theory are periodically driven ones. Usually, this refers to explicitly time-dependent systems with a Hamiltonian $\hat{H}(t)$ that is time-periodic with period T: $\hat{H}(t+T) = \hat{H}(t)$. A treatment of such Hamiltonian is usually carried out within *Floquet theory* [82], which one can understand as an analogue to Bloch wave theory in time. Floquet theory is based on a separation of time scales argument, where the dynamics within a period (called *micromotion* in this context) is split off from the "stroboscopic" time evolution over periods. If properties of a periodically driven system are measured over a sufficiently long time span that encompasses a number of periods, they can be associated with properties of a time-independent *Floquet Hamiltonian*. An interesting application of this machinery is presented by the field of *Floquet engineering* [83, 84, 85], in which periodic driving protocols are designed such that the effective Floquet Hamiltonian corresponds to a Hamiltonian with desirable equilibrium properties. Floquet theory predicts a number of phenomena like a transient manipulation of material properties [86] during the periodic driving, which have been confirmed in experiments [87, 88, 89]. A challenge both to theory and experiments are periodically driven strongly interacting systems, which absorb energy during the driving and will eventually heat up (theoretically) to infinite temperature [90]. One can, however, identify regimes like high-frequency driving [91] that leads to slow heating and the formation of prethermal states on experimentally accessible time scales [92, 93].

Variations of these topics like, for instance, systems, which are periodically driven only over a limited period of time as in experiments with ultrashort laser pulses or quenches in systems with complicated competing ordering tendencies possess less general theoretical descriptions and a precise microscopic modeling of the excitations is required. We consider a periodically driven interacting model system in Chapter 3 as well as driving with a finite pulse in Chapter 5.

1.2 Ordered Phases of Matter In- and Out-of-Equilibrium

1.2.1 General Concepts In Equilibrium

The equilibrium properties of materials are typically classified into ordered phases of matter. In this thesis, we mostly consider order in the "Landau sense", which is based on the idea of *spontaneous symmetry breaking (SSB)* and the existence of a *local order parameter* $\mathcal{O}_i$ that is non-zero in the symmetry-broken phase [94]. If a phase of matter is completely homogeneous, one can as well speak of a global order parameter $\mathcal{O} = \frac{1}{V}\sum_i \mathcal{O}_i$. One can show that SSB implies the formation of long-range order [95], which is present if the order parameter correlation functions remain non-zero at large spatial separations:

$$\lim_{|i-j|\to\infty} \lim_{V\to\infty} \langle \mathcal{O}_i \mathcal{O}_j \rangle \neq 0 \qquad \text{(LRO)} \tag{1.2}$$

The most common example is magnetism, where a non-vanishing value of the magnetization $M \sim \left\langle \hat{S}^z \right\rangle \neq 0$ indicates ferromagnetic order. The orientation of the magnetization spontaneously selects a direction and thereby breaks a symmetry (Z_2 in the Ising case, $O(3)$ in the Heisenberg case). This spontaneous selection of a direction of the order parameter hints at the conceptual difficulty that symmetry-broken states are realized in different *ergodic components*. The question, in which direction the magnetization vector in a ferromagnetic phase points, is ultimately determined by the dynamics of the phase transition and cannot be answered with equilibrium tools alone. To circumvent this problem, one often add a weak symmetry-breaking field to the Hamiltonian, for instance, a weak magnetic field in the case of the ferromagnet. This approach is generically only valid if the thermodynamic limit $V \to \infty$ (for constant particle density) is performed first [94]. If h is the infinitesimal symmetry-breaking field, one can define

$$\mathcal{O} = \lim_{h\to\infty} \lim_{V\to\infty} \langle \frac{1}{V} \sum_i \mathcal{O}_i \rangle \tag{1.3}$$

In the case of Bose condensates, a variation of the long-range order concept was introduced by Yang [96] and is called *off-diagonal long-range order*, which occurs if off-diagonal elements of a one-particle reduced density matrix remain finite at large separation of the indices. We add, for completeness, that a class of order, which does not belong to the Landau category is topological order [97]. It is characterized by additional global (quantum) numbers like, for instance, the Chern number which determines the quantum Hall conductance although it is not related to any kind of symmetry breaking.

1.2.2 Order parameters in interacting electron systems

In interacting electron systems there is typically not only one type of order, which can be present or not, but a number of different ordering tendencies [98]. Prominent examples include anti-ferromagnetism (AFM), superconductivity (SC) and charge-density wave order (CDW) [99]. We do not aim to give a full overview here, instead, we highlight some principles. Often ordered phases lead to translational invariance of the system only with respect to unit cells that encompass more than one lattice site, i.e. spontaneous breaking of the full lattice translational symmetry. Such a situation implies a reduction of the electronic Brillouin zone with a new reciprocal lattice vector $\vec{Q}$. Electronic order parameters may often conveniently be expressed in k-space, using this vector $\vec{Q}$. CDW order requires a unit cell size of at least two sites with a real space order parameter $\mathcal{O}_{\mathrm{CDW}} = \sum_i \big(\langle n_{iA}\rangle - \langle n_{iB}\rangle\big)$, where A and B label the atoms in a unit cell. On a hypercubic lattice one obtains $\vec{Q} = (\pi, \pi, \dots)$ and a transformation rule

$$c_{i\alpha}^{\dagger} = \frac{1}{\sqrt{V}} \sum_{\vec{k}\in \mathrm{rBZ}} \big(\mathrm{e}^{-i\vec{k}\cdot\vec{r}_{i\alpha}} c_{\vec{k}}^{\dagger} + \mathrm{e}^{-i(\vec{k}+\vec{Q})\cdot\vec{r}_{i\alpha}} c_{\vec{k}+\vec{Q}}^{\dagger}\big). \tag{1.4}$$

Here, rBZ refers to the reduced Brillouin zone. The order parameter transformed to momentum space reads

$$\mathcal{O}_{\mathrm{CDW}} = 2\sum_{\vec{k},\sigma} \big(\langle c_{\vec{k}\sigma}^{\dagger} c_{\vec{k}+\vec{Q},\sigma}\rangle + \mathrm{c.c.}\big). \tag{1.5}$$

Hence, charge-density waves correspond to a coupling of the modes $\vec{k}$ and $\vec{k}+\vec{Q}$ in momentum space and therefore $\vec{Q}$ is also often called the *ordering vector*. A simpler alternative order parameter definition would be $\mathcal{O}_{\mathrm{CDW}} \sim \langle c_{\vec{k}\sigma}^{\dagger} c_{\vec{k}+\vec{Q},\sigma}\rangle$, which can be more convenient in mean-field calculations. In the same spirit there is anti-ferromagnetic order. Superconducting order is typically understood as Cooper pairing $\mathcal{O}_{\mathrm{SC}} = \langle c_{k\uparrow}^{\dagger} c_{-k\downarrow}^{\dagger}\rangle$. In the Hubbard model one may view Cooper pairing also as one realization of a more general pairing scheme called η-pairing [100]. Cooper pairs have zero center-of-mass momentum $Q = 0$, while $Q = \pi$ pairing is possible as well. The latter, with order parameter $\mathcal{O}_{\eta} = \langle c_{\vec{k}\uparrow}^{\dagger} c_{-(\vec{k}+\vec{Q})\downarrow}^{\dagger}\rangle$, is often just referred to as “the” η-pairing. While η-pairing is of interest out-of-equilibrium [101, 102], it is impossible as a ground state of the Hubbard model [100] with a finite interaction strength U, unless pair hopping terms are added to the Hamiltonian [103]. These types of orders are only the most prominent, in addition there are more complex variants of spin order, nematic phases, spin liquid states [104], etc.

In real materials, order will rarely occur in pure form but in one of many, possibly inhomogeneous, variations and combinations [105]. In particular, certain types of order may be seen as composites of fundamental “primary orders” [106] like superconductivity and CDW. An important aspect of ordering tendencies in solids is that they will in general be coupled. One possibility – despite criticism [106] – is a competition between orders, i.e. not both order parameters can be non-zero at the same time. The more general situation, in which a coexistence of multiple orders is as well possible, is referred to as *intertwined order* [106]. A typical phenomenological approach to model such scenarios is based on Ginzburg-Landau functionals. They can be obtained from an expansion of the thermodynamic free energy in the order parameters under consideration.

For microscopic studies of interacting electron systems, (Hartree-Fock) mean-field theory is the most important approach, which is based on a neglect of quantum correlations. However, if combined with other analytical approaches like Fermi liquid theory [107] or effective Hamiltonians [108], mean-field theories can also be quite predictive.

1.2.3 Order parameters out-of-equilibrium

The experimental advances in time-resolved laser spectroscopy have opened up the (transient) manipulation of order by light as a very active research topic [34]. While the description of order in strongly correlated systems is already very challenging in equilibrium, non-equilibrium setups may in general require even more advanced numerical and analytical techniques. Nevertheless, one feasible and successful approach is based on mean-field descriptions and Ginzburg-Landau free energies [109, 55, 54]. In these coarse-grained theories one assumes the existence of order parameters $\mathcal{O}_1(\vec{r})$, $\mathcal{O}_2(\vec{r})$ and formally writes down a free energy functional like [109]

$$F[\mathcal{O}_1, \mathcal{O}_2, t] = \int \mathrm{d}^D\vec{r}\, \Big(f_1[\mathcal{O}_1, t] + f_1[\mathcal{O}_2, t] + f_c[\mathcal{O}_1, \mathcal{O}_1] + \dots \Big) \tag{1.6}$$

for suitable functions f_i with possibly time-dependent coefficients. The order parameters evolve according to an equation of motion of the form $\frac{1}{\gamma_i}\partial_t \mathcal{O}_i(\vec{r}, t) = -\frac{\delta F}{\delta \mathcal{O}_i(\vec{r}, t)}$. Such theories can be used for qualitative comparison to experiments [110, 56] and for the development of fit functions for experimental data. However, Ginzburg-Landau models can only take a very limited amount of microscopic details of a material into account. In addition, excitation protocols like photoexcitations are incorporated on the level of time-dependent parameters in the free energy functionals, which is not a very precise modeling of the excitation process. Hence, connecting the macroscopic Ginzburg-Landau dynamics to microscopic theories of order parameter dynamics is one of the important challenges for theory.

Microscopic modeling of light-induced order parameters is, in contrast, generically complicated because of the high computational complexity. Often, microscopic mean-field approaches are used. A nice example is a study by Sentef et al. [111], in which CDW, SC and η-pairing order parameters in a two-dimensional Hubbard system under periodic driving are simulated using time-dependent Hartree-Fock theory. The order parameters are coupled due to an intrinsic $SO(4)$ symmetry in the model. While in equilibrium CDW and SC are degenerate, the coupling to a time-dependent field can be used to lift this degeneracy and enhance SC, which contributes to the understanding of a mechanism behind light-induced superconductivity. The study shows that mean-field theories can already yield valuable physical insights. However, there are also clear limitations: the theory lacks intrinsic relaxation mechanisms like dephasing beyond coherent order parameter oscillations. The development of a beyond mean-field scheme for the dynamics of competing order parameters, which incorporates some interaction-induced effects like dephasing, is the topic of Chapter 5.

1.3 Outline of the Thesis

The main part of this thesis in Chapters 4 and 5 is concerned with the development and benchmarking of a new approach to simulate the dynamics of competing order parameters in correlated materials based on a semiclassical time evolution technique called *fermionic truncated Wigner approximation* [112]. It is based on time-dependent Hartree-Fock theory but allows to include in addition the effect of quantum fluctuations via the generation of random initial conditions to these equations of motion, sampled from a probability distribution, which is known as the *Wigner function*. In Chapter 4 we apply this scheme to the well-understood problem of the interaction quench in the two-dimensional Hubbard model [73, 75] and assess carefully the range of its validity. We conclude that dephasing-induced quasiparticle formation is indeed correctly described by the theory, while its long-time dynamics can become unphysical. In order to work in a well-controlled theoretical environment, we consider SU(N)-symmetric generalizations of lattice models with $\alpha = 1, \dots, N$ degenerate fermion states instead of two spin states $\sigma = \uparrow, \downarrow$.

In a second step in Chapter 5, we apply the method to a two-dimensional SU(N)-symmetric model with two competing order parameters, which are a bond density wave phase and a so-called staggered flux phase. We model a photoexcitation with a finite duration and study the formation of order subsequent to the pulse. The fTWA dynamics allows for qualitative insights how the transition between the two phases depends on the driving frequency of the pulse. We find a frequency regime for which the transition occurs with a very low amount of absorbed energy, i.e. without much additional heating. An advantage of the semiclassical method is that we can simulate comparably large 2D systems with more than 240 lattice sites. We give an outlook on how the scheme can be used to study spatially local excitations with inhomogeneous ordering dynamics.

In addition to these method development-related aspects, we present results related to spectral properties of driven electron systems in Chapter 3. The first project in the chapter is a direct collaboration with the experimental group of Stefan Mathias [3] and concerns the modeling of so-called Floquet and Volkov side bands in time-resolved ARPES experiments. We derive analytical formulas for the side band intensities of electron states with parabolic bands in the presence of a pump laser field. The second project summarizes contributions to a collaboration [4] with Constantin Meyer and Salvatore Manmana on the formation of an in-gap band in a one-dimensional charge-density wave insulator, which is periodically driven. Finally, we summarize the main results and give an outlook on possible future research directions.

Chapter 2

Theoretical Background and Methods

2.1 Non-Equilibrium Green's Functions

Green's functions (GFs) are mathematical objects that contain information about spectral and dynamical properties of many-body systems. A good reference for the following definitions is the text book by Stefanucci and van Leeuwen [113]. Single-particle GFs are expectation values of a combination of two $c_i(t)$ operators at different or equal times. Let us denote the time evolution operator of a generic explicitly time-dependent Hamiltonian $\hat{H}(t)$ by $\hat{U}(t, t_0)$. In general,

$$\hat{U}(t, t_{0\text{¸}}) = \mathcal{T}\mathrm{e}^{-\frac{i}{\hbar}\int_{t_0}^{t}\hat{H}(t')\mathrm{d}t'}. \tag{2.1}$$

A density matrix $\hat{\rho}(t)$ evolves as follows:

$$\begin{aligned}\hat{\rho}(t) &= \hat{U}(t, t_0)\hat{\rho}(t_0)\hat{U}(t_0, t) \\ &= \Big(\tilde{\mathcal{T}}\mathrm{e}^{+\frac{i}{\hbar}\int_{t_0}^{t}\hat{H}(t'_+)\mathrm{d}t'_+}\Big)\hat{\rho}(t_0)\Big(\mathcal{T}\mathrm{e}^{-\frac{i}{\hbar}\int_{t_0}^{t}\hat{H}(t'_-)\mathrm{d}t'_-}\Big).\end{aligned} \tag{2.2}$$

One can read this expression as a time propagation on two copies of the real time axis, one with forward propagation direction (chronological time ordering $\mathcal{T}$) and one with backward propagation direction (antichronological time ordering $\tilde{\mathcal{T}}$). This is known as the real-time Keldysh contour or "roundtrip". The most fundamental Green's function, which contains all real-time spectral information, is the *contour-ordered* (or *causal*) single-particle Green's function

$$G_{\alpha\beta}(z, z') = -i\big\langle\mathcal{T}_C c_\alpha(z)c^\dagger_\beta(z')\big\rangle, \tag{2.3}$$

where $\langle\hat{A}\rangle = \mathrm{tr}(\hat{\rho}\hat{A})$ denotes the expectation value with respect to the density matrix ρ. $\mathcal{T}_C$ is ordering on the real-time Keldysh contour (forward branch before backward branch). Here, the time parameters z, z' live on the real Keldysh contour, i.e. they can lie on the forward ($z = t_+$) or on the backward branch ($z = t_-$). The contour-ordered GF can be written in a 2×2 matrix form, where the time arguments are on the forward and backward branches, respectively. The *lesser* and *greater* Green's functions are defined as follows:

$$G^{<}_{\alpha\beta}(t,t') := i\big\langle c^\dagger_\beta(t'_+)c_\alpha(t_-)\big\rangle, \tag{2.4}$$

$$G^{>}_{\alpha\beta}(t,t') := -i\big\langle c_\alpha(t_+)c^\dagger_\beta(t'_-)\big\rangle. \tag{2.5}$$

In the following we leave out the $+/-$ indices and need to remember that t and t' can be freely chosen for all GFs. One can define a Hermitian conjugate of the lesser and greater Green's functions

$$\left[G^{<,>}\right]^\ddagger(t,t') := -\left(G^{<,>}(t',t)\right)^\dagger \tag{2.6}$$

such that $G^<$ and $G^>$ are *Hermitian symmetric*, i.e. $\left[G^{<,>}\right]^\ddagger = G^{<,>}$. The *retarded* Green's function is defined as follows:

$$\begin{aligned} G^{\mathrm{ret}}_{\alpha\beta}(t,t') &:= \theta(t-t')\Big(G^>(t,t') - G^<(t,t')\Big) \\ &= -i\theta(t-t')\big\langle\big\{c_\alpha(t), c^\dagger_\beta(t')\big\}\big\rangle. \end{aligned} \tag{2.7}$$

It is instructive to evaluate these definitions in equilibrium $\hat\rho = \mathrm{e}^{-\beta\hat H}$ and for a very simple Hamiltonian $\hat H = \sum_k \epsilon_k c^\dagger_k c_k$. One obtains $c_k(t) = \mathrm{e}^{-i\epsilon_k t}c_k$ and

$$\begin{aligned} G^<_{kl}(t,t') &= i\mathrm{e}^{-i(\epsilon_k t-\epsilon_l t')}\langle c^\dagger_l c_k\rangle = i\delta_{kl}\mathrm{e}^{-i\epsilon_k(t-t')}\langle n_k\rangle, \\ G^>_{kl}(t,t') &= -i\mathrm{e}^{-i(\epsilon_k t-\epsilon_l t')}\langle c_k c^\dagger_l\rangle = -i\delta_{kl}\mathrm{e}^{-i\epsilon_k(t-t')}(1-\langle n_k\rangle), \\ G^{\mathrm{ret}}_{kl}(t,t') &= -i\delta_{kl}\theta(t-t')\mathrm{e}^{-i\epsilon_k(t-t')}. \end{aligned} \tag{2.8}$$

The GFs only depend on diagonal ks and on the difference between the two time arguments, which is expected from the spatial translational invariance of the system and from the time translational invariance in equilibrium, respectively. This motivates a Fourier transform (FT) with respect to the time difference. Unfortunately, conventions regarding the normalization and signs of the transform in this context vary a lot in the literature. The most commonly used convention (e.g. [114]) seems to be to set $\tau := t-t'$ and to define $G(\omega) = \int_{-\infty}^{\infty}\mathrm{e}^{i\omega\tau}G(\tau)\mathrm{d}\tau$, i.e. using a non-unitary FT. For now, we stick to this convention: Using $\mathcal{F}[\theta(\tau)](\omega) = 1/(i\omega) + \pi\delta(\omega)$, one obtains

$$\begin{aligned} G^<_k(\omega) &= i2\pi\delta(\omega-\epsilon_k)\langle n_k\rangle, \\ G^>_k(\omega) &= -i2\pi\delta(\omega-\epsilon_k)\big(1-\langle n_k\rangle\big), \\ G^{\mathrm{ret}}_k(\omega) &= -i\int_{-\infty}^{\infty}\mathrm{d}\tau\ \theta(\tau)\mathrm{e}^{-i(\epsilon_k-\omega)\tau} \\ &= -i\big(1/(i\omega)+\pi\delta(\omega)\big) = -\frac{1}{\omega-\epsilon_k} - i\pi\delta(\omega-\epsilon_k). \end{aligned} \tag{2.9}$$

The imaginary part of the retarded Green's function is known as the *spectral function*

$$A_k(\omega) = -\frac{1}{\pi}\,\mathrm{Im}\,G^{\mathrm{ret}}_k(\omega) \tag{2.10}$$

and in our simple equilibrium example it is given by $\delta(\epsilon_k-\omega)$.

The calculation highlights the following interpretation of the physical content of the Green's functions, which carries over to the non-equilibrium case [115]: The retarded

Green's function, via the spectral function, contains information on the k-resolved density of states (like $\delta(\epsilon_k - \omega)$), while the lesser and greater Green's functions contain spectral information, which is weighted with the occupation numbers. To be precise, the lesser Green's function contains the occupied part of the spectrum, while the greater contains the unoccupied part.

2.1.1 Time-plane coordinates

One would like to formulate similar Fourier space quantities out-of-equilibrium to get access to instantaneous spectral information. ω continues to be defined with respect to the *relative time* $\tau = t - t'$. In the presence of two time arguments, however, there is an ambiguity, which time to choose as the "base time" that one associates the spectral content to. Two choices are the most commonly used ones: Firstly, the *average time* $t_{\text{ave}} = \frac{t+t'}{2}$, which, together with $\tau = t - t'$ defines a set of so-called *Wigner coordinates* [113]. A second option is to simply choose the time t'. In the two-time plane this gives rise to a set of "*horizontal coordinates*". In a nice study by Kalthoff et al. [114], both definitions are compared in the case of driven non-interacting fermions. Both definitions display reasonable physical properties and one can show that in the case of periodic driving both definitions imply the same period-averaged density of states [114, 116], which agrees with the Floquet theory expectation.

The main application of the formalism in this thesis is the calculation of non-equilibrium spectral functions from the retarded Green's function. For wave function based numerical methods (like MPS-based time-evolution schemes [58]) it is more convenient to consider the horizontal time coordinates because a single time propagation calculation along t' already fixes one of the times. The definition of the non-equilibrium retarded Green's function with horizontal coordinates reads as follows,

$$G^{\text{ret}}_{\alpha\beta}(t_{\text{hor}}, \tau) = -i\theta(\tau)\big\langle\big\{c_\alpha(t_{\text{hor}} + \tau), c^\dagger_\beta(t_{\text{hor}})\big\}\big\rangle, \tag{2.11}$$

where t_{hor} corresponds to the original t' variable. The non-equilibrium spectral function at time t_{hor} is in turn defined as (keeping the Fourier transform conventions from above)

$$A(t_{\text{hor}}, \omega) = -\frac{1}{\pi} \operatorname{Im} G^{\text{ret}}_{\alpha\beta}(t_{\text{hor}}, \omega). \tag{2.12}$$

For the evaluation of the Fourier transform $\tau \to \omega$ for numerical data that is only calculated up to a time τ_{max}, it is often useful to introduce a small complex shift $\omega \to \omega + i\eta$ for an $\eta > 0$ that leads to a broadening of the spectral signal and prevents noise in the frequency space data due to the unphysical time cutoff at t_{max}.

In order to compute the non-equilibrium spectral function numerically, one needs to calculate expectation values of the form

$$\big\langle c_\alpha(t+\tau)c^\dagger_\beta(t)\big\rangle \quad \text{and} \quad \big\langle c^\dagger_\beta(t)c_\alpha(t+\tau)\big\rangle \tag{2.13}$$

for $\tau \geq 0$ if one is only interested in the retarded GF because of the $\theta(\tau)$. The Hermitian symmetry of the full $G^<(t_{\text{hor}}, \tau)$ and $G^>(t_{\text{hor}}, \tau)$ is not helpful in this case because it would connect times $(t_{\text{hor}}, -\tau)$ to $(t_{\text{hor}} - \tau, \tau)$.

2.2 External Fields and Pump-Probe Spectroscopy

2.2.1 Coupling to electromagnetic fields

Let us consider electric and magnetic fields $\vec{E}(\vec{r},t)$ and $\vec{B}(\vec{r},t)$ with the respective potentials $\Phi(\vec{r},t)$ and $\vec{A}(\vec{r},t)$. They are connected by the following relations

$$\vec{E}(\vec{r},t) = -\vec{\nabla}\Phi(\vec{r},t) - \partial_t \vec{A}(\vec{r},t), \qquad \vec{B}(\vec{r},t) = \vec{\nabla} \times \vec{A}(\vec{r},t). \tag{2.14}$$

The most general coupling of the fields to a single-particle electron ($q = -e$) Hamiltonian $\hat{h} = \frac{\hat{\vec{p}}^2}{2m_e} + V(\vec{r})$, where $V(\vec{r})$ is a potential term from the Coulomb interaction of electrons and nuclei, proceeds as follows [117]:

$$\hat{h}^{\mathrm{em}} = \frac{1}{2m_e}\Big(\hat{\vec{p}} - q\vec{A}(\vec{r},t)\Big)^2 + q\Phi(\vec{r},t) + g_s\mu_B\vec{B}(\vec{r},t)\cdot\hat{\vec{S}}, \tag{2.15}$$

where $\vec{S}$ is the electron spin, μ_B is the *Bohr magneton* and $g_s \approx 2$ is called *Landé factor*. The whole last term is called *Zeeman* term and describes the coupling of the magnetic field to the spin magnetic moment. We will neglect this effect in this thesis. The shift $\vec{p} \to \vec{p} + e\vec{A}(t)$ is known as the *minimal coupling*.

Typical many-body Hamiltonians consist of one-particle and two-particle terms, where the latter is mostly of pair-interaction form (e.g. Coulomb interaction $v_{\mathrm{pair}} \sim |\vec{r}_i - \vec{r}_j|^{-1}$ with or without screening):

$$\hat{H}_{\text{1-p}} = \sum_{i=1}^{N} \hat{h}_i, \qquad \hat{H}_{\text{2-p}} = \frac{1}{2}\sum_{i\neq j} v_{\mathrm{pair}}(\hat{\vec{r}}_i - \hat{\vec{r}}_j) \tag{2.16}$$

Usually we prefer to work with Hamiltonians formulated in the language of second quantization. It is therefore desirable to reformulate the minimal coupling in terms of the second quantized matrix element. The resulting approach, which we review in the following, goes back to Peierls [118] and was later simplified by Luttinger [119]. A more recent overview can be found in [120].

We start from the definition of the matrix elements in terms of Wannier wave functions $\phi_\alpha(\vec{r},t)$, where $\alpha = (n, \vec{R}, \sigma)$ is a block quantum number of band index n, location $\vec{R}$ and electron spin σ. The hopping and interaction matrix elements can be written as follows (some authors only define the hopping matrix elements with respect to the deviation $\Delta U(\vec{r})$ from the local atomic potentials; in order to keep the notation simple, we also include the atomic part):

$$\begin{aligned} t_{\alpha\beta} &= \int \mathrm{d}^3\vec{r}\,\overline{\phi_\alpha}(\vec{r}-\vec{R}_\alpha)\,\hat{H}_{\text{1-p}}\,\phi_\beta(\vec{r}-\vec{R}_\beta) \\ v_{\alpha\beta\gamma\delta} &= \int \mathrm{d}^3\vec{r} \int \mathrm{d}^3\vec{r}'\cdot \\ &\quad \cdot\overline{\phi_\alpha}(\vec{r}-\vec{R}_\alpha)\,\overline{\phi_\beta}(\vec{r}'-\vec{R}_\beta)\,\hat{H}_{\text{2-p}}\,\phi_\gamma(\vec{r}-\vec{R}_\gamma)\,\phi_\delta(\vec{r}'-\vec{R}_\delta) \end{aligned} \tag{2.17}$$

Consequently, the many-body Hamiltonian has the structure

$$\hat{H}_{\text{m-b}} = \sum_{\alpha} t_{\alpha\beta} c_{\alpha}^{\dagger} c_{\beta} + \frac{1}{2} \sum_{\alpha\beta\gamma\delta} u_{\alpha\beta\gamma\delta} c_{\alpha}^{\dagger} c_{\beta}^{\dagger} c_{\gamma} c_{\delta}. \tag{2.18}$$

However, the one-particle Hamiltonian (2.15) with electromagnetic fields is not directly expressible in terms of these matrix elements due to the presence of additional terms like $\vec{p} \cdot \vec{A}$. Nevertheless, this problem can be solved by a formal redefinition of the Wannier orbitals

$$\phi_{\alpha}(\vec{r}, t) \quad \longrightarrow \quad \varphi_{\alpha}(\vec{r} - \vec{R}, t) = \mathrm{e}^{-ie\lambda_{\alpha}(\vec{r}, t)} \phi_{\alpha}(\vec{r} - \vec{R}), \tag{2.19}$$

where

$$\lambda_{\alpha}(\vec{r}, t) = \int_{\vec{R}_{\alpha}}^{\vec{r}} \vec{A}(\vec{r}', t) \cdot \mathrm{d}\vec{r}' \tag{2.20}$$

is defined such that $-i\vec{\nabla}\lambda_{\alpha} = e\vec{A}$. One obtains

$$\begin{aligned}
t_{\alpha\beta}^{\text{em}} &= \langle \varphi_{\alpha} | \hat{H}_{\text{1-p}}^{\text{em}} | \varphi_{\beta} \rangle \\
&= \sum_{i} \bigg(\int \mathrm{d}^3\vec{r}_i \, \overline{\varphi_{\alpha}}(\vec{r}_i - \vec{R}_{\alpha}) \cdot \\
&\qquad \cdot \left[\frac{1}{2m_e} \Big(\hat{\vec{p}} + e\vec{A}(\vec{r}_i, t) \Big)^2 + V(\vec{r}_i) \right] \varphi_{\beta}(\vec{r}_i - \vec{R}_{\beta}) \bigg) \\
&= \sum_{i} \int \mathrm{d}^3\vec{r}_i \, \overline{\phi_{\alpha}}(\vec{r}_i - \vec{R}_{\alpha}) \, \mathrm{e}^{-ie\left(\lambda_{\beta}(\vec{r}_i, t) - \lambda_{\alpha}(\vec{r}_i, t)\right)} \cdot \\
&\qquad \cdot \left[\frac{\hat{\vec{p}}^2}{2m_e} + V(\vec{r}_i) \right] \phi_{\beta}(\vec{r}_i - \vec{R}_{\beta}) \\
&= \sum_{i} \mathrm{e}^{-ie\lambda_{\beta}(\vec{R}_{\alpha}, t)} \int \mathrm{d}^3\vec{r}_i \, \overline{\phi_{\alpha}}(\vec{r}_i - \vec{R}_{\alpha}) \, \mathrm{e}^{ie\Lambda(\vec{r}, t)} \cdot \\
&\qquad \cdot \left[\frac{\hat{\vec{p}}^2}{2m_e} + V(\vec{r}_i) \right] \phi_{\beta}(\vec{r}_i - \vec{R}_{\beta}),
\end{aligned} \tag{2.21}$$

where

$$\Lambda(\vec{r}, t) = \int_{S} \mathrm{d}\vec{r}' \cdot A(\vec{r}', t) \tag{2.22}$$

and S is the closed path $\vec{R}_{\alpha} \to \vec{r} \to \vec{R}_{\beta} \to R_{\alpha}$. Now the usual approximation is to neglect the Λ-exponential. This can be justified under the assumption of *slow spatial variance* of the vector potential on the scale of a lattice constant because of the strong localization of the Wannier orbitals $\phi_{\alpha}(\vec{r} - \vec{R}_{\alpha})$ at the atomic positions. The phase factor $\Lambda(\vec{r}, t)$ does only contribute to a non-zero integral for arguments $\vec{r}$ in the immediate vicinity of $\vec{R}_{\alpha}$ or $\vec{R}_{\beta}$. Since without loss of generality we may assume the path $\vec{R}_{\alpha} \to \vec{R}_{\beta}$ in the integral to be a straight line, the integral over the full path S proceeds effectively back and forth along this line for the relevant $\vec{r}$ if $\vec{A}(\vec{r})$ does not vary. Using the definition (2.20), one obtains a modified phase factor

$$t_{\alpha\beta}^{\text{em}} = \exp\left(ie \int_{\vec{R}_{\alpha}}^{\vec{R}_{\beta}} \vec{A}(\vec{r}', t) \cdot \mathrm{d}\vec{r}' \right) t_{\alpha\beta}. \tag{2.23}$$

In non-equilibrium condensed matter applications, one often assumes a spatially homogeneous vector potential $\vec{A}(t)$ such that

$$\int_{\vec{R}_\alpha}^{\vec{R}_\beta} \vec{A}(\vec{r}\,',t)\cdot \mathrm{d}\vec{r}\,' = \left(\vec{R}_\beta - \vec{R}_\alpha\right)\cdot \vec{A}(t) = a\vec{e}_{\langle i,j\rangle}\cdot \vec{A}(t), \tag{2.24}$$

where we denote the unit vector in the direction of the nearest neighbor bond between site i and j by $\vec{e}_{\langle i,j\rangle}$. If we choose units such that the lattice constant a as well as the electric charge are unity, we obtain the common way to include a time-dependent vector potential into an electronic kinetic Hamiltonian), which is known as the *Peierls substitution*

$$\begin{aligned} & \hat{H}_{\text{kin}} = -t_h \sum_{\langle i,j\rangle} \left(c_i^\dagger c_j + \text{H.c.}\right) \\ \rightarrow \quad & \hat{H}'_{\text{kin}} = -t_h \sum_{\langle i,j\rangle} \left(\mathrm{e}^{-i\vec{e}_{\langle i,j\rangle}\cdot\vec{A}(t)} c_i^\dagger c_j + \text{H.c.}\right). \end{aligned} \tag{2.25}$$

A pictorial way to understand the general modification (2.23) is presented in Fig. 2.1. Depending on the spatial structure of the vector potential, it can induce a non-vanishing magnetic flux $\Phi(t)$, which the electrons feel while hopping around a lattice plaquette. Such a scenario is used frequently in ultracold atoms experiments to prepare phases with additional gauge fields [121]. In any case, a time-dependent vector potential will give rise to a non-vanishing electric field $E(t)$ in the model. Finally, it is important to keep in mind that electromagnetic fields are only defined up to gauge transformations $\left(\phi,\vec{A}\right) \rightarrow \left(\phi - \partial_t\chi, \vec{A} + \nabla\chi\right)$ for an arbitrary function $\chi(\vec{r},t)$. A gauge transformation like this gives rise to a unitary transformation $\hat{U}$ of the Hamiltonian

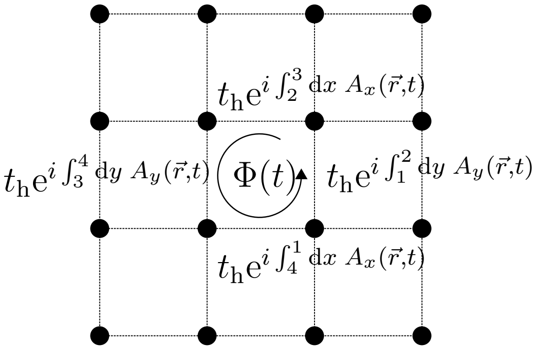

Figure 2.1: Sketch of Peierls substitution in a 2d lattice. In addition to an electric field, the phase factors of the hopping amplitudes may also give rise to a non-vanishing magnetic flux around the plaquettes.

$$\hat{H} \;\rightarrow\; \hat{U}^\dagger(t)\hat{H}\hat{U}(t) - i\hat{U}^\dagger\left(\partial_t\hat{U}\right), \qquad c_i \;\rightarrow\; c_i\mathrm{e}^{-i\chi(\vec{R}_i,t)}. \tag{2.26}$$

2.2.2 Description of time-resolved ARPES experiments

In a typical pump-probe time-resolved ARPES experiment two ultrashort (femtosecond scale) laser pulses shine on a sample at a time delay Δt, a pump pulse with photon energies typically in the infrared and a second, narrower probe pulse with high photon frequencies, e.g. in the (extreme) ultraviolet ((E)UV). The photon energy of the pump pulse is comparable to the energies of electronic transitions and excitation energies of the material. It induces energy absorption and the (transient) creation of excited electronic states. The high photon energy of the probe pulse allows to create transitions into the vacuum and, ultimately, the detector. In order to model interaction effects and real-time changes in the observed ARPES spectra resulting from scattering processes, a full many-body formulation involving two-time Green's functions is necessary. However, some effects of the driving with a laser pulse can be captured already on a single-particle level, in particular photon dressing effects that give rise to band structure replicas in the trARPES spectra. We will study such effects more in detail in Chapter 3. In the following we first introduce a simplified wave function model for photoemission processes in the presence of time-dependent electromagnetic fields before we introduce the more common many-body formalism.

2.2.2.1 Single-particle picture

In this section we follow mainly the presentation given by Madsen [122, 123] and Park [124]. The pump and the probe pulse are modeled on the level of vector potentials $\vec{A}(\vec{r},t)$. The pump pulse $\vec{A}_{\text{pump}}$, which we assume to be linearly polarized, can be thought of as a Gaussian-modulated cosine

$$\vec{A}_{\text{pump}} = \vec{A}^0_{\text{pump}} s_{\text{pump}}(t) \cos(\omega_{\text{pump}} t), \tag{2.27}$$

where $s_{\text{pump}}(t)$ is the envelope function. Typical experimental values for $\hbar\omega_{\text{pump}}$ would be in the range of one to two electron volts [125]. In addition, usually the *dipole approximation* $\vec{A}(\vec{r},t) = \vec{A}(t)$ is applied [122], which is based on a neglect of spatial variations of the vector potential on the scale of a lattice constant. One may write down a similar potential for the *probe pulse*

$$\vec{A}_{\text{probe}}(\vec{r},t) = \vec{A}^0_{\text{probe}} s_{\text{probe}}(t) \cos(\omega_{\text{probe}} t). \tag{2.28}$$

The experimental values for ω_{probe} vary a lot, the Göttingen setup [125] uses $\hbar\omega_{\text{probe}} \sim 26\,\text{eV}$. In addition to the dipole approximation, one usually assumes the *rotating wave approximation* for the probe pulse [122]:

$$\vec{A}_{\text{probe}}(t) = \frac{\vec{A}^0_{\text{probe}}}{2} \mathrm{e}^{i\omega_{\text{probe}} t} \qquad \text{(RWA)} \tag{2.29}$$

The photoionization process itself can be modeled within first order time-dependent perturbation theory ("Born approximation") if one treats the probe pulse as a linear perturbation [122, 124]: The kinetic Hamiltonian, in the presence of the probe pulse, is modified via minimal coupling (here we set $q = -e$)

$$\begin{aligned} \frac{\vec{p}^2}{2m_e} \quad \longrightarrow \quad & \frac{1}{2m_e}\left(\vec{p} + e\vec{A}_{\text{probe}}\right)^2 \\ &= \frac{\vec{p}^2}{2m_e} + \frac{e}{2m_e c}\left(\vec{A}_{\text{probe}} \cdot \vec{p} + \vec{p} \cdot \vec{A}_{\text{probe}}\right) + \frac{e^2}{2m_e}(\vec{A}_{\text{probe}})^2 \\ &\simeq \frac{\vec{p}^2}{2m_e} + \frac{e}{2m_e}\vec{A}_{\text{probe}} \cdot \vec{p} \end{aligned} \tag{2.30}$$

where $\vec{A}^0_{\text{probe}}$ is assumed so small that the quadratic terms can be neglected. Furthermore, $\vec{p} \cdot \vec{A}_{\text{probe}} \sim \vec{\nabla} \cdot \vec{A}^0_{\text{probe}} = 0$, which is always true in the Coulomb gauge $\nabla \cdot \vec{A} = 0$ if surface effects are neglected.

Let us first consider, for simplicity, the situation without a pump pulse. If one neglects many-body effects in the material, one can model (static) photoemission as a scattering process from a single-particle initial wave function $\psi_i(\vec{r})$ to a single-particle final state wave function. In the Born approximation, the scattering matrix element (with respect to the perturbation $\sim A_{\text{probe}}$) reads

$$\begin{aligned} (S^{\text{B}} - 1)_{fi} &= -\frac{i}{\hbar}\int_{-\infty}^{\infty} \mathrm{d}t \; \langle \psi_f(\vec{r}, t) | \, \vec{A}_{\text{probe}}(t) \cdot \vec{p} \, | \psi_i(\vec{r}, t) \rangle \\ &= -\frac{i}{\hbar}\int_{-\infty}^{\infty} \mathrm{d}t \; \langle \psi_f(\vec{r}) | \, \vec{A}_{\text{probe}}(t) \cdot \vec{p} \, | \psi_i(\vec{r}) \rangle \, \mathrm{e}^{-i(\omega_f - \omega_i - \omega_{\text{probe}})t} \\ &= -\frac{2\pi i}{\hbar} M_{fi} \delta\big(\omega_f - \omega_i - \omega_{\text{probe}}\big) \end{aligned} \tag{2.31}$$

where $\psi_\alpha(\vec{r}, t) = \psi_\alpha(\vec{r})\mathrm{e}^{i\omega_\alpha t}$ for $\alpha = i, f$ denote the inital and final states, respectively, with energies $E_\alpha = \hbar\omega_\alpha$. $M_{fi} = \langle \psi_f(\vec{r}) | \, \vec{A}_{\text{probe}}(t) \cdot \vec{p} \, | \psi_i(\vec{r}) \rangle$ is the time-independent transition matrix element. The transition rate (which is proportional to the measured photocurrent) between initial and final state is equivalent to Fermi's golden rule:

$$w_{i \to f} = \frac{2\pi}{\hbar} |M_{fi}|^2 \delta\big(\omega_f - \omega_i - \omega_{\text{probe}}\big). \tag{2.32}$$

The Dirac-δ expresses energy conservation as one of the important principles of photoemission. The second important principle is the *conservation of momentum parallel to the surface* $\vec{k}'_{\|} = \vec{k}_{\|}$, where $k_{\|}$ and $k'_{\|}$ are the initial and final state momenta parallel to the surface plane, respectively. The conservation law follows from the translational invariance in directions along this plane, which remains intact during the photoemission process. The z-component of the electron, in contrast, is not conserved and acts as measure for the kinetic energy.

This leads over to the most complicated part of the modeling: the wave functions. While in the single-particle picture one can simply assume the initial state to be a Bloch wave, the final state is more complicated. The classical reference for a detailed discussion is the book by Hüfner [126]. In modern "one-step" models of photoemission, the final state corresponds to a "time-inverted LEED state", i.e. a high lying Bloch state in the solid, which is matched to free electron states far away from the surface. These incorporate diffraction effects at the surface but are not so easy to describe analytically. A simpler, more pragmatic, model [127] is to assume the final state as a free electron state according to the vacuum free electron Hamiltonian $H_0^{\mathrm{vac}} = \frac{\vec{p}^2}{2m_e}$. Using such a model, one needs to introduce an artificial energy barrier V_0 to at least phenomenologically incorporate contributions to the energy balance like work functions etc. The advantage of such a model is that it allows one to determine the k_z-component of the photoelectron explicitly.

In such a single-particle theory of photoemission, the main role of a pump field is the electromagnetic dressing of the wave functions. In particular, the final free electron states turn into so-called *Volkov wave functions*, which we discuss in more detail in the introduction to Chapter 3.

2.2.2.2 Many-body picture

If interaction effects in the material become important, one needs to apply the many-body formalism, in which the initial state $|\Psi_i(N)\rangle$ as well as the final state $|\Psi_f(N)\rangle$ after photoemission are many-body states with N particles. We again consider a setup without pump pulse. A common assumption for theoretical calculations is the *sudden approximation*, which assumes that the photoelectron decouples immediately from the electron states in the solid and relaxation effects due to the probe pulse impact are neglected. A pedagogical introduction was written by Michael Sing in [127] and we only summarize the results. A generalization of the single-particle scattering theory to many-body states using the sudden approximation and the assumption of constant matrix elements yields a photocurrent $I(\vec{k}, E)$ at final momentum $\vec{k}$ and energy E, which is proportional to the spectral function $A_k(\omega)$ (cf. (2.10)) of the material, weighted by the equilibrium mode occupations of the initial state. The latter is generically a Fermi-Dirac distribution. In summary,

$$I(\vec{k}, E) \sim A_k(\omega)\langle n_k\rangle = A_k^<(\omega), \tag{2.33}$$

where $A_k^<(\omega) = -\frac{1}{\pi}\,\mathrm{Im}\,G_k^<(\omega)$. This shows the ability of photoemission to directly obtain information about the spectral function of a correlated material.

An adaptation of the many-body formalism to the pump-probe situation is more challenging and was first achieved by Freericks et al. [51]. Later, corrections [52, 128] of the theory to ensure gauge-invariance have been developed. The main result is that the time-resolved photocurrent $I(t, \vec{k}, E)$ is proportional to the Fourier transform of the lesser Green's function (which might need to be constructed in a gauge-invariant way) [52]:

$$I(t, \vec{k}, E) \sim -\frac{i}{\hbar^2}\int_{t_0}^{t} \mathrm{d}t_1 \int_{t_0}^{t} \mathrm{d}t_2\; s_{\mathrm{pr}}(t_1)s_{\mathrm{pr}}(t_2)\mathrm{e}^{i\omega(t_1-t_2)}G_{\vec{k}}^<(t_1, t_2). \tag{2.34}$$

Here, $s_{\mathrm{pr}}(t)$ is a shape function of the probe pulse. Although the relation between the Green's function out-of-equilibrium is more complicated than in equilibrium, one may stick to the picture that time-resolved photoelectron spectroscopy measures the non-equilibrium spectral function, weighted by the information how these non-equilibrium states are “occupied”.

2.3 Mean-Field Theory and Classical Limits

2.3.1 Overview

Mean-field theory is the starting point for various approximative treatments of interacting many-particle systems like self-energy based diagrammatic expansions. There are a number of different viewpoints on mean-field theory. One perspective is a replacement of quantum, or statistical, operators by their expectation values, $\hat{O} \approx \langle \hat{O} \rangle$, $\hat{O}_1\hat{O}_2 \approx \langle \hat{O}_1 \rangle \langle \hat{O}_2 \rangle$, etc. One can formalize this approach by introducing a fluctuation operator $\delta\hat{O}$ such that $\hat{O} = \big\langle \hat{O} \big\rangle + \delta\hat{O}$. The mean-field approximation on the operator level corresponds to neglecting quadratic fluctuation contributions:

$$\begin{aligned} \hat{O}_1\hat{O}_2 &= \big(\langle \hat{O}_1 \rangle + \delta\hat{O}_1\big)\big(\langle \hat{O}_2 \rangle + \delta\hat{O}_2\big) \\ &= \langle \hat{O}_1 \rangle \langle \hat{O}_2 \rangle + \langle \hat{O}_1 \rangle \delta\hat{O}_2 + \langle \hat{O}_2 \rangle \delta\hat{O}_1 + \delta\hat{O}_1\delta\hat{O}_2 \\ &\approx \langle \hat{O}_1 \rangle \langle \hat{O}_2 \rangle + \langle \hat{O}_1 \rangle \delta\hat{O}_2 + \langle \hat{O}_2 \rangle \delta\hat{O}_1 \\ &= \langle \hat{O}_1 \rangle \langle \hat{O}_2 \rangle + \langle \hat{O}_1 \rangle \big(\hat{O}_2 - \langle O_2 \rangle\big) + \langle \hat{O}_2 \rangle \big(\hat{O}_1 - \langle O_1 \rangle\big) \\ &= \langle \hat{O}_1 \rangle \hat{O}_2 + \langle \hat{O}_2 \rangle \hat{O}_1 - \langle \hat{O}_1 \rangle \langle \hat{O}_2 \rangle \end{aligned} \tag{2.35}$$

One can immediately see that $\langle \hat{O}_1\hat{O}_2 \rangle = \langle \hat{O}_1 \rangle \langle \hat{O}_1 \rangle$ within the approximation. In many-body applications, fluctuations typically occur in more than one channel, like particle-hole and exchange in the Hartree-Fock approximation, which gives rise to more terms in equations like (2.35). It can be introduced in various ways: one is based on the properties of Slater determinant wave functions in the language of first quantization. The more straightforward way in second-quantized language is based on Wick's theorem [129]: One introduces a Wick contraction

$$\overbracket{A_1 A_2} = A_1 A_2 - \ :A_1 A_2: \tag{2.36}$$

of two operators A_1 and A_2, where $:A_1A_2:$ denotes the normal ordering of the operators with respect to some state (e.g., the ground state of the many-body system). One can show that the contraction is a number instead of an operator, which implies that $\overbracket{A_1 A_2} = \langle A_1 A_2 \rangle$. Wick's theorem formulates a rule how to express products of operators $A_1 \ldots A_n$ in terms of contractions and normal ordered operators. We only need the expression for four operators [130] (upper signs: bosons, lower signs: fermions):

$$\begin{aligned} A_1A_2A_3A_4 =&: A_1A_2A_3A_4 : + \langle A_1A_2 \rangle : A_3A_4 : \pm \langle A_1A_3 \rangle : A_2A_4 : \\ &+ \langle A_1A_4 \rangle : A_2A_3 : + \langle A_2A_3 \rangle : A_1A_4 : \pm \langle A_2A_4 \rangle : A_1A_3 : \\ &\pm \langle A_3A_4 \rangle : A_1A_2 : \\ &+ \langle A_1A_2 \rangle \langle A_3A_4 \rangle \pm \langle A_1A_3 \rangle \langle A_2A_4 \rangle + \langle A_1A_4 \rangle \langle A_2A_3 \rangle \end{aligned} \tag{2.37}$$

The mean-field approximation is equivalent to a neglect of $: A_1A_2A_3A_4 :$. As an example we consider the Hubbard interaction term in position space, $c^\dagger_{i\uparrow}c_{i\uparrow}c^\dagger_{i\downarrow}c_{i\downarrow} = c^\dagger_{i\uparrow}c^\dagger_{i\downarrow}c_{i\downarrow}c_{i\uparrow}$. Its mean-field decoupling derived from Wick's theorem yields three types of contributions

$$\big\langle c^\dagger_{i\sigma}c_{i\sigma} \big\rangle : c^\dagger_{i\bar{\sigma}}c_{i\bar{\sigma}} : \qquad -\big\langle c^\dagger_{i\sigma}c_{i\bar{\sigma}} \big\rangle : c^\dagger_{i\bar{\sigma}}c_{i\sigma} : \qquad \big\langle c^\dagger_{i\sigma}c^\dagger_{i\bar{\sigma}} \big\rangle : c_{i\bar{\sigma}}c_{i\sigma} : \tag{2.38}$$

These are the Hartree, Fock and Bogoliubov terms, respectively. The third "pairing" channel needs to be included in a mean-field theory if superconducting fluctuations are relevant, otherwise it is often neglected.

A second perspective on mean-field theory is motivated from the field-theoretical approach to interacting many-body systems. One starts from a partition function Z and rewrites it in terms of a path integral over some coarse-grained field, e.g. an order parameter. Let us consider the Ising Hamiltonian (without transverse field, equivalent to the classical Ising model) for illustration:

$$\hat{H}_{\text{Ising}} = -J \sum_{\langle i,j \rangle} \hat{\sigma}_i^z \hat{\sigma}_j^z - h \sum_i \hat{\sigma}_i^z \tag{2.39}$$

The partition function reads (sum over all classical spin configurations $\underline{\sigma} = \{\sigma_1, \dots \sigma_N\}$)

$$Z_{\text{Ising}} = tr_{\mathcal{H}}\big(\mathrm{e}^{-\beta \hat{H}_{\text{Ising}}}\big) = \sum_{\underline{\sigma}} \mathrm{e}^{-\beta H_{\text{Ising}}(\underline{\sigma})} \tag{2.40}$$

Usually, one is interested in the equilibrium value of the magnetization $M = \frac{1}{N}\sum_i \sigma_i^z$. Formally, one can introduce a "coarse-grained" partition function in terms of the magnetization as follows,

$$Z_{\text{Ising}}(M) = \sum_{\underline{\sigma}} \delta\big(M - \frac{1}{N}\sum_i \sigma_i^z\big) \mathrm{e}^{-\beta H_{\text{Ising}}(\underline{\sigma})}. \tag{2.41}$$

If one is able to rewrite the Hamiltonian as a function of the magnetization (it is possible in the fully connected case), one has directly performed a coarse-graining step. The probability to measure the magnetization value M is $Z_{\text{Ising}}(M)/Z_{\text{Ising}}$ and the free energy $F(M)$ is defined as $Z(M) = \exp(-\beta F(M)))$. However, often this procedure is not possible directly. Alternatively, one can view $Z(M)$ and $F(M)$ as fundamental objects: This leads to the field theory formalism, in which one considers an abstract order parameter field $M(\vec{r})$ with a partition function of the form

$$Z_{\text{Ising}} = \int \mathcal{D}M(\vec{r})\ \mathrm{e}^{-\beta F_{\text{Ising}}[M(\vec{r})]}. \tag{2.42}$$

Here, $\mathcal{D}M(\vec{r})$ denotes the functional integration over all field configurations. It is the analogue to the restricted partition sum (2.41). The mean-field approximation is equivalent to a saddle point approximation of the integral, i.e. finding the order parameter configuration for which the free energy obeys $\partial_M F[M] = 0$. In the applications in this thesis, we usually implement the mean-field approximation directly for the Hamiltonian and derive a mean-field free energy. We then search for its saddle points to determine the self-consistent solution for the mean-fields.

2.3.2 Mean-field as a classical limit

An important class of interacting many-particle models are so-called mean-field models, which possess a parameter $\hbar_{\text{eff}}$ that controls the strength of quantum fluctuations in the theory. Usually, $\hbar_{\text{eff}} \to 0$ corresponds to a complete suppression of fluctuations, such that mean-field theory becomes exact. Values $\hbar_{\text{eff}} > 0$ allow to include the effect of fluctuations in a controlled way. That is one reason why mean-field models are also a very popular test bed for new theoretical methods. If quantum fluctuations are absent, one natural expectation is that the physics of the model should be describable in terms of a classical Hamiltonian. The limit $\hbar_{\text{eff}} \to 0$ is therefore also called a *classical limit*.

A prototypical mean-field quantum model is the fully connected transverse-field Ising model

$$\hat{H}_{\text{FC-TFIM}} = -\frac{1}{2N} \sum_{i,j=1}^{N} \hat{\sigma}_i^z \hat{\sigma}_j^z - h \sum_{i=1}^{N} \hat{\sigma}_i^x \tag{2.43}$$

with N spins and transverse field h. In nuclear physics it is also known under the name Lipkin-Meshkov-Glick (LMG) model [131]. In the model, $\hbar_{\text{eff}} = \frac{1}{N}$ and one can indeed formulate an effective classical Hamiltonian in the limit $N \to \infty$. One way to construct the classical Hamiltonian is to introduce the operator $\hat{\vec{m}} = \frac{1}{S} \sum_i \hat{\vec{\sigma}}_i$, where $S = N/2$, which allows to rewrite

$$\hat{H}_{\text{FC-TFIM}} = -N\Big(\frac{1}{2}(\hat{m}^z)^2 - hm^x\Big) \tag{2.44}$$

If one evaluates the $\hat{m}^i$-operators on coherent wave packets, one can introduce [132, 133, 134] classical conjugate variables Q and P to express the expectation values $m^z = Q$, $m^x = \sqrt{1 - Q^2}\cos(2P)$, such that

$$\hat{H}_{\text{class}} = -\frac{1}{2}Q^2 - h\sqrt{1 - Q^2}\cos(2P). \tag{2.45}$$

Models on fully connected lattices are a very convenient setup for semiclassical analysis. However, in applications one usually prefers to work on lattices with only nearest neighbor hopping. Therefore, it is desirable to explore mean-field limits that do not rely on that assumption. A related limit is the limit of high spatial dimensions d, which reproduces the aspect of a high lattice coordination number (despite the short-ranged hopping), which is also a core feature of the fully connected lattice. A famous example is presented by the Ising model on a d-dimensional cubic lattice, for which mean-field theory becomes exact in the limit $d \to \infty$ [135].

Similar results can be obtained for interacting electron models on cubic lattices. For most types of interactions, like nearest neighbor density-density, Hartree-Fock mean-field theory becomes exact in the limit $d \to \infty$ [136]. An important exception is presented by the Hubbard model with its site-local $\hat{n}_{i\uparrow}\hat{n}_{i\downarrow}$ interaction, for which Hartree-Fock is not the correct theory in high spatial dimensions [21]. Instead, one obtains *dynamical mean-field theory (DMFT)* [137].

Yet another category of mean-field theories is presented by bosonic Hamiltonians in the limit of high mode occupation numbers [138, 139]. A way to see this is to consider coherent state expectation values of the annihilation and creation operators $\langle\hat{b}\rangle \sim \sqrt{N}$ and rescale $\hat{b} \to \hat{b}/\sqrt{N}$. For the rescaled variables, $[b, b^\dagger] \sim \frac{1}{N} := \hbar_{\text{eff}}$ such that their quantum nature becomes negligible in the limit $N \to \infty$. Hence, one may formally introduce classical variables $\psi \sim \langle\hat{b}\rangle/\sqrt{N}$, which become non-fluctuating in the limit $N \to \infty$. Let us look at the Bose-Hubbard Hamiltonian as a prototypical example of an interacting many-boson Hamiltonian on a (cubic) lattice,

$$\hat{H}_{\text{BHM}} = -t_h \sum_{\langle i,j \rangle} \left(b_i^\dagger b_j + \text{H.c.} \right) + \frac{U}{2} \sum_i \hat{n}_i (\hat{n}_i - 1). \tag{2.46}$$

In the limit of large mode occupations N_i, the dynamics of the classical variables ψ_i is described by the classical *Gross-Pitaevskii Hamiltonian* [139]

$$H_{\text{GP}} = -\sum_{\langle i,j \rangle} \left(\psi_i^* \psi_j + \text{H.c.} \right) + \frac{\lambda}{2} \sum_i |\psi_i|^4, \tag{2.47}$$

where $\lambda = UN/t_h$.

2.3.3 Fermionic Large-N Models

The Gross-Pitaevskii limit of interacting bosons presents a very useful mean-field scenario that is able to capture many experimentally observable phenomena, even at strong coupling. (Spin-$\frac{1}{2}$-)Fermions lack this limit of high mode occupancy due to their intrinsic two-dimensional state space. However, one can artificially increase the number of fermion species (i.e. their degeneracy) by going from two spin species $\sigma = \uparrow, \downarrow$ to N species $\alpha = 1, \dots, N$. Such *large-N models*, also known as SU(N)-symmetric models can provide, on the one side, an analytical handle to interacting models beyond perturbation theory in the interaction strength. On the other hand, they also provide advantages for some numerical methods like quantum Monte Carlo (QMC), where a large value of N systematically suppresses the fermionic sign problem [140].

The large-N generalization of the Hubbard model (at half filling) reads as follows:

$$\hat{H}_{\text{FHM}} = -t_h \sum_{\langle i,j \rangle} \sum_{\alpha=1}^{N} (c_{i\alpha}^\dagger c_{j\alpha} + \text{H.c.}) + \frac{U}{N} \sum_i \left(\sum_{\alpha=1}^{N} \left(c_{i\alpha}^\dagger c_{i\alpha} - \frac{1}{2} \right) \right)^2 \tag{2.48}$$

For $N = 2$ the interaction term reads (using $\hat{n}_{i\sigma}^2 = \hat{n}_{i\sigma}$)

$$\begin{aligned} &\frac{U}{2} \sum_i \left(\left(\hat{n}_{i\downarrow} - \frac{1}{2} \right) + \left(\hat{n}_{i\uparrow} - \frac{1}{2} \right) \right)^2 \\ &= \frac{U}{2} \sum_i \left(2 \left(\hat{n}_{i\downarrow} - \frac{1}{2} \right) \left(\hat{n}_{i\uparrow} - \frac{1}{2} \right) + \hat{n}_{i\downarrow}^2 + \hat{n}_{i\uparrow}^2 - \left(\hat{n}_{i\downarrow} + \hat{n}_{i\uparrow} \right) + \frac{1}{2} \right) \\ &= U \sum_i \left(\hat{n}_{i\downarrow} - \frac{1}{2} \right) \left(\hat{n}_{i\uparrow} - \frac{1}{2} \right) + \text{const.} \quad , \end{aligned} \tag{2.49}$$

which coincides with the conventional fermionic Hubbard model. A very natural representation of SU(N)-symmetric models can be obtained in terms of the following flavor-averaged one-particle reduced density matrix operators,

$$\hat{\rho}_{ij} = \frac{1}{N} \sum_{\alpha=1}^{N} \left(c_{i\alpha}^\dagger c_{j\alpha} - \frac{1}{2} \delta_{ij} \right). \tag{2.50}$$

The Fermi-Hubbard model then reads

$$\hat{H}_{\text{FHM}} = \hat{H}_{\text{kin}} + \hat{H}_U = -Nt_h \sum_{\langle i,j \rangle} \big(\hat{\rho}_{ij} + \text{H.c.}\big) + UN \sum_i \hat{\rho}_{ii}^2 \tag{2.51}$$

The global prefactor N is a direct consequence of the semiclassical nature of the theory. Calculating the commutator of two ρ-operators yields

$$\big[\hat{\rho}_{ij}, \hat{\rho}_{mn}\big] = \frac{1}{N^2} \sum_{\alpha,\beta=1}^{N} \big[\hat{\rho}_{i\alpha,j\alpha}, \hat{\rho}_{m\beta,n\beta}\big] = \frac{1}{N}\big(\delta_{jm}\hat{\rho}_{in} - \delta_{in}\hat{\rho}_{mj}\big), \tag{2.52}$$

which shows that the effective $\hbar$ in the large-N models is given by $\hbar_{\text{eff}} = \frac{1}{N}$. As $N \to \infty$, the commutator vanishes and one can treat the ρ-operators like complex numbers (akin to the condensate wave function in Bose-Einstein condensates).

2.3.3.1 Equilibrium Phases in Large-N Models

In the case of the SU(N) Hubbard model the Hartree approximation (particle-hole channel) becomes exact as $N \to \infty$. We can also see this explicitly from a cluster decoupling of the interaction term:

$$\begin{aligned}
\big\langle \hat{\rho}_{ii}^2 \big\rangle &= \frac{1}{N^2} \sum_{\alpha,\beta} \big\langle c_{i\alpha}^\dagger c_{i\alpha} c_{i\beta}^\dagger c_{i\beta} \big\rangle + \ldots \\
&= \frac{1}{N^2} \sum_{\alpha,\beta} \Big(\big\langle c_{i\alpha}^\dagger c_{i\alpha} \big\rangle \big\langle c_{i\beta}^\dagger c_{n\beta} \big\rangle - \big\langle c_{i\alpha}^\dagger c_{i\beta} \big\rangle \big\langle c_{i\beta}^\dagger c_{i\alpha} \big\rangle \Big) + \ldots \\
&= \big\langle \rho_{ii} \big\rangle^2 - \frac{1}{N^2} \sum_{\alpha,\beta} \big\langle c_{i\alpha}^\dagger c_{i\beta} \big\rangle \big\langle c_{i\beta}^\dagger c_{i\alpha} \big\rangle \\
&= \big\langle \rho_{ii} \big\rangle^2 - \frac{1}{N^2} \sum_{\alpha} \big\langle c_{i\alpha}^\dagger c_{i\alpha} \big\rangle \big\langle c_{i\alpha}^\dagger c_{i\alpha} \big\rangle
\end{aligned} \tag{2.53}$$

In the last step we have assumed a flavor-diagonal state (which we consider in this thesis): the second "flavor-exchange" term is suppressed $\sim \frac{1}{N}$. Hence, in the SU(N)-Hubbard model at $N \to \infty$, only the Hartree term contributes. However, effectively, it only gives rise to a self-consistent shift of the chemical potential and therefore it cannot contribute to interesting real space order within mean-field theory. To obtain order already on the mean-field level, one needs to add additional SU(N)-symmetric terms to the Hamiltonian that stabilize certain types of order. One example is a density-density interaction term in the spirit of the extended Hubbard model

$$\hat{H}_V = NV \sum_{\langle i,j \rangle} \hat{\rho}_{ii} \hat{\rho}_{jj} \tag{2.54}$$

For a unit cell composed of at least two sites this model allows for charge-density wave order at $N \to \infty$ and even at $N = 2$.

A very important interaction term, which we will investigate later in this thesis, is given by the following Heisenberg-like Hamiltonian

$$\hat{H}_J = -\frac{NJ}{2} \sum_{\langle i,j \rangle} \big(\hat{\rho}_{ij}\hat{\rho}_{ji} + \hat{\rho}_{ji}\hat{\rho}_{ij}\big) \tag{2.55}$$

It is related to the conventional Heisenberg model: If we set $N = 2$, we can rewrite the Hamiltonian in terms of spin operators

$$\hat{\vec{S}}_i = \frac{1}{2} \sum_{\alpha,\beta=\uparrow,\downarrow} c^\dagger_{i\alpha} \vec{\sigma}_{\alpha\beta} c_{i\beta}, \tag{2.56}$$

and obtain (using that always $i \neq j$ in this case)

$$\begin{aligned} \frac{N}{2}\left(\hat{\rho}_{ij}\hat{\rho}_{ji} + \hat{\rho}_{ji}\hat{\rho}_{ij}\right) &= \frac{1}{2N} \sum_{\alpha,\beta=\uparrow,\downarrow} \left(c^\dagger_{i\alpha} c_{j\alpha} c^\dagger_{j\beta} c_{i\beta} + (i \leftrightarrow j)\right) \\ &= \ldots \overset{N=2}{=} -\hat{\vec{S}}_i \cdot \hat{\vec{S}}_j - \frac{1}{4}(n_i - 1)(n_j - 1) + \text{const.} \end{aligned} \tag{2.57}$$

The difference to the conventional Heisenberg model is a nearest-neighbor density-density interaction term. The composite SU(N)-symmetric model $\hat{H}_{\text{kin}} + \hat{H}_J + \hat{H}_U$ was first solved using field-theoretical methods by Affleck and Marston [141, 142]. The explicit inclusion of the Hubbard interaction term allows to consider the limit $U/t_{\text{h}} \to \infty$, which implies a complete suppression of charge fluctuations and would render the density-density interaction term irrelevant. The Hubbard-Heisenberg model has a rich phase diagram already for $N \to \infty$ and we give a more comprehensive overview of it and in general of research on SU(N) models in the Introduction to Sec. 5.

2.3.4 Numerical determination of self-consistent mean-field solutions

Hartree-Fock mean-field theory usually proceeds in three steps: Firstly, one needs to decouple all interaction terms such that the remaining Hamiltonian is only quadratic in the annihilation and creation operators. Secondly, one diagonalizes this mean-field Hamiltonian in order to obtain a set of mean-field modes and a set of self-consistency conditions. Thirdly, one needs to find a self-consistent solution for all mean-fields, which also agrees with the desired particle number and temperature.

For carrying out the third step, more than one method exists. In this thesis we view mean-field solutions as minima (more generally, saddle points) of a free energy function F, which at zero temperature coincides with the total energy $\langle H \rangle$. The free energy needs to be written in terms of all the mean-fields. A very flexible method to search for minima of such generically complicated functions is *simulated annealing*, which is based on an artificial thermal random walk in the free energy landscape. It is also suggested in Marston's and Affleck's paper [142] as a method to determine the mean-field solution of the Hubbard-Heisenberg model. The basic idea is as follows: One defines an artificial initial temperature $T_0 > 0$ and chooses a random initial state $\underline{x}_0$. In each iteration of the procedure a new random state $\underline{x}_{i+1}$ is generated from the old and one compares their free energies.

- If the free energy of the new state is lower than in the old state, the algorithm discards the old state and continues with the new.
- If the free energy of the new state is not lower than in the old state, one discards the old state with a Boltzmann probability $\exp\big(-(F(\underline{x}_{i+1}) - F(\underline{x}_i))/T_i\big)$.

The temperature T_i is lowered during each iteration at a predefined rate. The algorithm stops after a predetermined number of iterations and yields the state with the lowest free energy of all the iterations. An advantage of the algorithm is that it is able to escape from local minima, which are no global minima. After some experiments with a self-written code, we mostly used the `dual_annealing` routine of the `scipy` numerical library [143] for Python. It implements the idea described above but adds a few more tricks to speed up convergence. Usually, 3000 iterations yield good convergence. If self-consistent solutions with specific symmetry properties are desired, we reduced the number of mean-fields to a minimal amount. The self-consistency conditions are always used as a check to validate the correctness of the minimum.

2.3.5 Mean-field theory out-of-equilibrium

In order to apply mean-field theory for time evolution, one starts with a derivation of a mean-field Hamiltonian H^{HF} obtained within time-independent Hartree-Fock theory. The entries of the one-particle reduced density matrix $\rho_{i\sigma,j\tau} = \langle c^{\dagger}_{i\sigma} c_{j\tau}\rangle$ will usually occur as mean-fields, which are self-consistently determined in equilibrium. If one derives the equation of motion for the creation and annihilation operators $-i\partial_t c_{i\sigma} = \left[H^{\mathrm{HF}}[\rho(t)], c_{i\sigma}\right]$, while keeping the mean-fields as numbers, one obtains *time-dependent Hartree-Fock theory* [144]. Another, equivalent, perspective is to start from the equation of motion for $\rho_{i\sigma,j\tau}$ and to decouple the right hand side. This yields, in general, a non-linear equation of motion for the one-particle reduced density matrix that one needs to solve numerically. From the time-diagonal quantities $\rho_{i\sigma,j\tau}(t)$ one can also calculate, in a second iteration, Green's functions like $G^{<}_{i\sigma,j\tau}(t_{\mathrm{hor}}, \tau) = i\langle c^{\dagger}_{i\sigma}(t_{\mathrm{hor}} + \tau) c_{j\tau}(t_{\mathrm{hor}})\rangle$ by deriving their equations of motion and using the previously obtained time-diagonal data. Such equations of motion for the Green's functions generically have the following structure (for general time arguments t, t') [113]:

$$-i\partial_t G^{<,>}_{i\sigma,j\tau}(t,t') = \sum_{m\mu} \Big(h_{i\sigma,m\mu}(t) + \Sigma^{\mathrm{HF}}_{i\sigma,m\mu}[\rho(t)] \Big) G^{<,>}_{m\mu,j\tau}(t,t'), \tag{2.58}$$

This is the Hartree-Fock level of the Kadanoff-Baym equations of motion for the Green's function [113]. $\Sigma^{\mathrm{HF}}_{i\sigma,m\mu}$ is the Hartree-Fock self-energy, which depends on the time-diagonal $G^{<}(t,t)$, i.e. on $\rho(t)$.

Time-dependent Hartree-Fock is the lowest order of a whole dynamical hierarchy called the *Bogoliubov–Born–Green–Kirkwood–Yvon (BBGKY)* hierarchy [145]. The next order of the hierarchy would include the two-particle reduced density matrix $\langle c^{\dagger}_i c^{\dagger}_m c_n c_j\rangle$ (or its connected analogue) into the equations of motion and decouple three-particle terms into sums and products of one- and two-particle terms.

2.4 Phase Space Methods

The concept of phase space appears very naturally in classical mechanics as the space of all possible position-momentum pairs $(\vec{q}, \vec{p})$. A classical Hamiltonian gives rise to an incompressible (Liouville's theorem) flow on phase space via Hamilton's equations of motion. In a classical many-particle system one can easily define distribution functions $\rho(\underline{q}, \underline{p}, t)$ that encode the number of particles found in a unit volume element $\mathrm{d}^n \underline{q}\, \mathrm{d}^n \underline{p}$ at time t. A famous example is provided by the Boltzmann distribution.

In quantum mechanics, due to the non-vanishing commutator $\big[\hat{q}, \hat{p}\big] = i\hbar$, it is not possible to straightforwardly carry over the phase space concept. Most importantly, it is not possible to fix both the position and the momentum of a particle at the same time. The mathematical connections of quantum and classical mechanics, in particular the question how to systematically "quantize" a classical system, remains an active topic of research [146]. Nevertheless, it is possible to construct classical analogies to quantum systems in a systematic way. These allow for *semi-classical* approximations like the truncated Wigner approximation (TWA).

2.4.1 Phase Space Formulation of Quantum Dynamics

A deceptive analogy between classical and quantum mechanics is based on the apparent similarity of Poisson brackets and commutators. Both occur in equations of motion with the same algebraic structure, namely the Hamiltonian flow $\frac{\mathrm{d}}{\mathrm{d}t} f = \big\{f, H\big\} + \partial_t f$ of a phase space function $f(\underline{q}, \underline{p}, t)$ and Heisenberg's equation of motion $\partial_t \hat{O} = -\frac{i}{\hbar}\big[\hat{O}, \hat{H}\big] + \partial_t \hat{O}$ of an observable $\hat{O}$ (where $\partial_t \hat{O}$ refers to the time derivative in the Schrödinger picture).

However, it was noticed already early in the history of quantum mechanics that the quantization recipe to "replace Poisson brackets by commutators $\big\{\bullet, \bullet\big\} \to -\frac{i}{\hbar}\big[\bullet, \bullet\big]$" is incomplete. The *Groenewold-van Hove theorem* [147, 148] states that one cannot consistently quantize the Poisson algebra $\mathcal{P}$ of all polynomials in q_i and p_j. Quantization in the sense of the theorem refers to a map $\mathcal{Q}$ from (a subalgebra of) the Poisson algebra $\mathcal{P}$ to the space of Hermitian operators, which obeys a number of rules (see e.g. [149]) like $\mathcal{Q}\big(\big\{f, g\big\}\big) = -\frac{i}{\hbar}\big[\mathcal{Q}(f), \mathcal{Q}(g)\big]$. The proof of the theorem is based on contradiction: One can, for example, start from the classical equality $\big\{q^3, p^3\big\} = 3\big\{q^2 p, q p^2\big\}$ and show that the application of $\mathcal{Q}$ leads to different results on the two sides of the equation. Nevertheless, a quantization in the original sense is possible on certain subalgebras of $\mathcal{P}$ like the algebra of all polynomials of degree at most two, $\big\{1, q, p, q^2, qp, p^2\big\}$ or the "coordinate algebra" $\mathcal{C} = \big\{\sum_{i=1}^n f^i(\underline{q}) p_i + g(\underline{q})\big\}$ for polynomials f^i and g [149]. However, in applications beyond the harmonic oscillator, Hamiltonians (with quartic interaction terms) do usually not live in such closed subalgebras. Luckily, despite this famous Groenewold-van Hove no-go theorem, constructive ways to assign classical phase space functions to quantum operators exist. The most common approach is to relax the Poisson bracket/commutator correspondence and introduce *Moyal brackets* instead of Poisson brackets. Mathematically speaking, Moyal brackets are deformations of Poisson brackets that agree with them to leading order in $\hbar$.

There are many different possible choices how to construct Moyal brackets and classical phase space analogies to quantum operators. Usually, one associates a classical phase space function to a specific ordering of quantum operators. The most important scheme is **Wigner-Weyl quantization**, which corresponds to symmetric ordering of operators. Nevertheless, other ordering prescriptions are possible and give rise to the Husimi or Glauber-Sudarshan formalism, for instance. In the following, we will only discuss the Wigner-Weyl formalism in more detail.

The phase space function associated to the operators is called *Weyl symbol*. Let us look at the example of single-particle quantum mechanics with the operators $\hat{q}$ and $\hat{p}$. For now, we denote Weyl symbols with a lattice subscript W. We associate $\hat{x} \mapsto x_{\mathrm{W}}$, $\hat{p} \mapsto p_{\mathrm{W}}$ and $\frac{1}{2}\big(\hat{x}\hat{p} + \hat{p}\hat{x}\big) \mapsto x_{\mathrm{W}}p_{\mathrm{W}}$. In case one wants to calculate Weyl symbols of generic – not necessarily symmetrically ordered – operators, the following transformation formula exists (some authors exchange $\xi \leftrightarrow -\xi$):

$$\Omega_{\mathrm{W}}(\underline{q}, \underline{p}) = \int \mathrm{d}\underline{\xi}\ \mathrm{e}^{\frac{i}{\hbar}\underline{p}\cdot\underline{q}} \left\langle \underline{q} - \underline{\xi}/2 \,\middle|\, \hat{\Omega}(\underline{\hat{q}}, \underline{\hat{p}}) \,\middle|\, \underline{q} + \underline{\xi}/2 \right\rangle \tag{2.59}$$

Here $|\underline{q}\rangle$ are position eigenstates. For example ($d = 1$),

$$\begin{aligned} (\hat{q})_{\mathrm{W}} &= \int_{-\infty}^{\infty} \mathrm{d}\xi\ \mathrm{e}^{\frac{i}{\hbar}p\xi}\, \langle q - \xi/2 \,|\, \hat{q} \,|\, q + \xi/2 \rangle \\ &= \int_{-\infty}^{\infty} \mathrm{d}\xi\ \mathrm{e}^{\frac{i}{\hbar}p\xi} \Big(q - \frac{\xi}{2}\Big)\, \underbrace{\langle q - \xi/2 \,|\, q + \xi/2 \rangle}_{\delta(\xi)} = q \end{aligned} \tag{2.60}$$

$$\begin{aligned} (\hat{p})_{\mathrm{W}} &= \int_{-\infty}^{\infty} \mathrm{d}\xi\ \mathrm{e}^{\frac{i}{\hbar}p\xi}\, \langle q + \xi/2 \,|\, \hat{p} \,|\, q - \xi/2 \rangle \\ &= \int_{-\infty}^{\infty} \mathrm{d}\xi\ \mathrm{e}^{\frac{i}{\hbar}p\xi}\, \langle q - \xi/2 | \int_{-\infty}^{\infty} \mathrm{d}p'\ \ |p'\rangle\, \langle p' |\, \hat{p} | q + \xi/2 \rangle \\ &= \int_{-\infty}^{\infty} \mathrm{d}\xi\ \mathrm{e}^{-\frac{i}{\hbar}p\xi} \int_{-\infty}^{\infty} \mathrm{d}p'\ \mathrm{e}^{\frac{i}{\hbar}p' q + \frac{\xi}{2})} \mathrm{e}^{-\frac{i}{\hbar}p'(q - \frac{\xi}{2})} p'/h \\ &= \int_{-\infty}^{\infty} \mathrm{d}p'\ \underbrace{\int_{-\infty}^{\infty} \mathrm{d}\xi\ \mathrm{e}^{\frac{i}{\hbar}(p'-p)\xi}}_{h\delta(p-p')} p'/h = p \end{aligned} \tag{2.61}$$

$$\begin{aligned} (\hat{q}\hat{p})_{\mathrm{W}} &= \int_{-\infty}^{\infty} \mathrm{d}\xi\ \mathrm{e}^{\frac{i}{\hbar}p\xi}\, \langle x + \xi/2 \,|\, \hat{x}\hat{p} \,|\, x - \xi/2 \rangle \\ &= \int_{-\infty}^{\infty} \mathrm{d}p'\ p'/h \int_{-\infty}^{\infty} \mathrm{d}\xi\ (x + \frac{\xi}{2}) \mathrm{e}^{\frac{i}{\hbar}(p'-p)\xi} \\ &= xp + \frac{1}{2h} \int_{-\infty}^{\infty} \mathrm{d}p'\ p' \int_{-\infty}^{\infty} \mathrm{d}\xi\ \xi \mathrm{e}^{\frac{i}{\hbar}(p'-p)\xi} \\ &= xp + \frac{1}{2h} \int_{-\infty}^{\infty} \mathrm{d}p'\ p'(i\hbar\partial_p) \int_{-\infty}^{\infty} \mathrm{d}\xi\ \mathrm{e}^{\frac{i}{\hbar}(p'-p)\xi} \\ &\overset{p_{\mathrm{W}}}{=} xp + \frac{1}{2h}(i\hbar\partial_p)(ph) = xp + \frac{i\hbar}{2} \end{aligned} \tag{2.62}$$

The last identity demonstrates that the non-symmetric operator ordering leads to $\hbar$-corrections. One obtains $(\hat{p}\hat{q})_{\mathrm{W}} = qp - i\hbar/2$ and hence $\big([\hat{q}, \hat{p}]\big)_{\mathrm{W}} = i\hbar$ and $(\frac{1}{2}\{\hat{q}, \hat{p}\})_{\mathrm{W}} =$

qp, as expected. The last identity (2.62) can also be obtained by using *Moyal products*. In the Wigner-Weyl formalism, the Moyal product of two Weyl symbols Ω_1, Ω_2 can be written as follows [150],

$$\big(\Omega_1\Omega_2\big)_{\mathrm{W}}(\underline{q},\underline{p}) = \Omega_{1\mathrm{W}}\mathrm{e}^{-\frac{i\hbar}{2}\Lambda}\Omega_{2\mathrm{W}}, \quad \text{where} \quad \Lambda := \sum_i \Big(\frac{\overleftarrow{\partial}}{\partial p_i}\frac{\overrightarrow{\partial}}{\partial q_i} - \frac{\overleftarrow{\partial}}{\partial q_i}\frac{\overrightarrow{\partial}}{\partial p_i}\Big) \tag{2.63}$$

The arrows indicate the direction, in which the derivative needs to be executed. The Moyal bracket $\{\Omega_1, \Omega_2\}_{\mathrm{M}}$, which is the Weyl transform of $-\frac{i}{\hbar}[\hat{\Omega}_1, \hat{\Omega}_2]$, can be written in the following way:

$$\{\Omega_1, \Omega_2\}_{\mathrm{M}} = -\frac{2}{\hbar}\Omega_{1\mathrm{W}} \sin\Big(\frac{\hbar}{2}\Lambda\Big)\Omega_{2\mathrm{W}} \tag{2.64}$$

Insertion of the power series of the sine function precisely recovers the Poisson bracket to leading order. The Weyl symbol of the density matrix $\hat{\rho}(t)$ is called the *Wigner function* $W(\hat{q}, \hat{p}, t)$. A central property of the Weyl transform is that it translates traces of operator products into phase space integrals over their Weyl symbols,

$$\mathrm{tr}\,\big(\hat{\Omega}_1\hat{\Omega}_2\big) = \int \mathrm{d}^d\underline{q} \int \mathrm{d}^d\underline{p}\; \Omega_{1\mathrm{W}}(\underline{q},\underline{p})\Omega_{2\mathrm{W}}(\underline{q},\underline{p}) \tag{2.65}$$

A direct consequence of this is the following important formula for the evaluation of quantum mechanical expectation values:

$$\big\langle\hat{\Omega}(\hat{q},\hat{p},t)\big\rangle = \mathrm{tr}\,\big(\hat{\rho}\hat{\Omega}\big) = \int \mathrm{d}^d\underline{q} \int \mathrm{d}^d\underline{p}\; W(\underline{q},\underline{p},t)\Omega_{\mathrm{W}}(\underline{q},\underline{p},t) \tag{2.66}$$

Hence, if the full Wigner function at time t is known, one can evaluate expectation values of all quantum observables for which the Weyl symbols are known.

The Wigner-Weyl quantization scheme for positions $\hat{q}_i$ and momenta $\hat{p}_j$ can be carried over to bosonic mode operators $\hat{\psi}_i$ with $[\hat{\psi}_i, \hat{\psi}_j^\dagger] = \delta_{ij}$. Instead of position eigenstates, bosonic coherent states are used in the definition of the transformation rule. We write $|\psi_0\rangle = \exp(-\frac{1}{2}|\psi_0|^2)\sum_n \psi_0^n/\sqrt{n!}\,|n\rangle$ for a normalized coherent state (Caveat: Polkovnikov [150] uses non-normalized coherent states). The adapted transformation rule reads

$$\Omega_{\mathrm{W}}(\underline{\psi},\underline{\bar{\psi}}) = \int \mathrm{d}(\underline{\xi},\underline{\bar{\xi}})\; \mathrm{e}^{\frac{1}{2}\left(\underline{\bar{\xi}}\cdot\underline{\psi}-\underline{\xi}\cdot\underline{\bar{\psi}}\right)} \Big\langle \underline{\psi} - \underline{\xi}/2 \Big| \hat{\Omega}(\underline{\hat{\psi}},\underline{\hat{\psi}}^\dagger) \Big| \underline{\psi} + \underline{\xi}/2 \Big\rangle \tag{2.67}$$

In order to write down the classical phase space representation of the dynamics in the model, we need to calculate the Weyl symbol of the Hamiltonian. The hopping term transforms straightforwardly, the interaction term has to be symmetrized before.

2.4.2 Truncated Wigner Approximation

We have seen that eqn. (2.66) allows to calculate arbitrary time-dependent expectation values of observables if the full time-evolved Wigner function is known. The evolution equation for the Wigner function can be obtained from the von Neumann equation $i\hbar\partial_t\hat{\rho} = [\hat{H}, \hat{\rho}]$ upon Weyl transform:

$$\partial_t W(\underline{\psi},\underline{\bar{\psi}},t) = \big\{H_{\mathrm{W}}(\underline{\psi},\underline{\bar{\psi}},t), W(\underline{\psi},\underline{\bar{\psi}},t)\big\}_{\mathrm{M}} \tag{2.68}$$

As we have seen, one can expand the Moyal bracket (2.64) in $\hbar$ and we can truncate this expansion at the leading order, which gives rise to

$$\partial_t W(\underline{\psi}, \underline{\bar{\psi}}, t) = \big\{ H_\mathrm{W}(\underline{\psi}, \underline{\bar{\psi}}, t), W(\underline{\psi}, \underline{\bar{\psi}}, t) \big\}. \tag{2.69}$$

Here, the curly brackets refer to regular Poisson brackets. The dynamical scheme so obtained is called **truncated Wigner approximation (TWA)**. An important aspect about eqn. (2.69) is its formal analogy to the classical Liouville equation, which describes the propagation of a classical distribution function on phase space. In classical mechanics, the Liouville equation is usually derived from Hamilton's equations of motion. In the TWA context, one can argue the other way around via the method of characteristics [150]. The latter is a technique commonly used for the analysis of partial differential equations. It is based on the conservation of $W(\underline{\psi}, \underline{\bar{\psi}}, t)$ along the trajectories generated by H_W. Those trajectories are precisely governed by Hamilton's equations of motion for the classical Hamiltonian,

$$W(\underline{\psi}(t), \underline{\bar{\psi}}(t), t) = W(\underline{\psi}(t_0), \underline{\bar{\psi}}(t_0), t_0), \qquad \underline{\psi}(t) = \frac{\partial H_\mathrm{W}}{\partial \underline{\bar{\psi}}}. \tag{2.70}$$

This relation allows us to reformulate eqn. (2.66) for expectation values at time t in terms of propagated classical variables with initial conditions $\underline{\psi}(t = 0) = \underline{\psi}_0$ at time $t_0 = 0$:

$$\begin{aligned} \big\langle \hat{\Omega}(\underline{\hat{\psi}}, \underline{\hat{\psi}}^\dagger, t) \big\rangle &= \int \mathrm{d}^d(\underline{\psi}, \underline{\bar{\psi}})\; W(\underline{\psi}, \underline{\bar{\psi}}, t)\, \Omega_\mathrm{W}(\underline{\psi}, \underline{\bar{\psi}}, t) \\ &\equiv \int \mathrm{d}^d\big(\underline{\psi}(t), \underline{\bar{\psi}}(t)\big)\; W(\underline{\psi}(t), \underline{\bar{\psi}}(t), t)\, \Omega_\mathrm{W}(\underline{\psi}(t), \underline{\bar{\psi}}(t), t) \\ &= \int \mathrm{d}^d\big(\underline{\psi}_0, \underline{\bar{\psi}}_0\big)\; W(\underline{\psi}_0, \underline{\bar{\psi}}_0, t_0)\, \Omega_\mathrm{W}(\underline{\psi}(t), \underline{\bar{\psi}}(t), t) \end{aligned} \tag{2.71}$$

We have implicitly used the fact that the volume element $\mathrm{d}^d\big(\underline{\psi}_0, \underline{\bar{\psi}}_0\big)$ does not change under the Hamiltonian time propagation (Liouville's theorem). Eqn. (2.71) now offers a natural interpretation in terms of Monte Carlo sampling. The Wigner distribution at initial time t_0 plays the role of a statistical weight for the initial values of the classical variables, which are propagated using the classical equations of motion.

The derivation of TWA from the von Neumann equation is the most transparent but it is not very useful when it comes to a calculation of corrections to the mean-field dynamics beyond TWA. In fact, the next order in $\hbar$ in the expansion of the Moyal bracket gives rise to a very complicated partial differential equation, which is not solvable any more using the method of characteristics. However, another route – pioneered by Anatoli Polkovnikov [151, 150] – proceeds via the path integral representation of the Keldysh formalism. Here, TWA is the leading order result of an expansion in quantum fluctuations. Besides this reassuring fact, the path integral formalism also enables one to derive a scheme for corrections to TWA based on the concept of quantum jumps. Although one can indeed show for simple examples that quantum jump corrections lead to more accurate results, their implementation remains tedious and inefficient.

2.4.3 Variations on a Theme by Wigner

The original TWA method describes the dynamics of bosons in the regime of high occupation numbers. However, it turns out that the idea at the heart of TWA, i.e. averaging over mean-field trajectories with fluctuating initial conditions, can be applied as well to many other quantum systems. A very efficient tool to transfer the bosonic formalism to other setups is the Schwinger boson representation [152, 112]. If generic operators $\hat{X}_\alpha$ obey commutation relations $\left[\hat{X}_\alpha, \hat{X}_\beta\right] = i\sum_\gamma f_{\alpha\beta\gamma}\hat{X}_\gamma$ for structure constants $f_{\alpha\beta\gamma}$ one needs to find a $d \times d$ matrix form $(X_\alpha)_{ij}$ of these operators. The matrix allows to construct a bosonic representation ("Jordan map" [112]) $\hat{X}_\alpha \mapsto a_i^\dagger (X_\alpha)_{ij} a_j$ of $\hat{X}_\alpha$ for bosonic annihilation and creation operators a_i, $i = 1, \dots, d$, which obeys the original commutation relations by design. For TWA schemes, the advantage of such a representation is the possibility to straightforwardly define the Weyl symbols $X_\alpha^{\mathrm{cl}} := \left(a_i^\dagger (X_\alpha)_{ij} a_j\right)_{\mathrm{W}}$. The equation of motion follows automatically and reads [152]

$$\partial_t X_\alpha^{\mathrm{cl}} = \sum_{\beta\gamma} f_{\alpha\beta\gamma} \frac{\partial H_{\mathrm{W}}}{\partial X_\beta^{\mathrm{cl}}} X_\gamma^{\mathrm{cl}}. \tag{2.72}$$

The most straightforward extension of this type is TWA for spins. Let us consider a collection of spin operators $\left\{\hat{S}_i^\alpha\right\}$, which obey the spin algebra $\left[\hat{S}_i^\alpha, \hat{S}_j^\beta\right] = i\delta_{ij}\epsilon_{\alpha\beta\gamma}\hat{S}_i^\gamma$. $\alpha = x, y, z$ labels the spin component and i is the site index. One can introduce two families of bosonic operators $\{a_i\}$ and $\{b_j\}$ as follows:

$$\hat{S}_i^x = \frac{1}{2}\left(a_i^\dagger b_i + b_i^\dagger a_i\right), \quad \hat{S}_i^y = \frac{i}{2}\left(a_i^\dagger b_i - b_i^\dagger a_i\right), \quad \hat{S}_i^z = \frac{1}{2}\left(b_i^\dagger b_i - a_i^\dagger a_i\right) \tag{2.73}$$

If the bosons obey the canonical commutation relations, the spin operators obey the spin algebra. To be consistent, the Schwinger bosons need to satisfy the following constraint:

$$a_i^\dagger a_i + b_i^\dagger b_i = 2S, \tag{2.74}$$

where S is the total spin. Constraints of this kind are not problematic within TWA because $a_i^\dagger a_i + b_i^\dagger b_i$ commutes with all spin Hamiltonians and this conservation law is respected by the Hamiltonian dynamics [150]. This representation allows one to carry over the bosonic TWA formalism to spin systems. In the context of this "traditional" TWA method, one way to systematically improve the validity of the method is to artificially enlarge the classical phase space via the introduction of additional variables. One remarkable demonstration of this technique is due to Davidson and Polkovnikov [152], who embedded an interacting spin-$\frac{1}{2}$ system into a larger algebra of SU(3) spins allowing them to express certain operators like $\hat{S}_z^2$, which are quadratic in the SU(2) language, as linear operators in the SU(3) formulation. Because the dynamics of linear operators is exact within TWA, this increases the validity of the method. However, it is not so easy any more to determine exact Wigner functions for these extended sets of variables. Therefore, one would usually construct approximate (Gaussian) Wigner functions that correctly reproduce the lowest moments of the initial state. Another variation of the topic is the cluster truncated Wigner approximation (CTWA) scheme for spin systems [153]. It is based on the formation of real-space clusters of spins, which are represented as linear operators in TWA. The method has been used to study transport in spin chains [154]. However, the breaking of the spatial translational invariance due to the definition of the clusters is a downside of the method.

These extensions of the original TWA are usually based on smooth probability distribution models for the Wigner function (mostly Gaussians). However, modern variants of the TWA use a more fine tuned sampling scheme, which gives rise to the so-called *discrete TWA* [155] and provides another improvement of the TWA method.

2.5 Fermionic TWA (aka stochastic mean-field approach)

The "traditional" TWA described above is a theory for interacting bosonic (and spin) systems. Fermions, in contrast, do not allow for a classical limit of Gross-Pitaevskii type, their internal state space is usually two-dimensional ($\sigma =\uparrow,\downarrow$). Nevertheless, one can formulate a TWA scheme for fermionic degrees of freedom [112], which is based on a Schwinger boson representation of fermionic bilinears

$$\hat{\rho}_{\alpha\beta} = \frac{1}{2}\big(c^\dagger_\alpha c_\beta - c_\beta c^\dagger_\alpha\big) = c^\dagger_\alpha c_\beta - \frac{1}{2}\delta_{\alpha\beta} \quad \text{and} \quad \hat{\tau}_{\alpha\beta} = c_\alpha c_\beta. \tag{2.75}$$

These bilinears define a set of phase space coordinates by means of their closed so($2n$) commutator structure

$$\begin{aligned} \big[\hat{\rho}_{\alpha\beta}, \hat{\rho}_{\gamma\delta}\big] &= \delta_{\gamma\beta}\hat{\rho}_{\alpha\delta} - \delta_{\alpha\delta}\hat{\rho}_{\gamma\beta} \\ \big[\hat{\rho}_{\alpha\beta}, \hat{\tau}_{\gamma\delta}\big] &= \delta_{\alpha\gamma}\hat{\tau}_{\delta\beta} - \delta_{\alpha\delta}\hat{\tau}_{\gamma\beta} \\ \big[\hat{\tau}^\dagger_{\alpha\beta}, \hat{\tau}_{\gamma\delta}\big] &= -\delta_{\alpha\delta}\hat{\rho}_{\beta\delta} + \delta_{\alpha\gamma}\hat{\rho}_{\beta\delta} - \delta_{\beta\delta}\hat{\rho}_{\alpha\delta} + \delta_{\beta\delta}\hat{\rho}_{\alpha\gamma} \end{aligned} \tag{2.76}$$

The ρ-operators obey, in particular, $\hat{\rho}^\dagger_{\alpha\beta} = \hat{\rho}_{\beta\alpha}$. It is important to note that they already form a closed algebra such that one can also set up consistent TWA schemes without explicit inclusion of the τ-variables. These commutation relations can formally be implemented via the Schwinger boson scheme introduced in the last section. The operators $\hat{\rho}_{\alpha\beta}$ and $\hat{\tau}_{\alpha\beta}$ are replaced by their associated classical phase space variables $\rho_{\alpha\beta}$ and $\tau_{\alpha\beta}$. However, the classical representation of the Hamiltonian is non-unique as we discuss further below. The semiclassical scheme so obtained is called fermionic TWA (fTWA) and has not seen many applications so far. fTWA was used to study the thermalization and echo dynamics in SYK models [112, 156] as well as the non-equilibrium dynamics in disordered Hubbard models [157, 158, 159].

A natural index set of fermionic lattice models is $\alpha = i\sigma$ for lattice site i and spin index σ. As indices α for the Hubbard model we consider site index i and spin index σ: $\alpha = i\sigma$. For a lattice with L sites, the classical ρ-variables give rise to a Hermitian matrix

$$(\rho_{\sigma\tau}) = \begin{pmatrix} \rho_{0\sigma,0\tau} & \cdots & \rho_{0\sigma,L\tau} \\ \cdots & \cdots & \cdots \\ \rho_{L\sigma,0\tau} & \cdots & \rho_{L\sigma,0\tau} \end{pmatrix}, \qquad (\rho) = \begin{pmatrix} (\rho_{\uparrow\uparrow}) & (\rho_{\uparrow\downarrow}) \\ (\rho_{\downarrow\uparrow}) & (\rho_{\downarrow\downarrow}) \end{pmatrix} \tag{2.77}$$

of size $2L \times 2L$ with in general $2L^2 + L$ independent complex entries. Similarly, the τ operators constitute an anti-Hermitian matrix.

2.5.1 Equations of motion

The classical representation of a fermionic Hamiltonian is in general not unique (it is if flavor-averaged variables are used, which is the case for most of this thesis). Choices of classical Hamiltonians correspond to mean-field decouplings of interaction terms. Given a choice of a decoupling, the classical equations of motion coincide with the time-dependent Hartree-Fock equations for the respective decoupling. Equivalently, one can derive the equations of motion in purely classical terms using (for compactness only written for the $\rho_{i\sigma,j\tau}$)

$$i\partial_t \rho_{i\sigma,j\tau} = \{\rho_{i\sigma,j\tau}, H_\mathrm{W}\} \tag{2.78}$$

with the Poisson bracket

$$\{\rho_{i\sigma,j\tau}, H_\mathrm{W}\} = \sum_{k\kappa} \frac{\partial H_\mathrm{W}}{\partial \rho_{j\tau,k\kappa}} \rho_{i\sigma,k\kappa} - \sum_{k\kappa} \frac{\partial H_\mathrm{W}}{\partial \rho_{k\kappa,i\sigma}} \rho_{k\kappa,j\tau}. \tag{2.79}$$

These equations are precisely Hamilton's equations of motion for the classical Hamiltonian. As an example we consider the Hubbard interaction term

$$\hat{H}_U = U \sum_i c^\dagger_{i\uparrow} c_{i\uparrow} c^\dagger_{i\downarrow} c_{i\downarrow} \tag{2.80}$$

A decoupling in the Hartree ("direct") channel

$$\hat{H}_U = U \sum_i c^\dagger_{i\uparrow} c_{i\uparrow} c^\dagger_{i\downarrow} c_{i\downarrow} \quad \longrightarrow \quad H_\mathrm{W} = U \sum_i (\rho_{i\uparrow,i\uparrow} + \frac{1}{2})(\rho_{i\downarrow,i\downarrow} + \frac{1}{2}) \tag{2.81}$$

yields the following equations of motion for the ρs:

$$\begin{aligned} i\partial_t \rho_{i\sigma,j\sigma} &= U(\rho_{j\bar\sigma,j\bar\sigma} - \rho_{i\bar\sigma,i\bar\sigma})\rho_{i\sigma,j\sigma} \\ i\partial_t \rho_{i\sigma,j\bar\sigma} &= U(\rho_{j\sigma,j\sigma} - \rho_{i\bar\sigma,i\bar\sigma})\rho_{i\sigma,j\bar\sigma} \end{aligned} \tag{2.82}$$

In the classical formalism, these equations follow from

$$\frac{\partial H_\mathrm{W}}{\partial \rho_{i\sigma,j\tau}} = \delta_{\sigma\tau} \begin{cases} U\left(\rho_{i\bar\sigma,i\bar\sigma} + \frac{1}{2}\right), & i = j \\ 0, & \text{else.} \end{cases} \tag{2.83}$$

Note that the dynamics of the spin-diagonal ρ-variables is determined by the other spin-diagonal variables alone. In contrast, a decoupling in the Fock ("exchange") channel

$$\hat{H}_U \quad \longrightarrow \quad H_\mathrm{W} = -U \sum_i \rho_{i\uparrow,i\downarrow} \rho_{i\downarrow,i\uparrow} \tag{2.84}$$

gives rise to a different set of equations of motion

$$i\partial_t \rho_{i\sigma,j\tau} = -U(\rho_{j\bar\tau,j\tau}\rho_{i\sigma,j\bar\tau} - \rho_{i\sigma,i\bar\sigma}\rho_{i\bar\sigma,j\tau}). \tag{2.85}$$

One cannot say in general, which decoupling or which combination of decouplings gives rise to the most precise semiclassical description, this has to be figured out for each individual problem. A particularly curious case is presented by the SYK model, whose relaxation dynamics from an initial product state can be described very accurately within fTWA [112] but only for a pure τ-representation of the interaction term. It is not at all obvious why this is the case.

Instead of a solution in real space, one can as well solve the mean-field equations of motion in momentum space. The transformation of the c-operators for periodic boundary conditions,

$$c^\dagger_{\vec{k}\sigma} = \frac{1}{\sqrt{V}} \sum_{\vec{r}_i} \mathrm{e}^{-i\vec{k}\cdot\vec{r}_i} c^\dagger_{i\sigma}, \tag{2.86}$$

gives rise to a transformation of the ρ-operators yielding the following equation of motion

$$i\partial_t \rho_{k\sigma,l\sigma} = -\left(\epsilon(\vec{k}) - \epsilon(\vec{l})\right) \rho_{\vec{k}\sigma,\vec{l}\sigma} + \frac{U}{V} \sum_{\vec{s},\vec{p}} \left[\rho_{(\vec{p}+\vec{s}-\vec{l})\bar{\sigma},\vec{p}\bar{\sigma}} \rho_{\vec{k}\sigma,\vec{s}\sigma} - \rho_{(\vec{p}+\vec{k}-\vec{s})\bar{\sigma},\vec{p}\bar{\sigma}} \rho_{\vec{s}\sigma,\vec{l}\sigma}\right]. \tag{2.87}$$

Both representations are equivalent, the real space equations of motion are easier to solve numerically because the sum needs to be carried out only over nearest-neighbor sites in contrast to a sum over all momenta.

We close this subsection with a general remark on (f)TWA and symmetries. Although, e.g., the Hubbard model hosts many symmetries like translational invariance or spin-flip symmetry, not all of them can be used to reduce the computational complexity of fTWA. The guiding question is whether a reduced set of operators generates a closed Poisson algebra with the Hamiltonian. The spin-diagonal ρ-operators, for instance, do so for the Hubbard model and one can restrict the dynamics to this subset (unless non-diagonal are explicitly required, for example in the case of a decoupling in the Fock channel). In contrast, one cannot make use of translational invariance in the same way. This symmetry is only restored as a result of the Wigner function averaging and one can use the deviation from the perfect symmetry as a measure for the convergence of the calculation.

2.5.2 Model for the Wigner function

Within fTWA, the Wigner function $W(\underline{\rho})$ is usually modeled in terms of a multivariate Gaussian distribution [112] with means and connected covariances determined from the respective values of the quantum mechanical initial state. Since already the spin-diagonal ρs form a closed algebra, we focus on them:

$$\begin{aligned} \langle \rho_{i\sigma,j\sigma} \rangle_W &\overset{!}{=} \langle \hat{\rho}_{i\sigma,j\sigma} \rangle_{\mathrm{QM}}, \\ \left\langle \rho^*_{i\sigma,j\sigma} \rho_{k\tau,l\tau} \right\rangle^{\mathrm{c.c.}}_W &\overset{!}{=} \frac{1}{2} \left\langle \left\{ \hat{\rho}^\dagger_{i\sigma,j\sigma}, \hat{\rho}_{k\tau,l\tau} \right\} \right\rangle^{\mathrm{c.c.}}_{\mathrm{QM}}. \end{aligned} \tag{2.88}$$

A multivariate Gaussian distribution has the following form

$$W(z) \sim \exp\left\{ -\frac{1}{2} \left((\underline{z} - \underline{\mu})^T, (\underline{\bar{z}} - \underline{\bar{\mu}})^T \right) \begin{pmatrix} \Gamma & C \\ \bar{C} & \bar{\Gamma} \end{pmatrix} \begin{pmatrix} \underline{z} - \underline{\mu} \\ \underline{\bar{z}} - \underline{\bar{\mu}} \end{pmatrix} \right\}, \tag{2.89}$$

where $z \in \underline{z} = \underline{x} + i\underline{y}$ is a complex random variable, which models the variables $\rho_{\alpha\beta}$ (and $\tau_{\alpha\beta}$) at initial time. The distribution function is determined by the *location parameter* $\underline{\mu} = \langle \underline{z} \rangle_W$, the (Hermitian) *covariance matrix*

$$\Gamma_{\alpha\beta} = \left\langle (z_\alpha - \mu_\alpha) \left(\bar{z}_\beta - \bar{\mu}_\beta \right) \right\rangle_W, \tag{2.90}$$

and the (symmetric) *pseudo-covariance matrix*

$$C_{\alpha\beta} = \langle (z_\alpha - \mu_\alpha)\,(z_\beta - \mu_\beta) \rangle_W \,. \tag{2.91}$$

Mean and (connected) correlations of the Gaussian are fixed from the quantum mechanical expectation values of the operators and their (connected) correlations: (only the variables ρ are shown)

$$\mu_{\rho_{i\sigma,j\sigma}} = \langle \rho_{i\sigma,j\sigma} \rangle_W \overset{!}{=} \langle \hat{\rho}_{i\sigma,j\sigma} \rangle_{\mathrm{QM}}, \tag{2.92}$$

$$\begin{aligned} \Gamma(\rho_{i\sigma,j\sigma},\rho_{k\tau,l\tau}) &= \left\langle \rho^*_{i\sigma,j\sigma}\rho_{k\tau,l\tau} \right\rangle^{\mathrm{c.c.}}_{\mathrm{W}} = \int \mathrm{d}\underline{\rho}\; W(\underline{\rho}) \left[\rho^*_{i\sigma,j\sigma}\rho_{k\tau,l\tau}\right] - \mu_{\rho^*_{i\sigma,j\sigma}} \mu_{\rho_{k\tau,l\tau}} \\ &\overset{!}{=} \frac{1}{2} \left\langle \hat{\rho}^\dagger_{i\sigma,j\sigma}\hat{\rho}_{k\tau,l\tau} + \hat{\rho}_{k\tau,l\tau}\hat{\rho}^\dagger_{i\sigma,j\sigma} \right\rangle^{\mathrm{c.c.}}_{\mathrm{QM}} \end{aligned} \tag{2.93}$$

$$\begin{aligned} C(\rho_{i\sigma,j\sigma},\rho_{k\tau,l\tau}) &= \langle \rho_{i\sigma,j\sigma}\rho_{k\tau,l\tau} \rangle^{\mathrm{c.c.}}_{\mathrm{W}} = \int \mathrm{d}\underline{\rho}\; W(\underline{\rho}) \left[\rho_{i\sigma,j\sigma}\rho_{k\tau,l\tau}\right] - \mu_{\rho_{i\sigma,j\sigma}} \mu_{\rho_{k\tau,l\tau}} \\ &\overset{!}{=} \frac{1}{2} \langle \hat{\rho}_{i\sigma,j\sigma}\hat{\rho}_{k\tau,l\tau} + \hat{\rho}_{k\tau,l\tau}\hat{\rho}_{i\sigma,j\sigma} \rangle^{\mathrm{c.c.}}_{\mathrm{QM}} \end{aligned} \tag{2.94}$$

If one wishes to include the τ-variables, one can make use of the fact that they are statistically uncorrelated from the ρ-operators (at least for states with fixed particle number since an equal number of annihilation and creation operators is necessary for non-zero expectation values)

$$W(\underline{\rho},\underline{\tau}) = W_\rho(\underline{\rho}) W_\tau(\underline{\tau}). \tag{2.95}$$

For the practical implementation of the initial time sampling it is easier to work with multivariate real Gaussian distributions

$$W(\underline{x}) = \frac{1}{\sqrt{(2\pi)^M\,|\Sigma|}} \exp\left(-\frac{1}{2} (\underline{x} - \underline{\mu})^T \Sigma^{-1} (\underline{x} - \underline{\mu}) \right), \tag{2.96}$$

where the real covariance matrix Σ is defined as follows ($x, y \in \underline{x}$):

$$\begin{aligned} \Sigma_{x,y} &= \langle (x-\mu_x)(y-\mu_y) \rangle \\ &= \langle xy \rangle - \mu_x \mu_y. \end{aligned} \tag{2.97}$$

The (pseudo)covariance matrices Γ, C of the complex Gaussian are related to the real covariance matrices Σ_{xx} and Σ_{yy} of the real and imaginary parts in the following way:

$$\begin{aligned} \Sigma_{xx} &= \frac{1}{2} \mathrm{Re}\left\{\Gamma + C\right\}, &\quad \Sigma_{xy} &= \frac{1}{2} \mathrm{Im}\left\{-\Gamma + C\right\}, \\ \Sigma_{yx} &= \frac{1}{2} \mathrm{Im}\left\{\Gamma + C\right\}, &\quad \Sigma_{yy} &= \frac{1}{2} \mathrm{Re}\left\{\Gamma - C\right\}, \end{aligned} \tag{2.98}$$

where $x = \mathrm{Re}(z)$ and $y = \mathrm{Im}(z)$. The mean values are determined from the first moments of the distribution

$$\mu_x = \int \mathrm{d}\underline{x}\; W(\underline{x})\, \underline{x} \tag{2.99}$$

and the covariances from the second moments.

2.5.3 Product initial states

In this thesis, we mostly work with product states as initial state. In this case, all means and covariances of the initial state are real-valued. This implies that the real probability distribution factorizes into two independent distributions for the real and imaginary parts ($\Sigma_{x,y} = 0$). Hence, real and imaginary parts can be drawn independently from each other. For product states in position and momentum space, one can explicitly determine all initial data via Wick's theorem:

$$\langle c_\alpha^\dagger c_\beta^\dagger c_\gamma c_\delta \rangle = \langle c_\alpha^\dagger c_\delta \rangle \langle c_\beta^\dagger c_\gamma \rangle - \langle c_\alpha^\dagger c_\gamma \rangle \langle c_\beta^\dagger c_\delta \rangle \tag{2.100}$$

The symmetrized connected correlations of the ρ-operators can thus be computed in terms of the following formulae:

$$\begin{aligned} \frac{1}{2}\left\langle \hat{\rho}_{\alpha\beta}^\dagger \hat{\rho}_{\mu\nu} + \hat{\rho}_{\mu\nu} \hat{\rho}_{\alpha\beta}^\dagger \right\rangle_c &= \frac{1}{2}\left(\delta_{\alpha\mu} \langle c_\beta^\dagger c_\nu \rangle + \delta_{\beta\nu} \langle c_\mu^\dagger c_\alpha \rangle \right) - \langle c_\beta^\dagger c_\nu \rangle \langle c_\mu^\dagger c_\alpha \rangle \\ \frac{1}{2}\left\langle \hat{\rho}_{\alpha\beta} \hat{\rho}_{\mu\nu} + \hat{\rho}_{\mu\nu} \hat{\rho}_{\alpha\beta} \right\rangle_c &= \frac{1}{2}\left(\delta_{\beta\mu} \langle c_\alpha^\dagger c_\nu \rangle + \delta_{\alpha\nu} \langle c_\mu^\dagger c_\beta \rangle \right) - \langle c_\alpha^\dagger c_\nu \rangle \langle c_\mu^\dagger c_\beta \rangle \end{aligned} \tag{2.101}$$

For a many-body state described by a diagonal single-particle density matrix $\rho_{\alpha\beta} = \delta_{\alpha\beta} n_\alpha$ (like the Fermi sea), the formulas simplify as follows,

$$\begin{aligned} \langle \hat{\rho}_{\alpha\beta} \rangle = \left\langle \hat{\rho}_{\alpha\beta}^\dagger \right\rangle &= \delta_{\alpha\beta} \left(n_\alpha - \frac{1}{2} \right), \\ \left\langle \hat{\rho}_{\alpha\beta}^\dagger \hat{\rho}_{\mu\nu} \right\rangle_c &= \delta_{\alpha\mu} \delta_{\beta\nu} \left(n_\beta - n_\alpha n_\beta \right), \\ \left\langle \hat{\rho}_{\mu\nu} \hat{\rho}_{\alpha\beta}^\dagger \right\rangle_c &= \delta_{\alpha\mu} \delta_{\beta\nu} \left(n_\alpha - n_\alpha n_\beta \right) \\ \left\langle \hat{\rho}_{\alpha\beta} \hat{\rho}_{\mu\nu} \right\rangle_c &= \delta_{\alpha\nu} \delta_{\beta\mu} \left(n_\alpha - n_\alpha n_\beta \right), \\ \left\langle \hat{\rho}_{\mu\nu} \hat{\rho}_{\alpha\beta} \right\rangle_c &= \delta_{\alpha\nu} \delta_{\beta\mu} \left(n_\beta - n_\alpha n_\beta \right) \end{aligned} \tag{2.102}$$

such that the symmetrized connected correlation functions are given by

$$\begin{aligned} \Gamma_{\alpha\beta,\mu\nu} &= \frac{1}{2}\left\langle \hat{\rho}_{\alpha\beta}^\dagger \hat{\rho}_{\mu\nu} + \hat{\rho}_{\mu\nu} \hat{\rho}_{\alpha\beta}^\dagger \right\rangle_c = \frac{1}{2} \delta_{\alpha\mu} \delta_{\beta\nu} \left(n_\alpha + n_\beta - 2 n_\alpha n_\beta \right), \\ C_{\alpha\beta,\mu\nu} &= \frac{1}{2}\left\langle \hat{\rho}_{\alpha\beta} \hat{\rho}_{\mu\nu} + \hat{\rho}_{\mu\nu} \hat{\rho}_{\alpha\beta} \right\rangle_c = \frac{1}{2} \delta_{\alpha\nu} \delta_{\beta\mu} \left(n_\alpha + n_\beta - 2 n_\alpha n_\beta \right). \end{aligned} \tag{2.103}$$

It follows from these expressions that only connected correlations of the form $\langle \rho_{\alpha\beta} \rho_{\beta\alpha} \rangle_c$ (covariance $\Gamma_{\alpha\beta,\alpha\beta}$) are non-zero. Pseudo-covariances of the form $C_{\alpha\beta,\alpha\beta}$ are zero. Only in the case $\alpha = \beta$ both the covariance and the pseudo-covariance are non-zero (and equal). In the following tables we summarize the initial data for a product state in the diagonal basis (for the Fermi sea state at zero temperature we only need $n_\alpha = 0, 1$ but for illustration we also list $n_\alpha = 0.5$.
If $\alpha = \beta$, one has

n_α	$\mu_{\rho_{\alpha\beta}}$	$\Gamma_{\alpha\alpha,\alpha\alpha}$	$C_{\alpha\alpha,\alpha\alpha}$	$\Sigma^{\mathrm{Re}}_{\alpha\alpha,\alpha\alpha}$	$\Sigma^{\mathrm{Im}}_{\alpha\alpha,\alpha\alpha}$
0	−0.5	0	0	0	0
0.5	0	0.25	0.25	0.25	0
1	0.5	0	0	0	0

If $\alpha \neq \beta$,

n_α	n_β	$\mu_{\rho_{\alpha\beta}}$	$\Gamma_{\alpha\beta,\alpha\beta}$	$C_{\alpha\beta,\alpha\beta}$	$\Sigma^{\text{Re}}_{\alpha\beta,\alpha\beta}$	$\Sigma^{\text{Im}}_{\alpha\beta,\alpha\beta}$
0	0	0	0	0	0	0
0	0.5	0	0.25	0	0.125	0.125
0	1	0	0.5	0	0.25	0.25
0.5	0.5	0	0.25	0	0.125	0.125
0.5	1	0	0.25	0	0.125	0.125
1	1	0	0	0	0	0

2.5.4 Stochastic mean-field approach

fTWA is an example of a method that has been independently developed more than once.[1] In 2008, Sakir Ayik proposed a method called "stochastic mean-field approach" (SMF) to the nuclear physics community [160], which is basically identical to fTWA. A few publications [161, 162, 163, 164, 165, 166] in the nuclear physics community (most of them by Denis Lacroix) have further developed the method since then and we summarize some interesting insights: In one of the papers [165], the authors ask the generically interesting question if one can choose better distributions than a Gaussian to represent the correlations of initial product states. They derive expressions for the third and fourth moments of the operators $\hat{\rho}_{\alpha\beta}$ in the quantum state. Their interesting conclusion is that one cannot in general find a distribution that exactly mimics the initial quantum correlations. However, they propose to use a two-point distribution function $\frac{1}{2}\big(\delta(x-\sigma)+\delta(x+\sigma)\big)$ instead of a Gaussian based on an analysis of the kurtosis of various distributions. They report an improvement of the SMF with two-point functions instead of Gaussians for an application to the LMG model. In Chapter 4 we also compare Gaussian and two-point sampling but do not find a difference. In a method comparison paper [163] with non-equilibrium Green's functions in Hubbard systems, the SMF yields results of comparable quality to self-energy approaches based on the second Born approximation. The most interesting development in terms of perspectives how to further improve fTWA/SMF is a recent publication on a combination of stochastic sampling with equations of motion derived from the BBGKY hierarchy [166]. Similar (but slightly different) proposal also exist for TWA in spin systems [167, 168]. In the context of the stochastic mean-field approach the improved equations of motion yield a significant improvement upon the mean-field equations of motion at the cost of an increased computational complexity and the necessity to propagate significantly more variables. We further discuss their proposal in the Conclusion of this thesis.

2.5.5 Numerical implementation and convergence

2.5.5.1 Numerical solution of the equations of motion

The non-linear equations of motion can in general not be solved analytically and one needs to solve them numerically. In order to remove redundancies from the data, we only store the upper triangular part $i \leq j$ of the Hermitian matrix $\rho_{i\sigma,j\tau}$. For most

---

[1] One might want to consider this as a proof of quality.

of this thesis we consider spin/flavor-averaged variables $\rho_{ij} = \frac{1}{N}\sum_{\alpha=1}^{N} \rho_{i\alpha,j\alpha}$ such that one can ignore the spin index.

For the numerical solution of the equations of motion we use ODE solvers with adaptive stepsize control as implemented in the standard `odeint` library [169]. We mostly use their implementation of the Runge-Kutta-Fehlberg algorithm [170] of 8th order or of the Runge-Kutta-Cash-Karp algorithm [171] of 5th order. Adaptive error control proceeds roughly as follows: At each propagation step the algorithm proposes a step size for the next step and estimates the error of this next step (e.g. by comparing to two steps with half the step size each). This error is compared to predefined error tolerances and if the error is too large the step size is reduced. The procedure is iterated until the error is below the threshold. The two relevant error tolerances are the absolute error ε_{abs} and the relative error tolerance ε_{rel}. The former is mostly relevant if values are close to zero, while the latter controls the relative error made in each propagation step. For the applications in this thesis we always choose $\varepsilon_{\text{abs}} = 10^{-10}$ and $\varepsilon_{\text{rel}} = 10^{-8}$ or lower.

2.5.5.2 Convergence of the Monte Carlo simulations

The initial conditions for the equations of motion $\rho_{ij}^{(k)}(t=0)$ are sampled from (mostly Gaussian) random distributions. In the usual mathematical language, the $\rho_{ij}^{(k)}(t=0)$ for each k are independent and identical (i.i.d.) random variables. Expectation values within the truncated Wigner scheme are obtained upon averaging over a finite number of samples $k = 1, \ldots, n$. We may assume that also at times $t > 0$ the distributions of the variables $\rho_{ij}^{(k)}(t)$ are i.i.d. for each value of k due to the in general chaotic nature of the non-linear equations of motion. If exact solutions are available for comparison, we can also check this assumption. The convergence of such an ensemble of (non-diverging) i.i.d. random variables is controlled by the **Strong Law of Large Numbers** [172], which states that

$$\langle \rho_{ij}(t) \rangle^{(n)} := \frac{1}{n} \sum_{k=1}^{n} \rho_{ij}^{(k)}(t) \tag{2.104}$$

converges to the true mean $\langle \rho_{ij}(t) \rangle$. The rate of the convergence is described by the **Central Limit Theorem**, which allows to define a confidence interval of the mean, which involves the standard deviation σ of the random variables. Since the true σ of the distribution (at times $t > 0$) is not known, one calculates an empirical estimate of σ from the data. This *empirical variance* of a data set with n samples is defined as

$$\sigma^2_{\text{emp},n} := \frac{1}{n-1} \sum_{k=1}^{n} \left(\rho_{ij}^{(k)}(t) - \langle \rho_{ij}(t) \rangle^{(n)} \right)^2 \tag{2.105}$$

or, equivalently,

$$\sigma^2_{\text{emp},n} := \frac{n}{n-1} \left(\left(\frac{1}{n} \sum_{k=1}^{n} \rho_{ij}^{(k)}(t)^2 \right) - \left(\langle \rho_{ij}(t) \rangle^{(n)} \right)^2 \right) \tag{2.106}$$

While the $\rho_{ij}(t)$ are in general complex variables, we usually only evaluate real observables like occupation numbers ρ_{kk} or absolute values of bonds $|\rho_{ij}|$. Therefore we can think of the involved quantities as real. Using this empirical variance, one can write down a confidence interval for the true mean $\langle\rho_{ij}(t)\rangle$: With a probability of close to 95%, the true mean lies in the interval

$$\left[\langle\rho_{ij}\rangle^{(n)} - \frac{1.96\sigma_{\mathrm{emp},n}}{\sqrt{n}},\ \langle\rho_{ij}\rangle^{(n)} + \frac{1.96\sigma_{\mathrm{emp},n}}{\sqrt{n}}\right] \tag{2.107}$$

We note for completeness that often this estimate is too conservative and can be improved using, e.g., the Berry-Esseen theorem [172].

We can also use the same principle for error estimates without explicit reference to the number of TWA trajectories by identifying sets of observables which we expect to be identical due to symmetry reasons. If a system is translationally invariant, we may use, for instance, the local occupations ρ_{ii} on lattice sites i as a set of random variables with identical mean. Calculating the empirical variance of all these local densities also gives access to an estimator for the convergence.

The error obtained from the central limit theorem is an absolute error, which is as such not a meaningful quantity. Whether an absolute error of, say, ±1 is good or bad, depends on the value of the mean. This is to say that one should better look at the relative error, which is defined as the error divided by the mean, to check for convergence. In our SU(N)-fTWA simulations this is a relevant aspect since the standard deviations of the ensembles, from which the initial conditions are generated, typically scale like $\sim \frac{1}{N}$, while means can be of order one. One example of such a situation is presented by the order parameters in Chapter 5. In their case, typically only a small number of samples (~ 100) is needed to converge the expectation values of observables.

2.5.5.3 Checkpointing scheme

When calculating averages and variances of observables from the trajectories, we would like to update all statistical data for each new trajectory without the need to save all past trajectories. In addition, the numerical error from repeated additions of numbers with a finite floating point accuracy should be as minimal as possible. A solution to both these problems is provided by Welford's algorithm [173]. The expectation values and variances of the $\rho_{ij}(t)$ are updated "on-line": Given the running mean $\langle\rho_{ij}(t)\rangle^{(n)}$ over n trajectories and a new sample $\rho_{ij}^{(n+1)}(t)$, the update rule is as follows:

$$\big\langle\rho_{ij}(t)\big\rangle^{(n+1)} = \big\langle\rho_{ij}(t)\big\rangle^{(n)} + \frac{1}{n+1}\left(\rho_{ij}^{(n+1)}(t) - \big\langle\rho_{ij}(t)\big\rangle^{(n)}\right). \tag{2.108}$$

The equal-time covariances of the data,

$$\Sigma^{(n)}(\rho_{ij}(t),\rho_{mn}(t)) = \frac{1}{n}\sum_{k=1}^{n}\left[\left(\rho_{ij}^{(k)}(t) - \big\langle\rho_{ij}(t)\big\rangle^{(n)}\right)\left(\rho_{mn}^{(k)}(t) - \big\langle\rho_{mn}(t)\big\rangle^{(n)}\right)\right], \tag{2.109}$$

are computed similarly:

$$\begin{aligned}\Sigma^{(n+1)}(\rho_{ij}(t),\rho_{mn}(t)) = \frac{1}{n+1}\Bigg[& n\cdot\Sigma^{(n)}(\rho_{ij},\rho_{mn}) \\ &+ \frac{n}{n+1}\left[\left(\rho_{ij}^{(n+1)}(t) - \big\langle\rho_{ij}(t)\big\rangle^{(n)}\right)\left(\rho_{mn}^{(n+1)}(t) - \big\langle\rho_{mn}(t)\big\rangle^{(n)}\right)\right]\Bigg]\end{aligned} \tag{2.110}$$

For complex data we process independently the real and imaginary parts.

In addition, the formulae allow for a trivial parallelization of the sampling into several runs $A, B, \dots$. Statistical quantities from two data batches A and B can be merged as follows [173]:

$$\big\langle \rho_{ij}(t) \big\rangle^{(n_A+n_B)} = \frac{1}{n_A+n_B} \Big(n_A \cdot \big\langle \rho_{ij}(t) \big\rangle^{(n_A)} + n_B \cdot \big\langle \rho_{ij}(t) \big\rangle^{(n_B)} \Big) \tag{2.111}$$

$$\begin{aligned} \Sigma^{(n_A+n_B)}(\rho_{ij}(t), \rho_{mn}(t)) = \frac{1}{n_A+n_B} \Bigg(& n_A \cdot \Sigma^{(n_A)}(\rho_{ij}(t), \rho_{mn}(t)) + n_B \cdot \Sigma^{(n_B)}(\rho_{ij}(t), \rho_{mn}(t)) \\ & + \frac{n_A \cdot n_B}{n_A+n_B} \Big(\big\langle \rho_{ij}(t) \big\rangle^{(n_A)} - \big\langle \rho_{ij}(t) \big\rangle^{(n_B)} \Big) \Big(\big\langle \rho_{mn}(t) \big\rangle^{(n_A)} - \big\langle \rho_{mn}(t) \big\rangle^{(n_B)} \Big) \Bigg) \end{aligned} \tag{2.112}$$

2.6 Basic concepts of Floquet theory

In this thesis we will occasionally draw analogies to periodically driven systems and in Chapter 3 we will also make explicit use of the effective Floquet Hamiltonian formalism. We therefore give a condensed overview of important concepts in Floquet theory. Details can be found in specialized reviews [82, 174]. The starting point is a time-periodic Hamiltonian $\hat{H}(t+T) = \hat{H}(t)$ with time evolution operator $\hat{U}(t, t_0) = \mathcal{T} \exp\big(-\frac{i}{\hbar} \int_{t_0}^{t} \hat{H}(\tau) \mathrm{d}\tau \big)$. From its group property it follows $\hat{U}(t+T, t_0) = \hat{U}(t, t_0) \hat{U}(t_0+T, t_0)$. This representation corresponds to a time scale separation: The slow evolution over (several) periods is described by $\hat{U}(t_0+T, t_0) =: \exp\big(-\frac{i}{\hbar} T \hat{H}_F[t_0] \big)$, where $\hat{H}_F[t_0]$ is called the *Floquet Hamiltonian*. The fast dynamics within a period is governed by the *stroboscopic kick operator* $\hat{K}_F[t_0](t)$ defined such that

$$\hat{U}(t, t_0) = \mathrm{e}^{-\frac{i}{\hbar} \hat{K}_F[t_0](t)} \mathrm{e}^{-\frac{i}{\hbar}(t-t_0) \hat{H}_F[t_0]}. \tag{2.113}$$

The eigenvalues of $\hat{U}(t_0+T, t_0)$ are necessarily complex numbers on the unit circle, which we denote by $\exp\big(-\frac{i}{\hbar} T \epsilon_n \big)$. Written in this way, it becomes clear that the ϵ_n are only defined up to the addition of multiples of $\hbar \frac{2\pi}{T}$, therefore the ϵ_n are called *quasi-energies*. They are the eigenvalues of the Floquet Hamiltonian.

The operators in the exponentials of ansatz (2.113) retain an explicit gauge dependence on the choice of t_0. Although the quasi-energies are gauge-independent, t_0 can show up explicitly in perturbative approximations of $\hat{H}_F[t_0]$ and ϵ_n [174]. In order to get rid of this dependence, one defines a new set of *non-stroboscopic kick operators* $\hat{K}_{\text{eff}}(t)$ such that $\mathrm{e}^{-\frac{i}{\hbar} \hat{K}_F[t_0](t)} =: \mathrm{e}^{-\frac{i}{\hbar} \hat{K}_{\text{eff}}(t)} \mathrm{e}^{\frac{i}{\hbar} \hat{K}_{\text{eff}}(t_0)}$. This allows to define the *effective Hamiltonian*

$$\hat{H}_{\text{eff}} = \mathrm{e}^{\frac{i}{\hbar} \hat{K}_{\text{eff}}(t_0)} \hat{H}_F[t_0] \mathrm{e}^{-\frac{i}{\hbar} \hat{K}_{\text{eff}}(t_0)}, \tag{2.114}$$

which is independent of t_0. The time-evolution operator for arbitrary times t_1, t_2 now reads as follows:

$$\hat{U}(t_2, t_1) = \mathrm{e}^{-\frac{i}{\hbar} \hat{K}_{\text{eff}}(t_2)} \mathrm{e}^{-\frac{i}{\hbar}(t_2-t_1) \hat{H}_{\text{eff}}} \mathrm{e}^{\frac{i}{\hbar} \hat{K}_{\text{eff}}(t_1)} \tag{2.115}$$

The great value of such a decomposition lies in the fact that it allows to explain properties of the periodically driven system in terms of the time-independent Hamiltonian

H_{eff}. One can construct systematic approximations to the effective Hamiltonian, in particular using the high-frequency expansion [175], which assumes $\Omega = \frac{2\pi}{T}$ to be large (larger than the other energy scales in the problem). In terms of the Fourier modes

$$\hat{H}_m = \frac{1}{T}\int_0^T \mathrm{d}t \mathrm{e}^{-im\Omega t}\hat{H}(t), \tag{2.116}$$

the lowest order (in $\frac{1}{\Omega}$) terms of the expansion read:

$$\begin{aligned} \hat{H}_{\text{eff}}^{(0)} &= \hat{H}_0, & \hat{K}_{\text{eff}}^{(0)} &= 0 \\ \hat{H}_{\text{eff}}^{(1)} &= \frac{1}{\hbar\Omega}\sum_{m>0}\frac{\left[\hat{H}_m, \hat{H}_{-m}\right]}{m}, & \hat{K}_{\text{eff}}^{(1)} &= -\frac{1}{\hbar\Omega}\sum_{m\neq 0}\frac{\mathrm{e}^{im\Omega t}}{m}\hat{H}_m. \end{aligned} \tag{2.117}$$

Chapter 3

Spectral Properties of Driven Systems

3.1 Introduction

Driving correlated materials with time-dependent electromagnetic fields can affect the physical properties of those materials in various ways: Heating and charge carrier transfer, i.e. changes of occupation numbers during and subsequent to a pulse are among the most basic effects. Those effects can occur for static band structures and motivate descriptions of the electronic excitation dynamics using temperature models and quantum Boltzmann scattering equations [176, 177, 178]. However, on ultrafast time scales (e.g., femtoseconds) and in the presence of electronic correlations, more subtle non-thermal [34] effects can appear, like transient changes of material properties. This can go as far as to enable transitions into "hidden" states of matter, which are not even accessible in equilibrium [179]. Among the most interesting consequences of light-matter coupling beyond heating are photon-dressed states, which can lead, for instance, to a renormalization of band structures. One can roughly distinguish dressing effects at weak and strong light-matter coupling. The latter can, e.g., give rise to the formation of complex polariton quasiparticles in cavities [39]. While in this context the number of involved photons is typically low, they are confined to small cavity volumes, which causes the strong light-matter interaction. Potential applications include cavity-mediated superconductivity and ferroelectricity [39]. In this thesis we concentrate on the case of weak coupling, sometimes also referred to as the classical regime. Photon numbers are typically large, like in a laser beam, such that one may treat the macroscopically populated field modes as classical objects. Theoretical studies of the crossover regime have recently started [180].

A successful theoretical framework to describe transient manipulations of band structures and spectra in the classical driving regime is Floquet theory, which idealizes the driving field as infinite and periodic (cf. Sec. 2.6). It allows for approximate descriptions of periodically driven systems in terms of time-independent effective Hamiltonians in certain regimes, in particular in the high-frequency regime. Such descriptions are generally only valid on time scales significantly longer than the period of the driving (time scale separation). As the simplest example it is instructive to consider a tight-binding chain subject to an infinite sinusoidal vector potential $A(t) = A_0 \sin(\Omega t)$

(coupled via Peierls substitution, cf. Sec. 2.2, with units $a = e = \hbar = 1$) in the high-frequency regime "band width $\ll \Omega$":

$$\hat{H} = -t_{\mathrm{h}} \sum_{\langle i,j \rangle} \left(\mathrm{e}^{-iA(t)} c_i^\dagger c_j + \mathrm{H.c.} \right) \tag{3.1}$$

In order to derive an effective high-frequency Hamiltonian, one needs to calculate the Fourier modes

$$\hat{H}_m = \frac{1}{T} \int_0^T \mathrm{d}t \; \mathrm{e}^{-im\Omega t} \hat{H}(t), \tag{3.2}$$

which one can do based on the formula

$$\mathrm{e}^{-iA(t)} = \mathrm{e}^{-iA_0 \sin(\Omega t)} = \sum_{k=-\infty}^{\infty} J_k(A_0) \mathrm{e}^{ik\Omega t}, \tag{3.3}$$

where $J_k(x)$ is the k-th Bessel function of first kind. Hence, one obtains

$$\begin{aligned} \hat{H}_m &= \sum_{k=-\infty}^{\infty} J_k(A_0) \frac{1}{T} \int_0^T \mathrm{d}t \; \mathrm{e}^{-i(m-k)\Omega t} (-t_{\mathrm{h}}) \sum_{\langle i,j \rangle} \left(c_i^\dagger c_j + \mathrm{H.c.} \right) \\ &= -t_{\mathrm{h}} J_m(A_0) \sum_{\langle i,j \rangle} \left(c_i^\dagger c_j + \mathrm{H.c.} \right). \end{aligned} \tag{3.4}$$

The zeroth-order term in the high-frequency expansion (2.117) of the effective Hamiltonian is $\hat{H}_{\mathrm{eff}}^{(0)} = \hat{H}_0$, while the non-stroboscopic kick operator (ibid.) vanishes at that order: $K_{\mathrm{eff}}^{(0)} = 0$. In the Floquet picture one obtains thus an effective description in terms of a Hamiltonian with renormalized hopping matrix element (band width). One may view this as an elementary example of *Floquet engineering*, which can be used to dynamically modify matter properties on a transient time scale. A simple consequence of the example above is *dynamical localization* [181], i.e. a suppression of the hopping amplitude (since $|J_0(x) < 1|$ for all x), which is particularly relevant if other competing energy scales are involved, for example due to interaction terms. In such interacting models, practical implementations of Floquet engineering can be challenging on long time scales because of the heating due to energy absorption from the driving field. Generically, one expects that periodically driven non-disordered systems, which are not driven in the high-frequency regime [91], will heat up to infinite temperatures [182, 82]. Exceptions include strongly disordered systems (many-body localization [77]), which can stabilize Floquet-MBL phases [90]. These can be used, among other applications, to build a special version of quantum time crystals [183]. Nevertheless, periodically driven systems at and below the high-frequency limit may remain in *prethermal* states [92, 184] on experimentally accessible time scales, which allows to engineer models with fascinating new properties like emerging gauge fields [82]. Another important field of application, which we do not consider in this thesis, is the creation of topological states using periodic driving [185].

So far we have focused on parameter renormalization and generation of non-trivial effective Hamiltonians as one hallmark of driven many-body systems. Another effect that occurs in periodically driven systems is the formation of so-called *sidebands*, which are visible in non-equilibrium spectral functions, in particular also in experimental ARPES spectra [46]). They occur due to the structure of the quasi-energies in Floquet theory, which are only defined up to shifts by the driving frequency. Therefore, the observation of such side bands is often interpreted as an experimental proof of the existence of a dressed state. The simplest and most transparent example is presented by a kinetic single-particle continuum Hamiltonian with the corresponding plane wave eigenstate,

$$\hat{H} = \frac{\hat{p}^2}{2m}, \qquad \psi(\vec{r}, t) = \frac{\mathrm{e}^{i\vec{p}\cdot\vec{r}}}{(2\pi)^{3/2}} \tag{3.5}$$

The time-dependent vector potential is included via minimal coupling ($m = m_e$ and $q = -e$ for an electron):

$$\hat{H}(t) = \frac{1}{2m}\big(\hat{\vec{p}} - q\vec{A}(t)\big)^2. \tag{3.6}$$

This Hamiltonian allows for an exact solution of the time-dependent wave function [122], which is known as the *Volkov wave function* for a driving field $\vec{A}(t) = A_0 \cos(\omega t)$:

$$\begin{aligned} \psi_V(\vec{r}, t) &= \frac{1}{(2\pi)^{3/2}} \mathrm{e}^{\frac{i}{\hbar}\left(\vec{p}\cdot\vec{r} - \frac{1}{2m}\int_0^t \mathrm{d}t' \, (\vec{p} - q\vec{A}(t))^2\right)} \\ &= \frac{1}{(2\pi)^{3/2}} \mathrm{e}^{\frac{i}{\hbar}\vec{p}\cdot\vec{r}} \sum_{n=-\infty}^{\infty} \mathrm{e}^{-\frac{i}{\hbar}\left(\frac{p^2}{2m} + U_p + n\hbar\omega\right)t} J_n\Big(\vec{\alpha}_0/\hbar \cdot \vec{p}, \frac{U_p}{2\hbar\omega}\Big) \\ &= \frac{1}{(2\pi)^{3/2}} \mathrm{e}^{i\vec{k}\cdot\vec{r}} \sum_{n=-\infty}^{\infty} \mathrm{e}^{-\frac{i}{\hbar}\left(\frac{\hbar^2 k^2}{2m} + U_p + n\hbar\omega\right)t} J_n\Big(\vec{\alpha}_0 \cdot \vec{k}, \frac{U_p}{2\hbar\omega}\Big), \end{aligned} \tag{3.7}$$

where $\vec{p} = \hbar\vec{k}$ and $U_p = \frac{q^2 A_0^2}{4m} = \frac{q^2 E_0^2}{4m\omega^2}$ is the ponderomotive potential (which one can usually neglect). In addition, $\alpha_0 = -\frac{q\vec{A}_0}{m\omega} = -\frac{q\vec{E}_0}{m\omega^2}$. The functions $J_n(x, y)$ with two arguments are generalized Bessel functions that reduce to the conventional ones for $y = 0$. It is instructive to inspect the complex phase factor of the Volkov wave function, whose arguments correspond to energies $\mathrm{e}^{-\frac{i}{\hbar}(\epsilon_k + n\hbar\omega)t}$. The ϵ_k are precisely the quasi-energies $\frac{\hbar^2 k^2}{2m} + U_p$ of the periodically driven problem. The way the wave function is written corresponds to an *extended space representation* [175], in which every Fourier component of the Floquet modes occurs explicitly. Hence, for all integers n the wave function contains copies of this original dispersion, shifted by multiples of the photon energy $\hbar\omega$ (if one does not like the photon terminology for effectively classical light fields one can just think in terms of the driving frequency).

The Bessel functions assign non-equal weight to these side bands in the wave function such that side bands with a large number of photons are suppressed. It is important to stress that the energy replicas occur as phase factors of the wave function in the original Hilbert space and do not imply an enlarged physical Hilbert space, although extended spaces can be constructed as tools [175]. Nevertheless, the side bands lead to observable consequences in photoemission experiments.

The, arguably, most basic effect is known as the *laser-assisted photoelectric effect (LAPE)* [186, 187, 188, 189, 123], which occurs in transitions of a bound electron into the dressed vacuum. The latter can approximately be described as a Volkov wave function. In a simple single-particle scattering description of photoemission according to (2.31), one can model LAPE within first order time-dependent perturbation theory by the following scattering matrix [122]

$$(S^{\mathrm{B}}-1)_{fi} = -\frac{i}{\hbar}\int_{-\infty}^{\infty} \mathrm{d}t \, \langle \psi_V | \vec{A}_{\mathrm{probe}}(t)\cdot\vec{p}|\Phi_0\rangle \,, \tag{3.8}$$

where ψ_V is the Volkov wave function (corresponding to the dressing field frequency ω_{pump}) and $\Phi_0 = \phi_0(\vec{r})\mathrm{e}^{iE_b t}$ is a bound electron state with binding energy $E_b = \hbar\omega_b$. Assuming the rotating wave approximation for the probe field, one can formally introduce the time-independent matrix element $M_{fi} = \langle\psi_V|\,\frac{\vec{A}^0_{\mathrm{probe}}}{2}\cdot\vec{p}|\phi_0\rangle$ such that the integral turns into an energy conservation condition (we follow, for simplicity, the 2π-convention of the Fourier transform used in Refs. [122, 124]: $\delta(\omega) = \frac{1}{2\pi}\int_{-\infty}^{\infty}\mathrm{d}t\,\mathrm{e}^{i\omega t}$):

$$(S^{\mathrm{B}}-1)_{fi} = -\frac{2\pi i}{\hbar}M_{fi}\sum_n a_n\delta\left(\frac{p_f^2}{2m_e} + \hbar\left(n\omega_{\mathrm{pump}} - \omega_{\mathrm{probe}} + \omega_b\right)\right), \tag{3.9}$$

where $a_n = J_n(\alpha_0)$. The binding energy $\hbar\omega_b$ is needed to release the electron from the sample such that $\hbar(\omega_{\mathrm{probe}} - \omega_b) = \frac{p_f^2}{2m_e} + n\hbar\omega_{\mathrm{pump}}$ is the available energy for the Volkov state. The photoemission intensity I_n for the n-th side band (how strong the signal of the side band is relative to the total photoemission intensity $\simeq$ number of detected photoelectrons) is proportional to $|a_n|^2 = J_n(\alpha_0)^2$, i.e. the transition probability from the initial state to the final state, if the static matrix element is ignored, which is a common approximation [190].

This simple theory already allows for a few predictions, for example, how the sideband intensity depends on the polarization of the electric field relative to the initial state momentum $\vec{k}$ of the photoelectron. Let us assume an electron with initial momentum component $\vec{k}_{\|}$ parallel to the surface (which is conserved in photoemission, $\vec{k}'_{\|} = \vec{k}_{\|}$, where primed quantities denote the final state momenta) and let $\theta_{\vec{k}_{\|}} := \tan^{-1}\left(\frac{k_y}{k_x}\right)$. Given an electric field

$$\vec{E}^0_{\mathrm{pump}} = \begin{pmatrix} E_{\|}\cos(\theta_{\vec{E}}) \\ E_{\|}\sin(\theta_{\vec{E}}) \\ E_z \end{pmatrix}, \tag{3.10}$$

one can calculate the LAPE parameter as a function of these angles as follows (we insert $\vec{k}_{\|} = \vec{k}'_{\|}$):

$$\begin{aligned} \alpha &= \frac{e}{m_e\omega^2_{\mathrm{pump}}}\left(E_{\|}k_{\|}\left[\cos(\theta_{\vec{k}_{\|}})\cos(\theta_{\vec{E}}) + \sin(\theta_{\vec{k}_{\|}})\sin(\theta_{\vec{E}})\right] + E_z k'_z\right) \\ &= \frac{e}{m_e\omega^2_{\mathrm{pump}}}\left(E_{\|}k_{\|}\cos\left(\left|\theta_{\vec{k}_{\|}} - \theta_{\vec{E}}\right|\right) + E_z k'_z\right) \end{aligned} \tag{3.11}$$

Experimentalists typically distinguish two types of field polarizations that are defined according to the direction of the field modes relative to the plane of incidence (which we choose to be the y-direction without loss of generality):
In the case of *s-polarization* ("senkrecht", perpendicular to the plane of incidence), only in-plane components in the x-direction are present: $E_z = 0, \theta_{\vec{E}} = 0$ such that $\alpha \sim E_{\|}k_{\|}\cos(\theta_{\vec{k}_{\|}})$. For *p-polarization* (parallel to the plane of incidence), there are non-zero

components in the y- and z-direction ($\theta_{\vec{E}} = \pi/2$) such that $\alpha \sim \left(E_\parallel k_\parallel \sin(\theta_{\vec{k}_\parallel}) + E_z k'_z\right)$. Therefore, a common rule of thumb says that one should use s-polarized light to suppress the LAPE effect [47].

We have concentrated the discussion of side bands on the final states so far. They can as well occur – in addition to the band structure renormalization discussed at the beginning – for the initial states. To distinguish them from the final state dressing one often speaks of *Floquet side bands* (although there is no fundamental difference in the theory). One aspect, which is in fact mostly different for Floquet side bands as compared to Volkov/LAPE side bands, is the complexity of the underlying band structure. While final states will always be parabolic in spatial regions away from the surface, electrons in materials can realize all kinds of complicated band structures. A famous example is graphene with its linear dispersion around the K and K' points [191]. For this band structure, side bands will intersect each other, giving rise to avoided crossings and, consequentially, gap openings. For graphene, this effect was predicted theoretically [192] but has not been observed in experiments as of now [193, 194]. In contrast, Floquet states have been detected for Bi_2Se_3 in a famous experiment by Wang et al. [46]. Not only Floquet side bands can interfere with other Floquet side bands but also Floquet sidebands with Volkov side bands. This type of interference has been observed experimentally in Bi_2Se_3 as well [47].

As a final aspect for this introduction, we would like to emphasize that modern time-resolved photoemission spectroscopy allows to directly measure the non-equilibrium spectra of excited states in correlated materials. This enables experimentalists to directly observe transient effects like band-width renormalization or the formation of excitations governed by a complicated effective Floquet Hamiltonian. A strong link between theory and experiments is based on the non-equilibrium spectral function (2.11) [51], which serves as one of the main tools for theorists to make predictions for ongoing and future experiments.

3.1.1 Scope of this Chapter

This Chapter summarizes contributions to projects, which are connected to the transient manipulation of spectra during and subsequent to a non-equilibrium excitation. The first project is directly related to the formation of side bands for time-resolved ARPES experiments on gold. It makes use of the single-particle scattering formalism to model the Floquet-Volkov interference in this system (although a posteriori LAPE is sufficient to describe the results as will be explained further below) and to support the explanation of an experimental finding in terms of field screening. Secondly, we consider a periodically driven strongly interacting chain of electrons with a charge-density wave (CDW) phase in equilibrium and analyze how the periodic driving leads to the formation of an additional band in the CDW gap.

3.2 Side band formation in time-resolved ARPES spectra

3.2.1 Background

We have given a general introduction to the concept of side bands and to the laser-assisted photoelectric effect (LAPE) in the introduction to this Chapter. In the following, we discuss the theoretical modeling of experimental time-resolved momentum microscopy results for the photon dressing of electron bands of a gold crystal (the sp-band and a surface state), which are both approximately parabolic. Time-resolved momentum microscopy is an advanced version of trARPES, which allows to simultaneously measure both in-plane momenta k_x, k_y of the photoelectrons as well as their kinetic energy (and, as a consequence, k_z'). The setup in Göttingen [125] benefits in addition from very high probe-photon energies in the extreme ultraviolet (EUV) of $\hbar\omega_{\mathrm{EUV}} \approx 26.5\,\mathrm{eV}$. This allows to map the full first surface Brillouin zone of the gold surface up to large in-plane momenta $k_{xy} \sim 2.4\,\text{Å}^{-1}$. Previous momentum-resolved works on side bands have mostly focused on graphene-like dispersions, either at the Γ point [46, 47] in the center of the Brillouin zone or at the K, K' points [192]. Setups with lower probe photon energies (e.g., 6.3 eV in Ref. [47]) are more restricted in their "photoemission horizon" of accessible in-plane momenta and therefore studies have often focused on interesting dispersions close to the Γ-point. In contrast, in our project [3] we have investigated the properties of photon dressing for parabolic initial states as well at high electron momenta. A posteriori, it turned out that the observed data could be explained with LAPE alone, due to a screening of the electric field in the material. Nevertheless, in the theoretical model, we address the situation with both initial and final state dressing present. A rough sketch is given in Fig. 3.1: Both the initial and the final state dispersion are parabolic albeit with possibly different effective masses. To photoemit an electron, the vacuum energy needs to be surpassed: the remaining excess energy determines the energy of the free electron state. An important constraint is provided by the condition that momenta perpendicular to the surface are conserved. A calculation for a similar situation with Dirac spinor initial states has been carried out by Park [124] within the single-particle scattering formalism. In the theory part of the experimental study by Mahmood et al. [47], LAPE was introduced as an additional phase factor in a second quantized calculation.

Exemplary experimental data is shown in panel (a) of Fig. 3.2. The upper two plots show the photoemission signal for electrons that originate from close to the Fermi energy (n_0), while the lower two plots show photoemission data at energy $E_F + \hbar\omega_{\mathrm{IR}}$ (n_1). One can see very well how the original band structure is replicated. Two types of states can be identified: firstly, a Shockley surface state (SS) [3] around the Brillouin zone (BZ) center and, secondly, the sp-band, which is closer to the edge of the BZ at the energy chosen. On the right-hand side of the figure, two quantitative evaluations of the data are shown: The data dots in panel (b) show the total intensity of the signal n_1 as a function of the field polarization from p to s. The experimental signal follows nicely a cosine. We discuss the conclusions from the comparison to theory in section 3.2.3. In (c) the relative intensity of the first side band (for p-polarized light) is plotted for both states as a function of the in-plane momentum k_{xy} orientation. The precise data handling is explained in the Supplemental Information to the publication [3] and makes use of the fact that side bands are most strongly suppressed for s-polarized light in order to eliminate the effect of the inhomogeneous photoemission signal. The main conclusion is that the side band intensity is independent of the Brillouin zone direction, which is a strong qualitative statement for a comparison to experiments. In the following, we present our theoretical modeling (which agrees with the respective text in the Supplement of the publication) and then close with a summary of the conclusions drawn in the collaboration.

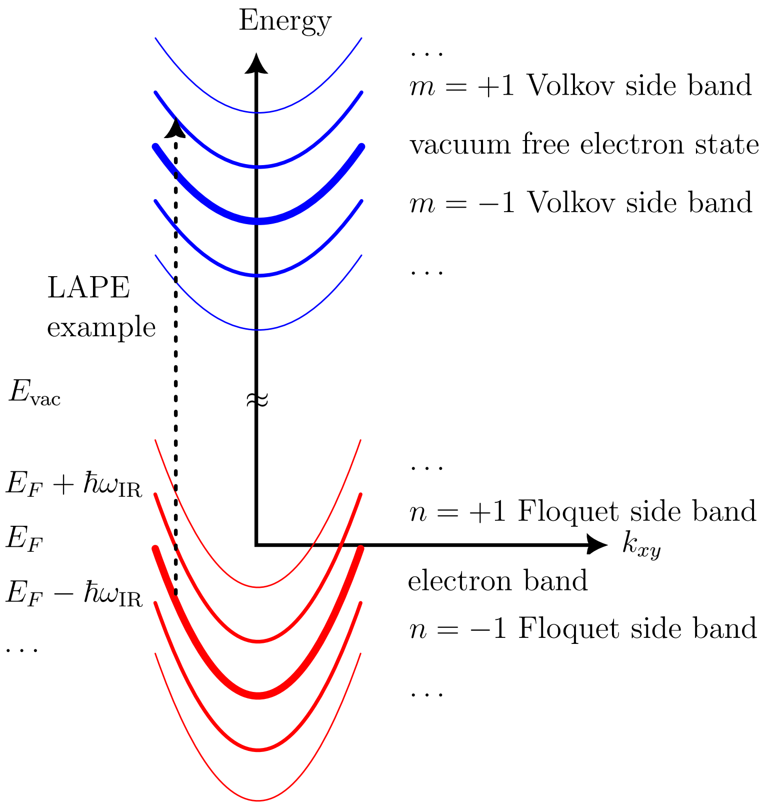

Figure 3.1: Sketch of Floquet and Volkov states: The red lines correspond to the initial parabolic electron state with a general effective mass (in our case $m^*_{\mathrm{SS}} < m_e$ but $m^*_{\mathrm{sp}} \approx m_e$). Blue: dressed vacuum states (Volkov). The photoemission spectrum is influenced by all possible "transitions" between the states. An example of a transition from the electron band to Volkov states (LAPE) is sketched with a dashed line.

3.2.2 Theoretical modeling (cf. [3])

The text and the results of this subsection are also contained in the supplement (section III.) of the publication [3], *Electromagnetic dressing of the electron energy spectrum of Au(111) at high momenta*, Phys. Rev. B **102**, 161403(R) (2020).

The theoretical description of the laser-assisted photoelectric effect here follows precedent work by Madsen et al., and others [122, 123, 188, 124]. We start with a linearly polarized driving laser field

$$\mathbf{E}(t) = \mathbf{E}\cos(\omega_{IR} t) \tag{3.12}$$

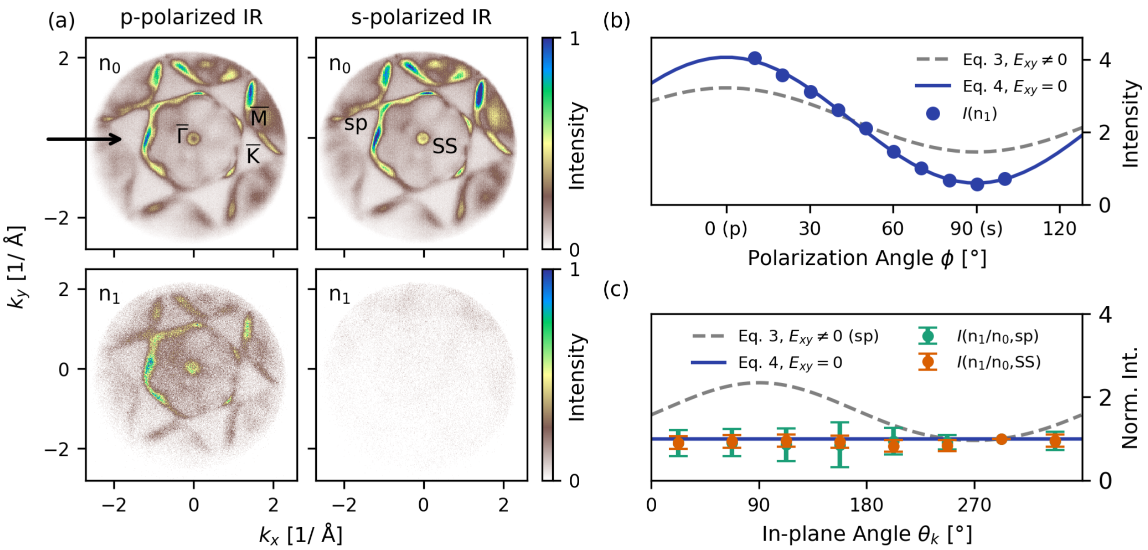

Figure 3.2: Figure from the publication [3] (Creative Commons Attribution 4.0 International license, the figure was created by Marius Keunecke): (a) Photoemission intensities of the main signal (n_0, zeroth side band) and of the first side band (n_1) for both s- and p-polarized pump field. (b) total intensity of the first side band n_1 as a function of the polarization of the electric field (from p- to s-polarization). (c) relative side band intensity I_1/I_0 as a function of the xy-Brillouin zone direction. The experimental data is shown in (a) and as dots in (b) and (c). The solids lines in (b) and (c) are due to the theoretical formulas developed below.

where

$$\mathbf{E} = \begin{pmatrix} E_{xy}\sin(\theta_E) \\ E_{xy}\cos(\theta_E) \\ E_z \end{pmatrix} = \begin{pmatrix} E_0\cos(68^\circ)\cos(\phi) \\ E_0\sin(\phi) \\ E_0\sin(68^\circ)\cos(\phi) \end{pmatrix}, \tag{3.13}$$

with $\theta_E = \arctan\left(\frac{E_x}{E_y}\right)$, the in-plane angle of the electric field (cf. Fig. 2 in [3]), and ϕ the polarization angle, where $\phi = 0^\circ$ (90°) corresponds to a p- (s-)polarized driving light. The latter description can be seen as the transition to the laboratory frame with an incidence angle of 68°.

3.2.2.1 Model for the final state

In general, photoemission final states are free electron states in the vacuum that become distorted at the surface and are matched to high-lying Bloch waves giving rise to so-called time-inverted LEED states [51]. For metals a common simple surface model is a step potential model, the so-called "jellium" model [123]. Here, the final states are modelled as plane waves parallel to the surface and exponentially damped waves normal to the surface. The dressing by the laser field, however, can be treated in an approximate way by using the phase of free electron states dressed by a driving laser field [195, 123], which are known as Volkov waves [122, 196]. Also plain Volkov waves have proven to be useful as final states for analytical photoemission calculations [124].

Hence, our model for the final state is

$$\phi_V(\mathbf{r},t) = \frac{\mathrm{e}^{i\mathbf{k}_{xy}\cdot\mathbf{r}_{xy}}}{2\pi}\phi_{k_z}(z)\mathrm{e}^{-\frac{i}{\hbar}(\hbar\omega_f+U)t}\sum_{n=-\infty}^{\infty}\mathrm{e}^{-in\omega_{IR}t}J_n\left(\alpha,\frac{U}{2\hbar\omega_{IR}}\right), \tag{3.14}$$

where $\phi_{k_z}(z)$ is the surface-normal part of the wave function, $\hbar\omega_f(\mathbf{k})$ is the eigenenergy of the state, which is $\approx \frac{\mathbf{p}'^2}{2m_e}$. $U = \frac{e^2E_0^2}{4m_e\omega_{IR}^2}$ is the ponderomotive potential and J_n are generalized Bessel functions.

$$\alpha = \frac{e}{m_e\omega_{IR}^2}\mathbf{E}^{\mathrm{IR}}\cdot\mathbf{k} \tag{3.15}$$

is the LAPE parameter and $\mathbf{k}$ is the momentum in the final state.

3.2.2.2 Model for the initial state

The initial state in photoemission is generically a complicated Bloch wave. However, in the case of the sp band transition the *in-plane* dispersion is well approximated as parabolic $E_{\mathrm{SP}}(\mathbf{k}_{\mathrm{xy}}) = -E_0^{\mathrm{SP}} + \frac{\hbar^2}{2m_e}\mathbf{k}_{\mathrm{xy}}^2$ when measured with respect to E_{Fermi}. This is in the spirit of the free electron approximation for noble metals [7], which is a common simple but often quite predictive approximation for many quantities. Note that $\mathbf{k}_{xy}$ of the initial and final states coincide due to conservation of in-plane momentum in the photoemission process.

A realistic modelling of the perpendicular momentum dispersion is more complicated. Estimating the initial state k_z^{in} from the photoemission energies reveals that for a probing photon energy of 26.5 eV, k_z^{in} is typically close to the bulk Γ-point where the dispersion is flatter than at high momenta, i.e. close to the L point (see band structure calculation and photon energy dependent photoemission data in Ref. [197] and [198]). For flat dispersions we expect a strong suppression of the sideband generation since the dressing field couples to the momentum-dependent part of the dispersion. This is consistent with the picture of a parabolic dispersion with high effective mass in that direction.

Furthermore, we model the initial state dressing as due to an averaged damped electric field $\mathbf{E}^{\mathrm{IR,in}}$ inside the metal as a first approximation. Hence, we can work with a wave function similar to Eq. (3.14) but consider a Floquet parameter

$$\beta = \frac{e}{m_e\omega_{IR}^2}\mathbf{E}_{xy}^{\mathrm{IR,in}}\cdot\mathbf{k}_{xy} + \beta_z(E_z^{\mathrm{IR,in}}, k_z^{\mathrm{in}}) \tag{3.16}$$

instead of the LAPE parameter α.

The occupied part of the Shockley surface state (SS) has a two-dimensional parabolic dispersion with an effective mass $m^*_{\mathrm{SS}} \approx 0.26m_e$ [199]: $E_{\mathrm{SS}}(\mathbf{k}_{xy}) = -E_0^{\mathrm{SS}} + \frac{\hbar^2}{2m^*_{\mathrm{SS}}}{\mathbf{k}_{xy}}^2$. At the same level of modelling as above we may hence use a Floquet parameter similar to (3.16) but with $m_e \to m^*_{\mathrm{SS}}$ and possibly a different average electric field.

3.2.2.3 Photoemission amplitude

The transition in photoemission from the initial state to the final state is calculated within first order time-dependent perturbation theory (Born approximation [122, 124]) employing a scattering matrix description. The transition amplitude from an initial state ϕ_i to a final state ϕ_f reads:

$$(S^B - 1)_{fi} = -\frac{i}{\hbar} \int_{-\infty}^{\infty} dt \, \langle \phi_f | \mathbf{A}_{\text{EUV}} \cdot \hat{p} | \phi_i \rangle \,, \tag{3.17}$$

with the vector potential of the EUV probe $\mathbf{A}_{\text{EUV}} = \frac{\mathbf{A_0}}{2} \exp(-i\omega_{\text{EUV}} t)$, where we used the dipole and the rotating wave approximation (cf. Sec. 2.2.2). In the experiment a driving laser fluence of $F = 5$ mJ/cm^2 with $\tau = 37$ fs pulse duration resulting in an incident electric field amplitude $E_0 = \sqrt{\frac{2}{c\epsilon_0} \frac{F}{\tau}} \approx 1 \cdot 10^9$ V/m was used. The ponderomotive potential $U = \frac{e^2 E_0^2}{4 m_e w_{IR}^2}$ is then of the order of 10 meV, and the term $\frac{U}{2\hbar\omega_{IR}} \approx 0$ can therefore safely be neglected. The generalized Bessel function reduces to the ordinary Bessel function of the first kind.

Plugging the model for the sp wave functions into (3.17) yields

$$\begin{aligned}(S^{\text{B}} - 1)_{fi} &= -\frac{i}{\hbar} M_{fi} \sum_{mn} \int_{-\infty}^{\infty} \mathrm{d}\, t \; \mathrm{e}^{i\left(\omega_f(\mathbf{k}) - \omega_i(\mathbf{k}') - (m-n)\omega_{\text{IR}} - \omega_{\text{EUV}}\right)t} J_m\big(\beta\big) J_n\big(\alpha\big) \\ &= -\frac{2\pi i}{\hbar} M_{fi} \sum_{mn} \delta\left(\omega_f(\mathbf{k}) - \omega_i(\mathbf{k}') - (m-n)\omega_{\text{IR}} - \omega_{\text{EUV}}\right) J_m\big(\beta\big) J_n\big(\alpha\big) \\ &= -\frac{2\pi i}{\hbar} M_{fi} \sum_{mn} \delta\left(\omega_f(\mathbf{k}) - \omega_i(\mathbf{k}') - m\omega_{\text{IR}} - \omega_{\text{EUV}}\right) J_{n+m}\big(\beta\big) J_n\big(\alpha\big)\end{aligned} \tag{3.18}$$

where

$$M_{fi} = \left\langle \phi_f(\mathbf{r}) \middle| \frac{\mathbf{A}_0^{\text{EUV}}}{2} \cdot \mathbf{p} \middle| \phi_i(\mathbf{r}) \right\rangle \tag{3.19}$$

is the photoemission matrix element generated by the spatial parts of the wave function [123]. Since we are only interested in the relative k-space structure of the sidebands we neglect M_{fi} in the following. Using a Bessel function identity allows to simplify the expression for the sideband amplitudes

$$a_m := \sum_n J_{n+m}\big(\beta\big) J_n\big(\alpha\big) = J_m\big(\beta - \alpha\big). \tag{3.20}$$

The Dirac-δ in (3.18) describes energy conservation during photoemission and restricts the final momentum $\mathbf{k}$ in addition to the momentum conservation parallel to the surface. The photoemission intensity of the m-th order sideband is

$$I_m \sim |a_m|^2 = J_m\big(\beta - \alpha\big)^2 = J_m\big(\beta_{xy} - \alpha_{xy} + \beta_z - \alpha_z\big)^2. \tag{3.21}$$

Note that the Bessel function obeys: $J_{-m}(\alpha) = (-1)^m J_m(\alpha)$ for integer m so that the intensity of the sidebands $I_m = I_{-m}$. We can approximate the Bessel function J_1 for small parameters $|\beta - \alpha| \ll \sqrt{2}$ resulting in a sideband amplitude ($m = 1$)

$$|a_1|^2 \sim \frac{1}{4} \left(\beta - \alpha\right)^2. \tag{3.22}$$

This is roughly justified in our case with an incident electric field $E_0 = 1 \cdot 10^9$ V/m yielding a maximum LAPE parameter of $\alpha_{\max} = 1.28$ and only small corrections due to β because of the efficient screening, i.e. $\beta \approx 0$. Generically, since $\beta_{xy} - \alpha_{xy} = \frac{e}{m_e \omega_{IR}^2}\left(\mathbf{E}_{xy}^{\mathrm{IR,in}} - \mathbf{E}_{xy}^{\mathrm{IR}}\right) \cdot \mathbf{k}_{xy}$ the sideband generation for the sp band states due to the in-plane electric fields will be suppressed if the electric field in the metal is only weakly screened.

Special case LAPE. Since we anticipate strong damping of the electric fields, which is underpinned by a Fresnel equation estimation (cf. next section), we consider the special case $\beta_{xy}, \beta_z \to 0$ of pure LAPE leading to a sideband amplitude

$$|a_m|^2 \sim J_m(\alpha)^2. \tag{3.23}$$

In previous works [124, 47] the in-plane component of the electric field was typically neglected if all electrons are photoemitted nearly perpendicular to the surface ($k_z \gg k_x, k_y$). In our case this approximation is a priori not valid, because we can detect electrons photoemitted under large photoemission angles and thus high in-plane momenta. If the in-plane components of the electric field are taken into account, the result, in contrast, yields a dependence on the azimuthal angle

$$|a_m|^2 \sim J_m\left(\frac{e}{m_e \omega_{IR}^2}\left(E_{xy}^{\mathrm{IR}} k_{xy} \cos\left(\theta_k - \theta_E\right) + E_z^{\mathrm{IR}} k_z\right)\right)^2. \tag{3.24}$$

We may use the same approximate form of the Bessel function as above such that the sideband amplitude for the first sideband ($m = 1$) is given by $J_1\left(\alpha\right)^2 \approx \frac{\alpha^2}{4}$:

$$|a_m|^2 \sim \frac{1}{4}\left(\frac{e}{m_e \omega_{IR}^2}\left(E_{xy}^{\mathrm{IR}} k_{xy} \cos\left(\theta_k - \theta_E\right) + E_z^{\mathrm{IR}} k_z\right)\right)^2 \tag{3.25}$$

A fit of (3.25) to the data as shown in Fig. 3.2 only works for $E_{xy} = 0$:

$$|a_m|^2 \sim \frac{1}{4}\left(\frac{e}{m_e \omega_{IR}^2} E_z^{\mathrm{IR}} k_z\right)^2 \tag{3.26}$$

3.2.3 Conclusion

We have derived Floquet and LAPE parameters that allow for qualitative insights into the interplay of field direction $\vec{E}_{xy}$ and in-plane momentum vector $\vec{k}_{xy}$. Due to the approximate parabolic nature of the initial and final state dispersions, we find side band intensities according to (3.21), which depend on the difference of the Floquet and LAPE parameters. In principle, this can lead to a destructive interference of the xy-components, in particular if the effective masses are similar. The role of the initial state momentum in the z-direction, k_z^{in}, is not so clear: In theory there can be initial state dressing with respect to that component. However, a realistic estimate of the field strength E_z^{in} below the surface yields such a strong damping that one can neglect the contribution in this case. Hence, the first side band intensity I_1 is effectively proportional to $J_1(\gamma)^2$, with

$$\gamma = \gamma_{xy} E_{xy} k_{xy} \cos(\theta_{k_{xy}} - \theta_E) + \gamma_z E_z k_z. \tag{3.27}$$

Destructive interference would lead to a suppression of γ_{xy}. Turning back to Fig. 3.2, panel (b) indeed shows that the measured data can only be fitted well if the contribution proportional to γ_{xy} is neglected. In this case, the simpler explanation is a strong screening of the electric field due to the almost perfect reflection at the metallic surface. This picture implies that one should set $E_{xy} \approx 0$ in (3.27), which also explains the observed data. Panel (c) in the figure shows that the relative side band intensity is independent of the momentum direction, which is also incompatible with significant dressing in the xy-direction. Still, we conclude that parabolic bands may give rise to interesting interference phenomena of the observed side bands in situations, in which the screening is weaker. In particular, the side band intensity would depend on the value of the effective mass of the bands, which could be an interesting point to address in future experiments.

The following calculation to estimate the value of the field strength in the z-direction was first carried out by Marius Keunecke [200], based on the formulas in [201, 202]. We summarize it here for completeness: If one assumes an abrupt metal-vacuum interface, one can apply the Fresnel equations in order to estimate the electric fields in the z-direction inside (E_{z_-}) and outside (E_{z_+}) of the metal surface. The relevant formulas in the paper by Whitaker are:

$$\begin{aligned} \frac{E_{z_+}^2}{E_0^2} &= \frac{4\sin(\theta_d)^2\cos(\theta_d)^2(\epsilon_1^2+\epsilon_2^2)}{(\epsilon_1^2+\epsilon_2^2)\cos(\theta_d)^2 + S^{1/2}\epsilon_d + \sqrt{2}\cos(\theta_d)u\epsilon_d^{1/2}(S^{1/2}+\epsilon_d\sin(\theta_d)^2)}, \\ \frac{E_{z_-}^2}{E_0^2} &= \frac{4\sin(\theta_d)^2\cos(\theta_d)^2}{(\epsilon_1^2+\epsilon_2^2)\cos(\theta_d)^2 + S^{1/2}\epsilon_d + \sqrt{2}\cos(\theta_d)u\epsilon_d^{1/2}(S^{1/2}+\epsilon_d\sin(\theta_d)^2)}. \end{aligned} \tag{3.28}$$

where E_0 is the incident electric field amplitude, $\theta_d = 68°$ is the angle of incidence and ϵ_d is the vacuum dielectric constant. Furthermore,

$$S := (\epsilon_1 - \epsilon_d\sin(\theta_d)^2 + \epsilon_2^2), \quad u := (S^{1/2} + (\epsilon_1 - \epsilon_d\sin(\theta_d))^{1/2}. \tag{3.29}$$

The dieletric function for gold are taken from the literature [203] ($\epsilon_1 = -44.252$, $\epsilon_2 = 2.0375$). The formula yields a drop to 2% field strength below the surface in comparison to above. Therefore, in this system, dressing of the initial state k_z^{in}-component can be neglected.

3.3 In-Gap Band Formation in a Periodically Driven CDW Insulator

3.3.1 Background

In the introduction to this Chapter we discussed the general idea of Floquet engineering as a means to manipulate material properties on prethermal time scales, i.e. before heating becomes dominant. Often in (theoretical) applications, the high-frequency limit, in which the driving frequency clearly exceeds the intrinsic energy scales of the model, is considered. In this limit, heating is suppressed [91] and effective Hamiltonians assume a particularly simple form. In the project presented in this section, we study the non-equilibrium spectral function (2.11) of a strongly correlated model, which is periodically driven with a large frequency but not in the extreme high-frequency limit. The Hamiltonian is defined as follows,

$$\begin{aligned} \hat{H}(t) = &-t_h \sum_{l=1}^{L-1} \left(e^{iA(t)} c_l^\dagger c_{l+1} + \text{H.c.} \right) \\ &+ V \sum_{l=1}^{L-1} \left(n_l - \frac{1}{2} \right) \left(n_{l+1} - \frac{1}{2} \right) + \sum_{l=1}^{L} \mu_l n_l \,, \end{aligned} \tag{3.30}$$

The equilibrium model ($A_0 \equiv 0$) is the t_h-V chain, a one-dimensional model of spinless fermions with a density-density interaction V. μ_l is an additional, l-dependent on-site potential, which can be set to a small value at the edge, thereby helping numerical matrix product state calculations to select one of the symmetry-broken CDW states. By means of the Jordan-Wigner transformation [204], the equilibrium model is equivalent in one spatial dimension to the XXZ spin chain, which is exactly solvable via Bethe ansatz [205]. It shows a Berezhinskii-Kosterlitz-Thouless (BKT) type transition [206] at half filling and zero temperature from a Luttinger liquid (LL) phase [207] to a charge density wave (CDW) insulator [15] at $V/t_h = 2$. A sketch of the phase diagram is shown in Fig. 3.3.

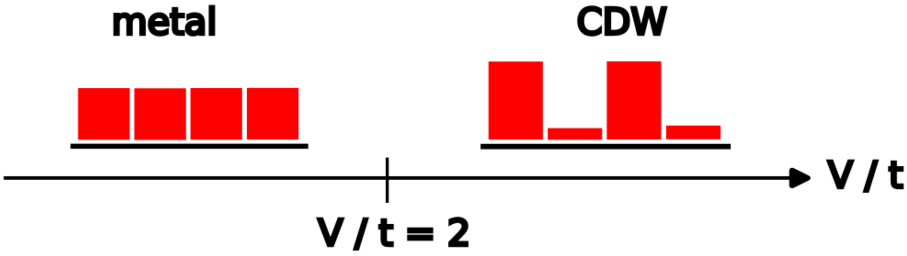

Figure 3.3: Sketch of the phase diagram of the interacting t_h-V model: The system undergoes a phase transition from a 1D metal (Luttinger liquid) to a charge-density wave insulator with non-zero CDW order parameter. The red bars illustrate the local charge distribution.

The charge-density wave order parameter is defined as follows,

$$\mathcal{O}_{\text{CDW}}(t) := \frac{2}{L} \sum_{i \text{ even}} \left(\langle n_{i+1}(t) \rangle - \langle n_i(t) \rangle \right). \tag{3.31}$$

For $V/t_h > 2$ the order parameter becomes non-zero and the single-particle spectrum is gapped, while the spectrum is gapless in the metallic phase. The model is often considered to be the simplest interacting electron model: It is both convenient for numerical methods because of the small local Hilbert space (2 states) as well as for analytical methods like mean-field theory or Bethe ansatz. Therefore, it is a suitable candidate model to study the effect of periodic driving in a simple strongly correlated system. Related previous works have focused on parameter renormalization in the high-frequency regime [86] and light-cone spreading of correlations [208]. Recently, these studies have been extended to the quantum Fisher information [209]. Similar works on the Hubbard model have studied the doublon formation upon driving [210, 211]. We complement these works by asking the questions how the momentum-resolved spectral signatures of the periodically driven model look like, which could be measured, e.g., in a time-resolved ARPES-like experiment. Therefore, we consider the non-equilibrium spectral function (2.11) of the system under driving. The starting point is data from a quasi-exact numerical calculation based on the matrix product state formulation of the time-dependent variational principle (TDVP) [58]. These calculations were carried out by Constantin Meyer (details in the PhD thesis [212]). The most interesting effect is the emergence of a cosine-shaped in-gap feature as a result of the periodic driving. In order to gain more insight into the mechanism behind this finding, we discuss results obtained for a driven non-interacting model for charge-density waves as well as for a mean-field treatment of the interacting model.

3.3.2 Results

The results and parts of the text in this section are also contained in the publication [4], *In-Gap Band Formation in a Periodically Driven Charge Density Wave Insulator*, Comm. Phys. **6**, 245 (2023). The DMRG/time-dependent MPS simulations have been carried out by Constantin Meyer. I created the figures used in the text here as well as in the publication.

We choose a monochromatic classical light-field $A(t) = \theta(t) A_0 \sin\big(\Omega t\big)$ in (3.30), which couples to the electrons in the system via Peierls substitution. Let us begin with expectations from Floquet theory. The leading order terms in the high-frequency expansion (2.117) of the effective Hamiltonian $\hat{H}_{\text{eff}}$ and of the kick operator $\hat{K}_{\text{eff}}$ in terms of the Fourier components $\hat{H}_m$ of the Hamiltonian read

$$\begin{aligned}
\hat{H}^{(0)}_{\text{eff}} &= \hat{H}_0, & \hat{K}^{(0)}_{\text{eff}} &= 0 \\
\hat{H}^{(1)}_{\text{eff}} &= \frac{1}{\hbar\Omega} \sum_{m>0} \frac{\big[\hat{H}_m, \hat{H}_{-m}\big]}{m}, & \hat{K}^{(1)}_{\text{eff}} &= -\frac{1}{\hbar\Omega} \sum_{m\neq 0} \frac{\mathrm{e}^{im\Omega t}}{m} \hat{H}_m .
\end{aligned} \tag{3.32}$$

In the case of the t_h-V Hamiltonian one obtains the harmonics (cf. calculation in the introduction to the chapter)

$$\hat{H}_m = \frac{1}{T} \int_0^T \mathrm{d}t \mathrm{e}^{-im\Omega t} \hat{H}(t) = J_m(A_0) \hat{H}_{\text{kin}} + \delta_{m,0} \hat{H}_{\text{int}} \tag{3.33}$$

Insertion in (3.32) yields

$$\begin{aligned}\hat{H}^{(0)}_{\text{eff}} &= \hat{H}_0 = -t_h J_0(A_0) \sum_{i=1}^{L-1} \left(c_i^\dagger c_{i+1} + \text{H.c.} \right) + V \sum_{i=1}^{L-1} n_i n_{i+1} \\ \hat{K}^{(1)}_{\text{eff}} &= -\hat{H}_{\text{kin}} \sum_{m \neq 0} \frac{\mathrm{e}^{im\Omega t}}{m\hbar\Omega} J_m(A_0).\end{aligned} \tag{3.34}$$

In the following we choose $A_0 = 1$ such that $J_0(A_0) \approx 0.765197$. The lowest order high-frequency correction for the model is therefore a renormalization of the hopping parameter $t_h \to t_h^{\text{eff}} = t_h J_0(A_0)$, which implies an effective increase of the interaction strength $V/t_h^{\text{eff}} > V/t_h$ and a larger CDW gap to be expected. The $\frac{1}{\Omega}$ contribution to the effective Hamiltonian, $H^{(1)}_{\text{eff}}$, vanishes in our case because the kinetic Hamiltonian commutes with itself.

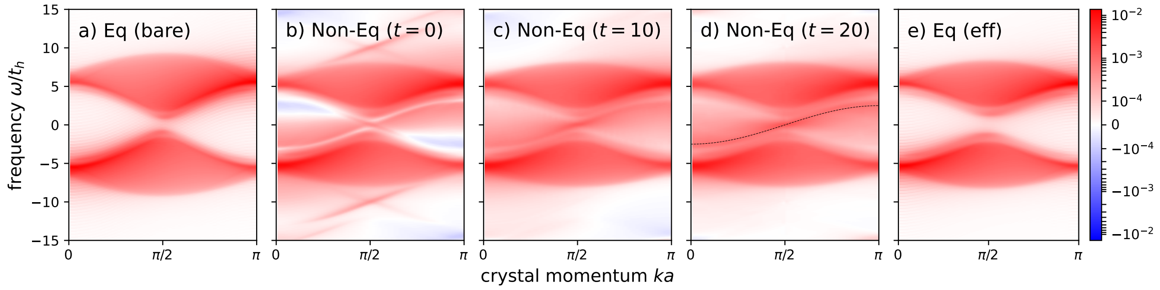

Figure 3.4: (Non-)Equilibrium spectral functions of the periodically driven CDW ground state at $V/t_h = 5$. a) and e) show the equilibrium spectral functions $A_k(\omega)$ of the system with bare and renormalized parameters, respectively. b)-d) show the non-equilibrium spectral functions $A_k(t,\omega)$ upon driving at the instances indicated. Times are measured in units of t_h^{-1}. The equilibrium spectral features in e) are also present in the spectral function of the driven system. In addition, there is clearly additional spectral weight appearing whose main feature is well approximated by $f(k) \approx -2.5\cos(ka)$ (black line in d)). The data has been obtained by Constantin Meyer [212] with MPS time evolution for a system with $L = 64$ chain sites and open boundary conditions. This figure was created by Alexander Osterkorn and is also published in [4] (Creative Commons Attribution 4.0 International license).

In Fig. 3.4 numerical results for the non-equilibrium spectral function $A_k(t,\omega)$ obtained from the MPS time evolution are shown. The definition of the spectral function is given in (2.11) in the Methods chapter, we use the horizontal time coordinates here. The value of the interaction strength is $V/t_h = 5$, for which the Bethe ansatz solution [205] of the model predicts a spectral gap of $\Delta/t_h \approx 1.576$. The driving frequency is $\Omega/t_h = 10$. The data is obtained using open boundary conditions (OBC), which is most efficient for matrix product state algorithms. The momentum eigenmodes of the system for OBC are standing waves [213] $c_k = \sqrt{2/(L+1)}\sum_k \sin(kr_i)c_i$ with $k \in \frac{\pi}{L+1} \cdot \{1,\dots,L\}$. The crystal momentum k therefore lies in the interval $[0,\pi]$. Panel (a) of the figure shows the equilibrium spectral function of the model without driving. The spectrum consists of two main excitation continua above and below zero energy. Since we consider the retarded Green's function, we always obtain the full density of states. At $k=\frac{\pi}{2}$ we find the gap, whose size agrees with the Bethe ansatz prediction. In panel (e) the equilibrium spectral function for the Hamiltonian with t_h^{eff} instead of t_h is shown. The spectral gap is indeed larger in (e) than in (a). Panels (b) to (d) show results for the non-equilibrium spectral function of the periodically driven chain (with the driving suddenly switched on at $t=0$). One finds that the excitation continua agree with the prediction of the zeroth order effective Hamiltonian. However, in addition, spectral weight appears in the band gap that is very well approximated by a cosine but is not part of the ground state spectrum of the effective Hamiltonian. Since $\hat{H}_{\mathrm{eff}}^{(1)}=0$ and second order terms are already quite strongly suppressed, one can anticipate an important role of the kick operator $\hat{K}_{\mathrm{eff}}$. Nevertheless, spectral effects can be subtle and a closure of the spectral gap upon melting of a charge-density wave was also observed in a non-interacting model by Shen et al. [214]. This study did not calculate a k-resolved spectral function. In order to distinguish the in-gap band from their effect, we reconsider the A-B model by Shen et al. with periodic driving. The model is based on the definition of two sublattices A and B and a staggered potential with values $\pm\frac{U}{2}$. We implement the model in one spatial dimension such that the Hamiltonian with Peierls substitution reads

$$\hat{H}=-t_h\sum_j\left(\mathrm{e}^{iA(t)}c_j^\dagger c_{j+1}+\mathrm{H.c.}\right)+\frac{U}{2}\Big(\sum_{i\in A}c_i^\dagger c_i-\sum_{i\in B}c_i^\dagger c_i\Big). \tag{3.35}$$

We introduce the following momentum space operators (for periodic boundary conditions)

$$\begin{aligned} c_{i\in A}^\dagger &= \frac{1}{\sqrt{V}}\sum_{k\in\mathrm{rBZ}}\mathrm{e}^{-ikr_i}\big(c_k^\dagger+c_{k+Q}^\dagger\big)\\ c_{i\in B}^\dagger &= \frac{1}{\sqrt{V}}\sum_{k\in\mathrm{rBZ}}\mathrm{e}^{-ikr_i}\big(c_k^\dagger-c_{k+Q}^\dagger\big), \end{aligned} \tag{3.36}$$

where $Q=\pi$ and $\mathrm{rBZ}=[-\pi/2,\pi/2]$ denotes the reduced Brillouin zone. A subsequent rotation to a particle-hole basis allows to bring the Hamiltonian to diagonal form,

$$\hat{H}=\sum_{k,\alpha\in\{\pm\}}\epsilon_{k\alpha}c_{k\alpha}^\dagger c_{k\alpha}, \tag{3.37}$$

where $\epsilon_{k\pm}=\frac{U}{2}-\mu\pm\sqrt{\epsilon_k^2+\frac{U^2}{4}}$ and $\epsilon_k=-2t_h\cos(k)$. It is noteworthy that the single-particle spectrum is gapped despite the absence of interactions. In the presence of the driving field $A(t)$, one can exactly write down the time-evolution operator $\hat{U}_k(t,t-\Delta t)$ for an infinitesimal time step Δt and momentum k as a 2×2-matrix based on a Trotter decomposition of $U_k(t,t_0)$. The calculation is detailed in the original publication by Shen et al. [215]. We use this result to solve for the retarded Green's function with a real-time step size of $10^{-6}t_h^{-1}$ and a chain length of $L=128$ sites with periodic boundary conditions.

Results for driving frequency $\Omega/t_h=10$ and $A_0=1$ are collected in Fig. 3.5. Panel (a) shows the equilibrium spectral function $A_k(\omega)$ of the A-B model without driving. The size of the band gap is U. Panels (b) to (d) show results for the non-equilibrium spectral function $A_k(t,\omega)$ of the driven system. The CDW order parameter is shown in

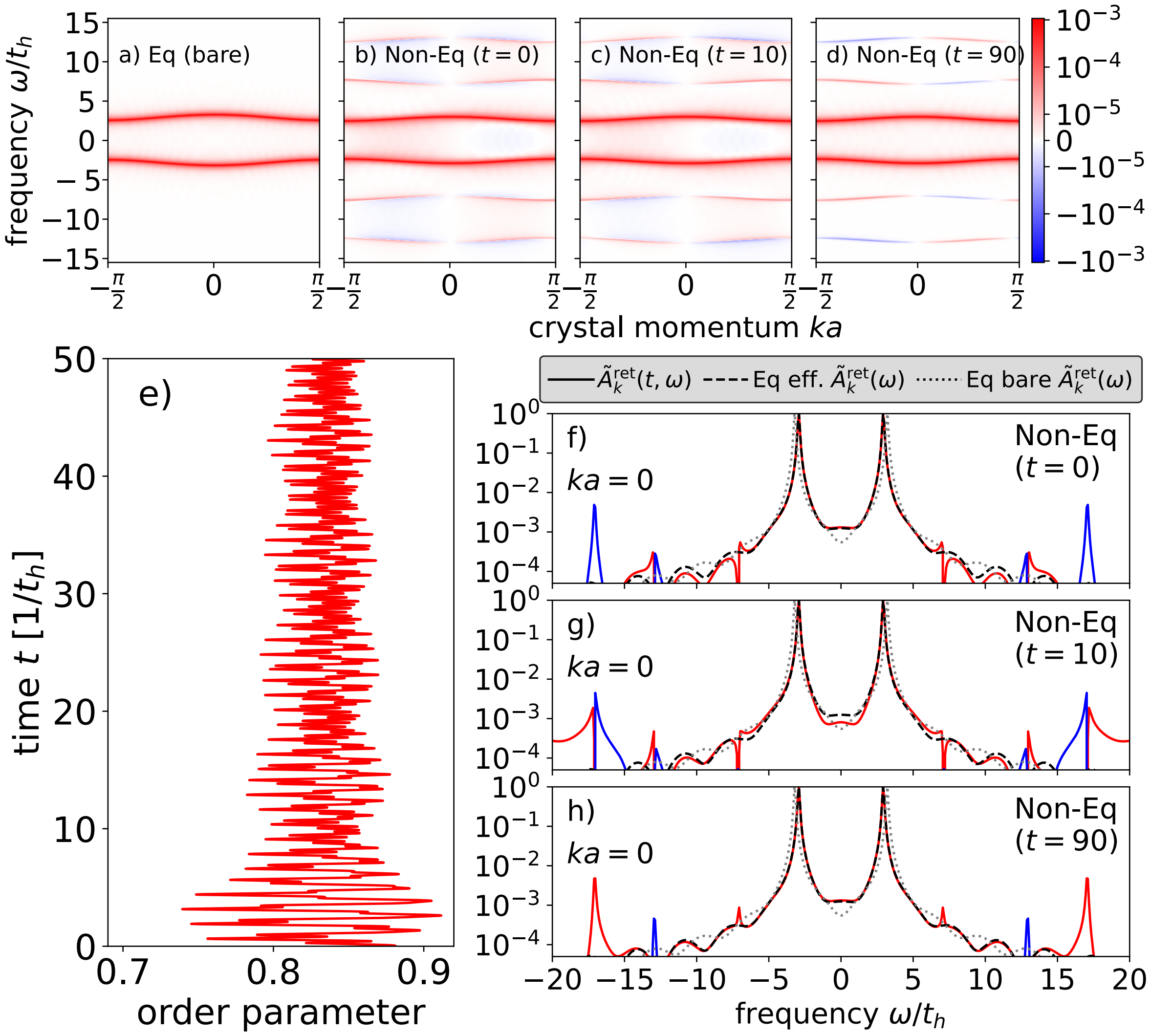

Figure 3.5: Simulation results for the A-B model in (3.35) with $U = 5t_{\mathrm{h}}$ and semi-infinite sinusoidal driving with amplitude one and frequency $\Omega = 10t_{\mathrm{h}}$. The panels a) to d) shows results for the non-equilibrium spectral functions at different times. Panel e) shows the dynamics of the CDW order parameter under driving and panels f) to h) show cross sections through the spectral functions of b) to d). The figure is also published in [4] (Creative Commons Attribution 4.0 International license).

(e). The periodic driving causes oscillations of $\mathcal{O}_{\mathrm{CDW}}$ on the time scales considered here. It oscillates around a value ≈ 0.84, which is slightly lower than the initial equilibrium value $\mathcal{O}_{\mathrm{CDW}}(t) \approx 0.88$ such that one can at least speak of a partial melting of the CDW. One can, however, not connect this order parameter dynamics to the emergence of a band in the spectral gap. We show this exemplarily in cuts through the spectral function at the center of the Brillouin zone at $k = 0$ in panels f) to h). Momentum cuts at other momenta agree qualitatively. Shortly after the start of the periodic driving (times $t = 0$, $t = 10$), the heatmaps (b) and (c) show some weak in-gap signals around $k \approx \pm\frac{\pi}{4}$, which is, however, a transient effect due to the switch-on procedure and is not related to the formation of a peak. We can conclude that the observed in-gap phenomenon is most likely interaction-induced. As a second interesting observation we note the formation of Floquet side band in the spectral function at separations ±Ω from the original bands. The spectral weight of every second side band becomes negative. The question under which conditions the non-equilibrium spectral function is manifestly positive is a topic of current research [114, 116]. One can show for the case of infinite periodic driving that period-averaging leads to a retarded Green's function without negative weights for fermions [116]. How useful this procedure is in the case of semi-infinite driving, which we consider here, remains unclear and so we stick with the non-averaged version of the non-equilibrium spectral function.

3.3.2.1 Hartree-Fock time evolution

In order to shed more light on the role of interactions, we continue with a time-dependent Hartree-Fock approximation of the dynamics in the t_h-V chain. We start from a decoupling of the interaction term and assume a two-site unit cell with sublattices A and B. Let us denote the mean-fields by

$$\begin{aligned} \rho_A &:= \langle c_i^\dagger c_i \rangle_{i\in A}, \quad \rho_0 := \langle c_i^\dagger c_{i+1} \rangle_{i\in A}, \\ \rho_B &:= \langle c_i^\dagger c_i \rangle_{i\in B}, \quad \rho_1 := \langle c_i^\dagger c_{i+1} \rangle_{i\in B}. \end{aligned} \tag{3.38}$$

Using periodic boundary conditions and again the momentum modes (3.36), we obtain, defining $\epsilon_k = -2t_h\cos(k)$, $\chi_k = V\big(\rho_0 \mathrm{e}^{-ik} + \rho_1^* \mathrm{e}^{ik}\big)$, the following momentum space representation of the Hamiltonian

$$(H) = \begin{pmatrix} c_k^\dagger & c_{k+Q}^\dagger \end{pmatrix} \begin{pmatrix} \epsilon_k - \mathrm{Re}(\chi_k) + V(\rho_A+\rho_B) - \mu & i\,\mathrm{Im}(\chi_k) + V(\rho_B-\rho_A) \\ -i\,\mathrm{Im}(\chi_k) + V(\rho_B-\rho_A) & -\epsilon_k + \mathrm{Re}(\chi_k) + V(\rho_A+\rho_B) - \mu \end{pmatrix} \begin{pmatrix} c_k \\ c_{k+Q} \end{pmatrix} \tag{3.39}$$

In the following, we only consider half filling $\mu = V(\rho_A+\rho_B)$. Diagonalization of the mean-field Hamiltonian yields the eigenenergies

$$\begin{aligned} E_k &= \pm\Big\{ - \Big[- \big(\epsilon_k - \mathrm{Re}(\chi_k)\big)^2 - \mathrm{Im}(\chi_k)^2 \\ &\qquad - V^2\big(\rho_B-\rho_A\big)^2 \Big] \Big\}^{1/2} \\ &= \pm\Big\{ \big|\epsilon_k - \chi_k\big|^2 + V^2(\rho_B-\rho_A)^2 \Big\}^{1/2}. \end{aligned} \tag{3.40}$$

The saddle point values of the mean-fields are determined by minimization of the total energy using a simulated annealing approach (cf. Sec. 2.3). The self-consistency conditions read

$$\begin{aligned} \rho_0 &\overset{!}{=} \langle c_i^\dagger c_{i+1} \rangle_{i\in A} \\ &= \frac{1}{V} \sum_{k\in \mathrm{rBZ}} \mathrm{e}^{ik} \Big(\langle c_k^\dagger c_k \rangle - \langle c_k^\dagger c_{k+Q} \rangle + \langle c_{k+Q}^\dagger c_k \rangle - \langle c_{k+Q}^\dagger c_{k+Q} \rangle \Big) \\ \rho_1 &\overset{!}{=} \langle c_i^\dagger c_{i+1} \rangle_{i\in B} \\ &= \frac{1}{V} \sum_{k\in \mathrm{rBZ}} \mathrm{e}^{-ik} \Big(\langle c_k^\dagger c_k \rangle + \langle c_k^\dagger c_{k+Q} \rangle - \langle c_{k+Q}^\dagger c_k \rangle - \langle c_{k+Q}^\dagger c_{k+Q} \rangle \Big) \end{aligned} \tag{3.41}$$

By inspection of the eigenenergies (3.40), one finds that the spectral gap is given by $2V(\rho_B - \rho_A)$. The self-consistent solutions turn out to obey $\rho_0 = \rho_1$ with real ρ_0 and ρ_1. In order to calculate the dynamics of the driven system, we first solve the time-diagonal problem and obtain the full one-particle reduced density matrix $\rho_{ij}(t) = \langle c_i^\dagger(t) c_j(t)\rangle$ using the equation of motion

$$
\begin{aligned}
\partial_t \rho_{lp} = -it\Bigg[\sum_{a(l)} \mathrm{e}^{-i\varphi_{la}(t)}\rho_{ap} - \sum_{a(p)} \rho_{la}\mathrm{e}^{-i\varphi_{ap}(t)}\Bigg] \\
+ iV\Bigg[\Bigg(\sum_{a(p)} - \sum_{a(l)}\Bigg)\big(\rho_{la}\rho_{ap} - \rho_{aa}\rho_{lp}\big)\Bigg],
\end{aligned}
\tag{3.42}
$$

where $\varphi_{ij}(t) = e_{\langle i,j\rangle}A(t)$ is the vector potential measured in the direction from site i to site j. $a(i)$ denotes the nearest neighbors of site i. In a second iteration we solve the equation of motion for the contributions from the lesser and greater Green's function to the retarded Green's function in horizontal coordinates, $\theta(\tau)G^<(t,\tau)$ and $\theta(\tau)G^>(t,\tau)$, for the relative time τ (only $\tau > 0$ is needed) using the time-diagonal data from the first iteration:

$$
-i\partial_t G_{ij}^{<,>}(t,\tau) = \sum_m \big(h_{im}(t) + \Sigma_{im}^{\mathrm{HF}}[\rho(t)]\big) G_{mj}^{<,>}(t,\tau),
\tag{3.43}
$$

where

$$
\begin{aligned}
h_{i,i+1} = -t_\mathrm{h}\mathrm{e}^{iA(t)}, \quad h_{i+1,i} = -t_\mathrm{h}\mathrm{e}^{-iA(t)} \\
\Sigma_{im}^{\mathrm{HF}}[\rho(t)] = V\delta_{im}\sum_{\langle n,m\rangle}\rho_{nn}(t) - V\delta_{\langle i,m\rangle}\rho_{im}(t)
\end{aligned}
\tag{3.44}
$$

The second expression is the Hartree-Fock self-energy (2.58) for the model. We choose a chain length of $L = 64$ sites and solve the equations of motion with a Runge-Kutta scheme (as implemented in the `solve_ivp` routine of Python's `scipy` library [143]) with a maximal step size of $10^{-3}t_h^{-1}$. We choose a large value $V = 8t_h$ to clearly separate V-dependent spectral features from Floquet side bands. For this value, the spectral gap size of the mean-field model is $\Delta \approx 15t_h$. We choose a driving frequency of $\Omega = 30t_h$, which yields the same ratio Δ/Ω as for the A-B model.

The results are shown in Fig. 3.6. Except for the different spectral gap size, the equilibrium spectral function of the non-driven system resembles the one obtained in the A-B model. The main peaks of the band structure of the driven system agree with the mean-field dispersion relation E_k if evaluated with the renormalized $t_{\mathrm{eff}} = t_h J_0(A_0)$. The driven model, however, shows additional signals separated by $\pm V$ from the main peaks (we checked this dependence on V with an additional calculation for $V/t_h = 12$). They gives rise to an in-gap signal around $\omega/t_h \approx 0$, which is stronger in amplitude than the signal, which is shifted by V away from the main peaks. Like in the A-B model the spectral function displays negative weights, which – in contrast to the MPS results – are pronounced at all times treated by us, while in the MPS case the negative weights seem to substantially decrease in time. We conclude, however, that the spectral function still contains relevant qualitative information, e.g. the position of spectral peaks. The order parameter in Fig. 3.6(e) is oscillatory with a slowly

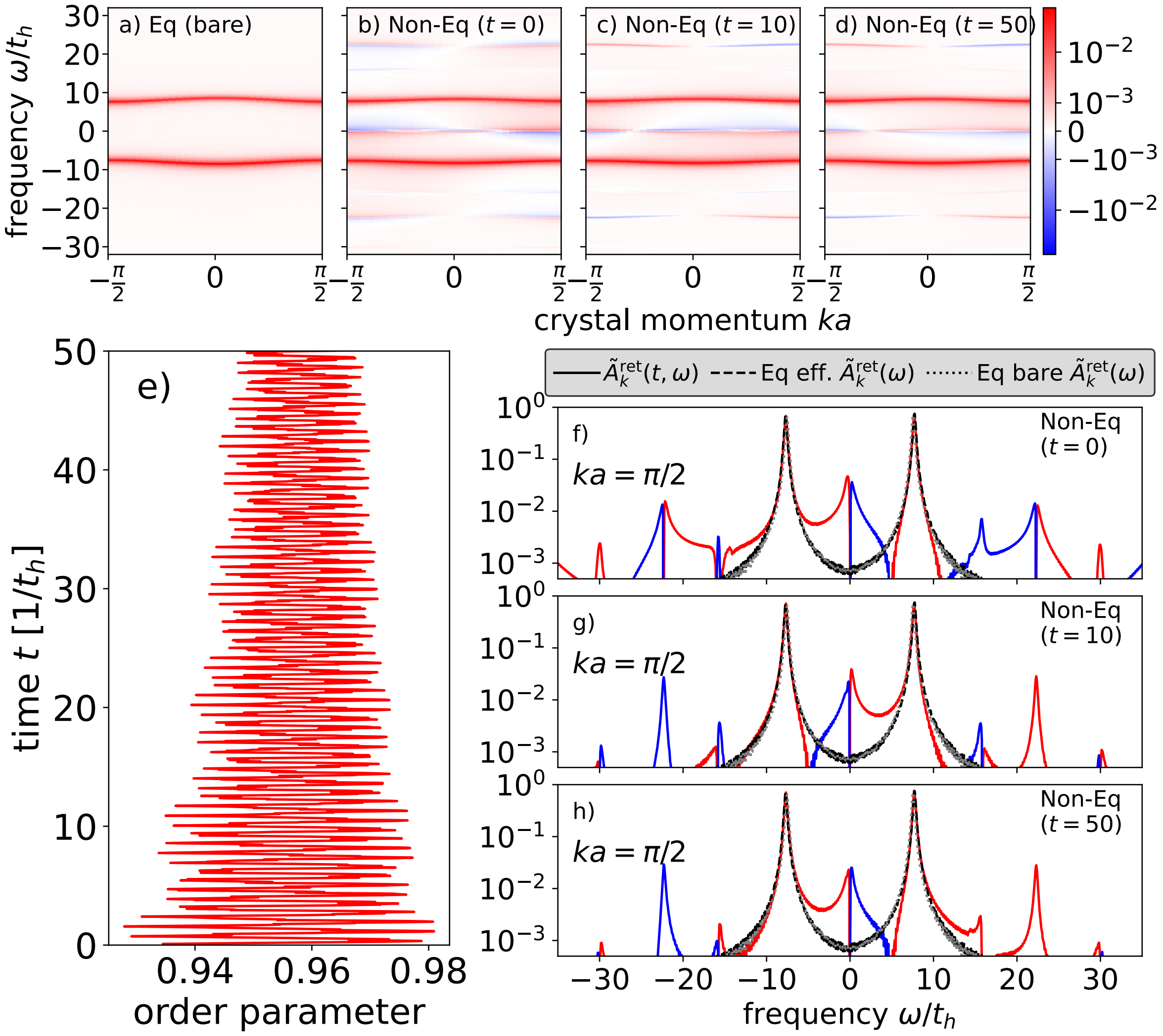

Figure 3.6: Simulation results for the t-V model within Hartree-Fock mean-field theory with $V = 8t_h$ and for semi-infinite sinusoidal driving with amplitude one and frequency $\Omega = 30t_\text{h}$. The data is obtained for a model with $L = 64$ sites and periodic boundary conditions. The heatmaps in a) to d) are drawn for the reduced Brillouin zone. Panel e) shows the dynamics of the CDW order parameter under driving and panels f) to h) show cross sections through the spectral functions of b) to d). The figure is also published in [4] (Creative Commons Attribution 4.0 International license).

decaying envelope. In fact, it oscillates around a larger order parameter value than in equilibrium. Still, the static equilibrium CDW configuration is broken up and charges can move in the system. We checked that if the driving is suddenly turned off, order parameter oscillations as well as the in-gap spectral features remain. The Floquet replicas of the main bands, however, disappear.

Remarkably, the shape of the observed in-gap signals coincides with the shape of the mean-field spectrum E_k (shifted into the band gap) if rescaled with a factor of two. Looking at the dispersing part $\left|\epsilon_k - \chi_k\right|$ of (3.40) for $\rho_0 = \rho_1$, we do indeed find a cosine-like dispersion if ϵ_k is neglected:

$$\left|\epsilon_k - \chi_k\right| \approx 2V\rho_0 \left|\cos(k)\right| \tag{3.45}$$

One needs to keep in mind that E_k is the particle addition/removal spectrum of the mean-field calculation in equilibrium, which does not need to coincide with the energy of excitations. The deviation by a factor of two is therefore not too surprising. The MPS time evolution in Fig. 3.4 did as well show an approximate shape of the in-gap signal $\sim \frac{V}{2}\cos(k)$. In physical terms, one can associate the emergence of the in-gap bands to the creation and destruction of doublon excitations in the system, which are also present in time-dependent Hartree-Fock theory but not in the A-B model.

3.3.3 Discussion and Conclusion

In this project we have extended previous studies of the periodically driven t_h-V chain by the perspective of non-equilibrium spectral functions. Starting from the numerical observation of emergent spectral weight in the gap of a periodically driven charge-density wave insulator, which displays a cosine-like dispersion, we studied two minimal models in order to see which ingredients are needed to reproduce the effect. While a periodically driven non-interacting A-B model does not show such a feature (although in-gap spectral weight can occur in such models upon driving [214]), we are able to reproduce some of its qualitative features within a time-dependent Hartree-Fock calculation. Nevertheless, a full explanation of the observed phenomenon in the MPS time evolution needs to take into account correlations effects, which will lead to an additional dressing of the excitations. An important method-related topic for future research concerns the question how to obtain a positive-definite spectral function in situations like the one considered here. If the system reaches a stationary state, period-averaging of the retarded Green's function might be a way to enforce positive semi-definiteness [116]. However, in the presence of heating and non-strictly periodic driving (e.g. with switch-on procedures), it is less clear how to proceed.

To further advance the understanding of the doublon-induced in-gap band formation, it will be useful to consider more in detail the effective Hamiltonian description within Floquet theory. Since the Fourier components $\hat{H}_m$ for $m \neq 0$ are only rescalings of the kinetic term in the Hamiltonian, one obtains that the $1/\Omega$-contribution $\hat{H}_{\text{eff}}^{(1)}$ to the effective Hamiltonian vanishes. The Ω^{-2} order is already strongly suppressed. It is important to note that non-equilibrium spectral functions, which depend on two times, will in general also be influenced by the effect of the non-stroboscopic kick operator $\hat{K}_{\text{eff}}(t)$ because of the representation (2.115) of the time evolution operator for arbitrary times t_1 and t_2. The kick operator contribution $\hat{K}_{\text{eff}}^{(1)}(t)$ in the high-frequency expansion is non-vanishing and proportional to the kinetic Hamiltonian. The kick operator will therefore induce hopping processes of electrons that can lead to a creation of doublon excitations in the interacting model. One way to analyze more in detail the doublon formation is the Floquet-Schrieffer-Wolff formalism developed by Bukov, Kolodrubetz and Polkovnikov [210]. We only give an outlook here (the original publication is about the Hubbard model, we calculated the analogous formulas for the t_h-V model). The formalism is based on a rotation to the comoving frame via the transformation

$$\begin{aligned}\hat{U}(t) &= \mathrm{e}^{-itV\sum_{i=1}^{L-1}\left(n_i-\frac{1}{2}\right)\left(n_{i+1}-\frac{1}{2}\right)} \\ &= \mathrm{e}^{-itV\sum_{i=1}^{L-1}n_in_{i+1}}\mathrm{e}^{-it\frac{V}{2}\sum_{i=1}^{L-1}\left(n_i+n_{i+1}\right)}\mathrm{e}^{-it\frac{V}{4}(L-1)}\end{aligned} \tag{3.46}$$

If we assume the limit $V \ll \Omega$, one can perform the leading order high-frequency approximation first [210] ($t_h \to t_h J_0(A_0)$) and rotate to the comoving frame afterwards. One obtains

$$\begin{aligned}
\hat{H}^{\mathrm{rot}}(t) =& \hat{U}^\dagger(t)\hat{H}(t)\hat{U}(t) + i\Big(\partial_t \hat{U}^\dagger(t)\Big)\hat{U}(t) \\
=& -t_h J_0(A_0) \sum_{i=1}^{L} \big(1 - n_{i-1}(1 - \mathrm{e}^{itV})\big) c_i^\dagger c_{i+1} \big(1 - n_{i+2}(1 - \mathrm{e}^{-itV})\big) + \text{H.c.} \\
=& -t_h J_0(A_0) \sum_{i=1}^{L} \big(1 - n_{i-1} + n_{i-1}\mathrm{e}^{itV}\big) c_i^\dagger c_{i+1} \big(1 - n_{i+2} + n_{i+2}\mathrm{e}^{-itV}\big) + \text{H.c.} \\
=& -t_h J_0(A_0) \sum_{i=1}^{L} \Big(\hat{g}_{i,i+1} + \mathrm{e}^{-itV}\hat{d}_{i,i+1} + \mathrm{e}^{+itV}\hat{k}_{i,i+1}\Big) + \text{H.c.}
\end{aligned} \tag{3.47}$$

with the following operators:

$$\begin{aligned}
\hat{g}_{ij} &= \big(1 - n_{i-1}\big) c_i^\dagger c_j \big(1 - n_{j+1}\big) + n_{i-1} c_i^\dagger c_j n_{j+1} \\
\hat{d}_{ij} &= \big(1 - n_{i-1}\big) c_i^\dagger c_j n_{j+1}, \qquad \hat{k}_{ij} = n_{i-1} c_i^\dagger c_j \big(1 - n_{j+1}\big)
\end{aligned} \tag{3.48}$$

$\hat{g}_{ij}$ describes a correlated hopping of electrons, $\hat{d}_{ij}, \hat{k}_{ij}^\dagger$ describe the destruction of doublons, while $\hat{k}_{ij}$ and $\hat{d}_{ij}^\dagger$ correspond to the creation of doublons. One may now apply the high-frequency expansion again, which in this case is equivalent to a Schrieffer-Wolff transformation. To leading order only the hopping terms $\sim \hat{g}_{ij}$ survive. The effective Hamiltonians so obtained are in general still complicated correlated models and require, in general, a numerical solution. Nevertheless, the formalism allows to develop a more detailed picture of the dynamical doublon creation as a response to the driving and is likely the best tool to develop a full analytical theory of the cosine-shaped in-gap feature.

Chapter 4

Interaction Quench in the large-N Hubbard Model

4.1 Introduction

Landau's Fermi liquid concept [9] provides a theory to describe the properties of – even strongly – interacting many-fermion systems. The central idea is that the properties of the interacting system and those of the non-interacting are *adiabatically connected*. This refers to the following: The non-interacting Fermi gas is a product state of all fermionic modes with momentum k whose single-particle energies are lower than the Fermi energy, $\epsilon_k < \epsilon_{k_F}$. Its elementary excitations correspond to the creation of particle-hole pairs. If an electron-electron interaction is switched on very slowly, such that the system follows the instantaneous eigenstates, the elementary excitations of the interacting system will be in a one-to-one correspondence to the excitations of the noninteracting system [9]. In particular, they carry the same quantum numbers, e.g. momentum and spin. The sea of electrons transforms into a sea of quasiparticles. The ground state distribution function $n(\epsilon)$ for the original electronic states in the interacting system displays a discontinuity $\Delta n_{k_F} := 1 - n_{k_F}$ at the Fermi energy, which is equal to the quasiparticle residue Z at the Fermi energy, which is a measure for the overlap of the bare electron wave function with the quasiparticle wave function.

One can now pose the questions what happens if the interaction is not turned on adiabatically but at a finite speed. This question was studied by Möckel and Kehrein in a series of papers [73, 216, 217]. The most interesting case is the one opposed to Landau's, namely infinitely fast switching, i.e. quenching. Möckel and Kehrein applied unitary perturbation theory [218] to the problem, which is a perturbative time evolution scheme for weak interactions based on Wegner's flow equations [219, 220]. In contrast to standard time-dependent perturbation theory, it does not suffer from secular terms because the time evolution operator remains unitary at every order of the approximation. The perturbative analysis was later refined by Kreye and Kehrein [221, 222] to include density-density correlations. Besides perturbative approaches, other methods have been applied to the interaction quench problem, usually with a particular focus on long times. Most prominently, non-equilibrium DMFT was used [75] to study the thermalization dynamics. Another line of analysis is based on kinetic equations [223].

In the following we provide more details about the interaction quench setup as well as a discussion of the most important physical expectations. At times $t < 0$ we start from a non-interacting tight-binding Hamiltonian

$$\hat{H}_{t<0} = \sum_{k\sigma} \epsilon_k c^\dagger_{k\sigma} c_{k\sigma}, \tag{4.1}$$

where ϵ_k is the single-electron dispersion of a nearest-neighbor hopping Hamiltonian on a cubic lattice, $\epsilon_k = -2t_h \sum_i \cos(k_i)$. As the initial state we choose the Fermi sea ground state of that Hamiltonian (at zero temperature). At time $t = 0$ a Hubbard interaction term with interaction strength $U > 0$ is switched on,

$$\hat{H}_{t\geq 0} = \sum_{k\sigma} \epsilon_k c^\dagger_{k\sigma} c_{k\sigma} + U \sum_i n_{i\uparrow} n_{i\downarrow}, \qquad |\psi_0\rangle = \prod_{\epsilon_k < \epsilon_F, \sigma} c^\dagger_{k\sigma} |\text{vac}\rangle \tag{4.2}$$

and we calculate the dynamics generated by this Hamiltonian. While $\hat{H}_{t<0}$ is trivially integrable, $\hat{H}_{t\geq 0}$ is non-integrable for $d \geq 2$. We continue with an overview of the basic physical phenomenology of the post-quench dynamics for weak to intermediate interaction strengths. A characteristic observable for the dynamics is the discontinuity $\Delta n_{k_F}(t)$ of the distribution function $n(\epsilon)$ at the Fermi energy, which has the interpretation in Fermi liquid theory mentioned above. Within unitary perturbation theory, the following behavior was found: The Fermi surface discontinuity decreases rapidly on a timescale $\sim \rho(\epsilon_F)^{-1} U^{-2}$, where $\rho(\epsilon) = \frac{1}{V} \sum_k \delta(\epsilon - \epsilon_k)$, until a non-vanishing value $\Delta n^{\text{pretherm}}_{k_F} > 0$ is reached, which then remains constant up to times $\sim \rho(\epsilon_F)^{-3} U^{-4}$. The formation of this “plateau” is a remarkable finding and can be interpreted as a dynamical remnant of the integrable pre-quench Hamiltonian, whose additional conserved quantities still constrain the dynamics on that timescale. Fig. 4.1 shows sketches of the distribution function in the different regimes. Interestingly, one finds $\Delta n^{\text{pretherm}}_k = 2\Delta n^{\text{FLT}}_k$, i.e. the non-equilibrium discontinuity differs by a factor of

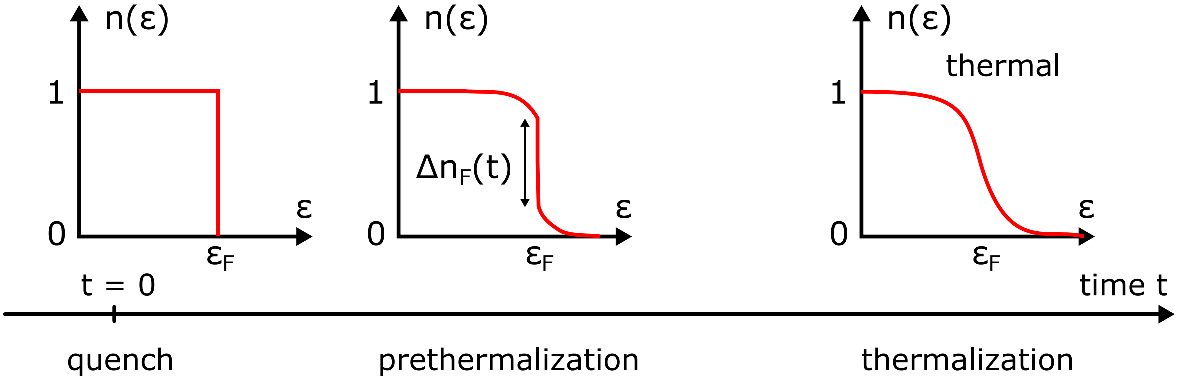

Figure 4.1: Sketch of the basic phenomenology of the interaction quench dynamics in the Hubbard model for weak to intermediate interaction strengths U on the single-particle level. The distribution function $n(\epsilon_k)$ with single-particle energy ϵ_k is shown for three characteristic time regimes. Initially, the system is prepared in a zero-temperature Fermi sea state with a discontinuity at the Fermi energy of size one. During the dynamics a reduction of the discontinuity can be observed corresponding to prethermalization. Ultimately, the distribution becomes thermal.

two from the Fermi liquid theory prediction in equilibrium. Such “mismatch” factors can be calculated as well for finite interaction ramp speeds [217] and one finds values between one and two. The long-lived quasi-steady regime is called *prethermal* [224]. On later timescales, a departure from the plateau is expected and the distribution function eventually thermalizes to a smooth Fermi-Dirac distribution. The thermalization dynamics was demonstrated explicitly using non-equilibrium DMFT [75, 225]. It was shown using random matrix theory that prethermalization is indeed a *typical*, i.e. characteristic for *almost all* (in a mathematical sense) applicable perturbations, phenomenon of weakly perturbed many-body systems [226]. In addition, it can also occur if the unperturbed dynamics is non-integrable as long as a suitable conservation law is respected [227].

In more physical terms, one can associate the observed dynamics to the formation and scattering of quasiparticles. The initial rapid decrease of the Fermi surface discontinuity is due to a correlation build-up, i.e. a formation of quasiparticles. In the prethermal phase the quasiparticles have formed but their scattering dynamics is not efficient on that timescale. Therefore, the prethermal regime is sometimes also described as *collisionless* [228]. In terms of the original electrons, one needs to distinguish between inelastic and elastic scattering processes. The prethermal phase is generated by inelastic scattering processes of the electrons that lead to a redistribution between kinetic and interaction energy. This process is known as *dephasing* because the one-particle density matrix becomes diagonal with respect to the quasiparticle basis in the prethermal phase. This is in contrast to the bare electron one-particle density matrix, which is diagonal in the initial Fermi sea state but non-diagonal in the prethermal state. The occupation numbers of the quasiparticles are constants of motion in the prethermal regime, or, *approximate constants of motion* of the whole dynamics [69]. One can expect an effective description of the prethermal state in terms of a *generalized Gibbs ensemble (GGE)*, which takes the additional constants of motion into account.

Finally, we discuss in more detail the post-quench dynamics from the viewpoint of the energy balance. In the original study [73] the interaction term is written in normal-ordered form with respect to the non-interacting ground state. Consequently, the total energy of the system before and after the quench is exactly the same. One can also keep the density-density representation and include the additional interaction energy into the energy balance which, due to the product structure of the initial state, is easy to calculate:

$$\langle \hat{H}_{\mathrm{int}} \rangle_{\mathrm{FS}} = U \sum_i \langle \hat{n}_{i\uparrow} \hat{n}_{i\downarrow} \rangle_{\mathrm{FS}} = U \sum_i \langle \hat{n}_{i\uparrow} \rangle_{\mathrm{FS}} \langle \hat{n}_{i\downarrow} \rangle_{\mathrm{FS}} = UV \left(\frac{N_{\mathrm{el}}}{V} \right)^2, \tag{4.3}$$

where we used $\langle \hat{n}_{i\uparrow} \rangle_{\mathrm{FS}} = \langle \hat{n}_{i\downarrow} \rangle_{\mathrm{FS}}$, V denotes the number of lattice sites and N_{el} the number of electrons. Since during the dynamics occupation numbers in real space remain constant, this“mean-field” interaction energy is not redistributed and does not further influence the dynamics. However, the ground state of the interacting system has a lower total energy than the post-quench state such that after the quench there is a finite amount of excitation energy in the system. One can readily learn from 2nd order perturbation theory [216] that the equilibrium kinetic energy of the interacting system happens to equal the excitation energy. Interestingly, the long-time average of the $\mathcal{O}(U^2)$ unitary perturbation theory result yields a kinetic energy of the prethermal state, which equals twice the excitation energy. Hence, during prethermalization all of the excitation energy is converted into kinetic energy. Ultimately, this additional kinetic energy will give rise to a non-zero temperature of the thermalized state. In contrast, the prethermal state is clearly non-thermal as can be seen from the discontinuity of $n(\epsilon)$ at the Fermi energy, which would not be present in a smooth Fermi-Dirac distribution. The thermalization dynamics is expected to be governed by a quantum Boltzmann equation (QBE) [73, 216, 75],

$$\begin{aligned}\partial_t n_{k\sigma}(t) = -2\pi\left(\frac{U}{V}\right)^2 \sum_{pq} \delta\big(\epsilon_{k+q} + \epsilon_{p-q} - \epsilon_p - \epsilon_k\big)\cdot \\ \Big(n_{k\sigma}(t) n_{p\bar{\sigma}}(t)\big(1 - n_{(k+q)\sigma}(t)\big)\big(1 - n_{(p-q)\bar{\sigma}}(t)\big) - \big(k, p \leftrightarrow k+q, p-q\big)\Big),\end{aligned} \tag{4.4}$$

which does not transfer energy between kinetic and interaction sector.

The energy balance illuminates the following principle [53]: Fast relaxation of momentum-averaged quantities like the kinetic energy and slow relaxation of mode quantities like the momentum distribution. The first is due to dephasing while the latter is due to elastic scattering. One needs to keep in mind that momentum redistribution can only happen via exchange in scattering processes. Those, however, are generally constrained by phase space factors like in the QBE or in Fermi's golden rule. This bottleneck delays the momentum relaxation to a later timescale than the energy relaxation and is the reason for the multi-stage structure of the dynamics.

4.1.1 State of the Art and Open Questions

The physics of the interaction quench problem in the Hubbard model is basically completely understood. A minor question concerns effects specific to two spatial dimensions, where Fermi surface nesting might suppress the prethermalization plateau at half filling [229]. However, the most interesting open challenge is method-related and concerns the bridging of timescales. While QBEs correctly describe the approach to thermal equilibrium, they do not capture the initial correlation build-up dynamics and and hence the prethermal electron distribution has to be constructed by hand as an initial condition to the QBE. On the other hand, the perturbative scheme does – at least so far – not yield thermalization dynamics at the present order of the calculations such that its validity is restricted to the prethermal regime. It is likely exactly the secular on-shell terms that give rise to the Boltzmann dynamics in the long-time limit. A description based on a more general kinetic equation was proposed [223] to include both regimes. The perturbative analysis was recently extended to photoexcitations in Fermi liquids [230].

Due to its combination of multiple timescales with different dynamical characteristics, the interaction quench problem is a well suited problem to assess the validity of new time evolution methods. Therefore, in the following, we apply the fermionic TWA scheme to a large-N generalization of the Hubbard model and compare the results to the exact solution in the prethermal regime.

4.2 Systematic large flavor fTWA approach to interaction quenches in the Hubbard model (cf. [1])

The results and parts of the text in this section are also contained in the preprint [1], *Systematic large flavor fTWA approach to interaction quenches in the Hubbard model*, `arXiv:2007.05063`. Sections, in which figures or parts of the texts are reprinted, are marked with a hint "(cf. [1])".

4.2.1 Model and Method Setup (cf. [1])

We study the interaction quench setup as described in the Introduction section but for the SU(N)-symmetric version of the Hubbard model. This allows for a detailed analysis of the validity of the fTWA method as a function of the effective $\hbar \sim \frac{1}{N}$. In the following, we always choose a finite $L \times L$ square lattice with tight-binding dispersion $\epsilon_k = -2t_\mathrm{h}\big(\cos(k_x) + \cos(k_y)\big)$.

The SU(N)-Hubbard Hamiltonian is given in eqn. (2.48) and in eqn. (2.51) in terms of $\hat{\rho}_{ij}$-operators. We note that the use of flavor-averaged phase space variables resolves an ambiguity [157] in the classical representation of the $N = 2$ interaction term, which is due to the quantum mechanical identity $n_{i\alpha}^2 = n_{i\alpha}$ for fermions. At $N = 2$, the "naive" representation

$$H_\mathrm{int}^{(I)} = U \sum_i \left(\rho_{i\uparrow,i\uparrow} + \frac{1}{2}\right)\left(\rho_{i\downarrow,i\downarrow} + \frac{1}{2}\right) \tag{4.5}$$

with $\hat{\rho}_{i\alpha,j\beta} = c_{i\alpha}^\dagger c_{j\beta} - \frac{1}{2}\delta_{ij}\delta_{\alpha\beta}$, is quantum mechanically, but not semiclassically, equivalent to the representation derived from the SU(N) invariant Hamiltonian

$$H_\mathrm{int}^{(II)} = \frac{U}{2} \sum_i \left(\rho_{i\uparrow,i\uparrow} + \rho_{i\downarrow,i\downarrow}\right)^2 . \tag{4.6}$$

However, for the problem considered in this text we did not observe differing results between the two representations. In other contexts [112, 157], a specific choice (corresponding to our SU(N)-invariant model) of the representation has turned out to yield better numerical results than other choices.

The equations of motion for the classical ρ_{ij} can be obtained from the classical Hamiltonian formalism [112] upon mean-field decoupling $\hat{\rho}_{ii}^2 \to \rho_{ii}^2$. Equivalently, they follow from the Heisenberg equations of motion corresponding to (2.51) in the limit $N \to \infty$,

$$\begin{aligned} i\partial_t \rho_{ij} = &-t_\mathrm{h} \sum_{a(j)} \rho_{i,a(j)} + t_\mathrm{h} \sum_{a(i)} \rho_{a(i),j} \\ &+ 2U(\rho_{jj} - \rho_{ii})\rho_{ij} . \end{aligned} \tag{4.7}$$

The equilibrium ground state of the model with $U = 0$ is given by the N-flavor Fermi sea $|\mathrm{FS}\rangle = \prod_{\alpha,\epsilon(\vec{k})\leq\epsilon_F} c_{\vec{k}\alpha}^\dagger |0\rangle$ whose initial data (2.88) in momentum space is given by

$$\begin{aligned}\left\langle\hat{\rho}_{kl}\right\rangle = \left\langle\hat{\rho}^{\dagger}_{kl}\right\rangle &= \delta_{k,l}\left(n_k - \frac{1}{2}\right),\\ \left\langle\frac{1}{2}\left\{\hat{\rho}_{kl},\hat{\rho}_{sp}\right\}\right\rangle^{\text{c.c.}} &= \frac{1}{2N}\delta_{kp}\delta_{ls}\left(n_k + n_l - 2n_k n_l\right)\end{aligned} \tag{4.8}$$

At $N \to \infty$, the Hubbard interaction U in the Hamiltonian (2.51) merely plays the role of a shift of the chemical potential such that non-trivial dynamics after the interaction quench can only occur at finite N.

There are many different probability distributions with a given mean μ and variance σ^2 of a random variable x. In the following, we will mostly choose a Gaussian distribution and, for comparison, a two point distribution $P_{\text{TP}}(x) = \frac{1}{2}\delta(\mu - \sigma) + \frac{1}{2}\delta(\mu + \sigma)$. In a study of the LMG model it was demonstrated [165] that the validity of fTWA (the stochastic mean-field approach) can be improved by using a two-point distribution instead of a Gaussian distribution.

4.2.2 Results for the SU(N)-fTWA (cf. [1])

4.2.3 Perturbative treatment of the e.o.m.

For weak Hubbard interaction strengths $U \ll t_{\text{h}}$, one can treat the classical equations of motion perturbatively and evaluate all expectation values with respect to the Gaussian Wigner function by hand. In order to do so, it is advantageous to work with the equations in momentum space. Using the Fourier transform

$$\rho_{ij} = \sum_{kl} \mathrm{e}^{i(kr_i - lr_j)}\rho_{kl} \tag{4.9}$$

one obtains the equations of motion in momentum space,

$$\begin{aligned}i\partial_t \rho_{kl} =& -\left(\epsilon_k - \epsilon_l\right)\rho_{kl}\\ &+ \frac{2U}{V}\sum_{sp}\left(\rho_{p+s-l,p}\rho_{ks} - \rho_{p+k-s,p}\rho_{sl}\right).\end{aligned} \tag{4.10}$$

A naive perturbative expansion of these equations in U is only valid up to times $\mathcal{O}(t^2)$. In order to avoid those restricting secular terms we switch to an interaction picture representation of the equations of motion by incorporating the free time-evolution into the variables $\tilde{\rho}_{kl} = \mathrm{e}^{-i(\epsilon_k - \epsilon_l)t}\rho_{kl}$ where $\Delta\epsilon_{pks} = \epsilon_{p+k-s} + \epsilon_s - \epsilon_p - \epsilon_k$. This yields

$$\begin{aligned}i\partial_t \tilde{\rho}_{kl} = \frac{2U}{V}\sum_{sp}\Big[&\mathrm{e}^{i\Delta\epsilon_{psl}t}\tilde{\rho}_{p+s-l,p}\tilde{\rho}_{ks}\\ &- \mathrm{e}^{i\Delta\epsilon_{pks}t}\tilde{\rho}_{p+k-s,p}\tilde{\rho}_{sl}\Big].\end{aligned} \tag{4.11}$$

We may now expand the variables order by order in U

$$\tilde{\rho}_{kl} = \tilde{\rho}^{(0)}_{kl} + \tilde{\rho}^{(1)}_{kl}\cdot U + \tilde{\rho}^{(2)}_{kl}\cdot U^2 + \dots. \tag{4.12}$$

Inserting the ansatz into (4.11) yields a hierarchy of equations, organized by powers of U. Since $i\partial_t\tilde{\rho}_{kl} = \mathcal{O}(U)$, $i\partial_t\tilde{\rho}^{(0)}_{kl} = 0$ follows immediately. Consequently, $\tilde{\rho}^{(0)}_{kl}(t) = \delta_{kl}n_k(0)$.

This fact allows to explicitely integrate all time dependencies in the equation for $\tilde{\rho}^{(1)}_{kl}$. In a last step all expectation values of products of $\tilde{\rho}^{(0)}_{kl}$ are evaluated using the Gaussian Wigner function. Successive application of this scheme results in an iterative procedure to solve for the dynamics to all orders of U.

The equation of motion for the $\mathcal{O}(U)$ contribution is

$$\begin{aligned} i\partial_t\tilde{\rho}^{(1)}_{kl} = \frac{2}{V}\sum_{sp}\Big[&\mathrm{e}^{i\Delta\epsilon_{psl}t}\tilde{\rho}^{(0)}_{p+s-l,p}\tilde{\rho}^{(0)}_{ks} \\ &- \mathrm{e}^{i\Delta\epsilon_{pks}t}\tilde{\rho}^{(0)}_{p+k-s,p}\tilde{\rho}^{(0)}_{sl}\Big]. \end{aligned} \tag{4.13}$$

We can integrate the dependencies on time explicitly using the integral

$$\begin{aligned} \mathcal{I}_1(\Delta\epsilon_{pab}) &= -i\int_0^t \mathrm{d}t'\mathrm{e}^{i\Delta\epsilon_{pab}t'} \\ &= \begin{cases} \frac{1}{\Delta\epsilon_{pab}}\left(\mathrm{e}^{i\Delta\epsilon_{pab}t} - 1\right) & \Delta\epsilon_{pab} \neq 0 \\ -it & \Delta\epsilon_{pab} = 0 \end{cases} \end{aligned} \tag{4.14}$$

The Wigner function averages are performed manually using

$$\langle\tilde{\rho}^{(0)}_1\tilde{\rho}^{(0)}_2\rangle = \langle\tilde{\rho}^{(0)}_1\tilde{\rho}^{(0)}_2\rangle^c + \langle\tilde{\rho}^{(0)}_1\rangle\langle\tilde{\rho}^{(0)}_2\rangle \tag{4.15}$$

and the initial data in (2.88). The structure of (4.13) is such that both terms cancel each other after the Wigner function averaging. Thus $\tilde{\rho}^{(1)}_{kl}(t) = 0$.

The next order $\mathcal{O}(U^2)$ already contains eight terms

$$\begin{aligned} \tilde{\rho}^{(2)}_{k,l}(t) = \frac{4}{V^2}\sum_{sps'p'}\Big[& \\ &\mathcal{I}_2(\Delta\epsilon_{p's's}, \Delta\epsilon_{psl})\tilde{\rho}^{(0)}_{(p+s-l),p}\tilde{\rho}^{(0)}_{(p'+s'-s),p'}\tilde{\rho}^{(0)}_{k,s'} \\ &- \mathcal{I}_2(\Delta\epsilon_{p'ks'}, \Delta\epsilon_{psl})\tilde{\rho}^{(0)}_{(p+s-l),p}\tilde{\rho}^{(0)}_{(p'+k-s'),p'}\tilde{\rho}^{(0)}_{s',s} \\ &+ \mathcal{I}_2(\Delta\epsilon_{p's'p}, \Delta\epsilon_{psl})\tilde{\rho}^{(0)}_{(p'+s'-p),p'}\tilde{\rho}^{(0)}_{(p+s-l),s'}\tilde{\rho}^{(0)}_{k,s} \\ &- \mathcal{I}_2(\Delta\epsilon_{p'(p+s-l)s'}, \Delta\epsilon_{psl})\tilde{\rho}^{(0)}_{(p'+p+s-l-s'),p'}\tilde{\rho}^{(0)}_{s',p}\tilde{\rho}^{(0)}_{k,s} \\ &- \mathcal{I}_2(\Delta\epsilon_{p's'l}, \Delta\epsilon_{pks})\tilde{\rho}^{(0)}_{(p+k-s),p}\tilde{\rho}^{(0)}_{(p'+s'-l),p'}\tilde{\rho}^{(0)}_{s,s'} \\ &+ \mathcal{I}_2(\Delta\epsilon_{p'ss'}, \Delta\epsilon_{pks})\tilde{\rho}^{(0)}_{(p+k-s),p}\tilde{\rho}^{(0)}_{(p'+s-s'),p'}\tilde{\rho}^{(0)}_{s',l} \\ &- \mathcal{I}_2(\Delta\epsilon_{p's'p}, \Delta\epsilon_{pks})\tilde{\rho}^{(0)}_{(p'+s'-p),p'}\tilde{\rho}^{(0)}_{(p+k-s),s'}\tilde{\rho}^{(0)}_{s,l} \\ &+ \mathcal{I}_2(\Delta\epsilon_{p'(p+k-s)s'}, \Delta\epsilon_{pks})\tilde{\rho}^{(0)}_{(p'+p+k-s-s'),p'}\tilde{\rho}^{(0)}_{s',p}\tilde{\rho}^{(0)}_{s,l}\Big] \end{aligned} \tag{4.16}$$

where

$$\mathcal{I}_2(\Delta\epsilon_{p'ab}, \Delta\epsilon_{pcd}) = -\int_0^t \mathrm{d}\,t'\int_0^{t'}\mathrm{d}\,t''\mathrm{e}^{i\Delta\epsilon_{pcd}t'}\mathrm{e}^{i\Delta\epsilon_{p'ab}t''}. \tag{4.17}$$

The third moments of the Wigner function are evaluated using Wick's theorem for a Gaussian distribution

$$\begin{aligned}\langle\tilde\rho_1^{(0)}\tilde\rho_2^{(0)}\tilde\rho_3^{(0)}\rangle &= \langle\tilde\rho_1^{(0)}\rangle\langle\tilde\rho_2^{(0)}\tilde\rho_3^{(0)}\rangle^c + \langle\tilde\rho_2^{(0)}\rangle\langle\tilde\rho_1^{(0)}\tilde\rho_3^{(0)}\rangle^c \\ &+ \langle\tilde\rho_3^{(0)}\rangle\langle\tilde\rho_1^{(0)}\tilde\rho_2^{(0)}\rangle^c + \langle\tilde\rho_1^{(0)}\rangle\langle\tilde\rho_2^{(0)}\rangle\langle\tilde\rho_3^{(0)}\rangle\end{aligned} \tag{4.18}$$

It turns out that after averaging over the Wigner function, (4.16) has the structure

$$\begin{aligned}\tilde\rho_{kl}^{(2)}(t) &= \delta_{k,l}\frac{4}{NV^2}\sum_{pp'}J_{pp'k}\cdot \\ &\cdot\Big[\mathcal{I}_2(-\Delta\epsilon_{pp'k},\Delta\epsilon_{pp'k}) + \mathcal{I}_2(\Delta\epsilon_{pp'k},-\Delta\epsilon_{pp'k})\Big]\end{aligned} \tag{4.19}$$

with

$$\begin{aligned}&\mathcal{I}_2(\Delta\epsilon_{pp'k},-\Delta\epsilon_{pp'k}) + \mathcal{I}_2(\leftrightarrow) = \\ &= \begin{cases} -\frac{4}{(\Delta\epsilon_{pp'k})^2}\sin^2\left(\frac{\Delta\epsilon_{pp'k}}{2}t\right) & \Delta\epsilon_{pp'k}\neq 0 \\ -t^2 & \Delta\epsilon_{pp'k} = 0\end{cases}.\end{aligned} \tag{4.20}$$

We have evaluated the expression for the elastic contributions $\Delta\epsilon_{pp'k} = 0$ directly at the level of the integral (4.17). Otherwise, they would lead to diverging energy denominators. Since the elastic terms yield secular contributions $\sim t^2$ they invalidate the perturbation theory and one can as well formally shift them into to the unperturbed part of the Hamiltonian. In the long-time limit we expect that these terms generate the thermalization dynamics governed by a Quantum Boltzmann equation.

In summary, up to order U^2, we obtain the following results:

$$\begin{aligned}\tilde\rho_{kl}^{(1)}(t) &= 0 \\ \tilde\rho_{kl}^{(2)}(t) &= -\delta_{k,l}\frac{16}{NV^2}\sum_{\substack{pp' \\ \Delta\epsilon_{pp'k}\neq 0}}\frac{\sin^2\left(\frac{\Delta\epsilon_{pp'k}}{2}t\right)}{(\Delta\epsilon_{pp'k})^2}J_{pp'k}\end{aligned} \tag{4.21}$$

where

$$\begin{aligned}J_{pp'k} &= n_k n_{p+p'-k}(1-n_p)(1-n_{p'}) \\ &- n_p n_{p'}(1-n_k)(1-n_{p+p'-k})\end{aligned} \tag{4.22}$$

is a phase space factor. These results agree precisely with those obtained from unitary perturbation theory [73]. It is worth noting that via the sampling of the initial conditions the truncated Wigner approach with its time-local mean-field equations of motion is able to reproduce an effect of the non-Markovian correlated dynamics.

4.2.4 Numerical results (cf. [1])

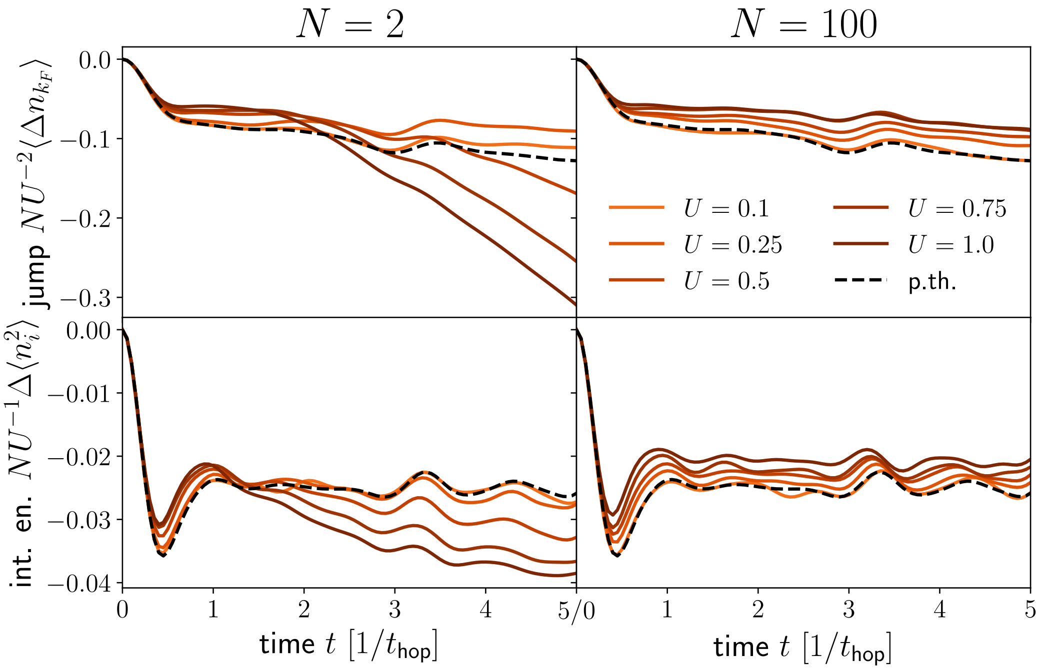

Figure 4.2: fTWA dynamics of a 10×10 square lattice Fermi sea at quarter filling ($N_p = 25$ particles) after an interaction quench to weak and intermediate values of U (in units of t_h). The two columns show results for degeneracy parameters $N = 2$ and $N = 100$, respectively. The upper two panels contain results for the jump of the momentum distribution at the Fermi energy, rescaled by a factor of N/U^2 that allows for a comparison to the result (4.21) obtained from perturbation theory. In the bottom row the dynamics of the interaction energy is shown. There the black dashed curve is calculated using the perturbative result for the occupation numbers in combination with energy conservation during time evolution. All fTWA data is averaged over at least 200000 trajectories.

In order to study the quench dynamics numerically, we implemented Hamilton's equations of motion using the odeint library [169] and the Armadillo library [231, 232]. To avoid the accumulation of numerical errors from the addition of floating point numbers, Welford's algorithm is used for checkpointing [173]. Two characteristic observables for the interaction quench dynamics are the change Δn_{k_F} of the momentum distribution n_k at the Fermi energy and the interaction energy $\langle \hat{H}_\text{int} \rangle \sim \langle n_i^2 \rangle$. The first is, as detailed above, related to the quasiparticle weight Z [73]. $\Delta n_{k_F} = 1$ for the initial zero-temperature Fermi-Dirac distribution. The interaction energy is, in contrast, a local quantity that is expected to relax in the prethermal regime to the equilibrium value of the post-quench Hamiltonian at the final temperature (determined by the amount of quench energy). It provides a generalization of the double occupation $d(t) = \langle n_{i\downarrow} n_{i\uparrow} \rangle$ used in the conventional $N = 2$ case. The conservation of the total energy allows to compute the exact time evolution of $\langle \hat{H}_\text{int} \rangle$ at order U^2 from the perturbative result (4.21).

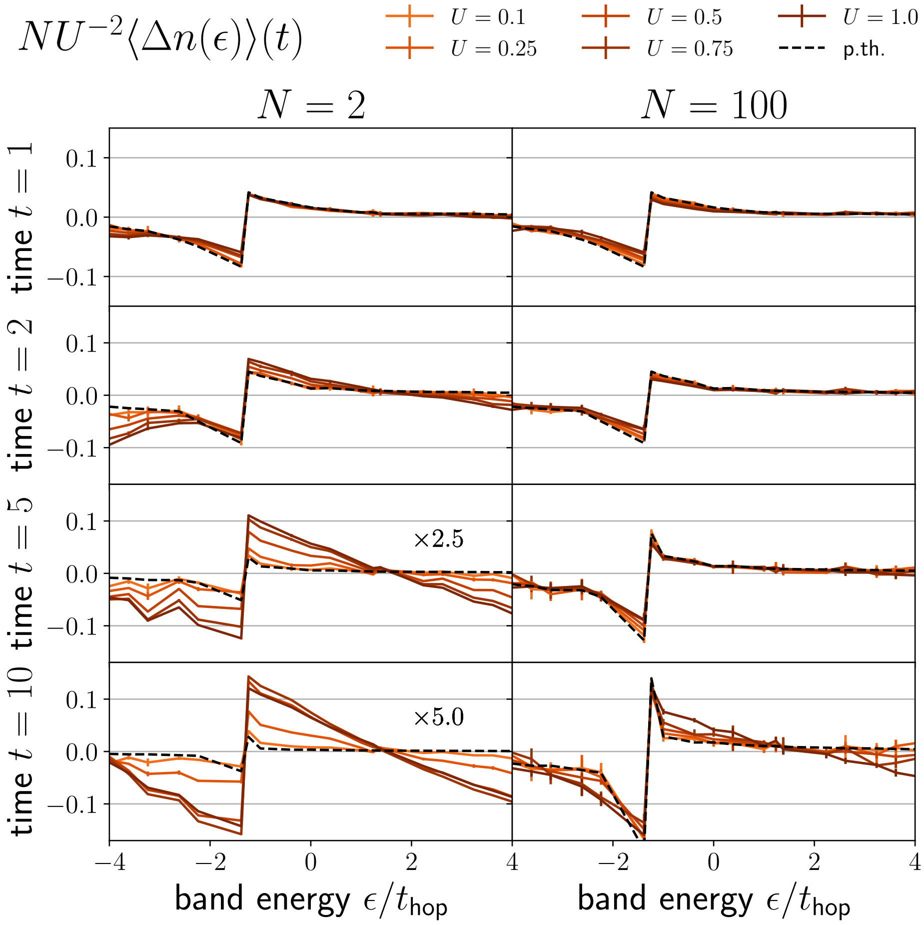

Figure 4.3: Momentum distribution $\Delta n_\epsilon(t) = n_\epsilon(t) - n_\epsilon(0)$ as a function of the band energies ϵ for a 10×10 square lattice at quarter filling ($N = 25$ particles) after a quench to Hubbard interactions $U \leq 1$. It corresponds to the data shown in Fig. 4.2. Error bars are determined from the error of the average over symmetry-related momentum modes.

Since prethermalization effects are possibly suppressed at half filling in the 2D model [229], we consider quarter filling in the following. For the finite system sizes we treat here, we choose a number of electrons so that all energy levels with identical single-particle energies below the Fermi energy are filled. This leads to a symmetric occupation of modes in momentum space such that the observed dynamics is not influenced by finite system degeneracy effects.

Fig. 4.2 shows the numerical results for Δn_{k_F} and the change of $\langle n_i^2\rangle$ in a 10×10 system at two fixed values of the degeneracy parameter N, whereas Fig. 4.4 shows data for a 20×20 system at a fixed value of $U = 0.5t_{\text{h}}$ and varying N. The case $N = 2$ is equivalent to the conventional Hubbard model. In the figures, we scaled the observables in a way that their order U^2/N contributions according to (4.21) coincide. This allows to focus on the deviations from the formula.

Let us start the discussion with Fig. 4.2: For small $U = 0.1t_{\text{h}}$, both observables agree well with the perturbative calculation. For larger $U \sim t_{\text{h}}$ there is a clear deviation from the perturbative result, which is also expected. However, note that qualitatively

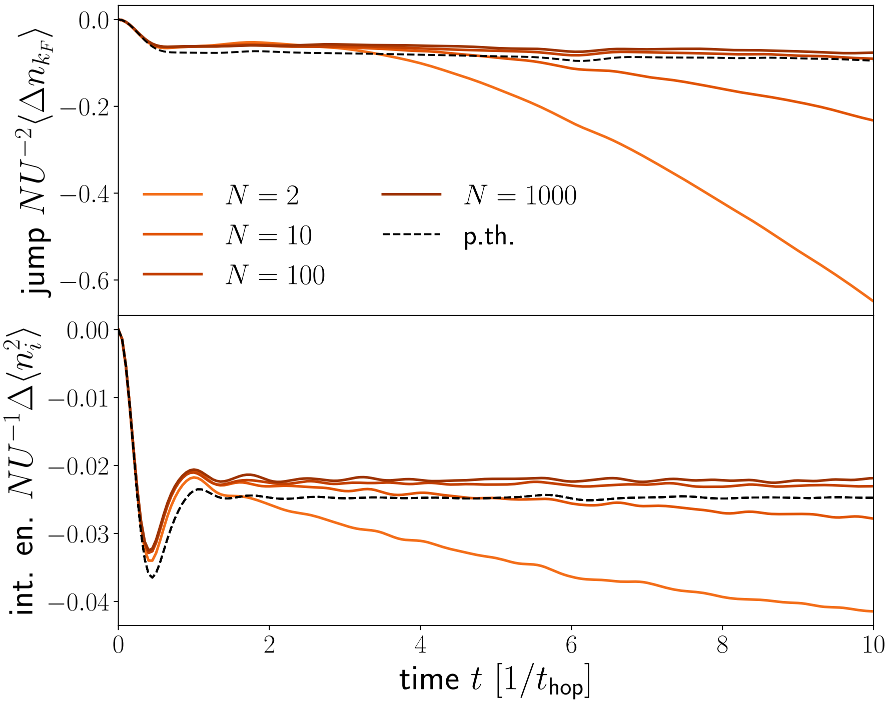

Figure 4.4: Fermi surface jump and interaction energy for a 20 × 20 square lattice Fermi sea at quarter filling ($N = 101$ particles) after an interaction quench to $U = 0.5$ at varying N.

the overall shape of the curve does not change much, in agreement with other exact numerical treatments [53] of the interaction quench problem. This indicates that the mechanism behind prethermalization is more general and not restricted to the perturbative regimes that are well accessible with perturbation theory.

After the initial correlation build-up a plateau is forming until, for $N = 2$, a further reduction of the jump sets in. One can observe in particular that the width of the plateau is smaller for greater values of U, whereas for $N = 100$ the prethermal dynamics extends over a much longer timespan. The onset of this reduction for varying N can well be seen in Fig. 4.4. Although the behaviour at $N = 2$ is in qualitative agreement with numerical calculations in infinite dimensions [53], the question needs to be addressed whether it describes the true thermalization dynamics. Looking at the interaction energy the expected equilibration in the prethermal regime is found for $N \geq 100$. For smaller values of N in contrast, $\langle n_i^2\rangle$ starts to decay even before the reduction dynamics is visible in Δn_{k_F}. The departure of the interaction energy from its prethermal value is clearly unphysical behavior since we do not expect energy redistribution between kinetic and interaction energy at this stage of the dynamics any more.

To shed more light on this question we consider the whole momentum distribution $\langle\Delta n(\epsilon)\rangle(t) = n_\epsilon(t) - n_\epsilon(0)$ at all single-particle energies ϵ_k shown in Figs. 4.3 and 4.5. At time zero, $n_\epsilon(0) = \theta(\epsilon_F - \epsilon)$. For small N negative occupation numbers are observable close to the band edge at $\epsilon = 4$ already at early times. This becomes worse at later times and clearly indicates the onset of unphysical behavior. We conclude that in the regime of weak to moderate interactions the method correctly captures the dynamics at order

$\frac{1}{N}$ and is valid at least up to and including the prethermal regime. The dynamics beyond prethermalization displays a qualitatively correct picture at the Fermi energy but this is not reliable due to the emergence of unphysical occupation numbers. Another way to look at this is that the stationary solutions in the long-time limit of the fTWA dynamics are no Fermi-Dirac distributions. Further below we will take a closer look at this long-time behavior.

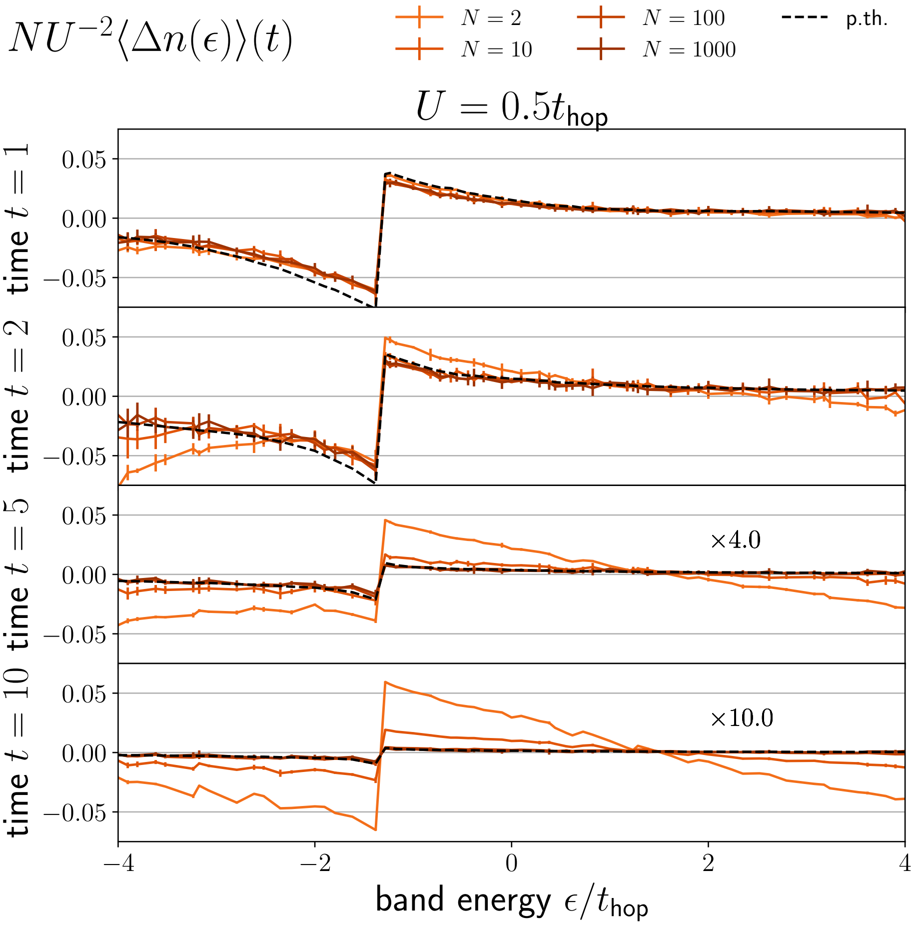

Figure 4.5: Momentum distribution $\Delta n_\epsilon(t) = n_\epsilon(t) - n_\epsilon(0)$ as a function of the single-particle energies ϵ corresponding to the data shown in Fig. 4.4. Errors are estimated from the deviations among symmetry-related momentum modes.

4.3 Convergence of the simulations

We continue with a closer look at the convergence of the simulations with the number of sampled trajectories N_{rep}. Multiple checks can be done to control the convergence of the simulation: As a simple tool, we calculate how well symmetries are restored in the data as a function of the number of Wigner function samples. In particular, we can use the momentum degeneracy of single-particle energies ϵ_k and check how much the values of n_k differ among the degenerate k-modes. In the diagrams, we always plot the degeneracy-averaged values. Due to the underlying symmetry, we can

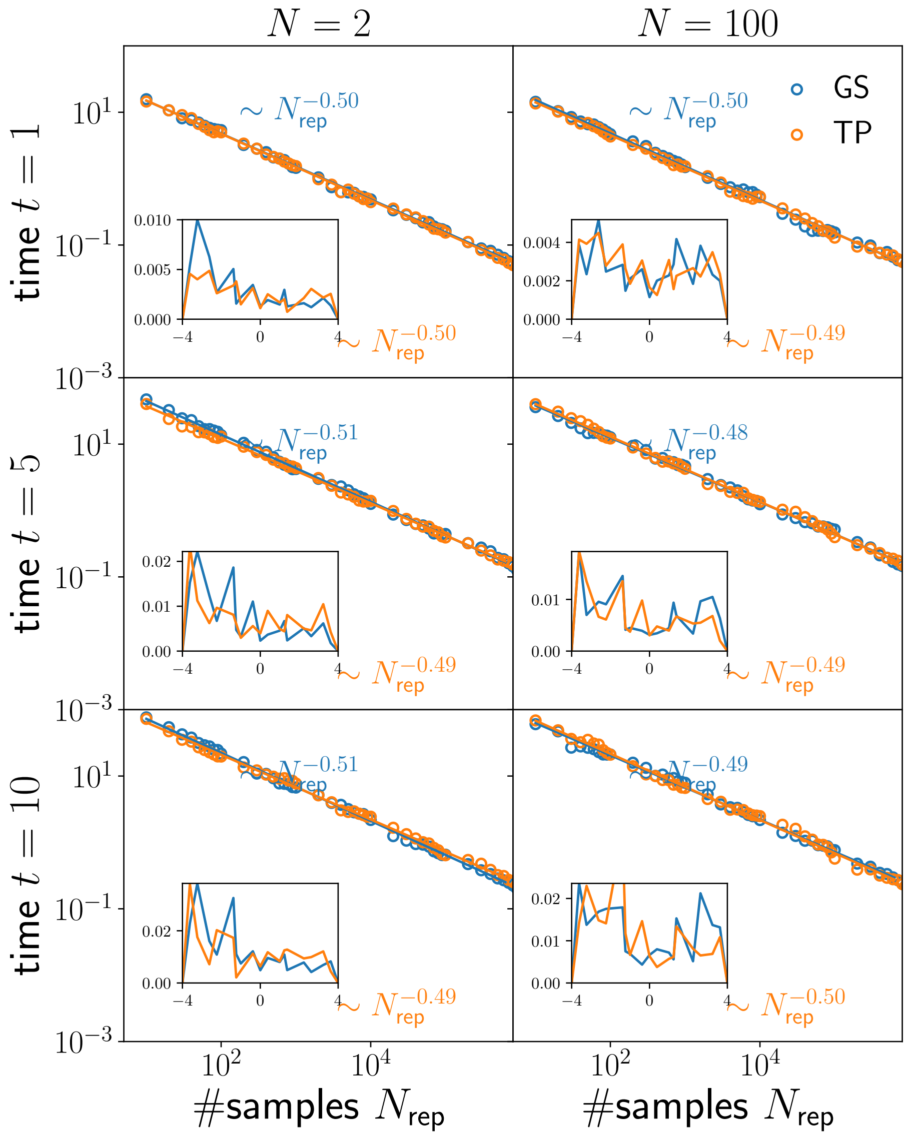

Figure 4.6: Error estimate based on how well the k-space symmetries are restored after the average over N_{rep} trajectories. Data obtained for a 10×10 system and a quench to $U = 0.1$. The GS data was obtained using a Gaussian Wigner function model, the TP data using a two-point distribution model.

interpret the individual values $n_k^{(1)}, \ldots, n_k^{(D)}$ for a given band energy ϵ_k as samples drawn from the same probability distribution. The uncertainty $\Delta\mu$ of this averaged value (the mean of that distribution) can be calculated from the empirical variance $\sigma_{\text{emp}}^2 = \frac{1}{D-1}\sum_i^D (n_k^{(i)} - \mu_{\text{emp}})^2$ and is given by $\Delta\mu = \sigma_{\text{emp}}/\sqrt{D}$. $\mu_{\text{emp}} = \frac{1}{D}\sum_i^D n_k^{(i)}$ is the sample mean. In Fig. 4.6 we show the uncertainties summed over all band energies ϵ_k as a function of the number of Wigner function samples N_{rep}. There is a clear $1/\sqrt{N_{\text{rep}}}$ scaling visible in the data. We have also checked that the estimated error is compatible with the generic Monte Carlo error based on the empirical variance of the observables obtained from the running average over N_{rep} trajectories.

One can also see that the curve moves to higher uncertainties at later times. This

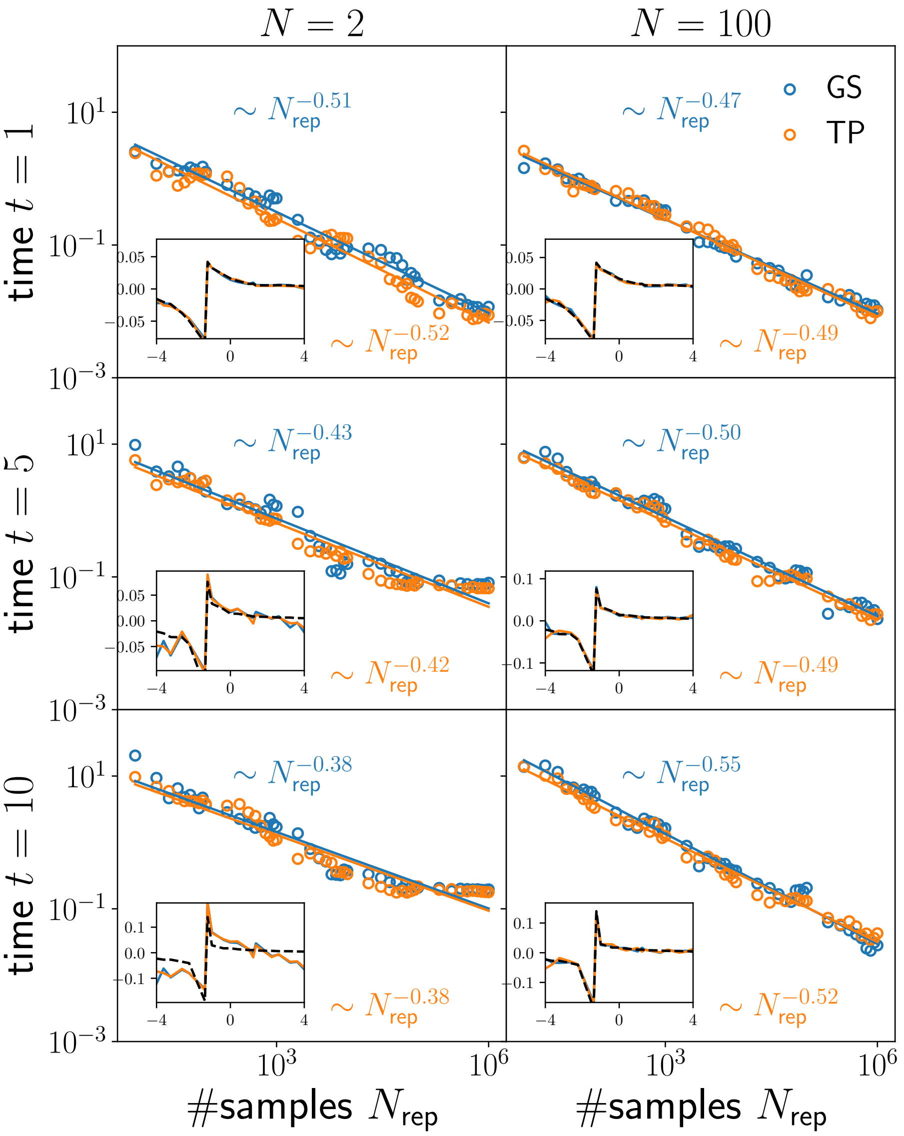

Figure 4.7: Deviations from the perturbative calculation in a system with 10 × 10 lattice sites and for a quench to $U = 0.1$. The inset shows the fTWA mode occupation distribution $n(\epsilon_k)$ (for the highest number of samples). Blue dots are obtained using a Gaussian Wigner function, orange dots using a two-point distribution and the dashed black line shows the perturbative result.

is due to the fact that fluctuations generated at initial time $t_0 = 0$ can grow because of the non-linear equations of motion. The errors so obtained are typically below 10% but can be as high as 100%. It is important to note that the slow convergence is a consequence of the fact that the observable $\Delta n(\epsilon)$ scales like $\sim \frac{1}{N}$. It is therefore of the same order of magnitude as the Wigner function fluctuations, which are also $\sim \frac{1}{N}$. Such large numbers of samples are not needed if one is interested in the leading $\mathcal{O}(1)$ contribution. To shed more light on the convergence of the simulation, we make use of the fact that the perturbative formula can serve as exact comparison data in the prethermal regime. Figs. 4.7 and 4.8 show results for the L^2-distance of the numerical

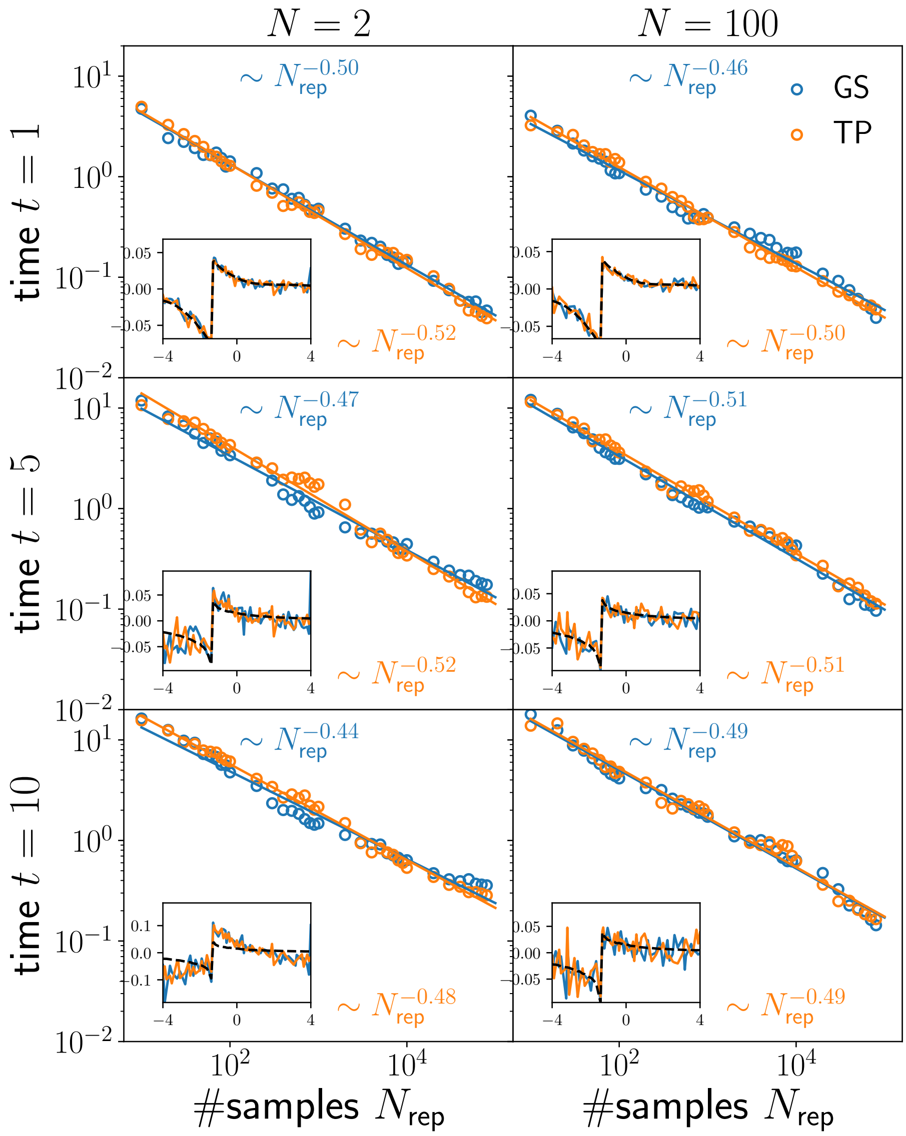

Figure 4.8: Deviations from the perturbative calculation in a system with 20 × 20 lattice sites and for a quench to $U = 0.1$. The inset shows the fTWA mode occupation distribution $n(\epsilon_k)$ (for the highest number of samples). Blue dots are obtained using a Gaussian Wigner function, orange dots using a two-point distribution and the dashed black line shows the perturbative result.

$n(\epsilon)$ curve to the perturbative result in 10×10 and 20×20 lattices, respectively. The quench is to $U = 0.1$ in both cases. In addition, we compare two Wigner function models: a Gaussian distribution and a two-point Wigner function model. The first obvious observation is that – at least for the problem considered here – Gaussian and two-point model converge at the same rate to the same result. Contrary to what was observed in [165], we do not find an advantage of fine-tuned Wigner function models: th reason is unclear. At early times, the fTWA data approaches the analytical result also at a $1/\sqrt{N_{\text{rep}}}$ rate. For comparison we provide a similar figure for a quench to $U = 0.5$ in Appendix A. One finds that in this case the deviations from the perturbation theory are more pronounced at early times and, for $N = 2$, $n(\epsilon)$ becomes clearly unphysical already at time $t = 5$. However, also in Fig. 4.7 one can see that the L^2-error levels off at times $t = 5$ and $t = 10$. The distribution is definitively not in the prethermal state any more and converges to another distribution. We note that this fixed point distribution is identical for the two Wigner function models.

If one compares quenches to two different values of U with each other, one finds that the relative strength of the fluctuations in the numerical data around the perturbative reference result is larger for smaller values of U. This is not too surprising since for $U \ll t_\mathrm{h}$ the magnitude of the statistical noise is closer to the mean values and hence the relative statistical error from the sampling will be larger than for values $U \sim t_\mathrm{h}$. For quenches to $U \sim 0.1t_\mathrm{h}$ we typically averaged the observables over at least $2 \cdot 10^5$ trajectories and for quenches to larger values of U over at least $2 \cdot 10^4$ trajectories. All discussed results so far have been obtained for quarter filling in order to circumvent possible complications due to Fermi surface nesting at half filling in 2D. Nevertheless, we also collected some data for quenches in systems at half filling and we find very similar behavior to the case of quarter filling. In particular, the system also flows to unphysical distribution functions. The plots are collected in Appendix A.

4.4 Long-time dynamics and thermalization

4.4.1 Numerical observations

We have seen so far that prethermalization is reproduced by the semiclassical dynamics but unphysical occupation numbers can occur at later times. This leads over to the more general question what the fixed points of the dynamics are, or, put differently, if one is able to observe some kind of thermalization within the fTWA scheme. Figures 4.9 and 4.10 show results for the dynamics of the occupation number $n(\epsilon_{k_F})$ at the Fermi energy on time scales beyond prethermalization for quenches to weak U and for two values of N. Empirically, one finds that a rescaling of the time by a factor of $U/\sqrt{N}$ approximately collapses the curves. The inset shows the band occupation numbers at the latest time instants of the simulations, when the system has reached a stationary state. The figures show that – independent of the value of U – the occupation numbers flow to a “straight line distribution”, with negative occupation numbers at the right band edge. While Fermi-Dirac distributions can indeed look like linear functions at high temperatures, the negative occupation numbers, as well as the missing dependence on U, point towards incorrect long-time behavior. The total particle number and total energy remain constant throughout the dynamics. The observed dynamics is therefore necessarily connected to a redistribution of energy between the kinetic and interaction budgets, which is not expected to occur after prethermalization. It is remarkable that in the prethermal phase fTWA exactly reproduces the occupation numbers and interaction energies of the true quantum system. In particular, also the amount of excitation energy induced by the quench is correctly described. This clearly hints to unphysical higher-order contributions in the dynamics.

In Fig. 4.11 we compare the long-time dynamics at different values of N for a fixed interaction strength $U = 0.5$. The data indicates that for large values of N there can be deviations from the “straight line distribution”. Nevertheless, negative occupation

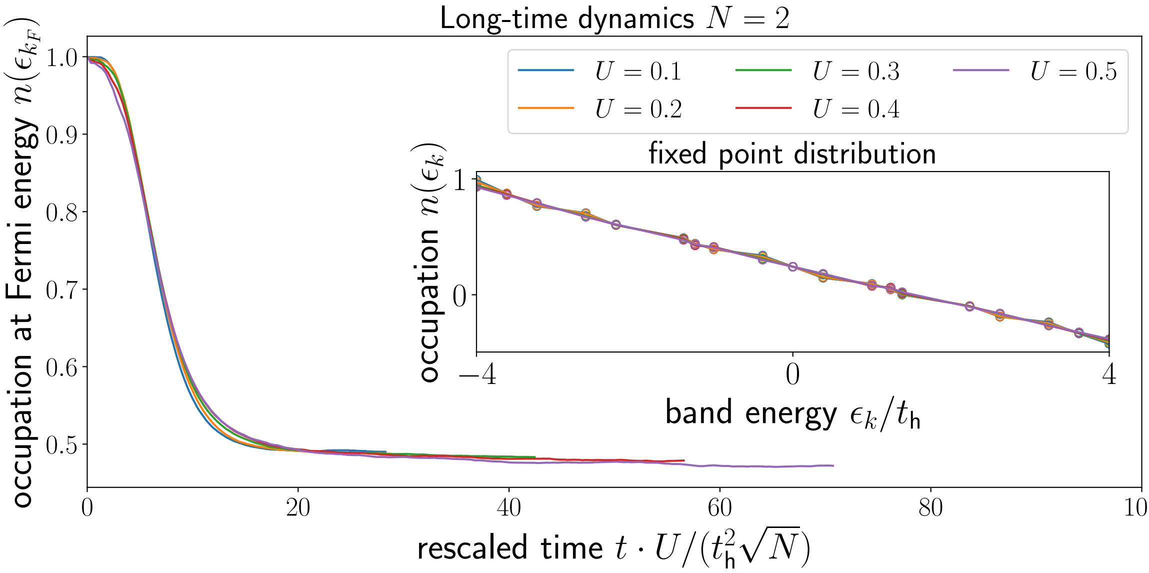

Figure 4.9: Long-time dynamics after an interaction quench to weak U in a SU(N)-Hubbard model on a 10×10 sites square lattice and $N = 2$. The inset shows the stationary distribution.

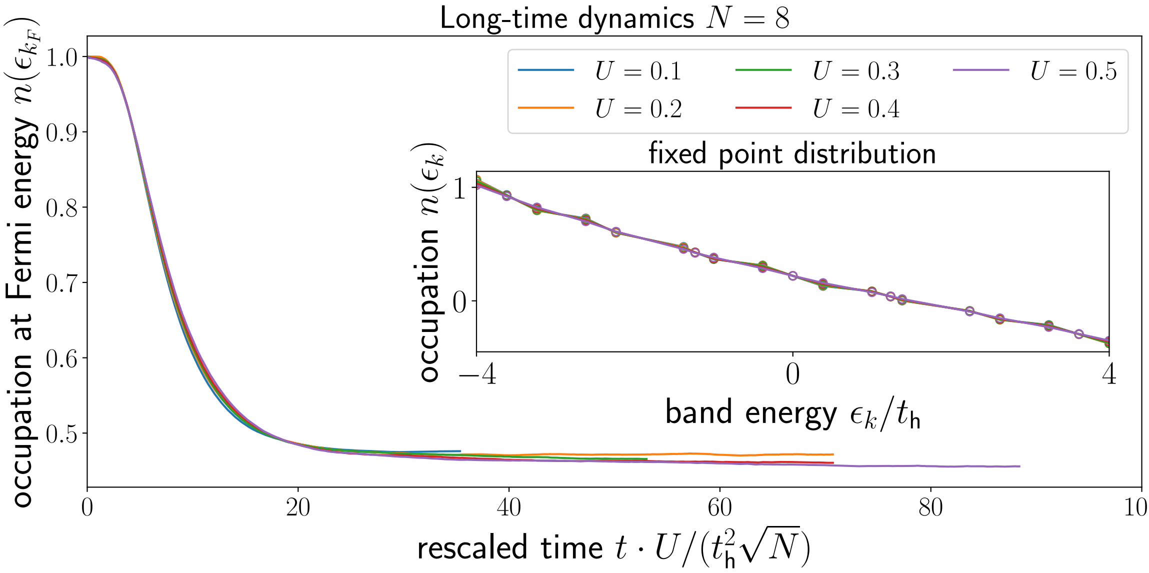

Figure 4.10: Long-time dynamics after an interaction quench to weak U in a SU(N)-Hubbard model on a 10×10 sites square lattice and $N = 8$.

numbers still occur. One needs to keep in mind that the dynamics becomes trivial in the extreme $N \to \infty$ limit. Therefore, also the amount of excitation energy is more and more suppressed at large N such that one can qualitatively expect mode occupation numbers $n(\epsilon_k)$ to remain closer to the original step function if N increases. Finally, we check in Fig. 4.12 that the system size does not play a role: The 40×40 and the 20×20 system evolve towards the same distribution.

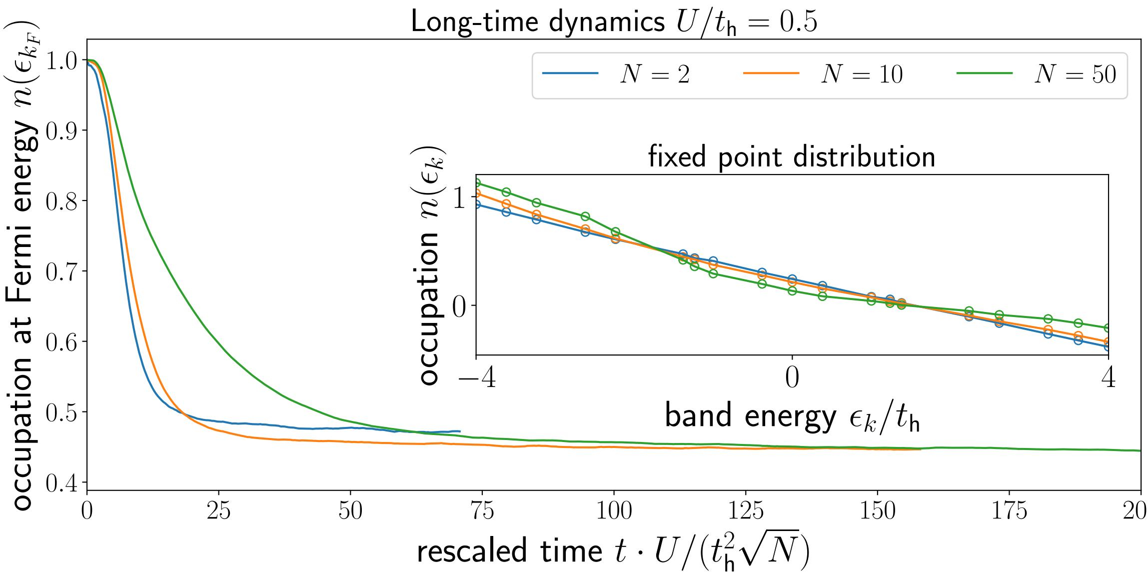

Figure 4.11: Comparison of the long-time dynamics after an interaction quench to a fixed $U = 0.5$ in a SU(N)-Hubbard model on a 10×10 sites square lattice for N equal to 2, 10 and 50.

4.4.2 Connection to the quantum Boltzmann equation

For a more systematic understanding of the long-time dynamics, one should try to connect fTWA to kinetic equations, which are expected to describe the approach to thermal equilibrium, in particular, the non-Markovian quantum Boltzmann equation (QBE), which we wrote down already in (4.4) in the Introduction section. We summarize the conventional derivation of the QBE in Appendix B. One can use this derivation to find conditions for fTWA to reproduce the physical thermalization dynamics:

The momentum space equation of motion for a momentum-diagonal fTWA variable (single trajectory) is given by

$$i\partial_t \rho_{kk}(t) = \frac{2U}{V} \sum_{pp'q} \left(\delta_{k,p+q} - \delta_{k,p}\right) \rho_{p+q,p}(t) \rho_{p'-q,p'}(t) =: \frac{2U}{V} \sum_{pp'q} C_{pp'q}(t). \qquad (4.23)$$

In order to obtain the TWA result for the quantum expectation value, one needs to average $\langle \ldots \rangle_W$ all variables over the Wigner function for the initial $\rho_{kl}(0)$. However, in order to draw a connection to the QBE, we take a look at the next order first:

$$\begin{aligned} &i\partial_t C_{pp'q}(t) + \Delta\epsilon_{p'p(p'-q)} C_{pp'q}(t) \\ &= \frac{2U}{V} \left(\delta_{k,p+q} - \delta_{k,p}\right) \sum_{ll'q'} \Big[\left(\delta_{p+q,l+q'} - \delta_{p+q,l}\right) \rho_{l+q',l-q}(t) \rho_{l'-q',l'}(t) \rho_{p'-q,p'}(t) + \\ &\qquad + \left(\delta_{p'-q,l+q'} - \delta_{p'-q,l}\right) \rho_{p+q,p}(t) \rho_{l+q',l+q}(t) \rho_{l'-q',l'}(t) \Big] \end{aligned} \qquad (4.24)$$

Now one needs to perform the Wigner function averaging to obtain $\langle C_{pp'q} \rangle_t$, which in turns allows to calculate $\langle \rho_{kk}(t) \rangle_W$.

By means of a comparison to the original calculation we have checked that one should be able to reproduce the Boltzmann dynamics if two conditions are satisfied:

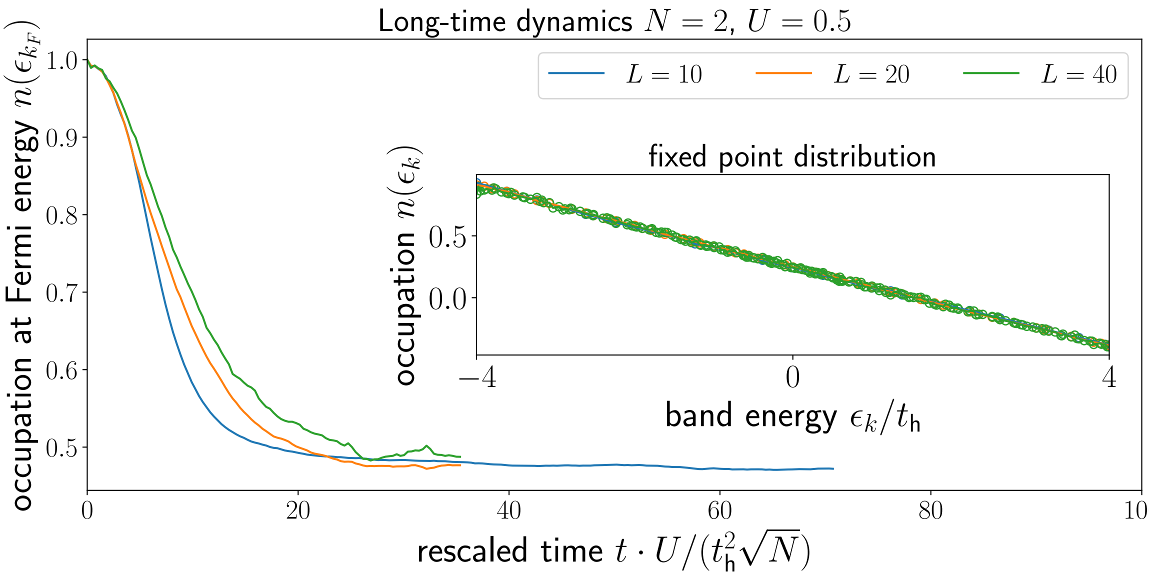

Figure 4.12: Long-time dynamics after an interaction quench to $U = 0.5$ in a SU(N)-Hubbard model on a $L \times L$ sites square lattice for $N = 2$. The data for $L = 40$ is averaged over 184 trajectories, the $L = 20$ data over 3336 trajectories and the $L = 10$ data over 25000 trajectories.

Firstly, the following Gaussian factorization of Wigner function expectation values at non-zero times,

$$\langle\rho_1\rho_2\rho_3\rangle_W = \langle\rho_1\rangle_W\langle\rho_2\rho_3\rangle_W^{\mathrm{cc}} + \langle\rho_2\rangle_W\langle\rho_1\rho_3\rangle_W^{\mathrm{cc}} + \langle\rho_3\rangle_W\langle\rho_1\rho_2\rangle_W^{\mathrm{cc}} + \langle\rho_1\rangle_W\langle\rho_2\rangle_W\langle\rho_3\rangle_W \tag{4.25}$$

and, secondly, the following form of the first and connected second moments:

$$\begin{aligned}\langle\rho_{kl}\rangle_W = \langle\hat\rho_{kl}\rangle_W &= \delta_{k,l}\left(n_k - \frac{1}{2}\right),\\ \langle\rho_{kl}\rho_{sp}\rangle_W^{\mathrm{cc}} = \frac{1}{2}\langle\{\hat\rho_{kl},\hat\rho_{sp}\}\rangle_W^{\mathrm{cc}} &= \frac{1}{2N}\delta_{kp}\delta_{ls}\left(n_k + n_l - 2n_k n_l\right)\end{aligned} \tag{4.26}$$

These expression are at least valid at initial times but there is a priori no reason why they should be fulfilled at non-zero times. Nevertheless, one can use analogies like this to propose improvements of the fTWA method, for example via explicit inclusion of dynamical variables composed of two ρs. This could allow one to derive equations of motion that obey those conditions by construction. Similar ideas (not with QBEs in mind) have been proposed in the context of BBGKY-enhanced phase space methods [168, 166].

4.5 Discussion and Conclusion

In this Chapter we adopted the fermion degeneracy N as a natural semiclassical expansion parameter, combined it with the fTWA method, and applied it to the well-understood problem of the interaction quench in the Hubbard model. This allowed us to analyze the range of validity of fTWA in a systematic way. Our analytical and numerical results showed that fTWA correctly describes the electronic dephasing dynamics which generates prethermalization. We observed that, applied at small N, the method is prone to produce unphysical results at time scales beyond the prethermalization regime. We have furthermore studied the long-time behavior of the dynamics and identified the “straight line” mode occupation function $n(\epsilon_k)$ as the fixed point distribution at low N and weak U. It is not clear why this distribution is obtained in the long time limit. We compared the derivation of the quantum Boltzmann equation to the fTWA equations of motion and identified conditions for their compatibility, which, however, need not be satisfied. A systematic look at the convergence of fTWA yields the following picture: Order one observables (e.g. n_{k_F}) converge quickly for a few 1000 trajectories. In contrast, observables of order $\frac{1}{N}$ like $\Delta n_{k_F}(t)$ converge slowly and orders of trajectories more are required.

These findings suggest the picture that fTWA correctly describes the dynamics at linear order of the effective $\hbar \sim \frac{1}{N}$. When N is small, the higher order contributions to the semiclassical dynamics differ from the exact theory. Nevertheless, fTWA is a powerful tool for applications since it allows, in contrast to unitary perturbation theory, for a straightforward application to explicitly time-dependent problems, which we make use of in the next chapter. A general advantage of fTWA is that its computational cost increases only polynomially in the system size, which allows the simulation of 2d lattice systems with a much larger number of sites than possible with exact diagonalization or tensor-network based approaches. In addition, no memory kernels need to be tracked during the evolution, which is always time-local.

There are a number of ideas how one can try to improve fTWA. Despite reports in the context of the “stochastic mean-field approach” of an increase of the predictive power of the method by using refined two-point Wigner functions [165], reminiscent of discrete TWA methods [155], we have not seen such an improvement for the problem considered here. Another, more promising, route is to add more complexity to the equations of motion by adding additional variables derived from the BBGKY hierarchy [166]. We have briefly discussed such possibilities at the end of Sec. 2.5. A preliminary implementation of a scheme based on the introduction of connected Weyl symbols following Pineiro-Orioli et al. [168] did unfortunately not yield an improvement of the long-time behavior so far.

4.5.1 fTWA in infinite spatial dimensions?

Here we briefly summarize some thoughts on fTWA in the limit of high spatial dimensions d. In many models, Hartree-Fock mean-field theory becomes exact as $d \to \infty$. The Hubbard model is a famous exception, for which site-local correlations $\langle n_{i\downarrow} n_{i\uparrow} \rangle$ continue to be important even in infinite spatial dimensions and lead to dynamical mean-field theory (DMFT). Although fTWA is based on Hartree-Fock mean-field theory, the Wigner function sampling can nevertheless incorporate fluctuations due to quantum correlations like $\langle n_{i\downarrow} n_{i\uparrow} \rangle$. It is therefore an interesting question to ask for connections between fTWA and DMFT or leastwise for simplifications of fTWA in high spatial dimensions. In infinite spatial dimensions, the density of states for a cubic tight-binding model is of Gaussian form [21, 136],

$$\bar{\rho}(\epsilon) = \frac{1}{\sqrt{\pi} t^*} \mathrm{e}^{-\epsilon^2}. \tag{4.27}$$

In order to have a finite index set we can think of a discretized energy axis with finite support on $[-D, D]$,

$$\int_{-\infty}^{\infty} \mathrm{d}\epsilon \; \bar{\rho}(\epsilon) \approx \Delta\epsilon \sum_{e=0}^{2D/\Delta\epsilon} \bar{\rho}(-D + e\Delta\epsilon). \tag{4.28}$$

An important simplification in $d \to \infty$ concerns momentum conservation at interaction vertices [136]. Here, momentum conserving delta functions (or, more precisely, the von Laue function, which ensures momentum conservation up to reciprocal lattice vectors) can formally be replaced by factors 1. Momentum summations then need to be replaced by energy integrals, weighted by the Gaussian density of states. If we apply the trivialization of momentum conservation at the level of the equations of motion, we can formally replace all momentum labels of the ρ-variables with energy indices:

$$\begin{aligned}
i\partial_t \rho_{k\sigma,l\sigma} &= -\left(\epsilon(\vec{k}) - \epsilon(\vec{l})\right) \rho_{\vec{k}\sigma,\vec{l}\sigma} + \frac{U}{V} \sum_{\vec{s},\vec{p}} \left[\rho_{(\vec{p}+\vec{s}-\vec{l})\bar{\sigma},\vec{p}\bar{\sigma}} \rho_{\vec{k}\sigma,\vec{s}\sigma} - \rho_{(\vec{p}+\vec{k}-\vec{s})\bar{\sigma},\vec{p}\bar{\sigma}} \rho_{\vec{s}\sigma,\vec{l}\sigma}\right] \\
&= -\left(\epsilon(\vec{k}) - \epsilon(\vec{l})\right) \rho_{\vec{k}\sigma,\vec{l}\sigma} + \frac{U}{V} \sum_{\vec{q},\vec{s},\vec{p}} \left[\delta_{\vec{q},\,\vec{p}+\vec{s}-\vec{l}}\; \rho_{\vec{q}\bar{\sigma},\vec{p}\bar{\sigma}} \rho_{\vec{k}\sigma,\vec{s}\sigma} - \delta_{\vec{q},\,\vec{p}+\vec{k}-\vec{s}}\; \rho_{\vec{q}\bar{\sigma},\vec{p}\bar{\sigma}} \rho_{\vec{s}\sigma,\vec{l}\sigma}\right] \\
&\xrightarrow{d\to\infty} -\left(\epsilon_k - \epsilon_l\right) \rho_{\epsilon_k\sigma,\epsilon_l\sigma} + U \int_{\epsilon_s} \int_{\epsilon_p} \int_{\epsilon_q} \left[\rho_{\epsilon_q\bar{\sigma},\epsilon_p\bar{\sigma}} \rho_{\epsilon_k\sigma,\epsilon_s\sigma} - \rho_{\epsilon_q\bar{\sigma},\epsilon_p\bar{\sigma}} \rho_{\epsilon_s\sigma,\epsilon_l\sigma}\right] \\
&= -\left(\epsilon_k - \epsilon_l\right) \rho_{\epsilon_k\sigma,\epsilon_l\sigma} + U A_\sigma[\rho] \int_{\epsilon_s} \left[\rho_{\epsilon_k\sigma,\epsilon_s\sigma} - \rho_{\epsilon_s\sigma,\epsilon_l\sigma}\right]
\end{aligned} \tag{4.29}$$

where $\int_\epsilon := \int_{-\infty}^{\infty} \mathrm{d}\epsilon \; \bar{\rho}(\epsilon)$ and

$$A_\sigma[\rho] := \int_\epsilon \int_{\epsilon'} \rho_{\epsilon\bar{\sigma},\epsilon'\bar{\sigma}} \tag{4.30}$$

is a scalar with

$$\begin{aligned}
i\partial_t A_\sigma[\rho] &= \int_\epsilon \int_{\epsilon'} i\partial_t \rho_{\epsilon\bar{\sigma},\epsilon'\bar{\sigma}} \\
&= \int_\epsilon \int_{\epsilon'} \left[(\epsilon' - \epsilon)\rho_{\epsilon\bar{\sigma},\epsilon'\bar{\sigma}} + U A_{\bar{\sigma}}[\rho] \int_{\epsilon''} \left(\rho_{\epsilon\bar{\sigma},\epsilon''\bar{\sigma}} - \rho_{\epsilon''\bar{\sigma},\epsilon'\bar{\sigma}}\right)\right] \\
&= \int_\epsilon \int_{\epsilon'} (\epsilon' - \epsilon)\rho_{\epsilon\bar{\sigma},\epsilon'\bar{\sigma}} + U A_{\bar{\sigma}}[\rho] \left(A_\sigma[\rho] - A_\sigma[\rho]\right) \\
&= -\int_\epsilon \int_{\epsilon'} (\epsilon - \epsilon')\rho_{\epsilon\bar{\sigma},\epsilon'\bar{\sigma}}.
\end{aligned} \tag{4.31}$$

In the same spirit we could rewrite the Hamiltonian (the shift of the chemical potential is moved into $\epsilon(k)$):

$$\begin{aligned}
H_{\text{Hub}} &= \sum_{\vec{k}\sigma}\left(\epsilon(\vec{k})+\frac{U}{2}\right)\rho_{\vec{k}\sigma,\vec{k}\sigma}+\frac{U}{V}\sum_{\vec{p},\vec{p}',\vec{q}}\rho_{(\vec{p}-\vec{q})\uparrow,\vec{p}\uparrow}\rho_{(\vec{p}'+\vec{q})\downarrow,\vec{p}'\downarrow}\\
&= \sum_{\vec{k}\sigma}\left(\epsilon(\vec{k})+\frac{U}{2}\right)\rho_{\vec{k}\sigma,\vec{k}\sigma}+\frac{U}{V}\sum_{\vec{p},\vec{p}',\vec{q},\vec{s},\vec{t}}\delta_{\vec{s},(\vec{p}-\vec{q})}\delta_{\vec{t},(\vec{p}'+\vec{q})}\rho_{\vec{s}\uparrow,\vec{p}\uparrow}\rho_{\vec{t}\downarrow,\vec{p}'\downarrow} \qquad (4.32)\\
&\xrightarrow{d\to\infty}\sum_{\sigma}\int_{\epsilon}\epsilon\rho_{\epsilon\sigma,\epsilon\sigma}+UA_{\uparrow}[\rho]A_{\downarrow}[\rho].
\end{aligned}$$

The dynamics so obtained does obey some desirable properties:

- $A_\sigma[\rho]$ **is real.**
- **Particle number conservation:**

$$i\partial_t\int_{\epsilon}\rho_{\epsilon\sigma,\epsilon\sigma}=UA_\sigma[\rho]\int_{\epsilon}\int_{\epsilon'}\left(\rho_{\epsilon\sigma,\epsilon'\sigma}-\rho_{\epsilon'\sigma,\epsilon\sigma}\right)=0. \qquad (4.33)$$

- **Energy conservation:** The kinetic energy $E_{\text{kin}}=\sum_\sigma\int_\epsilon\epsilon\rho_{\epsilon\sigma,\epsilon\sigma}$ obeys

$$\begin{aligned}
i\partial_t E_{\text{kin}} &= \sum_{\sigma}\int_{\epsilon}\epsilon\, UA_\sigma\int_{\epsilon'}\left(\rho_{\epsilon\sigma,\epsilon'\sigma}-\rho_{\epsilon'\sigma,\epsilon\sigma}\right)=U\sum_{\sigma}A_\sigma\int_{\epsilon}\int_{\epsilon'}\epsilon\left(\rho_{\epsilon\sigma,\epsilon'\sigma}-\rho_{\epsilon'\sigma,\epsilon\sigma}\right)\\
&= U\sum_{\sigma}A_\sigma\int_{\epsilon}\int_{\epsilon'}(\epsilon-\epsilon')\rho_{\epsilon\sigma,\epsilon'\sigma}=-U\sum_{\sigma}A_\sigma\left(i\partial_t A_{\bar{\sigma}}\right)=-i\partial_t\left(UA_{\uparrow}A_{\downarrow}\right).
\end{aligned} \qquad (4.34)$$

- **Fixed points:** ρ-variables of the form $\rho_{\epsilon\sigma,\epsilon'\sigma}=n(\epsilon)\delta(\epsilon-\epsilon')$ obey $i\partial_t\rho=0$.

The main challenge, however, is related to the setup of the Wigner function. Let us take the Fermi sea as an example: In k-space we obtain $\langle\rho_{k\sigma,l\tau}\rangle_{\text{FS}}=\delta_{\sigma\tau}\delta_{kl}\big(n(\epsilon_k)-\frac{1}{2}\big)$. Although occupation numbers are easily expressible in terms of energies alone, the momentum delta poses a problem: For two given single-particle energies ϵ, ϵ' only the diagonal momentum pairs on the two energy shells contribute. One could in principle remedy this by restricting $\rho_{\epsilon\sigma,\epsilon'\tau}$ to k-diagonal configurations but a similar issue occurs on the level of the variance, which is $\langle\rho_{k\sigma,l\tau}\rho_{s\sigma',p\tau'}\rangle\sim\delta_{kp}\delta_{ls}$ and leads to fluctuations of exactly the k-nondiagonal variables ρ. This hints towards the greater question of **coarse-graining** within truncated Wigner approaches. By introducing energy indices, we have formed groups of ρ-variables and need to determine a consistent set of correlation data to adapt the TWA scheme for those new variables. In the example at hand, one strategy could be to introduce two sets of energy-labeled variables, corresponding to k-diagonal and k-nondiagonal ρs. However, in high dimensions the latter group of variables will grow much faster than the former and so an adequate rescaling of the variables will be essential.

Chapter 5

Non-Equilibrium Order Parameter Dynamics in Large-N Models

Parts of this chapter are also published in the article [2], *Photoinduced prethermal order parameter dynamics in the two-dimensional large-N Hubbard-Heisenberg model*, Phys. Rev. B **106**, 214318 (2022). Sections, in which figures or parts of the texts are reprinted, are marked with a hint "(cf. [2])".

5.1 Introduction

As already highlighted in the introduction to this thesis, interacting many-electron systems can host a plethora of ordered phases at equilibrium, which will in general be intertwined with each other [98, 106]. The cuprate high-temperature superconductors are arguably the most famous example of a highly complex strongly correlated material with many competing ordering tendencies [233, 105, 11]. Their defining property is a superconducting state at temperatures up to $T_c \approx 140$K, way above the critical tempatures known from conventional superconductors. The precise mechanism that leads to superconductivity in these compounds is not yet fully understood. Nevertheless, it is consensus that the copper oxide planes play a key role [11], which has led theoretical studies to focus on the physics of correlated electrons in two spatial dimensions to make progress [10]. Quickly after the experimental discovery, simplified models for the planes have been proposed, in particular multi-band Hubbard models and t-J models – the latter in a famous paper by Zhang and Rice [234]. Another candidate model includes the Anderson lattice model [235]. The strong interest in two-dimensional correlated electron models did also stimulate the development and advancement of numerical as well as analytical techniques to investigate their equilibrium phase diagrams [236]. An analytical method which led to a number of influential publications in the late 80s/early 90s [141, 142, 237, 238] is the large-N expansion. It had already been successfully applied to mixed-valence compounds before [239, 240]. The technique relies on the fermionic degeneracy N as an expansion parameter, which is non-perturbative in the couplings. The core of its success lies in a simplification of diagrammatic calculations because only certain classes of diagrams survive the scaling $N \to \infty$ [241]. For the ease of calculations, large-N expansions are often combined with slave-boson representations [242, 243, 244, 245] of spin states. Following a proposal by Anderson [246], many authors became interested in searching for non-Néel ground states of quantum antiferromagnets. Using the large-N expansion, Read and Sachdev thus studied the equilibrium properties of various SU(N)-symmetric antiferromagnetic Heisenberg models in a series of papers [242, 247, 248, 237, 238]. Their Hamiltonian reads

$$\hat{H}_{\mathrm{Hei}} = \frac{J}{N} \sum_{\alpha,\beta=1}^{N} \sum_{\langle i,j \rangle} \hat{S}_{\alpha}^{\beta}(i) \hat{S}_{\beta}^{\alpha}(j), \tag{5.1}$$

where in a fermionic representation [140] one can write $\hat{S}_{\alpha}^{\beta}(i) = c_{i\alpha}^{\dagger} c_{i\beta} - \delta_{\alpha,\beta} \frac{1}{N} \sum_{\gamma} c_{i\gamma}^{\dagger} c_{i\gamma}$. These operators are generators of the SU(N) group, which obey

$$[\hat{S}_{\alpha}^{\beta}(i), \hat{S}_{\gamma}^{\delta}(j)] = \delta_{ij} \big(\delta_{\gamma,\beta} \hat{S}_{\alpha}^{\delta}(i) - \delta_{\alpha,\delta} \hat{S}_{\gamma}^{\beta}(i) \big). \tag{5.2}$$

They offer a very convenient way to write SU(N)-symmetric spin models. Note that one cannot formulate, e.g., kinetic hopping terms with these operators. Written in this way, it becomes apparent that here is the freedom to choose a representation of the SU(N) group on every site in (5.1). Without going too much into the details we mention that the all such irreducible representations can be labeled by Young tableaux, which are characterized by two integer numbers, in this context often called m and n_c [249]. The number $k = N/m$ allows for an interpretation as the minimum number of spins that are needed to form a singlet. The limit $n_c \to \infty$ is a semiclassical limit akin to the large-S limit (if $N = 2$ and $m = 1$, one exactly has $n_c = 2S$). Read and Sachdev as well as Affleck and Marston set $m = N/2$. In the fermionic model this corresponds to an equal distribution of electrons on the sites. A good overview of the various SU(N) representations and their physical implications was given by Hermele and Gurarie [249]. Similar studies to Read's and Sachdev's were performed by Arovas and Auerbach [243].

An important general conclusion from all these works is the possibility to construct non-Néel ordered ground states, which typically correspond to a fluctuating distribution of singlets ("valence bonds") on the lattice. In the limit $N \to \infty$, one finds, in particular, a class of *spin-Peierls* states, i.e. periodic bond-no bond patterns that can, for instance, occur in columnar or box shape [242, 247, 142]. Affleck and Marston [141, 142] also went beyond the pure Heisenberg case. They view the antiferromagnetic Heisenberg model as one limiting case of a more general hybrid Hubbard-Heisenberg model. Its Hamiltonian is a combination of the Heisenberg exchange interaction with a kinetic term and a Hubbard interaction. Although at half filling the Hubbard model reduces to the Heisenberg model in the limit $U/t_{\mathrm{h}} \to \infty$, one needs to write the Heisenberg interaction explicitly because the Hubbard interaction becomes trivial as $N \to \infty$. Put differently, the limits $U/t_{\mathrm{h}} \to \infty$ and $N \to \infty$ do not commute. If one sends $U/t_{\mathrm{h}} \to \infty$ in the Hubbard-Heisenberg model and sets $t_{\mathrm{h}} = 0$, one obtains back Read's and Sachdev's model. The $N \to \infty$ phase diagram of the hybrid model in two spatial dimensions is discussed in detail in the next section. However, we already briefly summarize the main findings here. In the mean-field limit, the Hubbard interaction U becomes irrelevant, a fact we already discussed in Chapter 2. In the extreme $J/t_{\mathrm{h}} \to \infty$ limit one obtains the spin-Peierls state of the SU(N) antiferromagnet as a ground state. Still, the additional kinetic energy scale t_{h} leads to a competition between the Peierls state and a new type of ground state, the so-called *staggered flux phase* [250, 251, 252]. Its characteristic feature is the emergence of a non-vanishing magnetic flux around the plaquettes of the two-dimensional lattice. The staggered flux phase becomes the ground state of the two-dimensional large-N model for intermediate values of J/t_{h}. Later, there was increased particular interest also in the staggered flux (SF) phase because numerical studies [252, 253], in particular based on the density-matrix renormalization group (DMRG), indicated that the SF phase may also be realized in more conventional interacting electron models on ladders, without the need for a large-N setup. In a later work, Marston and coworkers revisited the Hubbard-Heisenberg model on a two-dimensional triangular lattice [254] and studied the additional effect of frustration on the phase diagram, which, however, is beyond the scope of this thesis.

Besides the relevance of large-N setups for the approximate treatment of condensed matter models, there is another, more recent, motivation to study SU(N)-symmetric models, namely in the context of ultracold Fermi gases [255, 256, 257]. The paradigmatic examples are alkaline-earth atoms [258] like ^{87}Sr and ^{135}Ba. They are characterized by the absence of hyperfine interactions between nuclear and electronic spin degrees of freedom. This, combined with the almost perfect independence of electronic scattering properties (the scattering length, in particular) from the nuclear spins, implies an increased fermionic degeneracy of kinetic and interaction Hamiltonians for such kinds of atoms. The so far largest realized degeneracy is $N = 10$ for the spin-9/2 atom ^{87}Sr. [255]. Experimentalists have used alkaline-earth atoms to simulate ferromagnets and Mott insulators with SU(N)-symmetries [259]. A very specific application is the development of highly precise atomic clocks [260]. In the context of ultracold Fermi gases, there is also some interest to realize staggered Flux phases in experiments with optical lattices, either with SU(N) fermions with low values of N [261] or using time-dependent lattices [262].

5.1.1 State of the Art and Scope of this Chapter

The equilibrium properties of SU(N) models in the large-N limit are well explored analytically, at least in the case of the Heisenberg antiferromagnet. The finite-N equilibrium phase diagram of the Hubbard-Heisenberg model, however, is less explored except for one study based on Quantum Monte Carlo (QMC) [140]. Nowadays, there are also powerful numerical techniques available to treat SU(N)-systems, e.g. symmetry-enhanced DMRG or exact diagonalization codes for chains [263, 264, 265] and ladder systems [266]. QMC is in general a very powerful technique for many models, including the SU(N)-symmetric versions of the Hubbard model and the Kondo model [267, 268]. QMC's intrinsic sign problem is mitigated in the large-N limit [140].

Despite the availability of all these methods, the main focus of research on SU(N) models still seems to be their equilibrium physics. Of course, this is not to say that large-N techniques have not been used in non-equilibrium research. Large-N expansions have a tradition in field theories based on the Keldysh technique [269, 270, 271, 184, 272]. However, often these works deal with more coarse-grained scalar quantum field theories and the microscopic dynamics in interacting many-fermion systems seems indeed a bit less explored [268, 273, 274, 275].

The goal of this chapter is the following: We adopt the large-N Hubbard-Heisenberg model and view it as a model with an intrinsic competition of two different types of order, the Peierls phase, which one can view as a simple model for a bond-density wave phase, and the staggered Flux phase. It provides an ideal environment to study the dynamics of such ordered phases in response to non-equilibrium excitations like parameter quenches or driving with an electromagnetic field. In this thesis we mostly neglect the Hubbard Interaction ($U = 0$). This is justified since we are interested in the near mean-field dynamics, for which the influence of U is less important. In addition, the finite-N phase diagram for all three parameters t_h, J and U non-zero is not reported in the literature and to calculate it could be the topic of a thesis on its own. Furthermore, we concentrate mostly on the Peierls phase as an initial state since it represents a prototypical strong coupling phase, whose decay upon non-equilibrium excitations we would like to study.

We have chosen an SU(N) model because it allows us to use the semi-classical fermionic truncated Wigner (fTWA) approximation [112] as a time evolution technique in a very natural environment because of the effective $\hbar_\mathrm{eff} = \frac{1}{N}$. In the previous Chapter 4 we have seen that fTWA often yields good agreement with exact calculations on short and intermediate time scales [112] but without a small $\hbar_\mathrm{eff}$ the dynamics can run into unphysical fixed points in the long time dynamics. If we work at sufficiently large values of N, we can expect that the dynamics still remains reliable. By using fTWA and the Wigner function sampling we go beyond mean-field and include some electron-electron correlations in the dynamics. Based on our observations for the interaction quench in the Hubbard model, we assume that fTWA adds dephasing generated by inelastic scattering processes on top of the mean-field dynamics and will therefore generate stationary states that can be interpreted as prethermal states, i.e. stable on a transient timescale before the thermalization dynamics dominates.

To the best of our knowledge, we are the first to combine fTWA with large-N models and therefore many new technical questions have arisen, in particular ones related to the initial state preparation. We already mentioned above that except for sketches in the appendix to Marston's and Affleck's original paper [142], no closed-form results for the one- and two-particle reduced density matrices in the finite-N model are reported in the literature. However, exactly these would be required for the determination of a correlated initial state Wigner function. In general, fTWA has so far always only been used for initial product states and therefore we take the mean-field initial state to set up an approximate Wigner function. In the following Section 5.2 we discuss the mean-field phase diagram of the model and discuss issues related to the initial state preparation within fTWA. In Section 5.3 we discuss results related to parameter quenches, before we continue with the main part of this chapter, namely Section 5.4, which treats the photoinduced dynamics in the Hubbard-Heisenberg model. Before we conclude, we show results for spatially inhomogeneous photoexcitations in Section 5.5.

5.2 Initial State Preparation (cf. [2])

In this section we discuss the equilibrium properties of the Hubbard-Heisenberg model in the limit $N \to \infty$ and how we set up the Wigner function for fTWA. The $N \to \infty$ equilibrium zero temperature phase diagram was first obtained using a Hubbard-Stratonovich transformation with subsequent saddle point approximation [141, 142]. In 2005, Assaad re-examined the model using quantum Monte Carlo [140] for finite $N < \infty$. Since both the Peierls and the staggered flux phase break the translational invariance by one lattice site, one needs to select a unit cell of a least two sites to find a self-consistent mean-field solution. The smallest possible unit cell is made out of two sites and is depicted in the top row of Fig. 5.1. It is also the choice in Marston's and Affleck's original work. Note that it is tilted by 45° with respect to the original lattice vectors. It has been shown that larger unit cells can also host more complex spatial patterns at saddle points of the free energy, in particular box-shaped Peierls phases [142, 247]. However, at $N \to \infty$ they are degenerate with the Peierls state of the unit cell with two sites. In addition, the fTWA simulations use a computational basis in position representation such that there is no predefined unit cell any more and in principle more complex spatial patterns can emerge dynamically. We will always use periodic boundary conditions (with respect to the lattice of unit cells) for quadratic systems with at least 11×11 cells, i.e. $V = 2 \cdot 11^2 = 242$ lattice sites. The choice of the tilted unit cell with two sites corresponds to a reduced Brillouin zone, which is sketched with black color in the inset of Fig. 5.2.

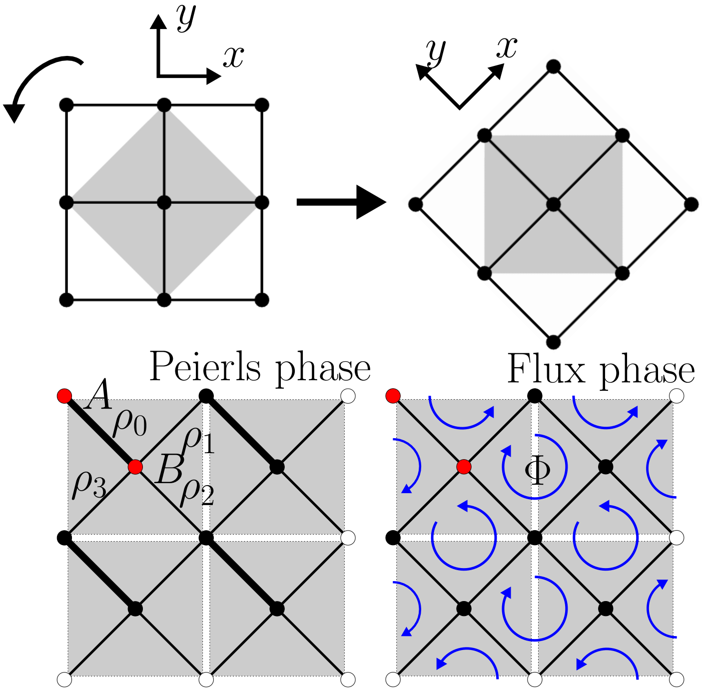

Figure 5.1: Upper row: Unit cell used in this paper with two atoms per cell. Lower row: Sketch of the spatial structure of the two competing equilibrium phases Peierls (one strong bond ρ_0 and three identical weak bonds $\rho_{1,2,3}$ per unit cell) and Flux (four complex bonds with equal magnitude and non-vanishing plaquette flux). This figure is also published in [2]. Copyright (2022) by the American Physical Society.

For $N < \infty$, it would be desirable to explicitly construct the equilibrium states of the model as controlled starting points for the light-driven dynamics. In complete generality, this requires the calculation of $1/N$ corrections to the saddle points and is a non-trivial task. The equilibrium states so obtained would be stationary under the semiclassical time-evolution. To proceed without a full calculation, we resort to a simpler strategy and make direct use of the fTWA dynamics. This is possible in at least two ways: We can adiabatically switch on the interactions or we can construct an approximate Wigner function which relaxes to a stationary state in the phase of interest. The first strategy has the advantage that for sufficiently slow switching the system can be prepared in an equilibrium ground state, i.e. without additional heating. However, it turns out to be challenging to implement this in practice. For switching times of $1000t_\mathrm{h}^{-1}$ the final state energies we obtained were significantly higher than those from the strategy discussed below. Another difficulty is posed by the fact that all three phases are stable and a suitable transient symmetry breaking might be required to reach the desired phase. We leave for future work a more detailed discussion of adiabatic switching with fTWA.

5.2.1 Mean-field solution at $N \to \infty$ (cf. [2])

The original calculation by Marston and Affleck [141, 142] was carried out by means of a saddle point analysis of the effective free energy, which only depends on the values of the nearest-neighbor bonds and densities within a unit cell. In order to directly obtain the full one-particle reduced density matrix from the calculation, we take a different approach and make use of the fact that the limit $N \to \infty$ is equivalent to a Hartree decoupling of the interaction term: The way we write the interaction terms with $\hat{\rho}_{ij}$ operators determines their decoupling. We introduce the deviations

$$\Delta\hat{\rho}_{ij} = \hat{\rho}_{ij} - \rho_{ij} \tag{5.3}$$

of the $\hat{\rho}_{ij}$-operators from their expectation value $\rho_{ij} = \langle\hat{\rho}_{ij}\rangle$. Plugging (5.3) into the model Hamiltonian yields the following representation of the interaction terms

$$\begin{aligned}
\hat{H}_\mathrm{Hei} &= -JN\sum_{\langle i,j\rangle}\big(\rho_{ij} + \Delta\hat{\rho}_{ij}\big)\big(\rho_{ji} + \Delta\hat{\rho}_{ji}\big) \\
&= -JN\sum_{\langle i,j\rangle}\big(|\rho_{ij}|^2 + \rho_{ij}\Delta\hat{\rho}_{ji} + \rho_{ji}\Delta\hat{\rho}_{ij}\big) + \mathcal{O}(\Delta\rho)^2 \\
&\simeq -JN\sum_{\langle i,j\rangle}\Big(-|\rho_{ij}|^2 + \frac{1}{N}\sum_{\alpha=1}^{N}(\rho_{ij}c^\dagger_{j\alpha}c_{i\alpha} + \rho_{ji}c^\dagger_{i\alpha}c_{j\alpha})\Big)
\end{aligned} \tag{5.4}$$

$$\begin{aligned}
\hat{H}_\mathrm{Hub} &= UN\sum_{i}\big(\rho_{ii} + \Delta\hat{\rho}_{ii}\big)^2 \\
&= UN\sum_{i}\big(|\rho_{ii}|^2 + 2\rho_{ii}\Delta\hat{\rho}_{ii}\big) + \mathcal{O}(\Delta\rho)^2 \\
&\simeq UN\sum_{i}\Big(-|\rho_{ii}|^2 + \frac{2}{N}\sum_{\alpha=1}^{N}\rho_{ii}\big(c^\dagger_{i\alpha}c_{i\alpha} - \frac{1}{2}\big)\Big)
\end{aligned} \tag{5.5}$$

In the following we neglect the order $(\Delta\rho)^2$ terms. In order to construct the ground state of the model we need to specify the lattice geometry and choose a unit cell. Let us concentrate, for simplicity, on a one-dimensional model and give the generalization to two spatial dimensions in the end. Here, we label the two sites of the unit cell as A and B. We call the on-site elements of the ρ-variables $\rho_A := \rho_{i\in A, i\in A}$ and $\rho_B := \rho_{i\in B, i\in B}$. The nearest neighbor bonds are called $\rho_0 := \rho_{i\in A,(i+1)\in B}$ and $\rho_1 := \rho_{i\in B,(i+1)\in A}$.

Next, we transform all non-local operators to momentum space. A way to do this is to work directly in the reduced Brillouin zone rBZ $\subseteq (-\pi/2, \pi/2]$. This corresponds to the following transformation rules with $Q = \pi$ (also described in Ref. [215])

$$\begin{aligned} c^\dagger_{i\in A} &= \frac{1}{\sqrt{V}} \sum_{k\in \mathrm{rBZ}} \mathrm{e}^{-ikr_i} \big(c^\dagger_k + c^\dagger_{k+Q}\big) \\ c^\dagger_{i\in B} &= \frac{1}{\sqrt{V}} \sum_{k\in \mathrm{rBZ}} \mathrm{e}^{-ikr_i} \big(c^\dagger_k - c^\dagger_{k+Q}\big) \end{aligned} \tag{5.6}$$

Introducing $\epsilon_k := 2t_\mathrm{h}\cos(k)$ and $\chi_k := J\big(\rho_0 \mathrm{e}^{-ik} + \rho_1^* \mathrm{e}^{ik}\big)$ we obtain the following representation of the Hamiltonian

$$(H) = \begin{pmatrix} c^\dagger_k & c^\dagger_{k+Q} \end{pmatrix} \begin{pmatrix} \epsilon_k - \mathrm{Re}(\chi_k) + U(\rho_A + \rho_B) - \mu & i\,\mathrm{Im}(\chi_k) + U(\rho_B - \rho_A) \\ -i\,\mathrm{Im}(\chi_k) + U(\rho_B - \rho_A) & -\epsilon_k + \mathrm{Re}(\chi_k) + U(\rho_A + \rho_B) - \mu \end{pmatrix} \begin{pmatrix} c_k \\ c_{k+Q} \end{pmatrix} \tag{5.7}$$

In the following, we will always only consider half filling, $\mu = U(\rho_A + \rho_B)$. Diagonalization of the Hamiltonian yields the following set of eigenenergies

$$\begin{aligned} E_k &= \pm\Big\{ - \Big[- \big(\epsilon_k - \mathrm{Re}(\chi_k)\big)^2 - \mathrm{Im}(\chi_k)^2 - U^2\big(\rho_B - \rho_A\big)^2 \Big] \Big\}^{1/2} \\ &= \pm\Big\{ \big|\epsilon_k - \chi_k\big|^2 + U^2(\rho_B - \rho_A)^2 \Big\}^{1/2}. \end{aligned} \tag{5.8}$$

In two spatial dimensions the procedure is analogous. However, since we use the rotated unit cell depicted in Fig. 5.1, the k-values are defined with respect to the tilted lattice of unit cells.

$$\begin{aligned} \epsilon_k &= 2t_\mathrm{h}\Big(\cos\Big(\frac{\sqrt{2}}{2}(k_x - k_y)\Big) + \cos\Big(\frac{\sqrt{2}}{2}(k_x + k_y)\Big)\Big), \\ \chi_k &= J\Big(\rho_0^* \mathrm{e}^{-i\frac{\sqrt{2}}{2}(k_x+k_y)} + \rho_1^* \mathrm{e}^{i\frac{\sqrt{2}}{2}(k_x-k_y)} \\ &\qquad + \rho_2 \mathrm{e}^{i\frac{\sqrt{2}}{2}(k_x+k_y)} + \rho_3 \mathrm{e}^{-i\frac{\sqrt{2}}{2}(k_x-k_y)}\Big). \end{aligned} \tag{5.9}$$

Rewritten in terms of the axes of the original lattice (here denoted k') by means of the following transformation,

$$\begin{pmatrix} k'_x \\ k'_y \end{pmatrix} = \frac{\sqrt{2}}{2} \begin{pmatrix} 1 & -1 \\ 1 & 1 \end{pmatrix} \begin{pmatrix} k_x \\ k_y \end{pmatrix}, \tag{5.10}$$

the variables read as follows

$$\begin{aligned} \epsilon_k &= 2t_\mathrm{h}\big(\cos(k'_x) + \cos(k'_y)\big), \\ \chi_k &= J\big(\rho_0^* \mathrm{e}^{-ik'_y} + \rho_1^* \mathrm{e}^{ik'_x} + \rho_2 \mathrm{e}^{ik'_y} + \rho_3 \mathrm{e}^{-ik'_x}\big). \end{aligned} \tag{5.11}$$

In summary, we have obtained single-particle eigenenergies with $E_{k\pm} = \pm\big(\big|\epsilon_k - \chi_k\big|^2 + U^2(\rho_B - \rho_A)^2\big)^{1/2}$. Charge-density wave (CDW) states $\rho_A \neq \rho_B$ would lead to a gap in the single-particle spectrum. Some caution needs to be taken when looking for a saddle point in the mean-field free energy. The saddle point curvature in the U-direction is inverse to one of the J-terms (some more details are given in the original publication [142]). The internal energy (expectation value of the Hamiltonian) per flavor is given by

$$\begin{aligned} H/N = \frac{V}{2}\Big(-U(\rho_A^2+\rho_B^2) + J\sum_{i=0}^{3}|\rho_0|^2\Big) \\ +\sum_k E_k\left(\rho_{k+,k+}-\rho_{k-,k-}\right), \end{aligned} \tag{5.12}$$

where V is the total number of lattice sites. Using

$$U\big(\rho_A^2+\rho_B^2\big) = \frac{U}{2}\big(\rho_A+\rho_B\big)^2 + \frac{U}{2}\big(\rho_A-\rho_B\big)^2, \tag{5.13}$$

where $\rho_A+\rho_B$ is fixed by the filling, we see that $\rho_A=\rho_B$ is required for a stable saddle point. It implies that in this model CDWs are thermodynamically unfavorable due to the U-term in the Hamiltonian. In particular, the value of U is irrelevant for the mean-field phase diagram. It is worth noting that this is different for nearest-neighbor density-density interactions instead of or in addition to the Hubbard interaction. Setting $\rho_A=\rho_B$, we obtain

$$\begin{aligned} H/N &= \frac{V}{2}J\big(|\rho_0|^2+|\rho_1|^2+|\rho_2|^2+|\rho_3|^2\big) \\ &\quad +\sum_k E_k\left(\rho_{k+,k+}-\rho_{k-,k-}\right), \\ E_k &= 2t_{\mathrm{h}}\big(\cos(k_x)+\cos(k_y)\big) \\ &\quad - J\big(\rho_0^*\mathrm{e}^{-ik_y}+\rho_1^*\mathrm{e}^{ik_x}+\rho_2\mathrm{e}^{ik_y}+\rho_3\mathrm{e}^{-ik_x}\big). \end{aligned} \tag{5.14}$$

Due to the symmetry of $E_{k\pm}$ around $E=0$, the ground state at half filling is always obtained by setting $\rho_{k-,k-}=\frac{1}{2}$ and $\rho_{k+,k+}=-\frac{1}{2}$ for all momenta k. The self-consistency conditions follow from the momentum space representation of the local bond variables:

$$\begin{aligned} \rho_0 \overset{!}{=} \rho_{(0|0)A,(0|0)B} \quad &\Leftrightarrow \quad \rho_0 = \frac{1}{2V_u}\sum_k \mathrm{e}^{-i\varphi_k}\left(\rho_{k+,k+}-\rho_{k-,k-}\right) \\ \rho_1 \overset{!}{=} \rho_{(0|0)A,(-1|0)B} \quad &\Leftrightarrow \quad \rho_1 = \frac{1}{2V_u}\sum_k \mathrm{e}^{i\sqrt{2}k_x}\mathrm{e}^{-i\varphi_k}\left(\rho_{k+,k+}-\rho_{k-,k-}\right) \\ \rho_2 \overset{!}{=} \rho_{(-1|-1)B,(0|0)A} \quad &\Leftrightarrow \quad \rho_2 = \frac{1}{2V_u}\sum_k \mathrm{e}^{-i\sqrt{2}(k_x+k_y)}\mathrm{e}^{i\varphi_k}\left(\rho_{k+,k+}-\rho_{k-,k-}\right) \\ \rho_3 \overset{!}{=} \rho_{(0|-1)B,(0|0)A} \quad &\Leftrightarrow \quad \rho_3 = \frac{1}{2V_u}\sum_k \mathrm{e}^{-i\sqrt{2}k_y}\mathrm{e}^{i\varphi_k}\left(\rho_{k+,k+}-\rho_{k-,k-}\right) \end{aligned} \tag{5.15}$$

We find self-consistent values for ρ_0, ρ_1, ρ_2 and ρ_3 at zero temperature from the numerical minimization of (5.14) using the simulated annealing algorithm described in Chapter 2.

Numerically, we indeed obtain the three equilibrium phases of the model at half filling: Firstly, the dimerized bond density wave *Peierls phase* at large J/t_h has got real-valued ρ_i with one strong bond $\rho_0 \gg \rho_1 = \rho_2 = \rho_3$. We introduce the following order parameter for the Peierls phase:

$$O_\mathrm{Peierls} = |\rho_0| - \max_{i=1,2,3} |\rho_i|. \tag{5.16}$$

Secondly, the *staggered Flux phase* (also known as DDW phase [253, 140]) at intermediate J/t_h comes with complex bonds ρ_i that are equal in magnitude and multiply to a flux operator $\Pi = \Pi_0 \mathrm{e}^{i\Phi}$ around a plaquette with non-vanishing phase $\Phi \neq 0$. Hence, we will consider

$$O_\mathrm{Flux} = \Phi. \tag{5.17}$$

Lastly, there is the *uniform phase* which is a stable saddle point at all values of J but has the lowest free energy only at $J = 0$. In the uniform phase the unit cell bonds are real and $O_\mathrm{Peierls} = O_\mathrm{Flux} = 0$. The single-particle band structures obtained from the mean-field calculation are plotted in Fig. 5.2 for the reduced Brillouin zone. The bands in the Figure roughly correspond to the electron removal/addition energies and do not directly contain information about excited states of the system.

We add, for reference, the relation of Affleck's and Marston's order parameter fields [141, 142] to our formalism: The field $i\phi_i$ corresponds to $2U\rho_{ii}$ and their χ_{ij} is our $-J\rho_{ij}$.

5.2.2 Non-zero temperatures (cf. [2])

Since we are interested in the values of the order parameters after energy absorption due to the driving, we would like to compare our results to equilibrium states at temperatures $T > 0$. In addition, the finite-temperature phase diagram of the $N \to \infty$ model is not reported in the literature yet. In order to determine finite-temperature states, we need to minimize the (Helmholtz) free energy, which includes both the total energy as well as the entropy term. The mean-field ground state is a simple product state of a single fermion species, which is labeled by the mean-field momentum modes $k\pm$,

$$|\tilde{\Psi}_0^\mathrm{MF}\rangle = \prod_{\epsilon_{k\pm} < \epsilon_F} c^\dagger_{k\pm} |0\rangle \,. \tag{5.18}$$

Hence, at finite temperature we can use the formula for the entropy of free fermions

$$S/N = \frac{1}{T} \sum_{\epsilon_k} \left[n_\mathrm{FD}(\epsilon_k)\big(\epsilon_k - \mu\big) + T \ln \left(1 + \mathrm{e}^{-(\epsilon_k - \mu)/T}\right) \right] \tag{5.19}$$

with the Fermi-Dirac distribution $n_\mathrm{FD}(\epsilon) = 1/\big(1 + \exp[(\epsilon - \mu)/(k_B T)]\big)$. Formally we write S/N and F/N. This is always to be understood in the limit $N \to \infty$. This yields the following (Helmholtz) free energy $F = \langle H \rangle - TS$,

$$F/N = J \sum_{\langle ij \rangle} |\rho_{ij}|^2 - \sum_{\epsilon_k} \beta^{-1} \ln \left(1 + \mathrm{e}^{-\beta(\epsilon_k - \mu)}\right), \tag{5.20}$$

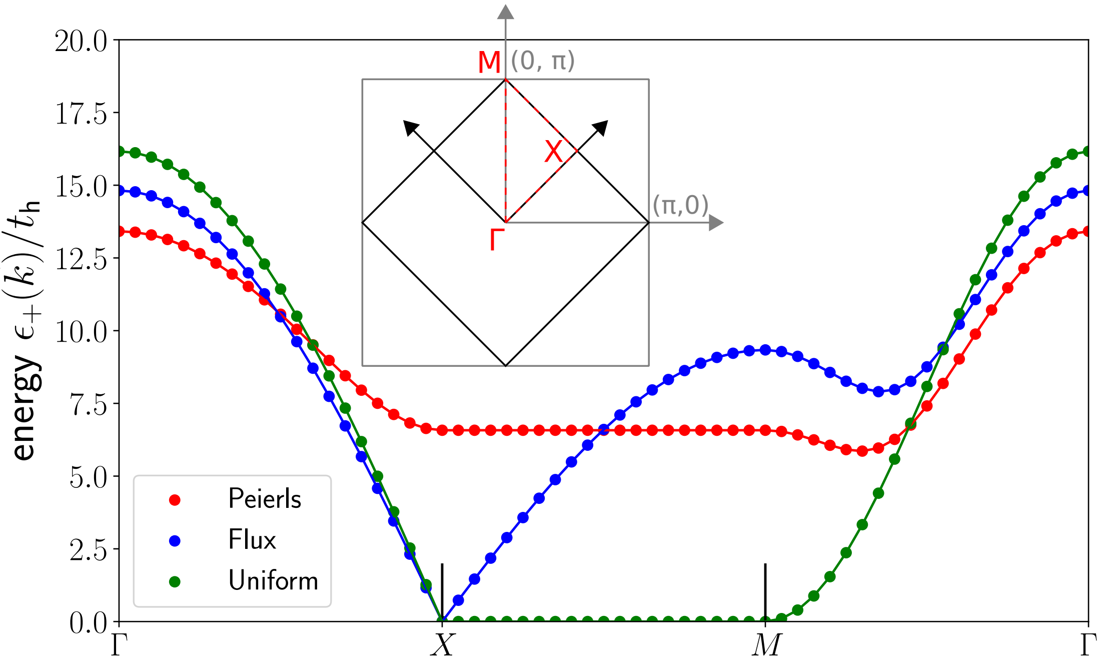

Figure 5.2: Single-particle mean-field band structure for $J/t_\mathrm{h} = 15$ and a system size of $V_u = 41 \times 41$ unit cells. The spectrum is symmetric around energy zero; here we only plot the upper half with positive energy. The Peierls phase is gapped, while the Flux phase is gapless. Inset: Sketch of the reduced Brillouin zone derived from the unit cell in Fig. 5.1. This figure is also published in [2]. Copyright (2022) by the American Physical Society.

where $\beta = 1/(k_B T)$.

We determined the minima of the free energy numerically using the simulated annealing algorithm described in Chapter 2. Special care must be taken to arrive at the targeted particle number because the single-particle basis changes during the stochastic iterations. We have therefore updated the chemical potential in each iteration step such that it yields the correct particle number for each intermediate basis. We checked the convergence of the annealing procedure using the self-consistency relations of the bonds.

We calculated the phase diagram at half filling, the results are presented in Fig. 5.3. On the left hand side, we plot the free energies of the three equilibrium phases at zero temperature. For weak interaction strengths, the Flux phase has the lowest free energy, while the Peierls phase only exists at a slightly higher free energy. At a value of $J/t_\mathrm{h} \approx 12$, the free energies of Peierls and Flux phase swap roles and the Peierls phase becomes the equilibrium phase of the model at strong coupling. Despite this first-order phase transition, Peierls and Flux phase are thermodynamically almost degenerate in the weak to intermediate coupling regime. The Uniform phase always has a much larger free energy. On the right hand side of Fig. 5.3 we plot the full finite-temperature mean-field phase diagram. At high temperatures the Uniform phase dominates the phase diagram, while at strong coupling there is a transition from Peierls to Flux at low temperature, followed by a second transition at higher temperatures from the Flux

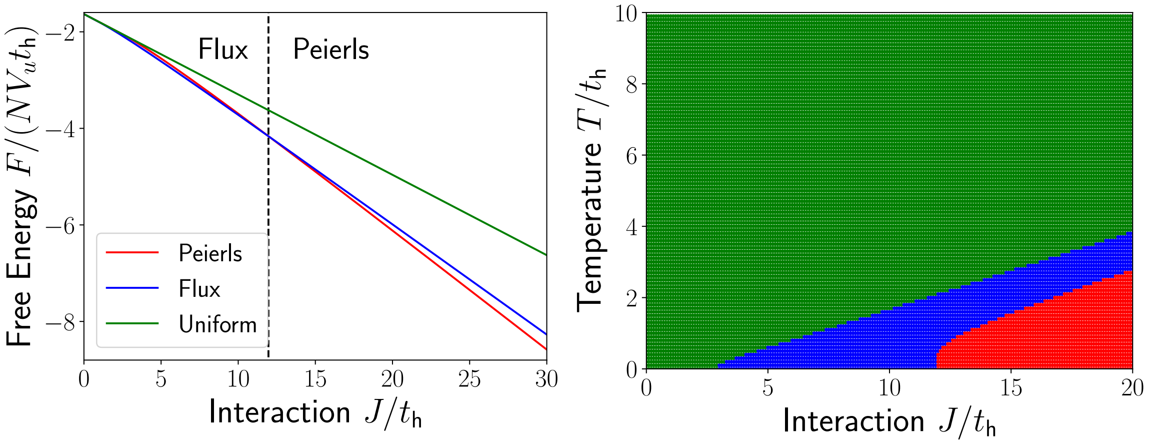

Figure 5.3: Equilibrium phase diagrams of the mean-field ($N \to \infty$) model. Left: Free energies at zero temperature as function of the interaction strength J/t_h. The mean-field transition occurs at the dashed line around $J/t_h \approx 11.96$. Right: Phase diagram at non-zero temperatures. The uniform phase is the generic high-temperature phase.

to the Uniform phase. Note that at low temperatures and for weak interaction strengths $J \sim t_h$, all free energies are practically identical, in these cases we just write Uniform phase in the diagram. In order to determine the nature of the phase transitions, we make a cut through the phase diagram at a fixed interaction strength and look at the free energies as a function of temperature. We select a value of $J = 15t_h$, which lies in a region of the phase diagram where the Peierls phase has the lowest free energy. The results are shown in Fig. 5.4. From temperature zero up to $T \approx 3.5t_h$ there is a regime in which all three phases are stable. Up to $T \approx 1.6t_h$, the Peierls phase has the lowest free energy, while at more elevated temperatures the Flux phase is preferred. The uniform phase is left as the generic high-temperature phase. The transition from Peierls to Flux is first order, one can see well the jump in the internal energy at the transition point. The transition from the Flux to the Uniform phase, in contrast, is second order and the order parameter displays the typical mean-field scaling with exponent $\beta \sim \frac{1}{2}$. We can observe, in addition, that there is a second “hidden” phase transition of the Peierls phase to the Uniform phase, which occurs at slightly lower temperatures. For larger values of J the range of temperatures with stable order beyond the uniform phase will be broader.

Because of the complex structure of the phase transitions, a value $J/t_h = 15$ is an interesting starting point to investigate the non-equilibrium dynamics in the model.

5.2.3 Order parameters in the finite-N model (cf. [2])

Before we continue to discuss possible state preparation techniques for the finite-N model, we would like to make a general remark on phases and order parameters in the Hubbard-Heisenberg model with $N < \infty$. It was demonstrated using quantum Monte Carlo [140] that the mean-field saddle points yield a qualitatively correct picture of the finite-N Hubbard-Heisenberg model down to $N = 6$, albeit with renormalized order parameters and phase boundaries. The respective phase diagram from the original publication can be seen in Fig. 5.5.

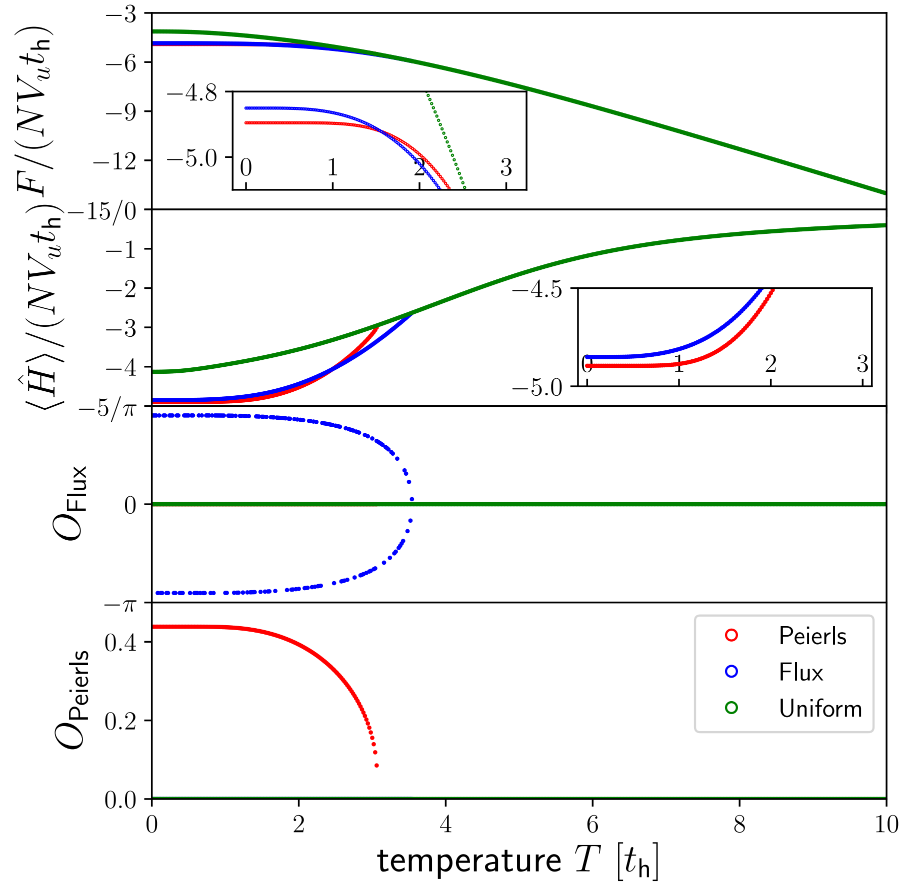

Figure 5.4: Finite-temperature equilibrium states for the $N \to \infty$ Hubbard-Heisenberg model with $V_u = 11 \times 11$ unit cells, $J/t_\mathrm{h} = 15$ and $U = 0$. Upper two rows: Helmholtz free energy F and total (internal) energy $\langle \hat{H} \rangle$ per unit cell. Lower two rows: Order parameters for the Flux and Peierls phases displaying the typical mean-field scaling. At temperature $T \approx 1.5 t_\mathrm{h}$ there is a first order transition from Peierls to Flux order. This figure is also published in [2]. Copyright (2022) by the American Physical Society.

Since we typically choose $250 \leq N$, we are safe to work with the same order parameter definitions as for the infinite-N model but we need to take care how to consistently calculate them within the TWA scheme.

We start with a remark related to the calculation of observables within the Wigner-Weyl scheme. The TWA expectation value of an operator $\hat{O}[\hat{\rho}_{ij}]$, which can be expressed in terms of the classical variables ρ_{ij}, reads

$$\langle \hat{O}(t) \rangle = \int \mathrm{d}\rho_{ij}(0) W\big(\rho_{ij}(0)\big) O_\mathrm{W}\big(\rho_{ij}(t)\big), \tag{5.21}$$

where $O_\mathrm{W}(\rho_{ij})$ is the Weyl symbol of $\hat{O}$. It can, in general, differ at order $\sim \frac{1}{N}$ for different ways of writing $\hat{O}$ in terms of the $\hat{\rho}_{ij}$ [157]. In order to extract the Peierls and Flux order parameters, respectively, we need to calculate absolute values and phase angles of the $\hat{\rho}_{ij}$. It is not obvious how the exact Weyl symbols of these operations

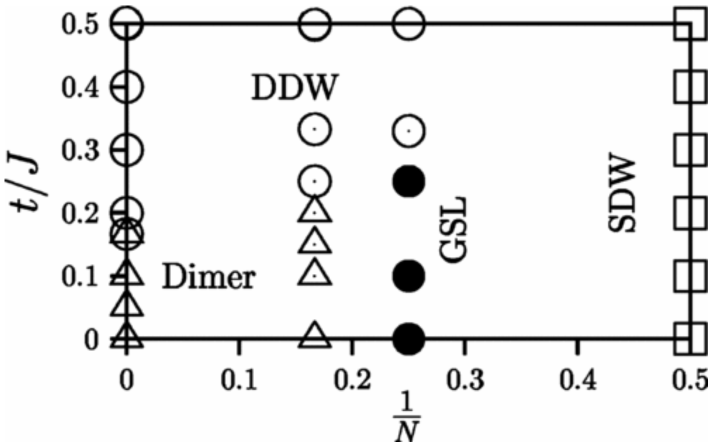

Figure 5.5: Phase diagram as a function of t/J and $\frac{1}{N}$ as obtained by Assaad within quantum Monte Carlo. The "Dimer" phase orresponds to our Peierls phase, the "DDW" phase is the staggered flux phase. These two phases determine the phase diagram down to values of $N = 6$. Reprinted figure with permission from "F.F. Assaad, Phys. Rev. B 71, 075103 (2005)". Copyright (2005) by the American Physical Society.

look like. However, it is clear that in the mean-field theory $N \to \infty$ one can calculate them straightforwardly from the $\rho_{ij}(t)$. Hence, we assume that corrections to Weyl symbols, if present at all, will scale like $\sim \frac{1}{N}$, e.g. $|\bullet|_W = |\bullet| + \mathcal{O}(\frac{1}{N})$. Since we will work at large N, we are justified to neglect these corrections. This is the philosophy of the stochastic mean-field approach as well (cf. Chap. 2).

In the numerical determination of the Flux order parameter we average $e^{i\Phi}$ over all trajectories, i.e. we work with numbers on the unit circle. However, one needs to take care of the spontaneous breaking of the orientation symmetry of the plaquette flux. There are two ergodic components, for which Φ lies in the intervals $[0, \pi]$ and $[-\pi, 0]$, respectively. Different fTWA trajectories can select different ergodic components such that direct averaging of the order parameter may become unphysical (analogous to averaging the magnetization of a ferromagnet without explicit symmetry breaking). Hence, in order to calculate the Flux order parameter directly, we introduce a weak symmetry breaking term $i\epsilon_{mn}(\hat{\jmath}_{mn} - \hat{\jmath}_{nm})$ that selects the $\Phi \in [0, \pi]$ component. The current operator (for lattice sites m, n) is given by

$$\hat{\jmath}_{mn} = it_{\mathrm{h}}(c_m^\dagger c_n - c_n^\dagger c_m) = -2t_{\mathrm{h}} \operatorname{Im}(\hat{\rho}_{mn}). \tag{5.22}$$

We tried out a few symmetry breaking strengths and concluded that $\epsilon \sim 10^{-3}$ yields the best balance of breaking the symmetry but not influencing the dynamics too much. For reference, we write down the equations of motion for a symmetry-breaking term in the Hamiltonian,

$$i \sum_{\langle i,j \rangle} \epsilon_{i,j} (\hat{\rho}_{i,j} - \hat{\rho}_{j,i}) = i \sum_{l} \sum_{\substack{a(l), \\ l \leq a(l)}} \epsilon_{l,a(l)} (\hat{\rho}_{l,a(l)} - \hat{\rho}_{a(l),l}). \tag{5.23}$$

They read

$$\begin{aligned}
-i\partial_t\hat{\rho}_{ij} &= i\sum_{l}\sum_{\substack{a(l),\\ l\leq a(l)}} \epsilon_{l,a(l)}\big(\delta_{i,a(l)}\rho_{lj} - \delta_{l,j}\rho_{i,a(l)} - (l \leftrightarrow a(l))\big)\\
&= i\sum_{a(i)<i} \epsilon_{a(i),i}\rho_{a(i),j} - i\sum_{i<a(i)} \epsilon_{i,a(i)}\rho_{a(i),j}\\
&\quad + i\sum_{j<a(j)} \epsilon_{j,a(j)}\rho_{i,a(j)} - i\sum_{a(j)<j} \epsilon_{a(j),j}\rho_{i,a(j)}\\
&= -i\sum_{a(i)} \epsilon_{i,a(i)}\rho_{a(i),j} + i\sum_{a(j)} \epsilon_{j,a(j)}\rho_{i,a(j)},
\end{aligned} \tag{5.24}$$

where $a(i)$ labels all nearest neighbors of site i. Since the flux in the flux phase is staggered, the symmetry breaking coefficients $\epsilon_{l,a(l)}$ need to alternate along a lattice direction.

The explicit breaking of the symmetry can be useful for spatially inhomogeneous situations like the type of photoexcitations considered in Sec. 5.5, where long-range order cannot be expected and where we would like to directly probe the local formation of order. In spatially homogeneous situations, there is another more convenient probe, which is also well defined without explicit symmetry breaking field: In numerical studies of staggered flux states in ladder systems of interacting fermions, Schollwöck et.al. [253] considered current-current correlators of the form $\langle\hat{j}_{mn}\hat{j}_{rs}\rangle$. This is similar to studying spin-spin correlation functions instead of the magnetization in a ferromagnetic model. We calculate current-current correlators for two bonds at the largest spatial separation in the system to detect long-range order. Usually, we select the bond ρ_0 (which is the strong bond in the Peierls phase) for the calculations. Making use of the translational symmetry of the system we determine the correlators for all translationally equivalent pairs of unit cells and average over them. This reduces the effect of the fluctuations on the observable within the truncated Wigner approach. For the adiabatic switching calculations we also need to introduce a weak symmetry breaking for the Peierls phase in order to select one of the four bonds as the strong one. Details will be given in the next section.

5.2.4 Adiabatic switching of interactions

A possible preparation procedure for initial states, which should in theory also be applicable to the finite-N model, is adiabatic switching of interactions. Starting from a non-interacting system, we expect that for slow enough changes of the interaction strength the system will always follow the instantaneous ground states. For the adiabatic switching procedure different ramping profiles can be chosen. A common choice (e.g. presented in Ref. [276]) are functions $f_m(t)$, whose lowest derivatives up to and including m-th order are smooth at the boundaries. For instance, $m = 0$ corresponds to linear ramping:

$$\begin{aligned}
&f_0(\tau) = \tau, \qquad f_1(\tau) = -\tau^2(2\tau - 3), \qquad f_2(\tau) = \tau - \sin(2\pi\tau)/(2\pi),\\
&f_3(\tau) = -\tau^4\big(20\tau^3 - 70\tau^2 + 84\tau - 35\big),\\
&f_4(\tau) = \tau^5\big(70\tau^4 - 315\tau^3 + 540\tau^2 - 420\tau + 126\big).
\end{aligned} \tag{5.25}$$

$\tau = t/T$ is the ramping parameter based on the total switching time T. All functions obey $f_m(0) = 0$, $f_m(1) = 1$.

Let us start the discussion of the results with mean-field theory $N \to \infty$. In the non-interacting state at initial time, all bonds in a unit cell are equivalent and a weak symmetry breaking is needed to push the system into the symmetry sector of the Peierls phase. This can be accomplished by adding a term $\varepsilon_{\mathrm{Pei}}|\rho_0|^2$ with $0 < \varepsilon_{\mathrm{Pei}} \ll 1$ to the Hamiltonian for each unit cell. Its effect is to slightly increase the value of J for one of the four bonds, which will then end up being the strong bond of the Peierls phase. All mean-field results are obtained using a value of $\varepsilon_{\mathrm{Pei}} = 10^{-3}$. Fig. 5.6 shows results for the bond strengths $|\rho_i|$ upon switching of the interaction $J(t) = Jf_m(t)$ for varying values of m and T. The final bond values depend, as expected, on the total ramping duration T. The larger T, the better do the bond strengths approach the correct equilibrium mean-field value. In addition, the oscillations in the numerical data are smaller for higher T. They would vanish as $T \to \infty$. The effect of m is twofold: Higher values of m lead to a smoother approach of the bond expectation values to the mean-field result. In addition, the branch-off of the bond strengths from their initial values occurs at later times. In Fig. 5.7 we plot the total energy per unit cell as a function of time during the switching. It follows the temporal profile of the interaction well and we can see on the right hand side of the plot that the final value of the energy approaches the expected mean-field result. Furthermore, the quantitative differences between the different switching profiles becomes negligible if the total ramping time is sufficiently large.

These numerical results for the mean-field model indicate that adiabatic switching should indeed be a possible strategy to prepare ordered states of the model in equilibrium. However, turning to the finite-N model, a simple adaptation of the strategy to $N < \infty$ fails. Fig. 5.8 shows results for linear ramps of J in a system with $N = 100$ starting from the Wigner function of a non-interacting Fermi sea state (uniform phase) and four different values of $\varepsilon_{\mathrm{Pei}}$. The switching procedure is completed at time $t = 95$ and we also turn off the symmetry breaking at the same time. The results show that the Peierls phase symmetry breaking indeed leads to a split-off of one bond in the course of the dynamics. However, after $\varepsilon_{\mathrm{Pei}}$ is reset to zero the bonds collapse back to a uniform configuration. The staggered Flux order parameter is also zero in the final state, while it is non-zero for some time during the switching. The final state thus resides in the uniform symmetry sector. Our observations for the bond strengths are consistent with the dynamics of the total energy, which shrinks linearly with time but reaches a higher final state energy than the state preparation procedure that we will describe below. The total energy is not affected much by the choice of $\varepsilon_{\mathrm{Pei}}$, which is as it should be. Paradoxically, the final state energy does not lower upon ramping over a longer time period: We have checked ramping times up to $T = 995$. In fact, the final total energy even increases slightly. The reason for this is not clear but it is likely rooted in the structure of the free energy landscape, where starting from the zero-coupling uniform phase one has to traverse the Flux phase to reach the Peierls phase. At intermediate couplings both phases exist as minima of the free energy but only at strong coupling is the Peierls phase the phase with the lowest free energy. While the Peierls phase is gapped, the Flux phase is semimetallic and therefore allows for low-energy excitations. It is hence likely that the fluctuating trajectories induce such excitations, which lead

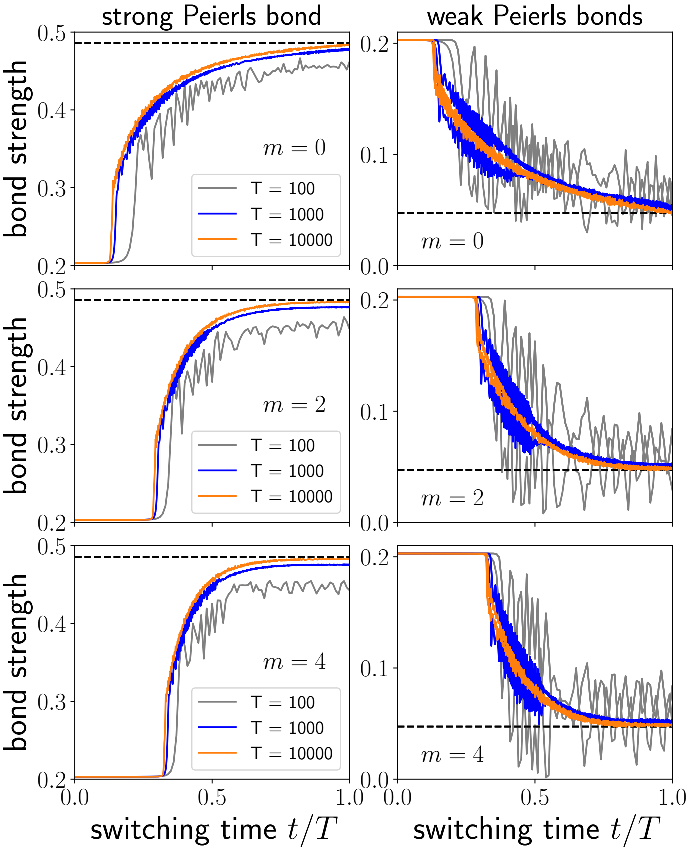

Figure 5.6: Bond strengths after adiabatic switching of J in the mean-field ($N \to \infty$) Hubbard-Heisenberg model on a 21×21 unit cells square lattice. The rows correspond to three different values of m. Dashed lines show the mean-field results from direct calculation.

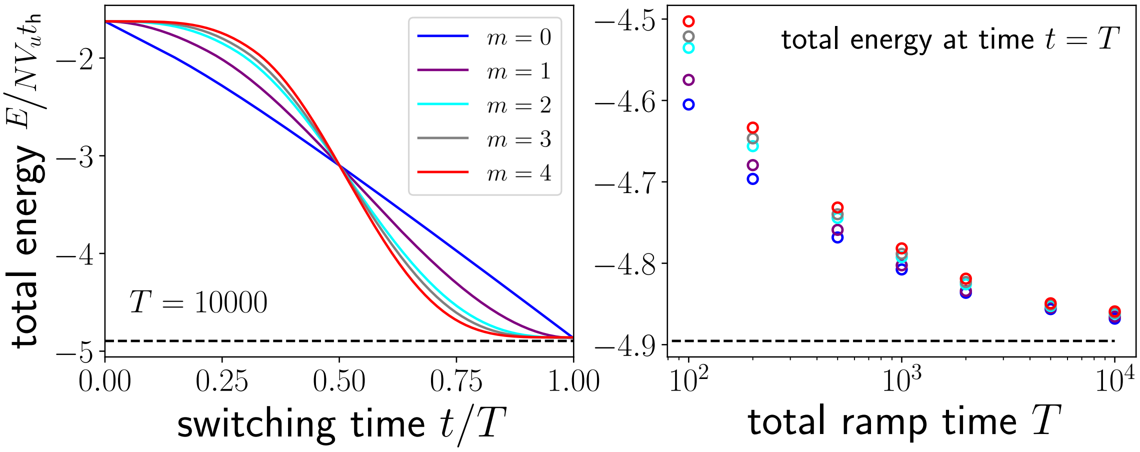

Figure 5.7: Total energies after adiabatic switching of J in the mean-field ($N \to \infty$) Hubbard-Heisenberg model on a 21×21 unit cells square lattice. m labels the switching model (5.25). Left: Total energy during switching with $T = 10000$. Right: Final value of the total energy for varying m and T. The final energy difference among different switching models m is more pronounced for short ramp times T.

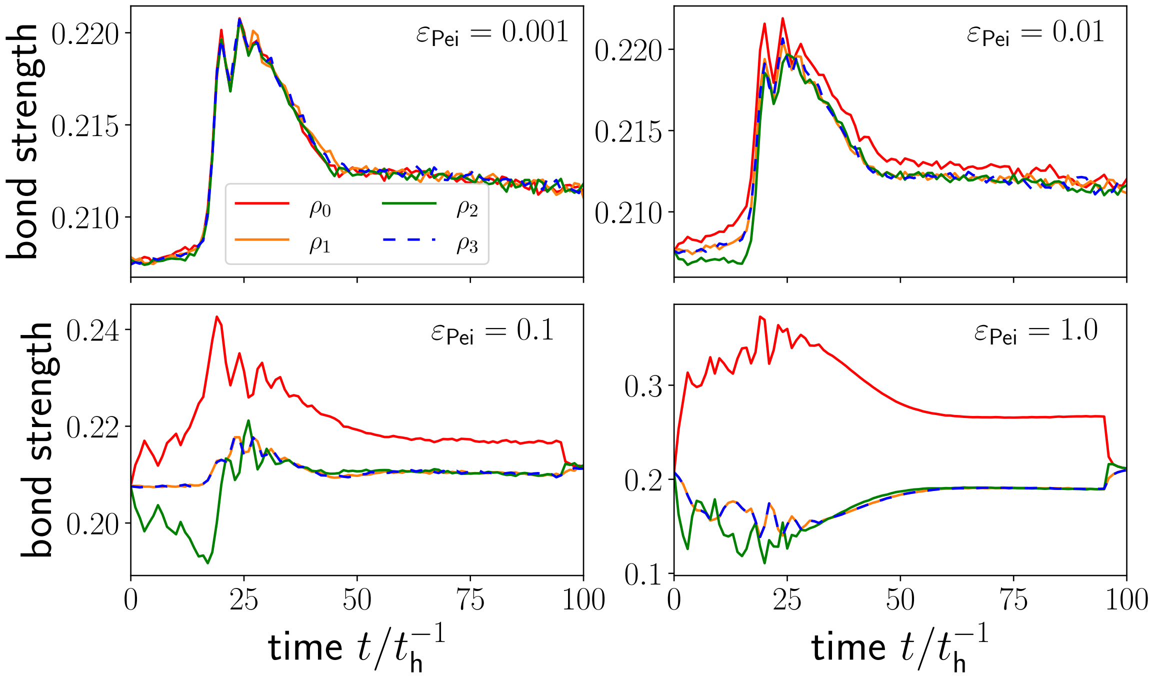

Figure 5.8: Bond dynamics due to slow linear ramps of the interaction strength $J = 0 \to 15$ over a time interval $T = 95$ with four different values of the Peierls symmetry breaking $\varepsilon_{\mathrm{Pei}}$. At time $t = 95$ we set $J = 15$ and switch off the symmetry breaking to monitor the stability of the final state. The system has $V = 11 \times 11$ unit cells and a fermion degeneracy $N = 100$.

to additional heating and may drive the system out of the Flux phase into the Uniform phase. For slower switching, one line of thought could be that the system remains longer in this intermediate regime such that even more trajectories induce excitations.

These explanations are for sure a bit speculative and more thorough analysis is required to understand the observed dynamics. For now, we can conclude that adiabatic switching is not – at least not in the way executed here – a suitable state preparation technique for the finite-N model.

5.2.5 Quench from mean-field to finite N (cf. [2])

The following approach is meant as a pragmatic procedure to construct a stationary initial state at least for some combinations of system size V and fermion degeneracy N. The idea is to adopt the mean-field basis $k\pm$ for the initial state but to only populate a finite number of degenerate fermion levels. This effectively amounts to constructing quantum fluctuations of ρ-operators around the mean-field state. Those fluctuations are then encoded in a Gaussian Wigner function, which leads to non-stationary dynamics at the initial time. Hence, we will need to wait for the system to relax. One can view this protocol as a quench from infinite N to a finite value $N < \infty$. However, one has to keep in mind that we continue to use the mean-field basis to define the initial occupation numbers of states. We assume that at large but finite N the self-consistent mean-field data for the one-particle density matrix will still be close to the true equilibrium states. In the following, we always only consider half filling such that the initial mean-field state has the following product structure:

$$|\Psi_0^N\rangle = \prod_k \prod_{\alpha=1}^{N} c^\dagger_{k-,\alpha} |0\rangle \,. \tag{5.26}$$

In order to correctly set up the Gaussian Wigner function, we need to make sure that we include all non-vanishing quantum correlations. The classical phase space includes all variables $\rho_{k\pm,l\pm}$ for arbitrary momenta k, l and the four combinations of $\pm$. However, as we have shown in Chapter 2, only covariances of the form $\langle\rho_{\alpha\beta}\rho_{\alpha\beta}\rangle$ and $\langle\rho_{\alpha\beta}\rho_{\beta\alpha}\rangle$ are non-zero for a product state. The complete initial data for a Gaussian Wigner function of this type is listed in Table 5.1 for general mode occupation numbers and in Table 5.2 for half filling according to (5.26).

$\rho_{\alpha\beta}$	$\rho_{k\pm,l\pm}$	$\rho_{k\pm,l\mp}$
$\mu_{\rho_{\alpha\beta}}$	$\delta_{kl}\left(n_{k\pm} - \frac{1}{2}\right)$	0
$\Gamma^{\text{symm}}_{\alpha\beta,\alpha\beta}$	$\frac{1}{2N}\left(n_{k\pm} + n_{l\pm} - 2n_{k\pm}n_{l\pm}\right)$	$\frac{1}{2N}\left(n_{k\pm} + n_{l\mp} - 2n_{k\pm}n_{l\mp}\right)$
$C^{\text{symm}}_{\alpha\beta,\alpha\beta}$	$\frac{\delta_{kl}}{N} n_{k\pm}(1 - n_{k\pm})$	0
$\sigma^2_{\text{Re}(\rho_{\alpha\beta})}$	$\frac{1}{4N}\left(1 + \delta_{kl}\right)\left(n_{k\pm} + n_{l\pm} - 2n_{k\pm}n_{l\pm}\right)$	$\frac{1}{4N}\left(n_{k\pm} + n_{l\mp} - 2n_{k\pm}n_{l\mp}\right)$
$\sigma^2_{\text{Im}(\rho_{\alpha\beta})}$	$\frac{1}{4N}\left(1 - \delta_{kl}\right)\left(n_{k\pm} + n_{l\pm} - 2n_{k\pm}n_{l\pm}\right)$	$\frac{1}{4N}\left(n_{k\pm} + n_{l\mp} - 2n_{k\pm}n_{l\mp}\right)$

Table 5.1: Correlation data for the Gaussian Wigner function for the mean-field product state: symmetrized covariance $\Gamma^{\text{symm}}_{\alpha\beta,\mu\nu} = \left\langle \frac{1}{2}\{\hat\rho_{\alpha\beta}, \hat\rho_{\nu\mu}\}\right\rangle^{\text{c.c.}}$, symmetrized pseudo-covariance $C^{\text{symm}}_{\alpha\beta,\mu\nu} = \left\langle \frac{1}{2}\{\hat\rho_{\alpha\beta}, \hat\rho_{\mu\nu}\}\right\rangle^{\text{c.c.}}$. For product states only combinations $(\mu,\nu) = (\alpha,\beta)$ or $(\mu,\nu) = (\beta,\alpha)$ can lead to non-zero entries.

$\rho_{\alpha\beta}$	$\mu_{\rho_{\alpha\beta}}$	$\Gamma^{\text{symm}}_{\alpha\beta,\alpha\beta}$	$C^{\text{symm}}_{\alpha\beta,\alpha\beta}$	$\sigma^2_{\text{Re}(\rho_{\alpha\beta})}$	$\sigma^2_{\text{Im}(\rho_{\alpha\beta})}$
$\rho_{k\pm,l\pm}$ $(k = l)$	$\frac{1}{2}, -\frac{1}{2}$	0	0	0	0
$\rho_{k\pm,l\pm}$ $(k \neq l)$	0	0	0	0	0
$\rho_{k\pm,l\mp}$	0	$\frac{1}{2N}$	0	$\frac{1}{4N}$	$\frac{1}{4N}$

Table 5.2: Special case half filling: all "$-$" states are occupied ($n_{k-} = 1$) and all "$+$" states are unoccupied ($n_{k+} = 0$). Hence, $n_{k\pm} + n_{l\pm} - 2n_{k\pm}n_{l\pm} = 0$ and $n_{k\pm} + n_{l\mp} - 2n_{k\pm}n_{l\mp} = 1$.

We sample real and imaginary parts of the $\rho_{k+,l-}$ and $\rho_{k-,l+}$ variables from a Gaussian distribution for all combinations k, l and rotate them to the $\rho_{kA,lB}$ sublattice basis using the mean-field particle-hole transformation

$$\begin{pmatrix} \rho_{kA,lA} & \rho_{kA,lB} \\ \rho_{kB,lA} & \rho_{kB,lB} \end{pmatrix} = U_k \cdot \begin{pmatrix} \rho_{k+,l+} & \rho_{k+,l-} \\ \rho_{k-,l+} & \rho_{k-,l-} \end{pmatrix} \cdot U_l^\dagger, \tag{5.27}$$

where

$$U_k = \frac{1}{\sqrt{2}} \begin{pmatrix} 1 & 1 \\ \mathrm{e}^{i\varphi_k} & -\mathrm{e}^{i\varphi_k} \end{pmatrix} \tag{5.28}$$

and $\epsilon_k \mathrm{e}^{i\varphi_k} := \epsilon_{\vec{k}} - \chi_{\vec{k}}$ as defined in the previous section. Written out, the right hand side reads:

$$\frac{1}{2}\begin{pmatrix} \rho_{k+,k+} + \rho_{k+,k-} + \rho_{k-,k+} + \rho_{k-,k-} & \mathrm{e}^{-i\varphi_k}\left(\rho_{k+,k+} + \rho_{k-,k-} - \rho_{k-,k+} - \rho_{k-,k-}\right) \\ \mathrm{e}^{i\varphi_k}\left(\rho_{k+,k+} + \rho_{k+,k-} - \rho_{k-,k+} - \rho_{k-,k-}\right) & \rho_{k+,k+} - \rho_{k+,k-} - \rho_{k-,k+} + \rho_{k-,k-} \end{pmatrix} \tag{5.29}$$

As a last step, we use the Fourier transform to obtain the ρ-variables in position space. The time propagation is always carried out in position space. The freely evolving system will relax to a stationary state on a characteristic warm-up time scale. Later, when we investigate the dynamics of the system under driving, we switch on the drive only after this warm-up. A disadvantage of the procedure is that the resulting stationary state is not a ground state. This, however, is not too problematic for now since we are primarily interested in obtaining a stationary reference state in the Peierls phase from which to launch the dynamics of interest. For a precise comparison of results at different values of N, though, it would be desirable to have better control over the initial states.

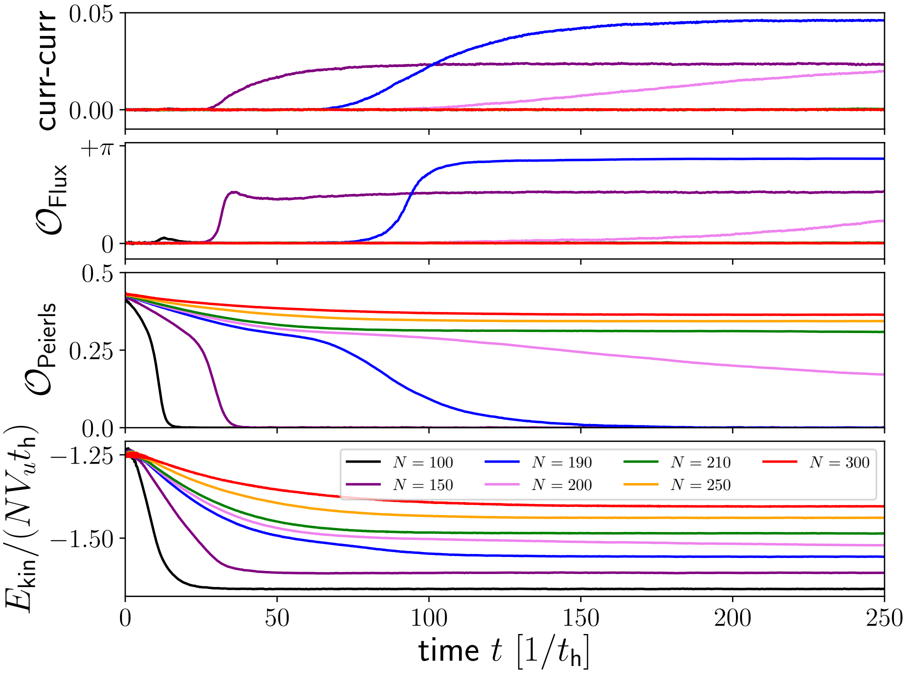

Figure 5.9: Initial relaxation dynamics generated by a Gaussian Wigner function corresponding to the state (5.26) in the finite-N Hubbard-Heisenberg model with $J = 15t_{\mathrm{h}}$, $U = 0$ and $V_u = 11 \times 11$ unit cells. The order parameters and the kinetic energy reach a stationary state before time $t = 250t_{\mathrm{h}}^{-1}$ for all shown values of N except for $N = 200$ for which the relaxation takes longer than $1000t_{\mathrm{h}}^{-1}$. This figure is also published in [2]. Copyright (2022) by the American Physical Society.

Fig. 5.9 shows the time evolution of the order parameters induced by a Gaussian Wigner function corresponding to the state (5.26) for multiple values of N and a system size of $V_u = 11 \times 11$ unit cells. The upper two panels show indicators of the staggered Flux order: the current-current correlator without symmetry breaking in the top row and the plain Flux order parameter obtained with explicit symmetry breaking $\epsilon_{\text{Flux}} \sim 10^{-3}$ in the row below. For $N \gtrapprox 200$, the dynamics leads to a decrease of the Peierls order parameter, while $\mathcal{O}_{\text{Flux}}$ remains zero at all times. In this regime the stationary state is clearly a Peierls state. Around $N \approx 200$ the system transitions to the Flux phase and the dynamics is very slow. This is also an interesting finding on its own since it shows – at least qualitatively – the slow tunneling between nearly degenerate free energy sectors. For smaller values $N \lessapprox 150$, the system ends up in the Uniform phase. The kinetic energy relaxes to a stationary value on the same timescale like the order parameters. The redistribution of energy between kinetic and interaction sector is in accordance with our findings in the SU(N) Hubbard models and suggests an interpretation in terms of quasiparticle formation. We collect the stationary values of the order parameters in Fig. 5.10. There is no data point for $N = 200$ as it was impossible to extract a definite order parameter on the timescale of our simulation. The lower row in the figure confirms that the system acquires a finite negative amount of correlation energy $\sim (-J)/N$ relative to the mean-field state. We checked that the total energy of the system prepared with this Wigner function is indeed independent of the system size if rescaled by the number of unit cells.

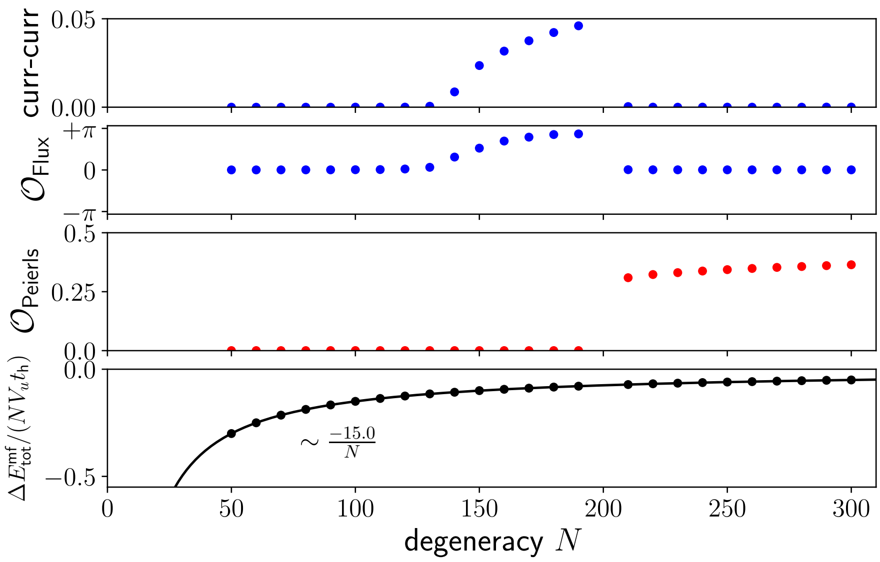

Figure 5.10: Stationary values of the order parameters after the warm-up shown in Fig. 5.9. $\Delta E^{\text{mf}}_{\text{tot}} = E_{\text{tot}} - E^{\text{mf}}_{\text{tot}}$ measures the amount of correlation energy that is added to the system at time $t = 0$. We omit the data at $N = 200$ because they were not relaxed after time $1000 t_{\text{h}}^{-1}$. This figure is also published in [2]. Copyright (2022) by the American Physical Society.

We conclude that during the warm-up dynamics the system can transition out of the Peierls phase, which restricts the range of N to which this strategy can be applied. While the true ground state in the finite-N model can be expected to show a similar $\frac{1}{N}$ scaling of the correlation energy, the prefactors need not agree. In analogy to the case of the SU(N) Hubbard model, this behavior will in general give rise to a finite amount of excitation energy in the system. We assume that the equilibrium states of the finite-N model – at not too low N – will be made up of quasiparticles consisting of mean-field modes dressed by particle-hole excitations (akin to an RPA picture). Our analysis of the SU(N)-Hubbard model has shown that fTWA is able to reproduce such quasiparticle formation (at least for weak U) in principle. However, in contrast to the spatially uniform case of the Hubbard model, there is the additional complication of nearly-degenerate competing instabilities with different spatial structures in the Hubbard-Heisenberg model. The quasiparticles will depend on their respective mean-field "vacuum state". It is hence possible that the additional excitation energy (which will in general also scale like $\frac{1}{N}$) destabilizes the quasiparticle formation in the Peierls phase and drives the system into the nearly degenerate Flux phase or into the spatially uniform phase. To investigate this aspect more, an analytical calculation of the true $\frac{1}{N}$-corrections to the mean-field state is required.

In addition and less expected, the system size turns out to play an important role. We find that in a system with $V_u = 21 \times 21$ unit cells the dynamics does not reach a stationary Peierls state for values of $N \lessapprox 600$. The system transitions into the Flux or, at low N, into the Uniform phase. One aspect are generic finite-size effects: The mean-field states do depend on the number of k-modes and again, via the near-degeneracy of the two non-uniform phases, this can lead to shifts in the transitions. However, 242 lattice sites in the $V_u = 11 \times 11$ system is already a large number and it is not clear why such corrections should lead to a systematic destabilization of Peierls order. A more likely attempted explanation is related to the number of fluctuating variables, which increases with the system size because all $\rho_{k\pm,l\mp}$ fluctuate. Let us focus on the bond ρ_0 as an example, it is related to the momentum modes via Fourier transform: $\rho_{i0} = \frac{1}{V_u}\sum_{k,l} \mathrm{e}^{i(k-l)r_i} \rho_{kA,lB}$. (The additional phase factor due to the sublattice translation A to B is absorbed into $\rho_{kA,lB}$.) All $\rho_{kA,lB}$ are fluctuating variables. If we anticipate the translational invariance and average over all unit cells i, the bond ρ_0 only depends on the diagonal $\rho_{kA,kB}$. At initial time, according to (5.27), the following equation holds:

$$\rho_{kA,kB} = \mathrm{e}^{-i\varphi_k}\left(\rho_{k+,k+} - \rho_{k+,k-} + \rho_{k-,k+} - \rho_{k-,k-}\right) \tag{5.30}$$

The variables $\rho_{k+,k-}$ and, consequently, $(\rho_{k+,k-} - \rho_{k-,k+}) \sim \mathrm{Im}(\rho_{k+,k-})$ are fluctuating with random real and imaginary parts that are drawn from identical and independent Gaussian distributions. In particular, they will have random phases that can average to zero, in particular, if the number of variables becomes large. Since $\rho_{k+,k+}$ and $\rho_{k-,k-}$ are not fluctuating at time zero, the system will always stay close to the mean-field configuration at early times. At later times, especially when the fluctuating variables become more mixed due to the non-linear dynamics, complex phases will also interfere and average out more. This is, in principle, a desired dephasing effect, which is in accordance with amplitude-phase fluctuations that one expects in a quantum theory. They give rise to the corrections to the mean-field dynamics that have shown to yield the right prethermal distribution in the case of the interaction quench in the Hubbard model. In the case of the Hubbard-Heisenberg model with non-trivial spatial order, if the number of fluctuating variables becomes too large (e.g. for large system sizes), a possible effect is that the dephasing will also more and more average out spatial order, e.g. $\rho_0 \sim \sum_k \rho_{kA,kB}$ and $\rho_1 \sim \sum_k \mathrm{e}^{i\sqrt{2}k_x}\rho_{kA,kB}$ become identical. Additional constraints like $\sum_k \left(\rho_{kA,kA} + \rho_{kB,kB}\right) = \text{const.}$ prevent a complete suppression. It seems like one needs to balance the amount of fluctuating variables with the strength of their fluctuations. If a matrix is populated with large random entries on all off-diagonals, one cannot expect a meaningful "real space" structure upon Fourier transform. These aspects deserve a more thorough analysis in the future, especially with focus on the question if a more fine-tuned construction of a Wigner function will be able to better stabilize spatial order. It is, however, far from obvious how to do that.

We conclude for now that for $J = 15t_\mathrm{h}$ and a lattice with 11×11 unit cells we can use this approximative approach for the initial Wigner function down to values of about $N = 200$.

5.3 Quench Dynamics

As a first simple non-equilibrium protocol we consider quenches of the interaction strength J. We study both quenches within the same phase as well as quenches across the Peierls-Flux boundary and compare the order parameter dynamics. Another point of interest is to study the effect of finite-N corrections in a simple setup. Nevertheless, interesting phenomena can also already occur in mean-field theories. Quenches in BCS theories [277, 278, 279] have displayed complex behavior like synchronization or Landau damping. Bose-Hubbard models are known to display dynamical transitions in their mean-field limit [132].

5.3.1 Mean-field dynamics

Before we discuss the mean-field results, let us start with a remark on the numerical solution of the equations of motion. One finds that a straightforward implementation in position space can lead to numerical instabilities, which are due to the finite floating point accuracy and to the non-linear structure of the equations. Spatially homogeneous protocols like quenches give rise to a lot of additional symmetries throughout the dynamics due to the preserved translational invariance of the system. The finite numerical accuracy can lead to small spatial inhomogeneities in the initial state, which grow exponentially during the time evolution with the non-linear equations of motion. A solution to this problem is to remove the artificial redundancy of dynamical variables and to go to a hybrid position-momentum representation of the equations of motion. The translational invariance of the system implies that the one-particle reduced density matrix always remains diagonal in momentum space: $\rho_{kl} \sim \delta_{kl}$. Using labels A and B for the sites within one unit cell, we obtain the following equations of motion if we transform to momentum space with respect to the unit cell lattice indices:

$$\begin{aligned} i\partial_t \rho_{kA,lA} = -i\partial_t \rho_{kB,lB} &= \delta_{k,l}\left[t_k \rho_{kA,kB} - t_k^* \rho_{kB,kA}\right] \\ i\partial_t \rho_{kA,lB} &= \delta_{k,l}\left[t_k^*(\rho_{kA,kA} - \rho_{kB,kB}) + 2U(\rho_B - \rho_A)\rho_{kA,kB}\right] \\ i\partial_t \rho_{kB,lA} &= \delta_{k,l}\left[t_k(\rho_{kB,kB} - \rho_{kA,kA}) + 2U(\rho_A - \rho_B)\rho_{kB,kA}\right], \end{aligned} \tag{5.31}$$

where

$$\begin{aligned} t_{\vec{k}} = 2t\Bigg(&\cos\left(\frac{\sqrt{2}}{2}(k_x - k_y)\right) + \cos\left(\frac{\sqrt{2}}{2}(k_x + k_y)\right) \\ &- J\left(\rho_0^* \mathrm{e}^{-i\frac{\sqrt{2}}{2}(k_x+k_y)} + \rho_1^* \mathrm{e}^{i\frac{\sqrt{2}}{2}(k_x-k_y)} + \rho_2 \mathrm{e}^{i\frac{\sqrt{2}}{2}(k_x+k_y)} + \rho_3 \mathrm{e}^{-i\frac{\sqrt{2}}{2}(k_x-k_y)}\right)\Bigg). \end{aligned} \tag{5.32}$$

The momentum vectors k_x, k_y are defined with respect to the tilted lattice of unit cells, not with respect to the original lattice. The instability problem can in principle also reoccur on the level of the unit cell, which in the Peierls phase has a reflection symmetry along the y-direction. In this case, one can reduce the number of dynamical variables even more. We note that the instabilities do not show up for the propagation of spatially inhomogeneous configurations (in particular with fluctuating initial conditions). In these cases there are no redundancies in the dynamical variables.

Let us now discuss the results. We start with J-quenches in the mean-field model $N \to \infty$. Fig. 5.11 shows results for the order parameter dynamics subsequent to quenches within the Peierls phase ($J = 15 \to 20$) as well as across the Peierls-Flux boundary ($J = 15 \to 5$ and $J = 5 \to 15$). In the mean-field model one can extract the Flux order parameter directly from the flux operator around the plaquettes. All quench combinations show undamped coherent oscillations of the order parameters. If the Flux order parameter is zero initially, it remains zero throughout. There are, however, qualitative differences in the oscillation patterns that develop after the quench. One finds that a quench within the Peierls phase leads to a relatively simple beat-like pattern, while the quenches across the phase boundaries are more complicated. Despite the simplicity of the mean-field approach, the non-linearity of the equations of motion can give rise to a complex dynamical response, even without a relaxation mechanism. It is in fact also difficult to obtain analytical insights: If one is interested in the dynamics of the bond variable ρ_0, one may start from $\rho_0 = \frac{1}{V_u}\sum_k \rho_{kA,kB}$ and apply the hybrid momentum-position representation of the equations of motion:

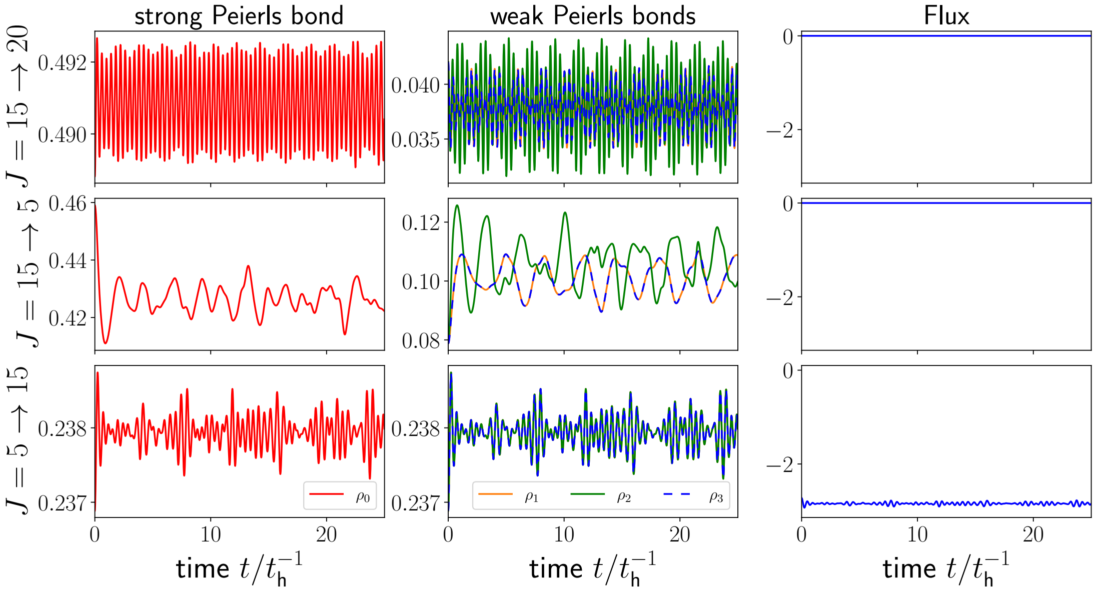

Figure 5.11: Mean-field order parameter dynamics upon quenches of the interaction strength J in a system with $V = 41 \times 41$ unit cells. The left column shows the strong bond ρ_0 of the Peierls phase, while the middle column contains the results for the three weak bonds. The right column shows the Flux order parameter phase angle $\mathrm{e}^{i\Phi}$.

$$i\partial_t \rho_0 = \frac{1}{V_u}\sum_k t_k^*\big(\rho_{kA,kA} - \rho_{kB,kB}\big) \tag{5.33}$$

The A/B-diagonal variables again couple to the non-diagonal ones but the time dependence of $t_{\vec{k}}$ (via the bonds ρ_i) prohibits a closure of the equation:

$$-\partial_t^2 \rho_0 = \frac{1}{V_u} \sum_k \Big(\big(i\partial_t t_{\vec{k}}^*\big)\big(\rho_{kA,kA} - \rho_{kB,kB}\big) + 2t_{\vec{k}}^*\big(t_{\vec{k}}\rho_{kA,kB} - t_{\vec{k}}^*\rho_{kB,kA}\big)\Big) \tag{5.34}$$

To make progress, a linearization of the equations of motion or other tools like a stationary phase approximation analysis [278] are required. Nevertheless, to obtain a more detailed picture of the mean-field response to quenches, we take a look at the frequency spectrum of the oscillations numerically. In order to do so, we calculate the (discrete) Fourier transform of the bond strengths $\tilde{\rho}_i(\omega) = \mathcal{F}\big(|\rho_i(t)|\big)$ and plot the resulting power spectrum $|\tilde{\rho}_i(\omega)|^2$. The results for quenches within the Peierls phase are shown in Fig. 5.12. We varied the final state interaction strengths J_f to obtain some qualitative insights. The oscillation spectrum of the strong bond is dominated by one frequency, which scales linearly with J_f. The same is true for the main peak of the weak bonds, while the second peak approaches the scaling for large J_f. This picture is consistent with the Peierls phase being a gapped phase, whose gap energy scale is mainly set by the dynamical J_f. The second peak in the power spectrum of the weak bond is likely due to corrections from the much smaller energy scale t_{h}, which becomes more and more irrelevant if $J_f \gg t_{\mathrm{h}}$. In the lower panel we can see that the frequencies of the oscillations do not depend on the initial state, while their amplitudes do. In contrast, for quenches from the Peierls to the Flux phase, one finds, next to one main peak, more frequencies that contribute. The most extreme case is presented by the quench in the opposite direction, starting from the Flux phase. In this case a full continuum of frequencies is present, although one has to keep in mind that the real space oscillations are quite weak and therefore the power spectrum has very low amplitudes as well. These results involving the Flux phase agree with its

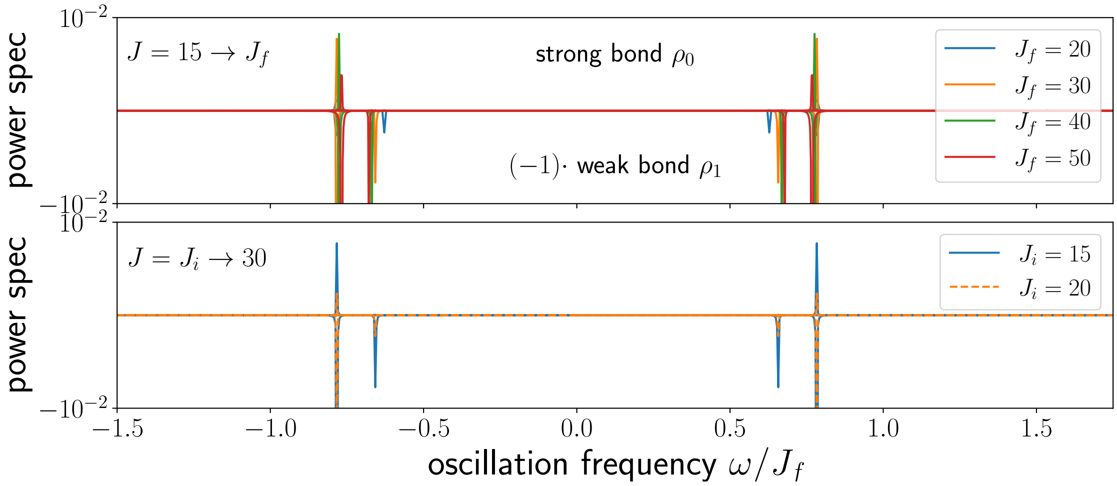

Figure 5.12: Power spectrum of the mean-field oscillations of the bond strengths after quenches within the Peierls phase. The x-axis is rescaled with the respective final state interaction strengths J_f. Upper panel: Quenches from $J_i = 15$ to values $J_f = 20, \dots, 50$. Lower panel: Quenches to $J_f = 30$ starting from two different initial values J_i. All data is obtained for a system with 41×41 unit cells.

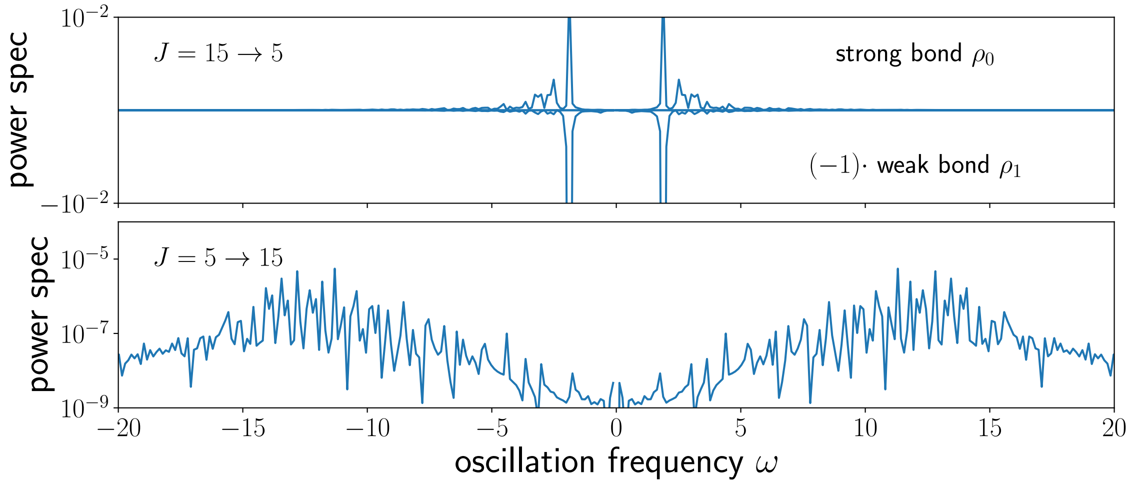

Figure 5.13: Power spectrum of the mean-field oscillations of the bond strengths after quenches across the first order phase transition between Peierls and Flux phase. Upper row: quench Peierls to Flux, lower row: quench Flux to Peierls. All data is obtained for a system with 41×41 unit cells.

gapless spectrum: the dominant energy scale is less obvious and many frequencies can contribute.

5.3.2 Finite-N dynamics

While the oscillation spectrum of the mean-field quenches already contains some information about the properties of the post-quench system, the mean-field oscillations can never reach a stationary state and a true transition is impossible. We now include the effect of dephasing corrections and turn to the results for quenches in the Hubbard-Heisenberg model with $N < \infty$. We always use the N-quench initial state preparation strategy outlined in the previous section. The parameter quench is only executed after a waiting time of $250t_{\mathrm{h}}^{-1}$ when the order parameters have become stationary. In Fig. 5.14 we show results for quenches within the Peierls phase and from the Peierls phase into the Flux phase for a model with $N = 300$. The deviations from the mean-field case are dramatic: In the Peierls to Peierls case, the bond oscillations are damped out, as can be seen from the inset. In addition, the bond order parameter values decay into new stationary states, which are also clearly Peierls-like. In the case of a quench across the phase boundary starting from the Peierls phase, the order parameter oscillations are damped as well and all the bond strengths become equal. In addition, we find that the current-current correlator indicates the formation of Flux order already very shortly after the quench. The results are encouraging and give a consistent picture: The semiclassical corrections due to fTWA allow the system to decay into a different minimum of the free energy. In analogy to the interaction quench in the Hubbard model, we can interpret these stationary states as prethermal order.

In Fig. 5.15 we compare the order parameter decay for varying values of N. The first observation is that the numerical data perfectly obeys an exponential decay law. This is true for both the strong and the weak bonds. Secondly, the temporal decay constant clearly follows a linear scaling $\tau \sim N$, i.e. the order parameter decays like

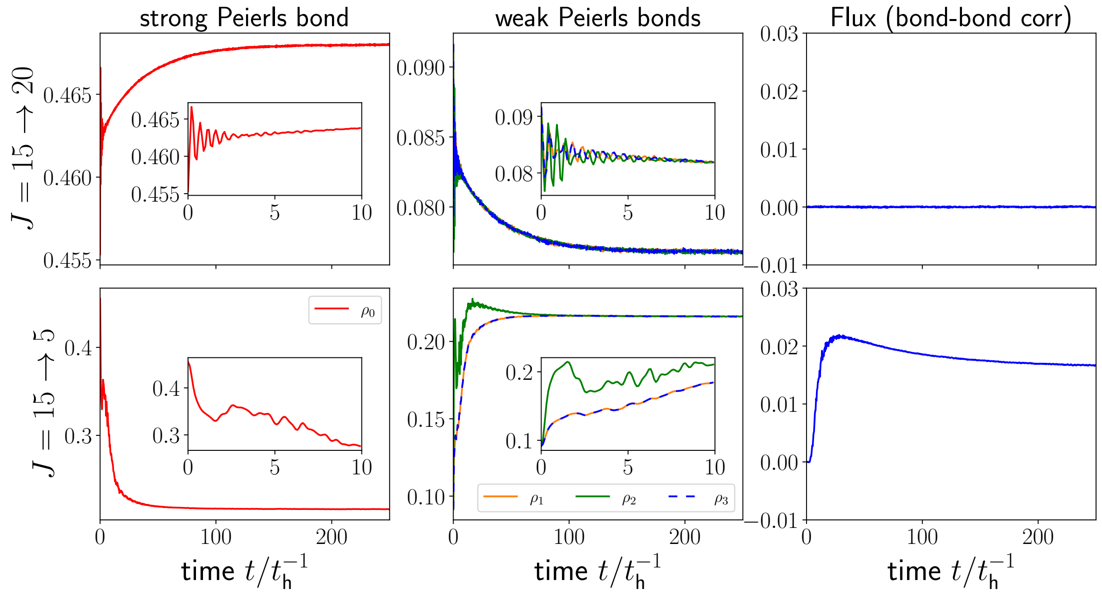

Figure 5.14: Quench dynamics in a system with $V_u = 11 \times 11$ unit cells. $N = 300$. Time zero in the figure corresponds to 250 time units after the start of the initial state preparation procedure. The left and the middle column show the dynamics of bond strengths, while the right column shows the dynamics of current-current correlators as a measure of the Flux order.

$\mathrm{e}^{-t/N}$. This is an interesting observation since it indicates a universal behavior of the order parameters in the large-N regime. Put differently: To obtain qualitative insights beyond mean-field it is sufficient to select a suitable value of N, which is "large enough".

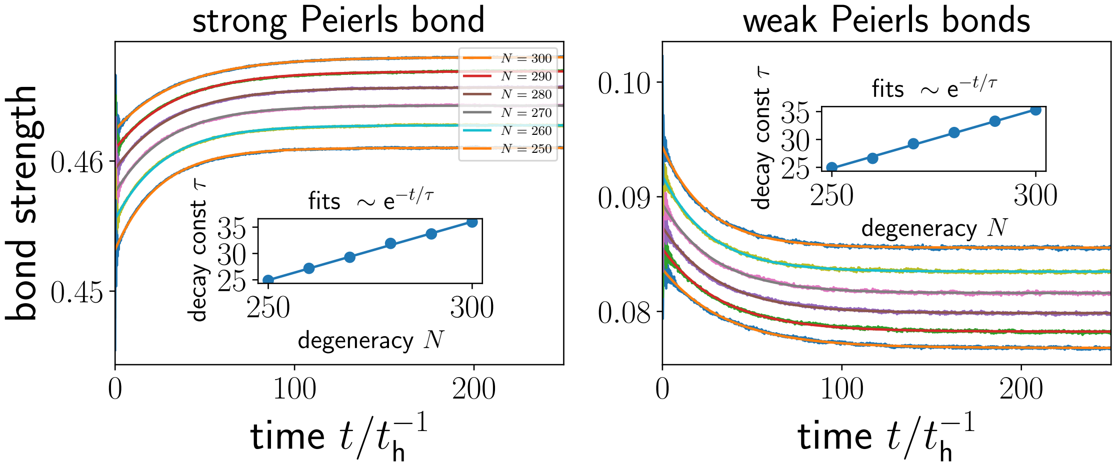

Figure 5.15: Quench $J = 15 \to 20$ within the Peierls phase. Scaling of the bond decay for varying values of N. The system size is 11×11 unit cells.

5.4 Photoinduced Dynamics (cf. [2])

Now we turn to the dynamics induced by a time-dependent electromagnetic field $E(t)$ using the Peierls substitution technique [118], which describes a classical electromagnetic field (i.e. no quantized photons). Within this approach the hopping matrix element acquires a time-dependent complex phase $t_{\mathrm{h}}\mathrm{e}^{iA_i(t)}, i \in \{x, y\}$, where $A_i(t)$ is the vector potential. It is related to the electric field $E_i(t) = -\partial_t A_i(t)$ but for simplicity we concentrate the discussion on the vector potential itself. We consider linearly polarized pulsed driving amplitudes of the form

$$A_i(t) = A_i^{\max}\mathrm{e}^{-\frac{1}{2\sigma^2}(t-t_0)^2}\sin\big(\omega(t-t_0)\big). \tag{5.35}$$

We will always work at a fixed pulse width $\sigma = 4/t_{\mathrm{h}}$. In the two-dimensional model there is an additional freedom of choice for the polarization direction. For initial Peierls states there are two special directions: along or orthogonal to the strong bond. We will mostly orient the vector potential along the direction of the strong bond ($A_x = 0, A_y \neq 0$) and for comparison orthogonal to it ($A_x \neq 0, A_y = 0$). The equations of motion with Peierls substitution incorporated read

$$\begin{aligned}\partial_t \rho_{ij} = &\sum_{a(i)} \big(it\mathrm{e}^{-i\varphi_{i,a(i)}(t)} + (-iJ)\rho_{i,a(i)}\big)\rho_{a(i),j} \\ &- \sum_{a(j)} \big(it\mathrm{e}^{-i\varphi_{a(j),j}(t)} + (-iJ)\rho_{a(j),j}\big)\rho_{i,a(j)} \\ &+ 2U(\rho_{jj} - \rho_{ii})\rho_{ij},\end{aligned} \tag{5.36}$$

where $\varphi_{i,j}(t) = \int_{\vec{r}_i}^{\vec{r}_j} \vec{A}(\vec{r}, t)\, \mathrm{d}\vec{r} = \vec{A}(t) \cdot \big(\vec{r}_j - \vec{r}_i\big)$

5.4.1 Mean-field dynamics $N \to \infty$ (cf. [2])

We again start with time-dependent mean-field theory. It corresponds to setting the variance of the Gaussian Wigner function to zero and to consider only a single trajectory. For now we set $U = 0$. Fig. 5.16 shows exemplary results for the order parameter dynamics with two different values of the driving amplitude A_y. In both cases there are undamped coherent oscillations of the bonds and of $\mathcal{O}_{\mathrm{Flux}}$ subsequent to the pulse. It illustrates that within mean-field theory for the Hubbard-Heisenberg model one does not reach a stationary state on the timescales considered here due to the absence of dephasing and collisions (however, this statement is not generally true for all mean-field theories [277, 278, 279]).

Nevertheless, the system can absorb energy and it is possible to induce Flux order parameter oscillations around a non-vanishing average value. However, the averaged absolute values of the bonds need not match with the saddle point symmetries of the equilibrium phases (e.g. all equal in the Flux phase) as can be seen in the right column.

Fig. 5.17 allows for a more systematic look at the energy absorption. In (a) we vary the driving amplitude for some fixed values of the frequency ω. All curves in the figure display similar behavior: There is almost no energy absorption up to a frequency-dependent threshold amplitude.

This is a very interesting finding since it allows to draw a connection to results in the context of dielectric breakdown in Mott insulators [280, 281]. Dielectric breakdown refers to the destruction of an insulating state upon the application of an electric field [280, 282] or a voltage bias between interacting leads [283]. An important contribution is due to Takashi Oka [284], who calculated the doublon production rate Γ in a

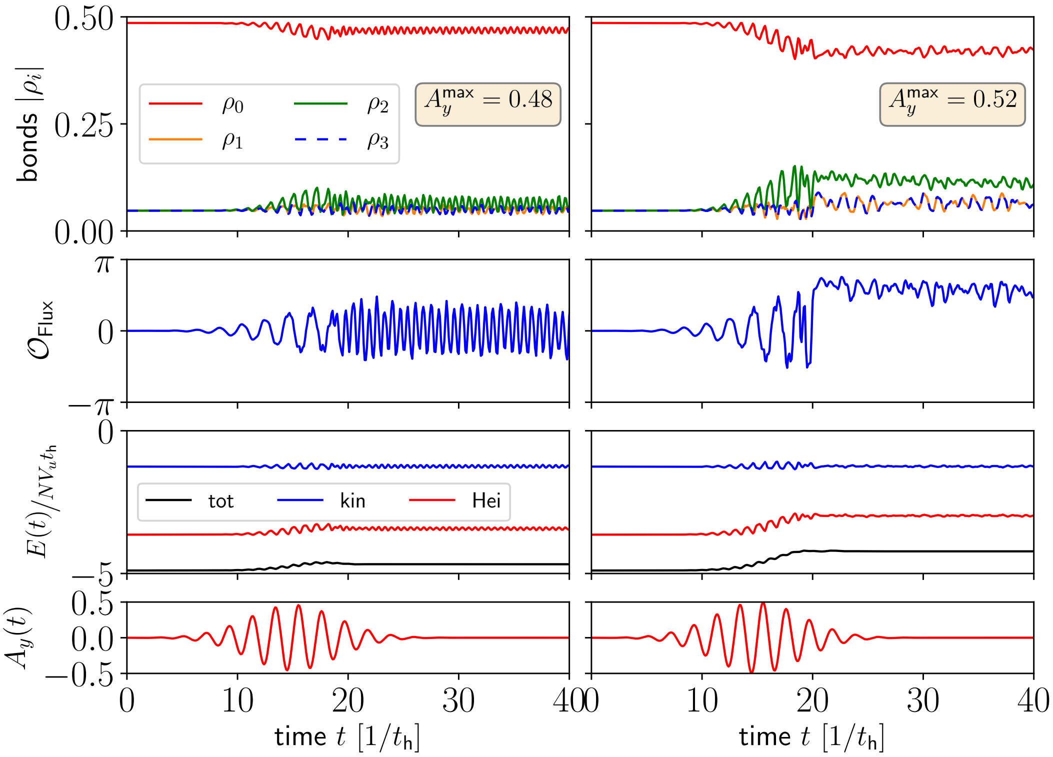

Figure 5.16: Mean-field dynamics of order parameters in the photoexcited Hubbard-Heisenberg model with $J = 15t_h$, $U = 0$ and $V_u = 41 \times 41$ unit cells. Left: Pulse amplitude of $A_y = 0.48$ yields oscillations of $\mathcal{O}_{\text{Flux}}$ around average value zero. Right: Pulse amplitude of $A_y = 0.52$ excites oscillations around non-vanishing average. This figure is also published in [2]. Copyright (2022) by the American Physical Society.

Hubbard model, which is driven by a sinusoidal electric field $E(t) = E_0 \sin(\omega t)$, using a generalization of the Landau-Zener model for diabatic single-particle transitions. This so-called *Landau-Dykhne method* predicts a threshold behavior for the doublon production rate [284] $\Gamma \sim e^{-\pi E_{\text{th}}/E_0}$ in the low frequency regime, where the dc threshold field $E_{\text{th}} = \Delta_{\text{Mott}}/(2\xi)$ is directly related to the Mott gap Δ_{Mott}. ξ is a doublon-holon correlation length. A consequence of this last expression is that one can view the threshold field as a constant of the model. In this thesis we work in units of the vector potential amplitude, so we can approximately expect that $\omega A_0^{\max,\text{th}} = \text{const}$. In Fig. 5.18 we plot the absorbed energy as a function of $\omega A_0^{\max}$ for small driving frequencies. One can indeed observe that the threshold regimes of the curves collapse very well, which is in agreement with the prediction of Landau-Dykhne theory. The threshold regime is characterized by quantum tunneling processes from the lower to the upper Mott band [284]. It is an interesting observation that in our model with a density wave insulator one can observe the scaling as well within Hartree mean-field theory.

Returning to the discussion of Fig. 5.17, we find that above the tunneling regime the total energy develops oscillatory patterns as a function of the driving amplitude. We found that – in contrast to the threshold regime – the precise shape of these patterns can depend on the system size. They are clearly remnants of the mean-field theory. Nevertheless, we checked that the averaged trends in the data are consistent for

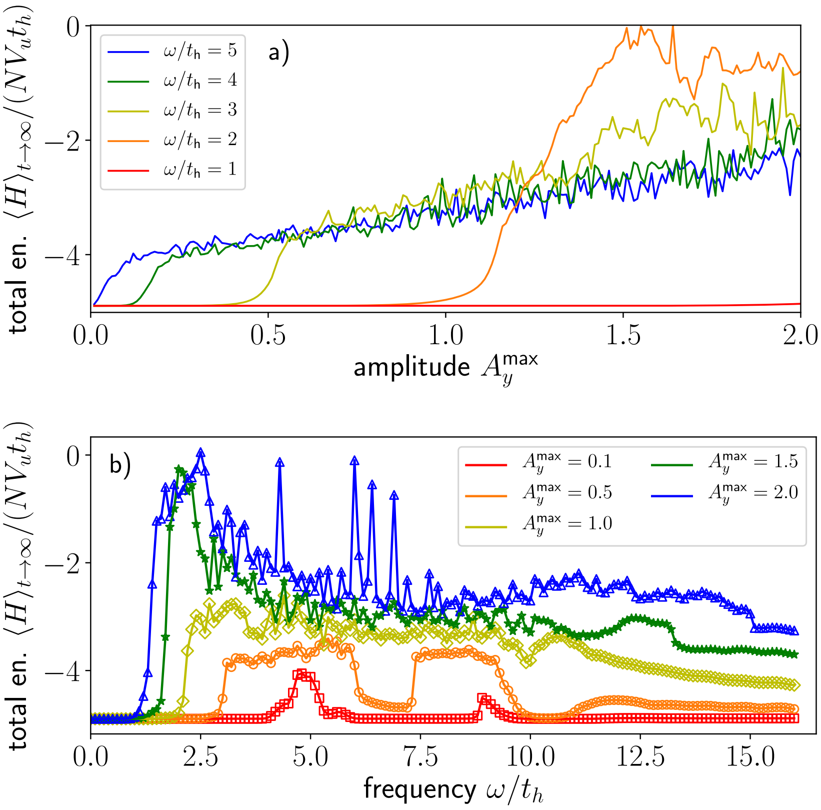

Figure 5.17: Energy absorption (mean-field dynamics) after a Gaussian pulse with $A_x = 0$, $A_y \neq 0$ in a Hubbard-Heisenberg square lattice with $V_u = 41 \times 41$ unit cells, $J/t_\mathrm{h} = 15$ and $U = 0$. (a) post-pulse total energy (per unit cell) plotted against the pulse amplitude. Energy absorption is efficient only beyond a frequency-dependent threshold amplitude. (b) total energy plotted against the driving frequency for fixed values of the amplitude. At small amplitudes two absorption peaks are visible. This figure is also published in [2]. Copyright (2022) by the American Physical Society.

different system sizes. A way to make sense of this is to think about the Peierls phase as a minimum in a free energy landscape [34] that is separated from other regions, e.g. the Flux phase minimum, by barriers. If the system is only weakly excited, order parameter oscillations around the immediate vicinity of the Peierls phase minimum are induced. At and beyond the threshold amplitude other regions of the landscape become accessible. The free energy (5.20) contains a discrete crystal momentum sum over the ϵ_k, which leads to an oscillatory fine structure of the mean-field free energy as a function of the bond operators and thereby likely affects the energy absorption if the system leaves the initial minimum. In the finite-N case, however, this fine structure will average out over many trajectories and so we do expect the system size to play a less significant role there. In Fig. 5.17(b) the roles of frequency and amplitude are exchanged. We observe two main peaks of the absorption at small amplitudes. This is reminiscent of results reported for a driven non-interacting two-band model [285]. The authors plot the occupation of the upper band against ω and observe a multi-peak structure. In their paper the main peak position corresponded to the

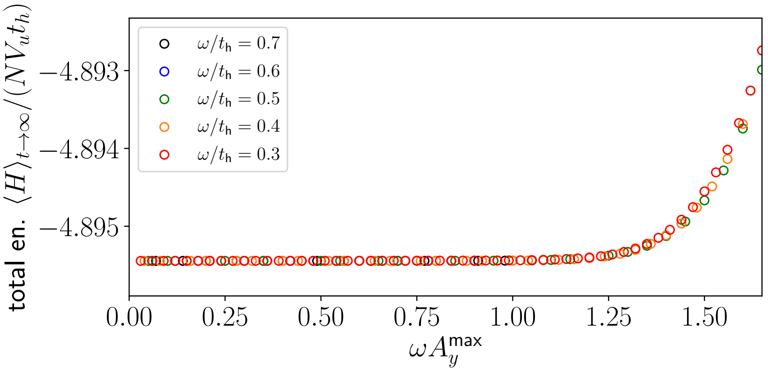

Figure 5.18: Energy absorption for small driving frequencies plotted against $\omega A_0^{\mathrm{max}}$, which is approximately equal to the field amplitude. The data is obtained in the mean-field model with 41 × 41 unit cells. The observed scaling is in qualitative agreement with the prediction from Landau-Dykhne theory.

band gap and the existence of amplitude-dominated and frequency-dominated driving regimes are proposed. It is not clear if similar arguments apply here since our band structure is not static and multiple phases with different single-particle spectra exist. The gap in the single-particle energy spectrum of the Peierls phase shown in Fig. 5.2 is larger than the peak positions observed in Fig. 5.17(b). However, the mean-field band structure approximates the electron addition-removal spectrum and does not necessarily describe single-particle excitations, which can well occur at a lower energy. For driving amplitudes $A_y^{\mathrm{max}} \gtrapprox 1$ the double peak structure disappears and some, sporadically large, oscillations occur. These are again most likely due to the discrete k-space structure and will average out if multiple trajectories are used.

5.4.2 Finite-N model: mean-field + dephasing (cf. [2])

In this section we refine the previous discussion by including dephasing dynamics with fTWA. This allows us to describe the formation of prethermal order subsequent to the pulse. In the following we will always work on a lattice with periodic boundary conditions and $V_u = 11 \times 11$ unit cells, i.e. $V = 2V_u = 242$ lattice sites. We keep $J/t_\mathrm{h} = 15$, $U = 0$ and prepare the system in the initial state (5.26) as outlined in the Method section assuming that a stationary Peierls state is reached after a time of about $200t_\mathrm{h}^{-1}$ (cf. Fig. 5.9). We center the pulse at $t_0 = 250t_\mathrm{h}^{-1}$. When we calculate the Flux order parameter $\mathcal{O}_{\mathrm{Flux}}$ directly, we always turn on a weak symmetry breaking $\epsilon_{\mathrm{Flux}} = 10^{-3}$. Peierls order parameters and current-current correlators are calculated without symmetry breaking field.

In Fig. 5.19 we show the time evolution of order parameters in an exemplary way for $\omega = 3t_\mathrm{h}$ and three values of the driving amplitude A_y along the direction of the strong bond. Time zero in the panels is set to $t_0 - 15t_\mathrm{h}^{-1}$. In contrast to the $N \to \infty$ case, coherent order parameter oscillations subsequent to the pulse are damped out and a stationary state is reached. Note that $|\rho_1| = |\rho_3|$ at all times, i.e. the spatial symmetry of the initial state and of the applied vector potential along the y-direction is preserved throughout the dynamics. The three driving amplitudes generate final

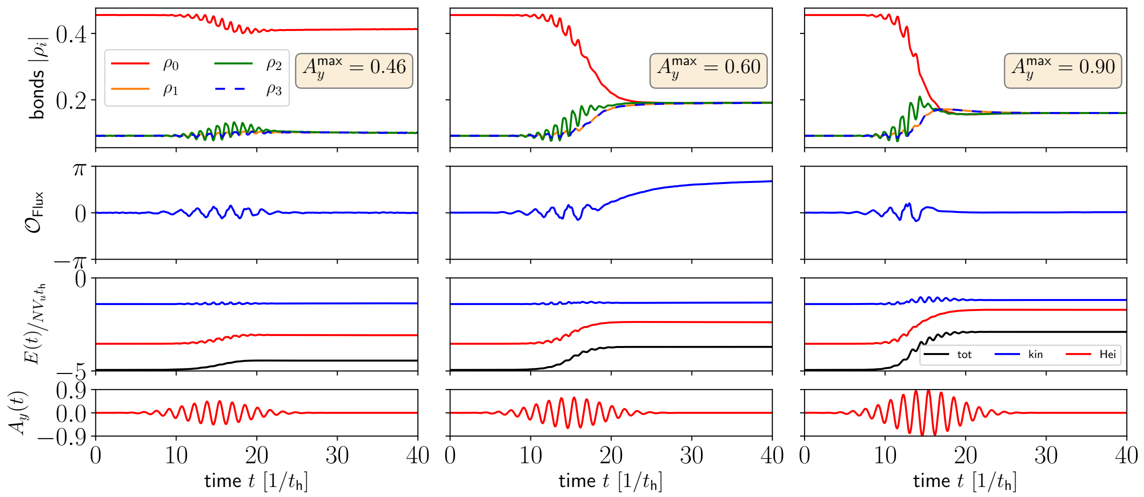

Figure 5.19: Dynamics of the order parameters during and subsequent to a photoexcitation in the Hubbard-Heisenberg model with $N = 300$ and for $V_u = 11 \times 11$ unit cells. The frequency of the sinusoidal drive is $\omega/t_h = 3$. The three columns represent three different maximum amplitudes of the vector potential $A_y(t)$ (i.e. fluences). The dynamics leads to transitions within the Peierls phase (left), from the Peierls phase to the Flux phase (middle) and to the uniform phase (right). This figure is also published in [2]. Copyright (2022) by the American Physical Society.

states corresponding to the three equilibrium phases at half filling: After weak driving the system remains in the Peierls phase with a smaller order parameter than in the initial state. For intermediate amplitudes the Flux order parameter becomes nonvanishing and the system is Flux-ordered, while strong driving pushes the system into the Uniform phase. The symmetries of the stationary state observables agree with the saddle point expectations. We further observe that the post-pulse order parameter dynamics can continue even if the total energy is already at its stationary value.

5.4.3 Convergence of the simulations

A conclusion of Chapter 4 on the interaction quench in the Hubbard model was that a large number of samples is needed to converge the fTWA simulations to the perturbative prethermalization result. This traces back to the fact that in this case averaged quantities of interest, in particular the Fermi surface discontinuity $\Delta n_{k_F}(t)$, are of equal magnitude to the fluctuations themselves: both scale with $\frac{1}{N}$. The situation is different for the observables of interest considered here since the leading order mean-field contribution to the order parameters is independent of N. The Flux order parameter and the current-current correlator depend on complex phases, which can lead to a more intricate and less obvious dependence on N. However, we observed that if the bond order parameters are sufficiently converged, so are the quantifiers of Flux order. The main role of the quantum fluctuations in the Hubbard-Heisenberg model is to give rise to a dephasing-induced decay of order parameters into stationary states.

To judge the convergence of the simulations, we used, firstly, the generic Monte Carlo sampling error of expectation values discussed in Chapter 2, which is based on

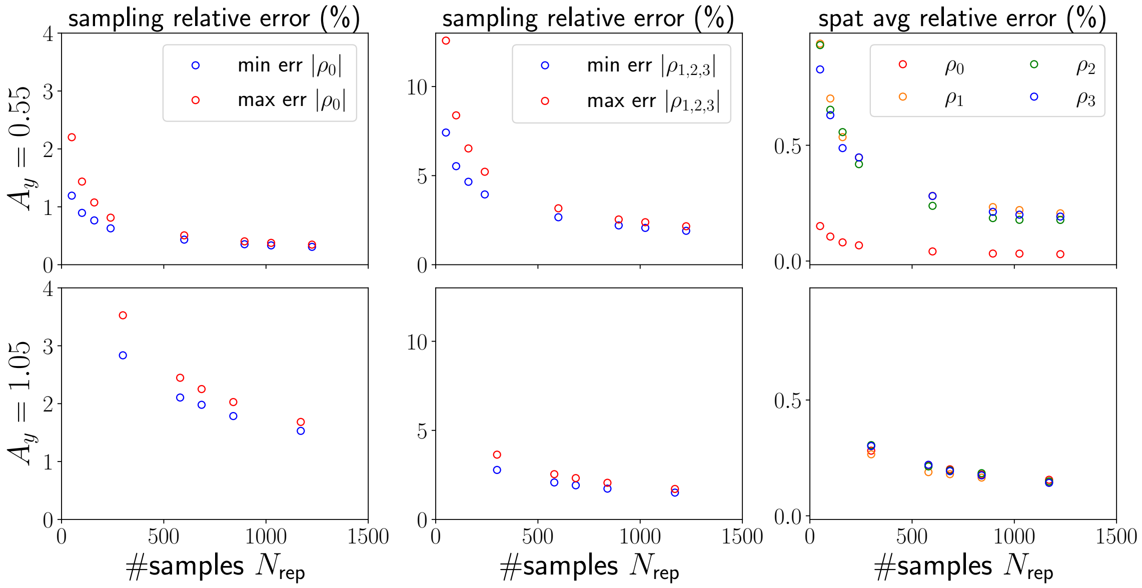

Figure 5.20: Exemplary error estimates of the TWA sampling procedure for a photoexcitation with $\omega/t_{\text{h}} = 12$ and two values of the vector potential A_y at time $t = 500t_{\text{h}}^{-1}$ (upper row: system remains in Peierls phase, lower row: transition to Flux phase). First two columns: Sampling error of the bond strengths based on the empirical variance of the set of N_{rep} trajectories. Right column: Relative error of the spatial average over all translationally invariant unit cell bonds.

the empirical variance σ^2_{emp} of the finite set of samples and is defined as $1.96\sigma_{\text{emp}}/\sqrt{N_{\text{rep}}}$. Secondly, we made use of the fact that we mostly consider observables $O := \frac{1}{V_u}\sum_i O_i$, which are averaged over all unit cells. Since in momentum space all fluctuating entries of the one-particle reduced density matrix are sampled from independent probability distributions at initial time, we may view its real space entries, e.g. the nearest neighbor bonds, as well as independent random numbers. Hence, the error of the mean over all unit cells is a second useful indicator of convergence. In Fig. 5.20 we show these two error estimates for the bond order parameters in two exemplary cases with different vector potential amplitudes. The first two columns show the relative (i.e. divided by the mean) Monte Carlo sampling error of the bond strengths in one unit cell. This data is not averaged over all unit cells. Instead, we plot the largest and the smallest error that we found in any of the unit cells. This is meant as a very rough estimate of error, which we find to be in the range of at most 2% if at least 1000 trajectories are averaged over. However, taking the average over all unit cells additionally suppresses the expected error by a factor of $1/\sqrt{V_u}$. In the rightmost column of the figure, we plot the relative error of the mean $\sim 1.96\sigma_{\text{emp,all}\rho_i}/\sqrt{V_u}$ of the set of equivalent bond strengths in all unit cells as a function of the number N_{rep} of trajectories. Since we expect the system to be translationally invariant if averaged over infinitely many trajectories, this quantity is another measure of error. For a few hundred samples we find it to be below 0.5%, which is already good accuracy. This estimate is well consistent with the relative sampling error divided by $1/\sqrt{V_u}$. In practice, we use at least 1000 trajectories in most cases to obtain the data discussed below.

5.4.4 Comparison of different values of N

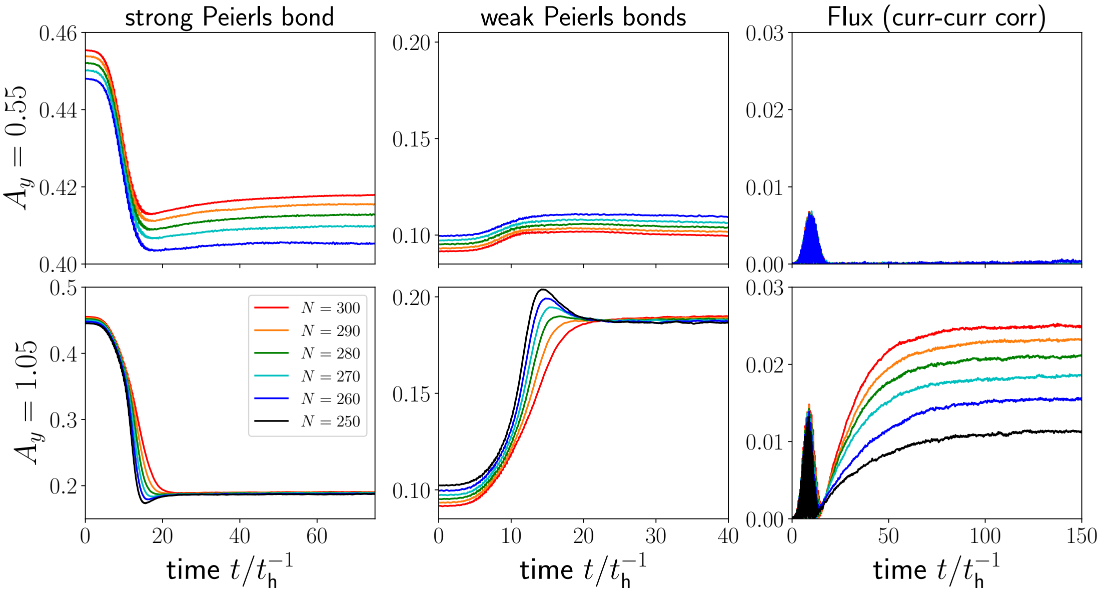

Figure 5.21: Order parameter dynamics after a photoexcitation with $\omega/t_\mathrm{h} = 12$ and two values of the vector potential amplitude A_y^max.

In Fig. 5.21 we compare the order parameter dynamics during and subsequent to a y-polarized photoexcitation with $\omega/t_\mathrm{h} = 12$ (same parameter set as in the preceding convergence section) for varying values of N. Overall, the picture is similar to the quenched case: lower values of N imply smaller values of the final state order parameters. The ordering dynamics is slightly more complicated in the case of a transition from Peierls to Flux phase since the values of the bond strengths overshoot their stationary final values. Nevertheless, their dynamics is faster if N is smaller, which is consistent with the results from the quench dynamics.

5.4.5 Prethermal dependence on drive parameters (cf. [2])

In this section we study the influence of drive parameters like frequency, amplitude and polarization direction on the post-pulse order parameters. Before we discuss the results, a comment on the dynamics after the photoexcitation is in order. For most of the parameters, the system evolves as shown in Fig. 5.19: a stationary state is reached quickly after the end of the pulse. However, for parameters close to the transition from Peierls to Flux order, we observe that the dynamics can become very slow. This is in agreement with the picture that a new minimum of the free energy becomes accessible but the tunneling between the minima is inefficient if the free energy difference is small. Fig. 5.22 shows an extreme case of this phenomenon: The current-current correlator of bond ρ_0 slowly increases while the gap between the bonds decreases. For infinite waiting time we expect the system to relax to a purely Flux-ordered state. This would be the anticipated behavior for a competing orders scenario. For practical reasons, we only carry out simulations up to a total time of $500t_\mathrm{h}^{-1}$. Therefore, we will always determine the order parameter values at this latest simulation time instant for the

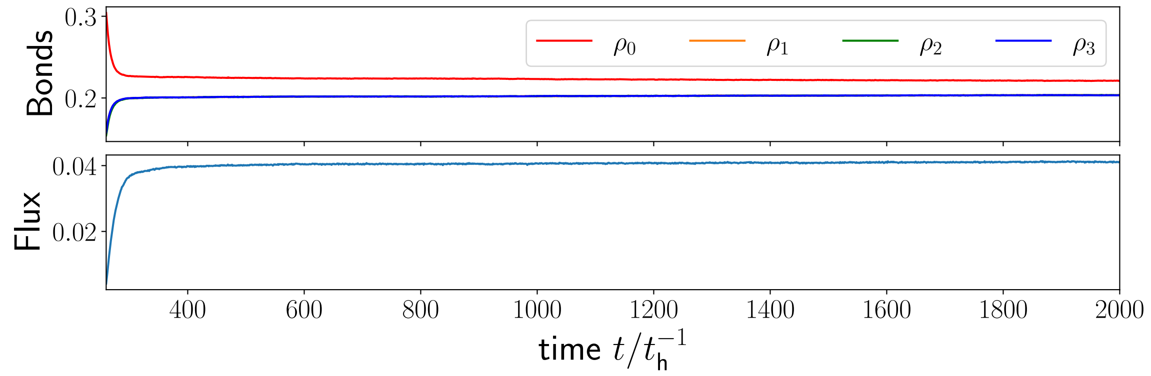

Figure 5.22: Very slow dynamics of order parameters after a photoexcitation with $\omega/t_{\mathrm{h}} = 8$ and $A_y = 0.35$. The pulse is centered at time $t = 250t_{\mathrm{h}}$.

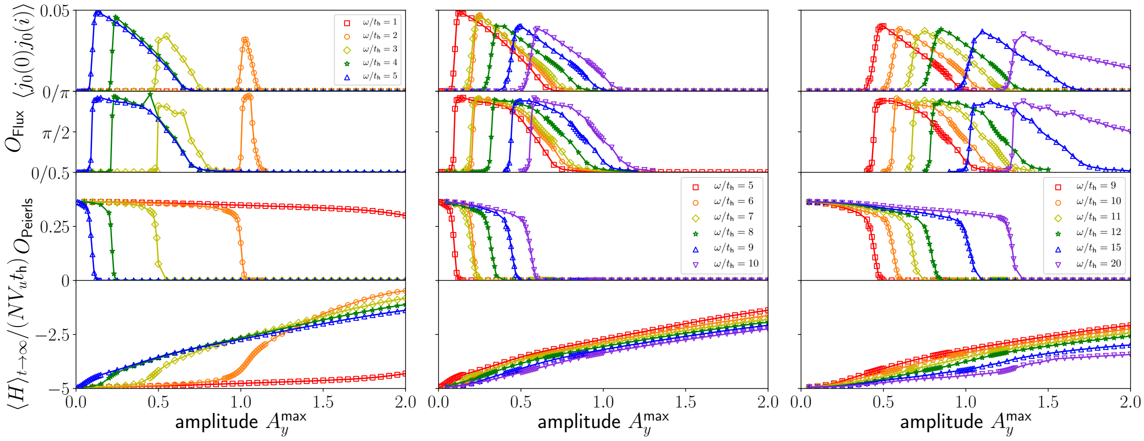

Figure 5.23: Late-time stationary values of the order parameters after photoexcitation with varying frequencies ω plotted against the amplitude of the vector potential $A_y^{\max}$. The top row shows current-current correlators of ρ_0 for two unit cells with the largest spatial separation in the system (averaged over all unit cell pairs related by translational symmetry). The three columns correspond roughly to three different frequency regimes (see text). The data in this figure is obtained for a 11×11 unit cells Hubbard-Heisenberg model with $J = 15t_{\mathrm{h}}$ and $U = 0$. This figure is also published in [2]. Copyright (2022) by the American Physical Society.

following discussion. However, we need to keep in mind that for longer waiting times the Peierls to Flux transition will become sharper.

Fig. 5.23 presents the numerical results as a function of A_y for varying drive frequencies ω. In the uppermost row we plot the current-current correlation function for one of the bonds in a unit cell (the strong bond of the Peierls phase), which displays a sharp transition from Peierls to Flux and a broad transition range from Flux to Uniform order. The Flux order parameter $\mathcal{O}_{\mathrm{Flux}}$ agrees well with the correlator data except for deviations at low frequencies $\omega/t_{\mathrm{h}} \leq 4$ and energies $-4 \leq E/t_{\mathrm{h}} \leq -3.5$. These deviations depend on the choice of the flux symmetry breaking strength and indicate that a slightly larger ϵ_{mn} might be needed in this regime. Current-current correlators are thus the more robust quantifiers of Flux order.

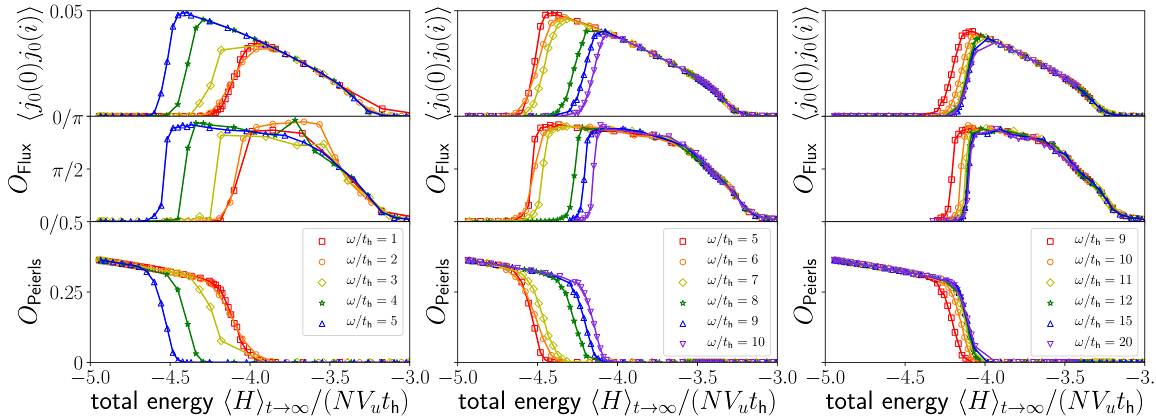

Figure 5.24: Same data as in Fig. 5.23 but all final state order parameters are plotted against the total energy. In the first and third column the order parameters display a similar behavior for very low and very high frequencies. In the middle column there is a clear influence of the driving frequency on the order parameter characteristics. This figure is also published in [2]. Copyright (2022) by the American Physical Society.

One can roughly identify three frequency regimes, which correspond to the three columns. At low values of the frequency $\omega \lessapprox 5t_{\text{h}}$, there is a threshold amplitude – analogous to the mean-field case but shifted to lower amplitudes – at the transition from Peierls to Flux order. The transition moves to lower amplitudes if the frequency increases. For $\omega = 5t_{\text{h}}$ the Peierls order parameter starts to decrease already at very low field amplitudes, which indicates that the drive is likely resonant with an elementary excitation of the system. At higher frequencies, in the middle and right columns of the Figure, there is no threshold amplitude any more and the electrons absorb energy also for small values of A_y. In these regimes, we find that the energy absorption decreases with increasing driving frequency. This agrees with the physical expectation that energy absorption should be suppressed in the high-frequency regime due to the absence of available states for drive-induced transitions. However, one cannot read off the elementary excitations of the system directly from the mean-field band structure in Fig. 5.2: Still, the Peierls phase has a large gap, while the Flux phase is gapless – although thermodynamically they are almost degenerate. One way to obtain a more detailed understanding of elementary excitations of the system would be to consider quantities like non-equilibrium spectral functions [5], which is beyond the scope of this work.

Fig. 5.25 is the finite-N analogue to Fig. 5.17. In contrast to the mean-field model, it is possible to extract final state order parameter information. Looking at the total energy, we find that, consistent with intuition, it also increases when the amplitude is raised. At low frequencies one finds a sharp absorption edge that corresponds to a transition from the Peierls to the Flux phase. In the frequency regime $4 \leq \omega/t_{\text{h}} \leq 10$ energy is already absorbed at low field amplitudes, which gives rise to a reduction of the Peierls order. The generic behavior at large driving frequencies is a suppression of the energy absorption.

Naturally, a question raised by the stationary states of Fig. 5.19 is whether the post-pulse order could as well be a result of heating. In particular, the mean-field

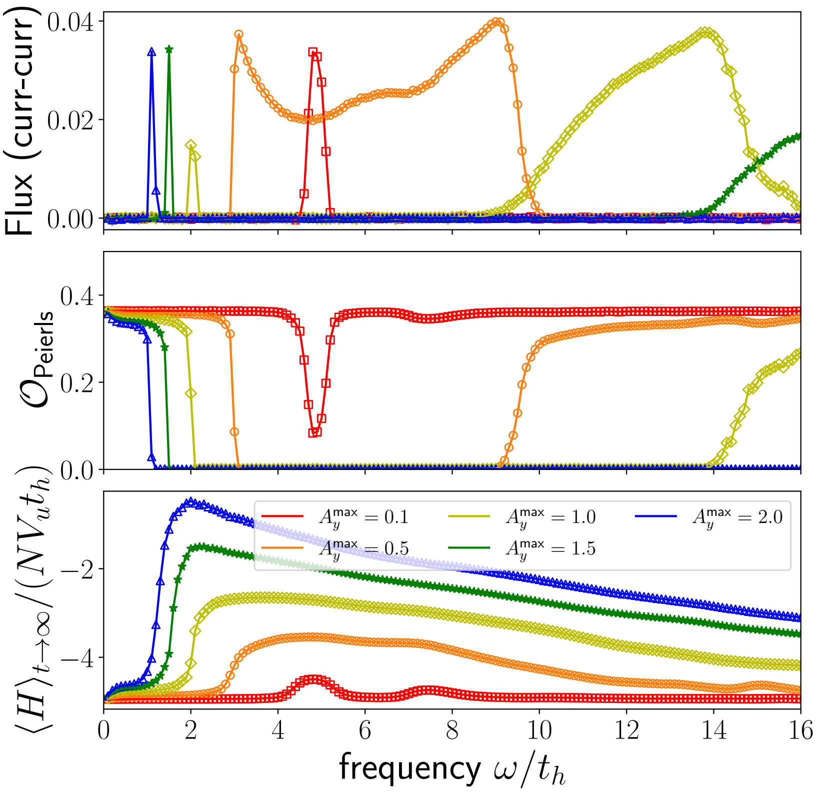

Figure 5.25: Energy absorption and order parameters as a function of the driving frequency for fixed amplitudes $A_y^{\max}$ of the y-polarized vector potential. All data is obtained in a Hubbard-Heisenberg system with 11×11 unit cells and at $N = 300$. The Flux phase order parameter is obtained from the current-current correlator.

finite-temperature equilibrium phases in Fig. 5.4 follow the same sequence Peierls to Flux to Uniform as a function of temperature. To shed more light on this question we plot the order parameters of Fig. 5.23 directly against the total energy of the system after the pulse, shown in Fig. 5.24 and again grouped by frequency. At very low and high energies, the order parameters follow universal lines, independent of ω. The transition from Peierls to Flux order, in contrast, depends explicitly on the driving frequency. The fact that not all curves lie on top of each other indicates the non-thermal nature of the stationary states. Let us look at the regime of low driving frequencies. As the total energy increases, the Peierls order parameter shrinks linearly down to a point where it decays and a non-zero Flux order parameter is found. With increasing driving frequency this transition point shifts to lower energies. In the intermediate frequency regime the transition moves back to higher energies. In the high-frequency regime, finally, we find that for $12t_\text{h} \lessapprox \omega$ the order parameter curves for all frequencies collapse. The initial Peierls order is stable over a maximal energy range.

So far we discussed pulses with $A_x = 0$, $A_y \neq 0$, i.e. polarized linearly along the direction of the strong bond in each unit cell of the Peierls phase. Let us compare the results to simulations with a vector potential along the x-direction. Fig. 5.26 shows results for the late-time stationary state value of the order parameters after a pulse with $A_x \neq 0$, $A_y = 0$ for three different values of the driving frequency ω. For frequencies

$\omega \lessapprox 6t_\mathrm{h}$, the amount of absorbed energy as a function of A_x^max is reduced compared to A_y-driving, in particular at high amplitudes. The transition from Peierls to Flux order in Fig. 5.26(b) takes place in a similar way to Fig. 5.24, although the regime with the earliest departure from Peierls order is shifted to higher frequencies.

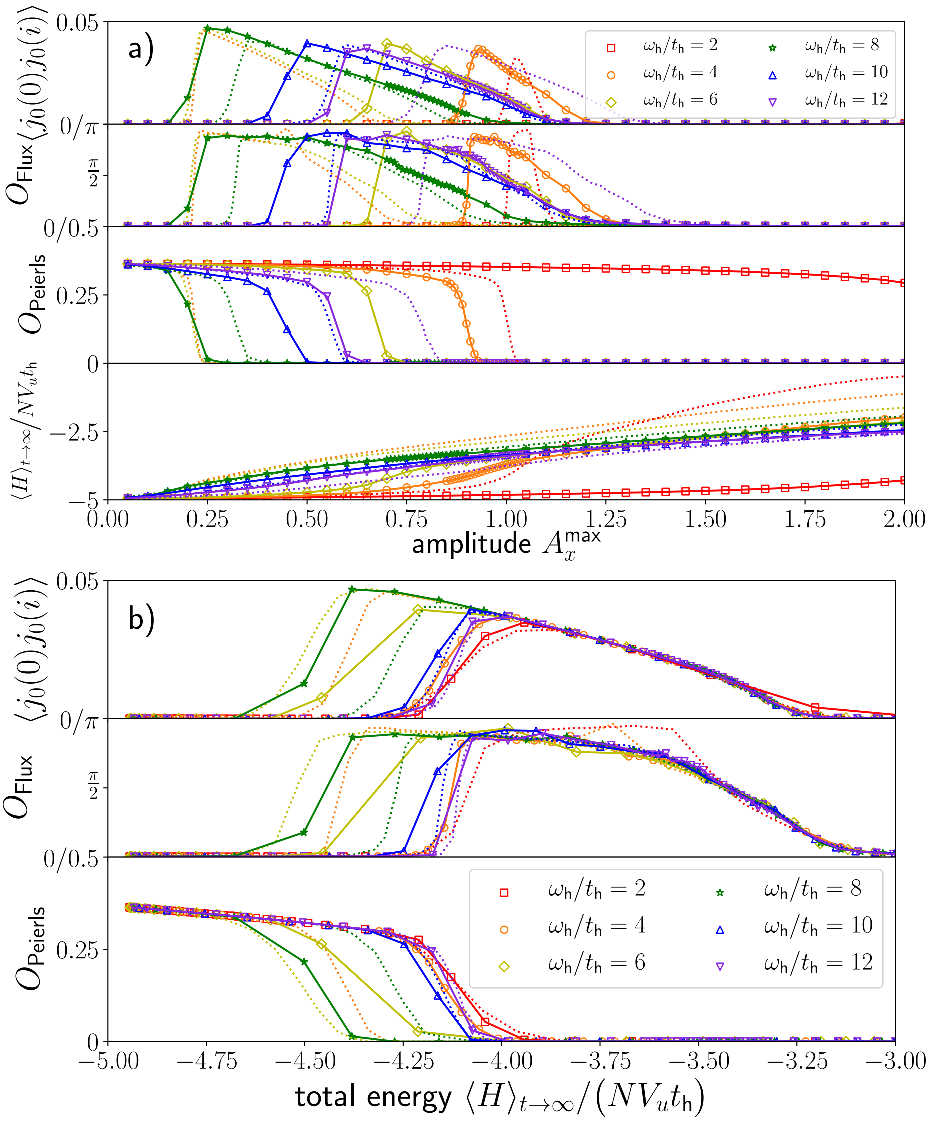

Figure 5.26: Late-time stationary values of the order parameters after a pulse with a vector potential that is polarized in the direction orthogonal to the strong bond of the Peierls phase ($A_x \neq 0$, $A_y = 0$) and for three different driving frequencies. The lattice has $V_u = 11 \times 11$ unit cells and $J/t_\mathrm{h} = 15$, $U = 0$. This figure is also published in [2]. Copyright (2022) by the American Physical Society.

Finally, we extract the transition energies from the order parameter curves in order to create the "prethermal phase diagram" in Fig. 5.28. At the Peierls-Flux transition we fit a sigmoid function to $\mathcal{O}_\mathrm{Peierls}$ at the transition and determine the energy value at the half-height sigmoid. An exemplary fit for $\omega/t_\mathrm{h} = 6$ is shown in Fig. 5.27. The broadness of the total transition range depends on the driving frequency and is approximately $0.2/(NV_u t_\mathrm{h})$. Nevertheless, the edge is sharp for all frequencies and the fits are usually well converged. The energy of the Flux-Uniform transition, which we fit from the current-current correlator, is slightly more difficult to determine since the remaining fTWA fluctuations in the data render it more difficult to determine the exact point, at which the correlator begins to become non-zero. Empirically, we find that the current-current correlator near the transition point roughly follows a parabolic energy dependence and so we fit a parabola and determine its zero point. An example is shown on the right hand side of Fig. 5.27. From the fit parameters and by looking at the data we can estimate an error of roughly $\pm 0.1/(NV_u t_\mathrm{h})$

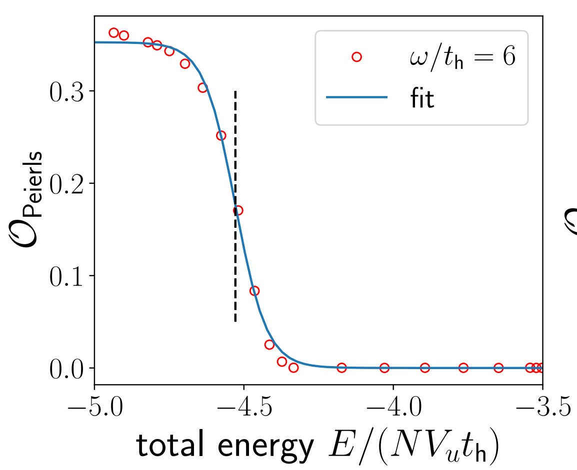

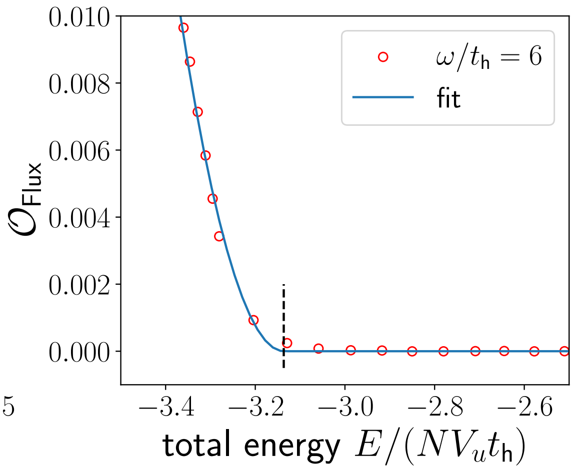

Figure 5.27: Exemplary determination of the transition energy via a parabolic fit function for the $\omega/t_\mathrm{h} = 6$ data ($L = 11$ and $N = 300$). The dashed line shows the transition energy we assign to the curves. We estimate the uncertainty of the transition energies due to the fit to be about ±0.1 in energy units.

We show two sets of data: the one with $N = 300$ discussed so far and for comparison another set obtained with $N = 250$, which we discuss more in detail below. The transition Flux to Uniform is mostly independent of the driving frequency and field orientation except for a little uptrend at low frequencies, which needs to be reexamined with more data points in the transition range. In contrast, the Peierls to Flux transition is clearly dependent on the parameters of the drive. We find a window of frequencies for which the transition occurs around a lowest energy. It is shifted to higher frequencies in the case of A_x-polarization, which demonstrates the relevance of the spatial structure of order for optical excitations in an extended 2D system. In this regime the transition occurs with the least amount of absorbed energy, i.e. avoiding additional heating. At low and high frequencies the transition energies approach similar values. It would be interesting to see if these limits coincided with the thermal transition of the system at finite N, which requires a more detailed knowledge of the thermal finite-N phase diagram. The $N = 250$ data contains the same qualitative signatures for the transition values but shifted to lower energies. A comparison with the mean-field lines suggests a linear downshift of the transition energy and a more complex N-dependence of the Peierls-Flux transition.

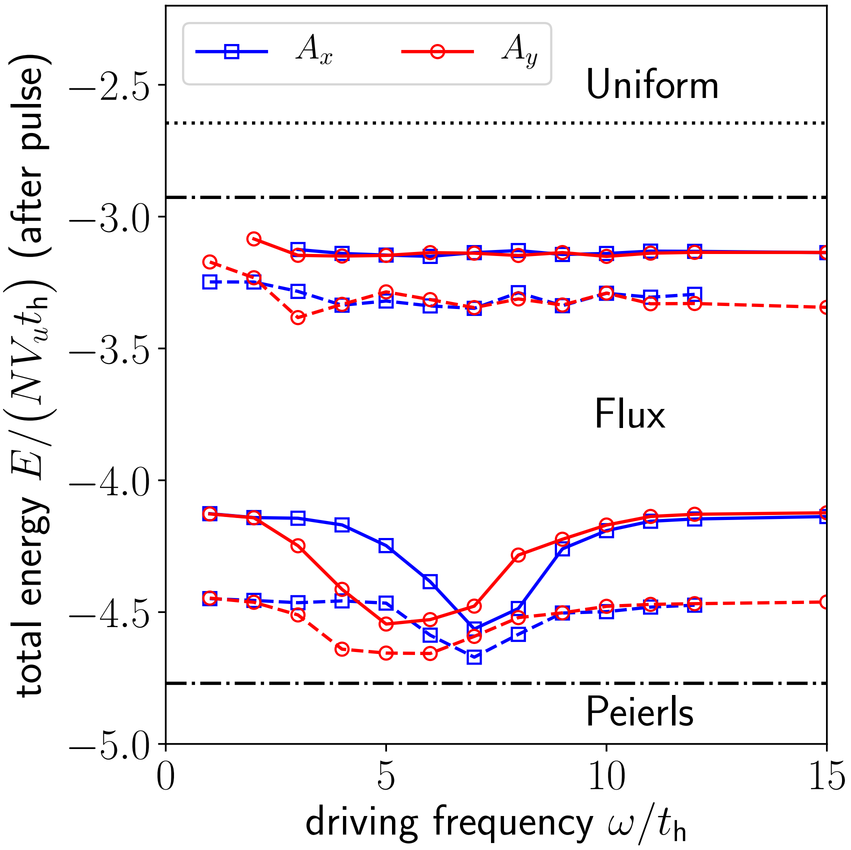

Figure 5.28: Transition energies between the three equilibrium phases in the Hubbard-Heisenberg model for $J/t_\mathrm{h} = 15$ and $V_u = 11 \times 11$ unit cells after a pulse with driving frequency ω. Red symbols correspond to pulses with $A_y = 0$, $A_x \neq 0$ (along the direction of the strong Peierls bond), blue symbols to the orthogonal direction. The dots connected with solid lines use $N = 300$, dashed lines $N = 250$. Black lines: mean-field model $N \to \infty$. Black dotted line: thermal transition from Flux to Uniform phase, upper black dashdotted line: energy E above which the Peierls saddle point disappears, lower black dashdotted line: energy of the Peierls state at which the first order transition to the Flux phase occurs. This figure is also published in [2]. Copyright (2022) by the American Physical Society.

5.4.6 The role of U (cf. [2])

Lastly, we would like to comment on the dynamical role of the Hubbard interaction U, which we omitted so far. A non-vanishing value of U will lead to a suppression of the on-site charge fluctuations during and subsequent to the pulse. At half filling, $U/t_\mathrm{h} \to \infty$ is the Heisenberg limit of the model. To illustrate the effect of the U-term we show the post-pulse total energy in the $N \to \infty$ model for a driving frequency $\omega/t_\mathrm{h} = 4$ in Fig. 5.29. The threshold amplitude for energy absorption is shifted to higher amplitudes upon increase of U. However, at high driving amplitudes the system seems to heat up more than in the $U = 0$ case. Without going into a detailed discussion of these effects, we can at least make the fundamental observation that parameters which are irrelevant in equilibrium (like U in this case) may be relevant out-of-equilibrium. In particular, one could design dynamical protocols to determine such parameters. In this work we will not discuss the role of U at finite values of N because then the value of U will also be relevant for the equilibrium phase diagram, which goes beyond the scope of this study.

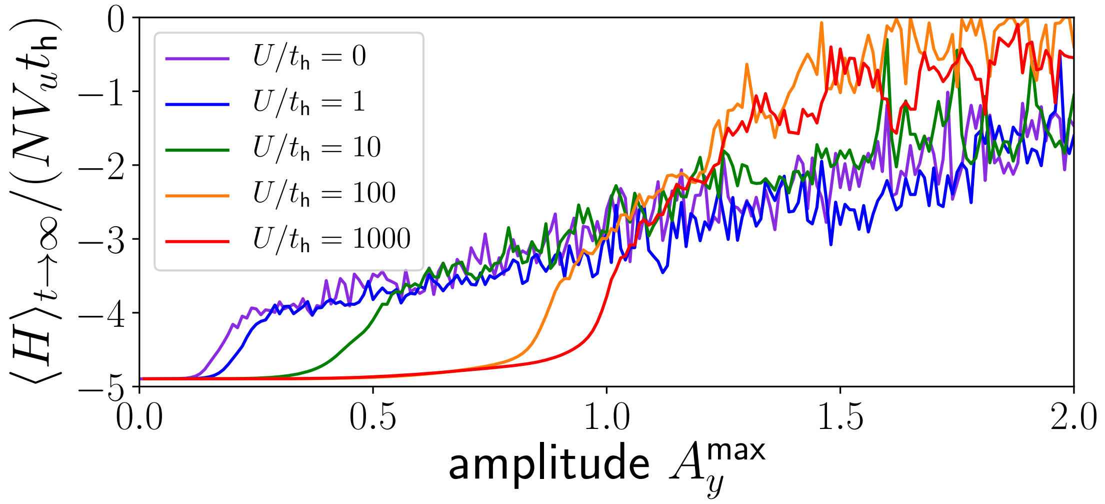

Figure 5.29: Total energy after a Gaussian pulse with frequency $\omega = 4t_\mathrm{h}$ as a function of the driving amplitude A_y for some values of the Hubbard interaction strength U ($J = 15t_\mathrm{h}$ is fixed). The data is obtained for the mean-field ($N \to \infty$) model on a lattice of 21×21 unit cells. This figure is also published in [2]. Copyright (2022) by the American Physical Society.

5.4.7 Comparison of $N = 300$ and $N = 250$ (cf. [2])

So far we have concentrated on a system with $V_u = 11 \times 11$ unit cells and a degeneracy $N = 300$. We would like to compare the results – at least qualitatively – to simulations obtained with different system parameters. In Fig. 5.30 we compare the final state order parameter data for $N = 250$ and $N = 300$, still in a system with 11×11 unit cells. In Fig. 5.30(a) we plot the total amount of absorbed energy, divided by N. Both energy data sets coincide for most of the considered driving amplitudes. This is because in both cases the contribution of the mean-field dynamics to the absorbed energy is dominating. In contrast, the corresponding stationary order parameter values differ more strongly. Still, their qualitative behavior as a function of the driving amplitude agrees. Fig. 5.30(b) presents the order parameters as a function of the total amount of absorbed energy. At $N = 250$ both the Peierls-Peierls as well as the Peierls-Flux transition occur at lower energies than for $N = 300$. This agrees with the expectation of an increased significance of quantum fluctuations at lower N, which destabilize non-trivial spatial order. If the fluctuations of a fixed number of off-diagonal k-modes become too strong, the fundamental mean-field order will be more and more washed out. Nevertheless, the qualitative behavior of the order parameters is consistent, which can also be seen from the similar shape of the transition lines in Fig. 5.28.

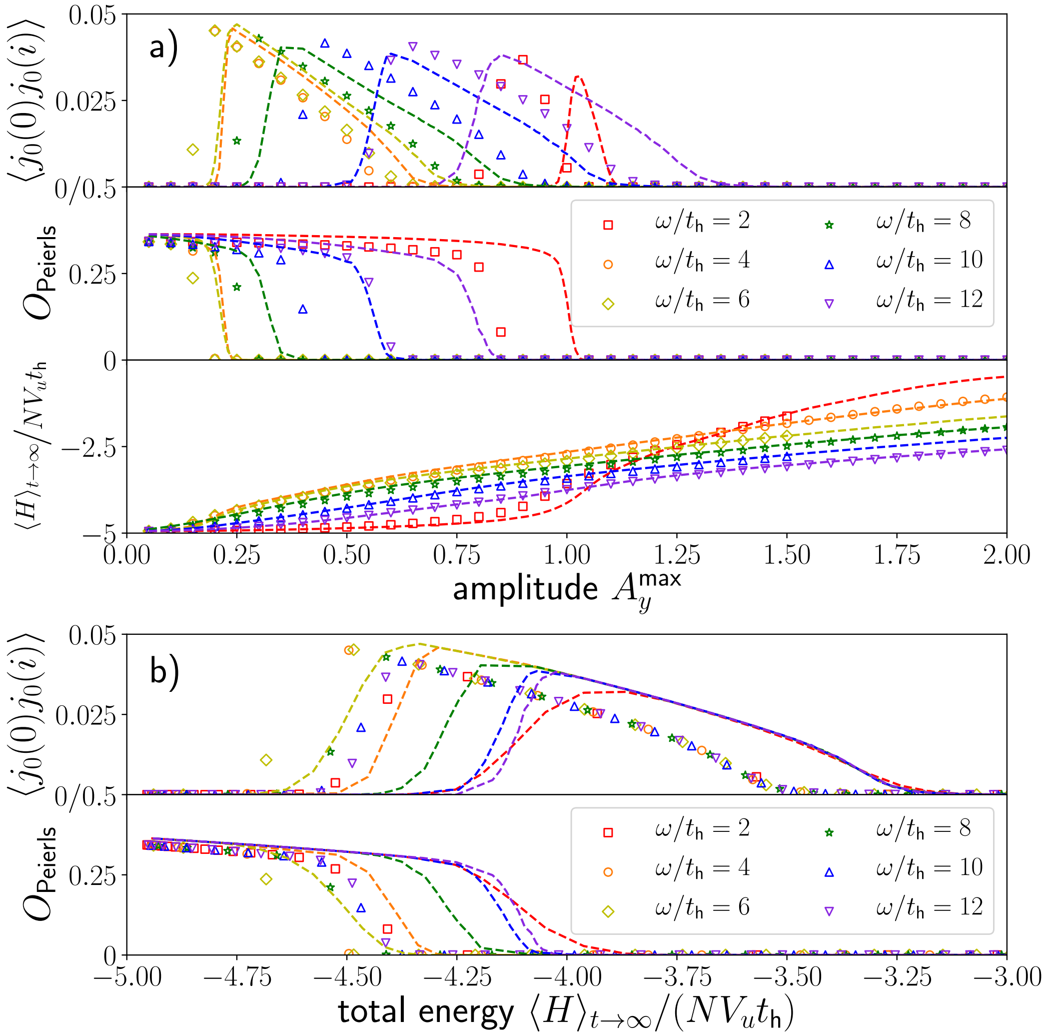

Figure 5.30: Order parameter dynamics for a Gaussian pulse ($A_x = 0$, $A_y \neq 0$) in the $N = 250$ Hubbard-Heisenberg model on a lattice with $V_u = 11 \times 11$ unit cells. The symbols represent $N = 250$ while the dashed line is the $N = 300$ case. This figure is also published in [2]. Copyright (2022) by the American Physical Society.

5.4.8 Comparison of $L = 11$ and $L = 13$

For a second comparison, we keep the degeneracy N fixed and compare two values of the system size with each other. Again, the order parameters display qualitatively similar profiles as functions of amplitude and absorbed energy. In Fig. 5.31 we directly plot the extracted non-equilibrium transition energies. The transition lines move down to lower total energies for the larger system size. The profile of the transition is more shallow as a function of the driving frequency but, nevertheless, the main features are still reproduced: A minimal energy of the first-order Peierls-Flux transition at intermediate driving frequencies and a mostly flat profile of the second-order Flux-Uniform transition. Finite-size corrections may lead to small shifts in the characteristic frequencies of the system but from the current frequency resolution of the data this is impossible to tell. In summary, like in the previous comparison, we conclude that both data sets are consistent with each other and an increased number of fluctuating variables at fixed strength of the fluctuations destabilizes the real space mean-field order more.

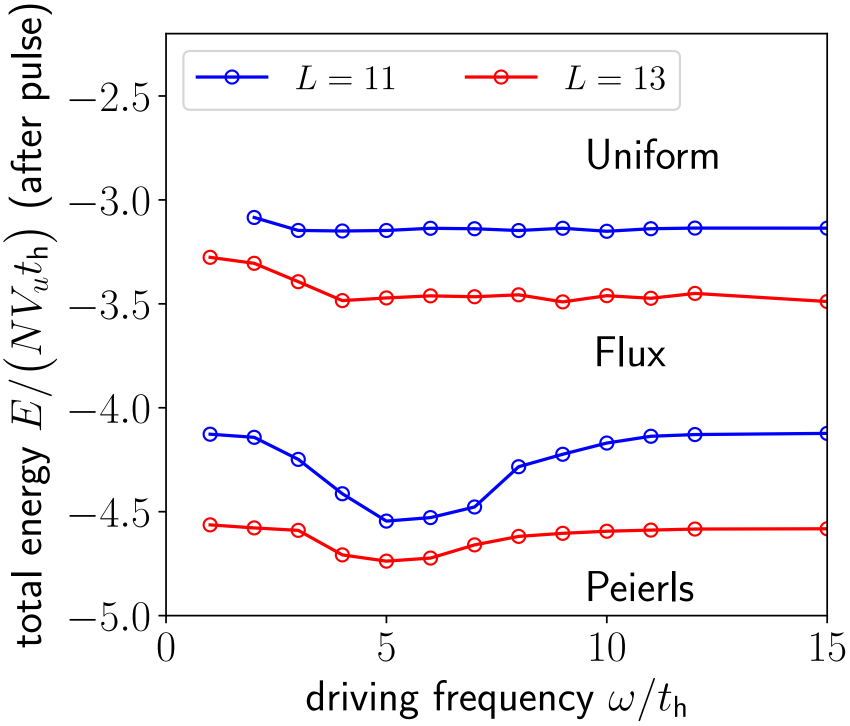

Figure 5.31: Comparison of the transition energies between the prethermal phases in the Hubbard-Heisenberg model for system sizes 11 × 11 and 13 × 13 unit cells.

5.5 Spatially Inhomogeneous Photoexcitations

So far in this Chapter we only considered excitations, which are spatially homogeneous, like quenches or uniform photoexcitations. This is also in accordance with the often applied simple Ginzburg-Landau picture based on a homogeneous order parameter field $\mathcal{O}(t)$. Spatial fluctuations can be incorporated in this framework by means of Gaussian terms $\left(\nabla\mathcal{O}(\vec{r})\right)^2$ in the Landau functional [54, 56]. However, spatial disordering beyond this Gaussian approximation has recently been proposed as a possible driving force behind ultrafast phase transitions [286, 287] and challenges the conventional Ginzburg-Landau picture. Studies of such inhomogeneous ordering scenarios on a microscopic level have only recently been started [288, 289] for charge-density wave systems. We do not aim to directly contribute to the development of a theory of disorder-mediated transitions at the present level of our theory. Instead, we consider a type of excitation, which is manifestly inhomogeneous in space, namely localized photoexcitations. Such types of excitations on correlated materials do not seem to be studied much in the literature. This is likely because of the difficulty to realize such a protocol experimentally since ultrashort as well as ultra-focused beams are required. In addition, one needs a detection technique, which is able to also spatially resolve the electronic dynamics to some extent. Nevertheless, some studies with tightly focused laser beams have been carried out to locally excite surface plasmon polaritons in metal systems [290]. On the theory side, local excitations pose a challenge to time resolved simulations because of the necessity to treat large system sizes without being able to make use of translational invariance for a reduction of the computational cost. In one spatial dimension, MPS-based time evolution approaches [58] might be sufficient for not too large system sizes ($L \lessapprox 100$). On the other hand, non-equilibrium DMFT [57] in its pure form relies on a local approximation to the self-energy such that – without suitable extensions of the technique – spatial correlations are not taken into account. A characteristic feature of the fTWA method is that it keeps every entry of the one-particle reduced density matrix as a dynamical variable explicitly. Spatial symmetries of the system are only restored after averaging over the trajectories and cannot be implemented from the start. Firstly, this prevents one from using, e.g., the translational invariance of the system to reduce the computational complexity. But, secondly, one may also view it as a feature of the method, which is particularly useful for the simulation of spatially inhomogeneous systems. Two-dimensional systems with random disorder have shown to be a promising field of application for fTWA [157].

Local photoexcitation protocols host the potential for new physical phenomena to be explored, for example the dynamical generation of interfaces [109, 55] between regions with different types of competing order. They also allow to study non-equilibrium transport phenomena, e.g. the spatial distribution of excitation energy, which is initially localized. Such studies have been performed numerically in one-dimensional systems for inhomogeneous initial states [291, 292]. Another interesting feature of spatially non-homogeneous vector potentials is their ability to induce time-dependent magnetic fields $\vec{B}(\vec{r},t) = \vec{\nabla} \times \vec{A}(\vec{r},t)$. To study their additional effect on the spin sector, one could add a Zeeman term to the Hamiltonian, which we neglect in this thesis. We consider photoexcitations in the framework of the Peierls substitution with an additional spatial envelope of the vector potential $\vec{A}(\vec{r},t)$, which is of Gaussian shape:

$$\vec{A}_0(\vec{r}) = A_0^{\max} \mathrm{e}^{-\frac{|\vec{r}-\vec{r}_0|^2}{2\sigma_{\mathrm{spat}}^2}} . \tag{5.37}$$

In the formula for the Peierls substitution phase factor (2.23), we approximate the integral for simplicity (which is justified for slowly varying vector potentials):

$$\int_{\vec{r}_i}^{\vec{r}_j} \mathrm{d}\vec{r} \cdot \vec{A}(\vec{r}, t) \approx (\vec{r}_j - \vec{r}_i) \cdot \frac{1}{2}\Big(\vec{A}(\vec{r}_i, t) + \vec{A}(\vec{r}_j, t)\Big). \tag{5.38}$$

We begin with results in the limit $N \to \infty$. The mean-field model allows us to treat comparably large system sizes, we have chosen $V_u = 41 \times 41$ unit cells in the initial state (3362 lattice sites) and periodic boundary conditions. The vector potential has a spatial width of $\sigma_{\text{spat}} = 4$. At initial time $t = 0$, the system is prepared in the Peierls phase with $J/t_\text{h} = 15$. Results for a pulse with $A_x = 0$, $A_y = 2$ are shown in Fig. 5.32.

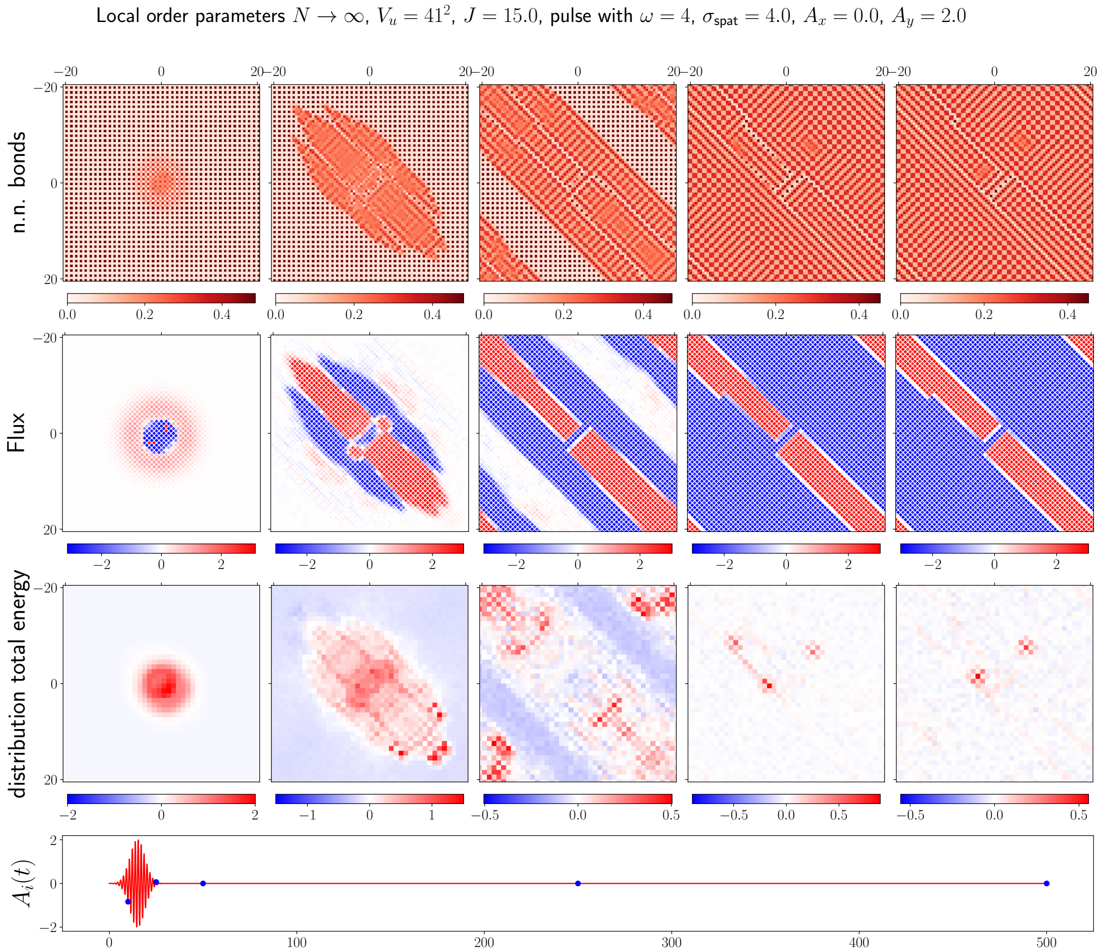

Figure 5.32: Mean-field dynamics of local order parameters in a two-dimensional Hubbard-Heisenberg model of size $V_u = 41 \times 41$ unit cells. The spatial excitation profile is Gaussian with a width $\sigma_{\text{spat}} = 4$. The frequency of the pulse is $\omega/t_\text{h} = 4$ and the field is polarized in the y-direction with amplitude $A_y = 2$.

The columns in the figure represent different time instances, which are represented pictorially by the little blue dots at the bottom. The first dot belongs to the first column etc. The rows show the local values of order parameters, for which we do not distinguish unit cells any more. Every square in the top row of the figure corresponds to the strength of a nearest neighbor bond. Initially, one out of four bonds is strong.

In the middle row each data dot corresponds to one plaquette in the model and shows the value of the local Flux order parameter obtained from the respective plaquette operator. The third row shows the local total energy of unit cells, from which we subtract the average total energy in the system. This allows to better visualize the redistribution of the excitation energy in the system. During the driving with the pulse and immediately after it (first two colums), the excitation remains localized. In the excited area, one finds a melting of the initial staggered bond condfiguration of the Peierls phase. Bonds become more equal in strength and one also finds a non-vanishing Flux order parameter.

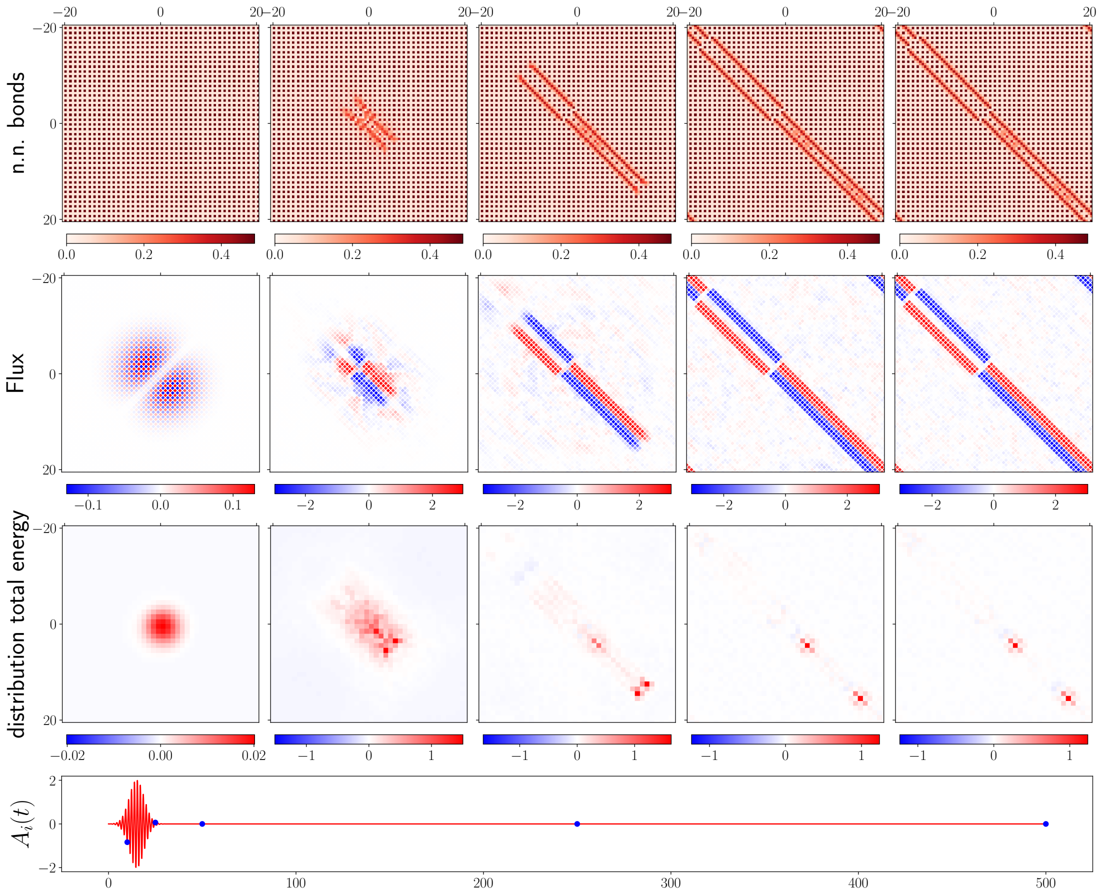

Local order parameters $N \to \infty$, $V_u = 41^2$, $J = 15.0$, pulse with $\omega = 4$, $\sigma_{\text{spat}} = 4.0$, $A_x = 2.0$, $A_y = 0.0$

Figure 5.33: Similar data to Fig. 5.32 but the field is polarized in the x-direction with $A_x = 2$. The local total energy is plotted relative to the average energy in the system.

In addition, the reflection symmetry along the main diagonal of the system remains conserved throughout the dynamics except for small deviations at late times. These are likely due to the finite floating point accuracy that pushes the system to choose one of two degenerate spatial arrangements. It is clear that such simulations in large non-linear chaotic systems are challenging and susceptible to little variations of, e.g., the initial conditions. We typically use error tolerances for the ODE solver of $\varepsilon_{\text{abs}} = 10^{-10}$

and $\varepsilon_{\mathrm{rel}} = 10^{-8}$. Variations of these tolerances or a non-zero value of the symmetry breaking $\varepsilon_{\mathrm{Flux}} = 10^{-3}$ can lead to different dynamics long after the pulse, however, the qualitative behavior agrees with the data shown. An interesting observation is the formation of a domain boundary shortly after the excitation (third column). The excitation energy is first distributed along the field direction (i.e. along the main diagonal in the picture), where it triggers the Peierls-to-Flux transition. While in the spatially homogeneous situations all unit cells obtain the same amount of excitation energy and cannot lower or redistribute their local energy, the situation is different in this inhomogeneous situation: Already within mean-field theory, transferring energy to a neighboring degree of freedom is possible and provides a mechanism to locally adapt to newly accessible free energy minima. Another conclusion one can draw from the data is the spatial relaxation of the energy: At late times, the energy of most local unit cells agrees with the average energy in the system except for a few defect-like structures.

In Fig. 5.33 we show results for an excitation with polarization in the x-direction (orthogonal to the main diagonal). Similar to the results obtained for homogeneous photoexcitations, we find a much weaker energy absorption for driving with this polarization. The explanation is likely that in the initial state the bonds in the y-direction are much stronger than the bonds in the x-direction, which can give rise to stronger currents and hence more energy absorption. Like in the y-polarized case the dynamics mainly occurs along the y-direction but we find much larger regions with unaffected Peierls order.

Finally, we discuss results for our default finite-N system with $V_u = 11\times11$ unit cells and for $N = 300$. In this smaller system we rescale the width of the spatial Gaussian envelope to $\sigma_{\mathrm{spat}} = 1$. We note that the spatial profile of the vector potential is now of the order of the lattice constant, which is, strictly speaking, not allowed in the Peierls substitution (cf. Chapter 2). Nevertheless, for now we ignore this circumstance because we are mainly interested in a comparison of the qualitative dynamical features to the mean-field case. As can be seen in the figure, we start with the initial state preparation warm-up dynamics before the pulse hits the model around time $t_0 = 250t_{\mathrm{h}}^{-1}$. To avoid problems connected to the averaging over the equivalent ergodic components of the Flux phase, we carry out this simulation with an explicit symmetry breaking parameter $\epsilon_{\mathrm{Flux}} = 10^{-3}$. Immediately after the end of the pulse, we see a suppression of the Peierls order in a central stripe, which is in a qualitative agreement with the mean-field results. The suppression of the bond order is accompanied by the emergence of non-vanishing values of the Flux order parameter (here, with the explicit symmetry breaking switched on, we consider the Flux order parameter defined via the plaquette operator). Late in the dynamics we find that the energy is distributed uniformly over the system (expect for remaining quantum fluctuations). In addition, the order parameters have homogenized. By analogy with the discussion for the heterogeneous photoexcitations we expect a slow tunneling dynamics into the thermodynamically preferred phase.

5.6 Summary and Discussion (cf. [2])

In this Chapter, we studied the non-equilibrium dynamics of order parameters in the large-N Hubbard-Heisenberg model with $U = 0$ under quenching and driving. We

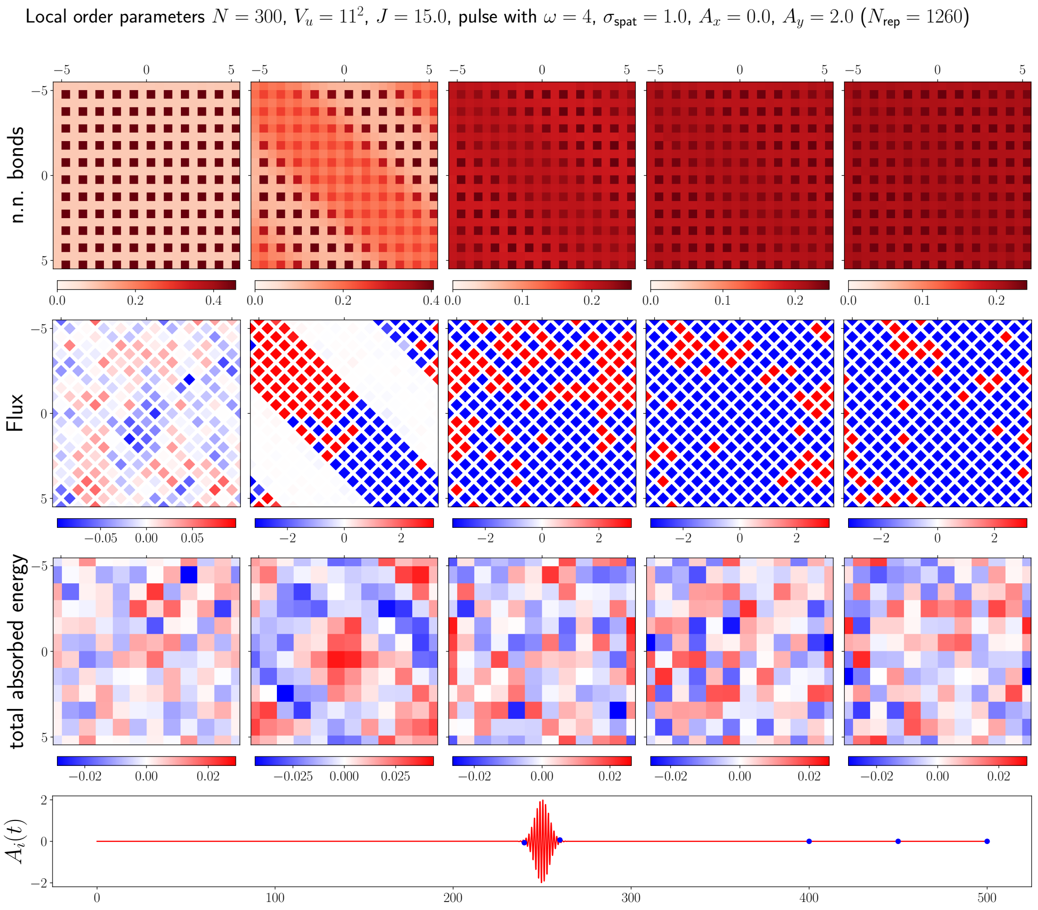

Figure 5.34: Local photoexcitation in the Hubbard-Heisenberg model on a lattice with $V_u = 11 \times 11$ unit cells and for $N = 300$. The width of the spatial Gaussian envelope is $\sigma_{\mathrm{spat}} = 1$. The interaction strength is $J/t_{\mathrm{h}} = 15$, the driving frequency $\omega/t_{\mathrm{h}} = 4$ and we use a y-polarized field with $A_y^{\max} = 2$.

started with a calculation of the mean-field solution of the model and presented for the first time a finite-temperature phase diagram in the limit $N \to \infty$. The model is characterized by an inherent competition of two types of order: a bond density wave ("spin-Peierls") phase and the staggered flux phase ("DDW phase" or "orbital antiferromagnet"). Within mean-field theory, one finds a first-order transition at zero temperature around $J/t \approx 12$ as well as a transition at finite temperature. This setup is well suited to study the competition of ordered phases out-of-equilibrium microscopically, i.e. not within a time-dependent Ginzburg-Landau approach. While the $N \to \infty$ dynamics should in principle still be equivalent to a Ginzburg-Landau description, we are also able to go beyond mean-field. The SU(N)-symmetry provides an ideal environment to apply phase space techniques like the fermionic truncated Wigner approximation (fTWA), which rely on the existence of a small semiclassical expansion parameter, $\hbar_{\mathrm{eff}} \sim \frac{1}{N}$ in this case. However, since this is the first application of the fTWA method in such a context, some technical issues are not yet completely solved. This concerns in particular the preparation of stationary initial states. It turns out to be a challenge to prepare stationary initial states with initial Peierls order. Since we do not have access to an analytical $\frac{1}{N}$ solution of the model currently, we started from an approximate initial state derived from the mean-field solution. While one can expect in theory a dressing of the mean-field modes by particle-hole fluctuations with respect to the mean-field "vacuum" state, in practice the spatial structure of the state becomes washed out and one ends up, ultimately, in the Uniform phase. It is important to keep in mind that this is a consequence of our approximate state preparation technique. The true quantum model does indeed allow for stable Peierls solutions at finite-N, a fact which has been demonstrated using quantum Monte Carlo [140]. Our pragmatic solution is to stick to parameter sets that allow for a reliable initial state preparation. Therefore, we mostly considered a lattice with $V_u = 11 \times 11$ two-site unit cells and to values of N in the range from 250 to 300. As a first application of the machinery, we looked at the dynamics of the Hubbard-Heisenberg model after a quench in the interaction strength J. While the mean-field solution yields undamped coherent order parameter oscillations as a response, we find a dephasing-induced damping of the oscillations for $N < \infty$. This allows transitions into stationary states of the post-quench Hamiltonian both for quenches within the Peierls phase as well as for quenches across the phase boundary. One finds that the dephasing time τ clearly scales $\sim N$. This indicates that the exponential decay is likely a generic feature of the large-N dynamics beyond mean-field.

In the main part of the Chapter, which is an extended version of the publication [2], we studied the photoinduced order parameter dynamics under driving with a pulsed sinusoidal vector potential. A guiding question is the formation of order subsequent to the pulse, in particular how a transition between the two competing ordering tendencies is influenced by the drive parameters. Again, the mean-field level dynamics leads to undamped coherent oscillations that do not allow for a direct extraction of order parameter information. We made use of the dephasing effects at finite N, which give rise to stationary states whose symmetries agree with those of the equilibrium phases. As a main result, we argued that the observed post-pulse order in the system cannot be thermal because otherwise the system should, for a given total energy E, approach a (unique) state with the lowest free energy. In the numerical data, in contrast, we observe that the final stationary state also explicitly depends on drive parameters like the driving frequency ω and the field polarization $A_i, i \in \{x, y\}$. We find a transition from the Peierls to the Flux phase with the lowest amount of absorbed energy in the intermediate frequency regime, while in the low and high frequency regimes the order parameter curves behave similarly, In addition, they collapse for both considered polarizations of the driving amplitude. For small driving frequencies one can make a connection to threshold behavior observed in Mott insulators based on the Landau-Dykhne formalism [284]. We observe a similar threshold behavior already within mean-field theory. The intermediate frequency deserves a better analysis in the future. Currently, we do not have direct access to spectral information about excited states in the system, the Hartree band structure, which is valid for the ground state, can only serve as an approximate guideline. Nevertheless, the Hartree-Fock calculation indicates – in agreement with the QMC data – that the Peierls phase is gapped, while the Flux phase corresponds to a gapless semimetal. The transition from the Peierls to the Flux phase is therefore likely connected to a resonance of the pulse with an elementary excitation of the Peierls phase. This would also be consistent with the observed shift of the transition line minimum for A_x-driving as compared to A_y-driving. Method-wise it is not clear how to obtain two-time quantities like Green's functions, which are necessary for the calculation of spectral functions, from fTWA. One could use fTWA for the time-diagonal quantities and reconstruct the full two-time plane using mean-field propagators. Whether this yields a consistent scheme remains to be shown. A more straightforward step would be the calculation of a ground state spectral function in the $N \to \infty$ model using time-dependent Hartree theory and to assume that the spectra do not change much at large but finite N.

In this Chapter we have demonstrated non-trivial examples of dephasing-induced prethermal order, which describes properties of an electron system on transient timescales before, in the full quantum theory, thermalization sets in. Our findings indicate that in a scenario with two competing ordered phases one can find an intermediate frequency regime, which allows to switch the order in the system (on this transient timescale) with a minimal amount of heating. Therefore, it might be particularly interesting for experimentalists to look for such a regime in experiments if they want to switch to thermodynamically unfavored order. Heating, i.e. additional excitation energy in the system, will suppress values of order parameters and also lifetimes of prethermal states, thereby rendering transient effects more difficult to observe. Our advantage compared to other studies of competing order is that we can simulate the photoinduced dynamics microscopically with more model-specific information (e.g. on excitation energy scales) than approaches based on coarse-grained Ginzburg-Landau functionals. Our findings motivate a search for similar frequency regimes in other models of competing ordered phases, for instance of superconductivity and charge density wave order. Lastly in this Chapter, we have shown examples of inhomogeneous photoexcitations that inject energy into the system, which is initially localized in space and then distributes over the system. One interesting observation is the formation of a domain boundary between Peierls and Flux phase subsequent to the excitation, which melts in the course of time. This phenomenology can also be seen in the finite-N model but studies on larger systems should be carried out in the future.

An important question for a refined analysis concerns the lifetimes of the prethermal states. While prethermalization corresponds to a formation of quasiparticles, thermalization is due to their scattering. A rough estimate can be based on the available scattering phase space in the spirit of "Landau's argument" for the lifetime τ of quasiparticles, which scales like $\tau \sim \varepsilon^{-2}$ for an excitation energy ε above the ground state [9]. In our case, if ΔE is the excitation energy relative to the ultimate equilibrium state (e.g. Peierls or Flux phase), we estimate that $\tau_{\text{scat}} \sim N/(\Delta E)^2$. For a small amount of excitation energy, this timescale will be larger than the dephasing timescale. A systematic study of the scattering dynamics is beyond the scope of our current work since it requires additional method development to incorporate higher-order correlations into the dynamics. One way to do so could be to take guiding from the BBGKY hierarchy [163, 167, 168] and to add more dynamical variables to the equations of motion. Another possible procedure is to derive a kinetic equation akin to the quantum Boltzmann equation (QBE), which is switched on after prethermalization. Such a QBE would manifestly evolve the system towards a thermal fixed point and it would allow for a more precise estimate of lifetimes of prethermal states [293].

In this Chapter, we mostly considered values of N between 250 and 300, which are clearly off the conventional condensed matter case of $N = 2$. Our choice of N is limited in practice by our state preparation procedure, which starts from a mean-field state and then switches to finite N. We have seen that a comparison between the results at different N and L is possible only qualitatively. This is definitively a weakness of the present approach. One can try to push the simulations to very high values of N, at which also large system sizes are accessible with the "N-quench approach". However, this will also significantly extend the dephasing times, which renders such simulations more and more inefficient. Contributions of order $1/N^2$ within fTWA need not agree with the correct quantum dynamics, as we have already explained using the example of the interaction quench in the Hubbard model in Chapter 4. Dynamical time scales and quantitative values of order parameters will depend on the chosen value of N but within the range of validity of our theory we do expect to observe the same qualitative behavior also at smaller values of N. The formalism developed here can directly be applied to other SU(N) models. Interesting candidates are, for instance, models with charge-density waves in equilibrium, like a SU(N) t-V model. While large-N models provide a very natural field of application for semiclassical methods, the fTWA method is not restricted to it and can be used to improve mean-field studies of more generic order parameter constellations, e.g. in the context of light-induced superconductivity [111]. The range of validity of fTWA, however, needs to be assessed carefully if no semiclassical expansion parameter is available. In order to overcome the limitations of our initial state preparation scheme, an explicit calculation of $1/N$ corrections to the saddle points are necessary. The Appendix to Marston's and Affleck's paper provides some ideas how to do this within the field theoretical approach, however the calculation is demanding and is left there at a proof-of-principle state. Therefore, it might be worthwhile to look for alternative calculation techniques. One scheme that might be able to describe the particle-hole dressing of the mean-field states is the self-consistent random-phase approximation (RPA) [294]. However, it is not clear to us if the approach will also lead to a destabilization of spatial order. In analogy to SU(N) spin systems, an adaptation of flavor wave [295] theory could be worth a try. Possibly the most promising approach might be calculation within the flow equation approach pioneered by Wegner [219]. Wegner happens to use the exact same flavor-averaged operators $\hat{\rho}_{ij}$ like we do in a one-dimensional model. In his spirit, one could try to derive a mean-field like Hamiltonian with renormalized interactions at order $\frac{1}{N}$ and find its equilibrium states self-consistently. If this approach is successful, one has also obtained a transformed Hamiltonian that allows for analytical results on the quench dynamics using unitary perturbation theory [218]. Besides these analytical approaches, efficient quantum Monte-Carlo (QMC) codes [296] exist for SU(N) models, which could allow one to take the initial equilibrium data for the setup of a Wigner function directly from a QMC calculation. As a last remark we note that we have only considered half filling in this thesis. Affleck and Marston predict interesting phases also in the case of non-zero doping, for instance a so-called "kite" phase close to the Peierls phase. Doping the model could also allow for interesting analogies to high-temperature superconductors, which are characterized by a Mott insulating phase, which is slightly doped. Not without reason did Affleck and Marston originally invent their Hamiltonian as a simplified model for the physics of those materials.

Chapter 6

Conclusion

This thesis is about the exploration of “non-thermal”[34] effects in correlated electron models during and subsequent to the interaction with a light field. The notion of non-thermality refers to phenomena that cannot easily be explained using equilibrium concepts like heating alone. Typical examples, which are considered in this thesis, are the dressing of electronic states with light, which is the foundation of Floquet engineering. Another example is provided by the generation of prethermal states of matter that are only stable on transient time scales before thermalization. Such non-equilibrium states created by time-dependent electromagnetic fields are a very attractive field of study for theoretical physicists due to the high complexity of the phenomena, which nourishes the hope of discovering something novel. It is fair so say, though, that no single theoretical framework exists, which is applicable to all models and to all kinds of questions. The true challenge – according to the opinion of the author – is to dynamically adapt to problems that come up in research and to be flexible enough with the methods. Along these lines, this thesis summarizes contributions to some questions of current interest in the field of photoexcited dynamics, using a variety of methods.

In Chapter 3 we presented a simple analytical model for the initial and final state dressing in a time-resolved ARPES experiment. The theory is based on the exact solution of plane wave states in the presence of a periodic pump field. In a direct collaboration with the experimental group of Stefan Mathias, we modeled the interference of side bands originating from the dressed initial and final states in photoemission experiments on a gold surface [3]. The experimental side band intensities could only be explained if the influence of the in-plane electric field is effectively zero. Although in the case of the gold surface a screening of the field turned out to yield the simplest explanation, the calculation offers a second possible mechanism due to the destructive interference of the two types of side bands. Future research in this direction could, for instance, look at possible interference patterns of Floquet and Volkov side bands for parabolic initial states, which are not localized at the Γ but, e.g., at the K point. Many TMDC materials [29] show such valley structure away from the Γ point. Besides, it turns out to be experimentally challenging to observe Floquet-Bloch states in graphene [193, 194]. Simple wave function models (akin to Park’s calculation [124]) allow to calculate Floquet-Volkov interference patterns and help to unambiguously identify Floquet states.

The second topic of Chapter 3 is about the effect of periodic driving on a simple one-dimensional model for a charge-density wave insulator, for which we have access to a quasi-exact reference calculations with matrix product states [212]. Based on an observation of emergent band-like spectral weight in the single-particle gap of the system in the exact simulations, we analyzed the minimal prerequisites for such an effect to occur by comparison to a non-interacting model and to a time-dependent Hartree-Fock treatment of the interactions. The results show that while such a feature is absent in the non-interacting model, one can find a similar signal in the mean-field model. This hints towards doublon excitations in a long-lived prethermal state [211] as the primary origin of the band. Beyond the specific results, these findings demonstrate that time-dependent mean-field theory can be a valuable tool to calculate non-equilibrium spectral functions of driven systems. An open issue, which should definitively be addressed in future research, is how to define non-equilibrium spectral functions which are manifestly positive-semidefinite. The spectral functions, which we obtain from mean-field theory, do contain significant negative weights. Nevertheless, the shape and relative intensities of the peak still yields physically reasonable results. The starting point should be the calculation by Uhrig et al. [116], who constructed a positive-semidefinite retarded Green's function using period averaging in the case of infinite periodic driving.

The main part of this thesis addresses the topic of order parameter dynamics out-of-equilibrium. Many experimental findings [45, 49, 50] indicate that one can make use of light-matter interaction (via laser pulses, for instance) in order to transiently manipulate the order in a system. One of the most prominent examples is presented by light-induced superconductivity [49, 50]. Theoretical models for the dynamics of competing order parameters, subject to driving with a laser pulse, are often based on phenomenological Ginzburg-Landau functionals [109, 55, 54], in which the laser pulse is represented by time-dependent coefficients. Although such a coarse-grained description is clearly useful, it necessarily neglects a lot of important microscopic details of materials like realistic dispersion relations. Microscopic descriptions based on time-dependent Hartree-Fock theory [111] are more realistic and can incorporate some specifics of the system-specific electronic structure. However, due to the neglect of correlations within mean-field theory, effects like dephasing and scattering are not included and the dynamics is mainly governed by coherent order parameter oscillations. Therefore, a primary goal of this thesis is to explore a new method to go beyond time-dependent mean-field theory, which is based on phase space methods, in particular, the truncated Wigner approximation (TWA). TWA methods have a long tradition in the physics of quantum gases [139, 150] but they are less often used in the condensed matter theory community. Only recently, Davidson et al. [112] presented an extension of TWA for fermions (fTWA), which is basically equivalent to a time evolution scheme in nuclear physics, called the stochastic mean-field approach [160]. fTWA integrates nicely into mean-field treatments of interacting systems because the equations of motion are the same. The new aspect is a stochastic sampling of initial conditions for these equations of motion. Every initial condition yields a trajectory in phase space and, according to the rules of the TWA, one needs to average operator expectation values over these trajectories in order to obtain quantum mechanical expectation values. In Chapter 4 we applied fTWA to the well-known problem of the weak interaction quench in the Hubbard model, which is an example of a quench to a nearly integrable model with approximate constants of motion on a prethermal time scale. Our application of fTWA to the problem yields the following main insights: The method reproduces exactly the dephasing-induced physics of the prethermal phase. However, on longer time scales, clear deviations from the expected dynamics occur and the system evolved towards unphysical fixed points. Our strategy to mitigate these problems is to extend the number of fermion modes from two ($\sigma = \uparrow, \downarrow$) to a number of N flavor modes $\alpha = 1, \ldots, N$. The interaction quench dynamics in such a generalized SU(N) Hubbard model remains controlled over long time periods if N is chosen large, e.g. $N = 100$. $\hbar_{\text{eff}} = \frac{1}{N}$ plays the role of a semiclassical expansion parameter that controls the strength of quantum fluctuations and can be used to separate leading semiclassical contributions $\sim \hbar_{\text{eff}}$ to the dynamics from unphysical higher order contributions. In Chapter 5 we use such a large-N scenario to study the photoinduced dynamics of order parameters. Before we turn to these results we would like to discuss perspectives for future method development. It is clear that the question of thermalization and a correct fixed point distribution needs to be addressed. Again, the weak interaction quench in the Hubbard model is a suitable test case because many higher-order correlations (in a correlation hierarchy sense) are irrelevant for the dynamics. Taking guidance from the BBGKY hierachy is probably the most promising path towards systematic improvements of the fTWA method. In the context of spin systems [167, 168], the introduction of connected Weyl symbols at the level of the semiclassical theory lead to significant improvements of the dynamics in comparison to an exact reference dynamics. A similar idea was formulated by Czuba et al. [166] in the context of the stochastic mean-field approach. They take higher order terms of the quantum BBGKY hierarchy into account and also report significant improvements. In contrast to the scheme with the connected Weyl symbols, it is less obvious how to adapt the scheme by Czuba et al. to a large-N setup. Having implemented such a scheme it will also be interesting to study quenches to intermediate and strong interaction strengths.

Despite the necessity of further method development, we may still conclude that fTWA is able to describe dynamics in correlated 2D systems on time scales, which can be controlled by $\hbar_{\text{eff}}$. This led us to apply it to a more complicated model of the SU(N)-type, namely to the Hubbard-Heisenberg model first introduced by Affleck and Marston [141]. The model mimics some features of the copper oxide planes in cuprate high-temperature superconductors and can be thought of as an SU(N)-symmetric version of the t-J model with additional charge fluctuations. The mean-field phase diagram of the model is characterized by a competition of two phases, a bond density wave phase (Peierls phase), which is related to the spin-Peierls phase in large-N quantum antiferromagnets [242] and the staggered flux phase. In order to be able to study dynamics in the model, we combine the SU(N) Hubbard-Heisenberg model with the fermionic truncated Wigner approximation. One of the big challenges turns out to be the initial state preparation procedure. We do not have access to the full correlation information $\sim \frac{1}{N}$ of the model. Therefore, we start from the mean-field modes at $N \to \infty$ and "quench" to a finite value of N. This leads to a warm-up dynamics, which one can interpret – in analogy to the Hubbard interaction quench – as a formation of quasiparticles. However, it turns out empirically that too large system sizes in combination with low values of N lead to a destabilization of spatial order in the system if so prepared. If there are too many too strongly fluctuating random variables, real-space order can become washed out. We discuss possible analytical strategies to obtain better initial data in the conclusions to Chapter 5. For a combination of system size 11×11 unit cells and value of $N = 300$ that lead to stable initial states in the Peierls phase, we implement a number of non-equilibrium protocols, first parameter quenches and then, primarily, spatially homogeneous photoexcitations. For all these protocols we find that fTWA leads to stationary states after the excitations, which we interpret as prethermal states in accordance with our findings in the SU(N) Hubbard model. One can think of those states as a sea of non-scattering quasiparticles built on top of the mean-field "vacuum". In the case of the homogeneous photoexcitations we study systematically the transition of an initial state Peierls phase into the competing Flux phase subsequent to a photoexcitation as a function of excitation parameters like driving amplitude and driving frequency. We find transitions, which are characterized by a large amount of absorbed energy in the low- and high-driving frequency regime and an intermediate regime in which a switching to the Flux phase occurs at a low amount of total energy. Unfortunately, we do not have access to detailed information about the elementary excitations of the system. It is reasonable to assume that this intermediate frequency regime is connected to a resonance with an intrinsic excitation energy of the system. Future work in this direction should shed more light on this aspect. Nevertheless, we can already draw the conclusion that fTWA is indeed able to yield qualitative insights into the ordering dynamics after a non-equilibrium excitation in a system with competing order parameters. It would be very worthwhile to extend this fTWA analysis to models of more realistic competing order parameters like CDW and superconductivity. However, a better initial state control is required first. An interesting research direction, which we present as an outlook is the ordering dynamics of inhomogeneous photoexcitations that selectively excite one spatial region of the model. Our preliminary results show that interesting phenomena like domain boundaries can occur. Exploring this further might be a very interesting research direction, which makes use of the fact that fTWA is capable of simulating comparably large system sizes.

We would like to add a remark about further possible applications of semiclassical techniques like the truncated Wigner approximation. A very straightforward application is the application to phononic degrees of freedom, e.g. in a Holstein model. In this context, TWA is equivalent to a quantum chemistry method, the so-called multitrajectory Ehrenfest approach [297]. Another idea is to set up TWA schemes for quasiparticles. If one transforms Hamiltonians into (approximate) representations in terms of quasiparticle operators (dressed electrons, doublons, polarons, polaritons, etc.), one can try to implement TWA exactly for those quasiparticle operators. Care needs to be taken that one obtains a closed dynamical algebra and it is not guaranteed that such a scheme would work for all kinds of excitations. However, in principle, quasiparticle TWA would allow to push the validity of semiclassical methods into the strong coupling regime. A development of this idea for doublons in the Hubbard model is currently in progress. Overall, bridging the gap between macroscopic free energy pictures of order parameters and microscopic dynamical descriptions seems to be one of the most promising research directions in the field of light-induced phenomena in quantum materials. Although many open challenges remain, phase space methods present a new powerful approach, which allows to incorporate interaction effects beyond mean-field while still being able to efficiently simulate large two-dimensional systems.

Appendix A

Interaction Quench: Additional Figures

This Appendix collects some supplemental figures to Chapter 4. The figures show the deviation from the perturbative result as a function of the number of trajectories N_{rep}. The inset always shows the distribution function $n(\epsilon_k)$ for the data set with the highest number of trajectories. Fig. A.1 shows data for a quench to $U = 0.5$ in a 10×10 system at quarter filling. Figs. A.2 and A.3 show data for an 11×11 system at half filling ($N_p = 61$ electrons) with quenches to $U = 0.1$ and $U = 0.5$, respectively.

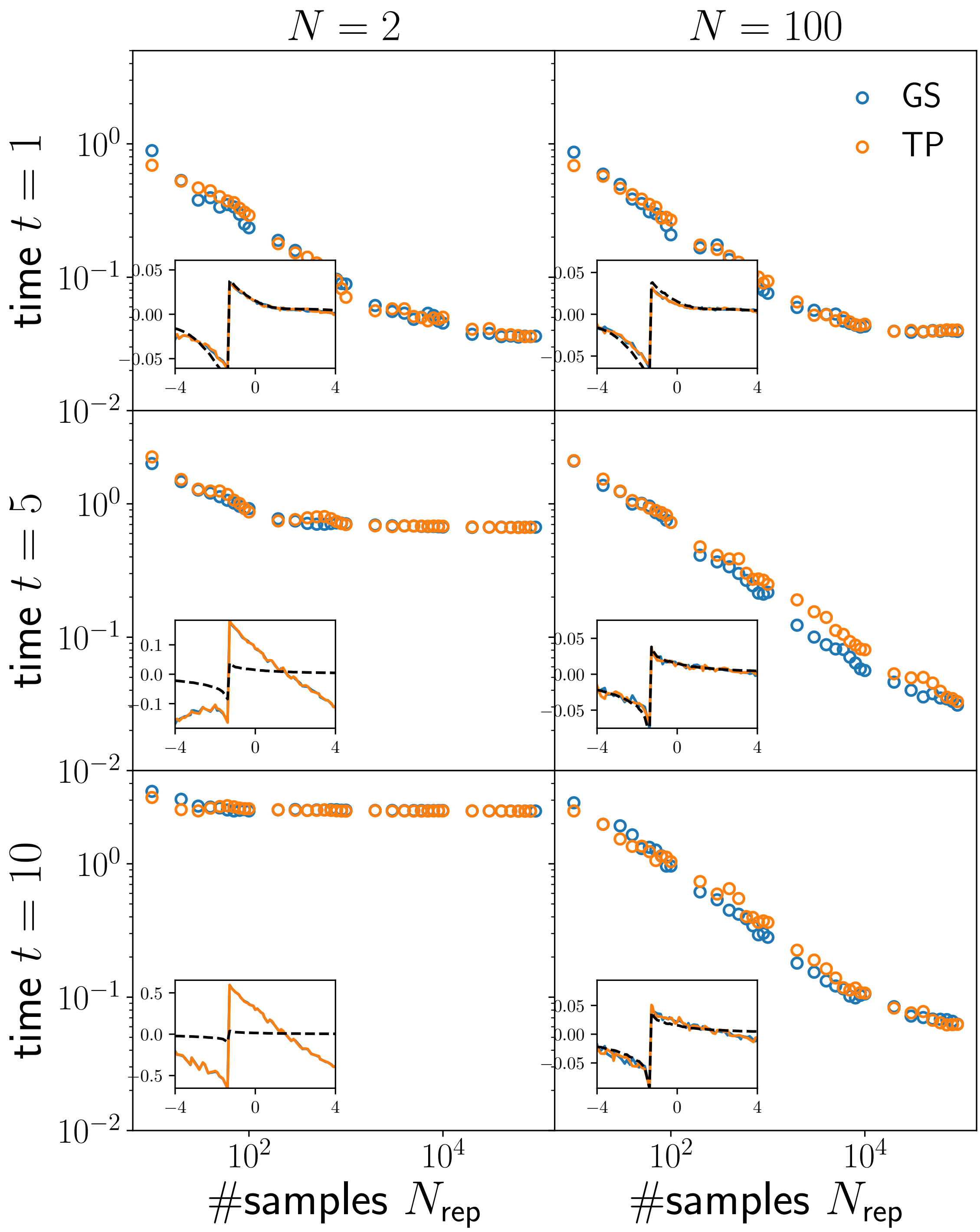

Figure A.1: Interaction quench to $U = 0.5$ in a system with 20×20 lattice sites at quarter filling ($N_p = 101$ electrons)

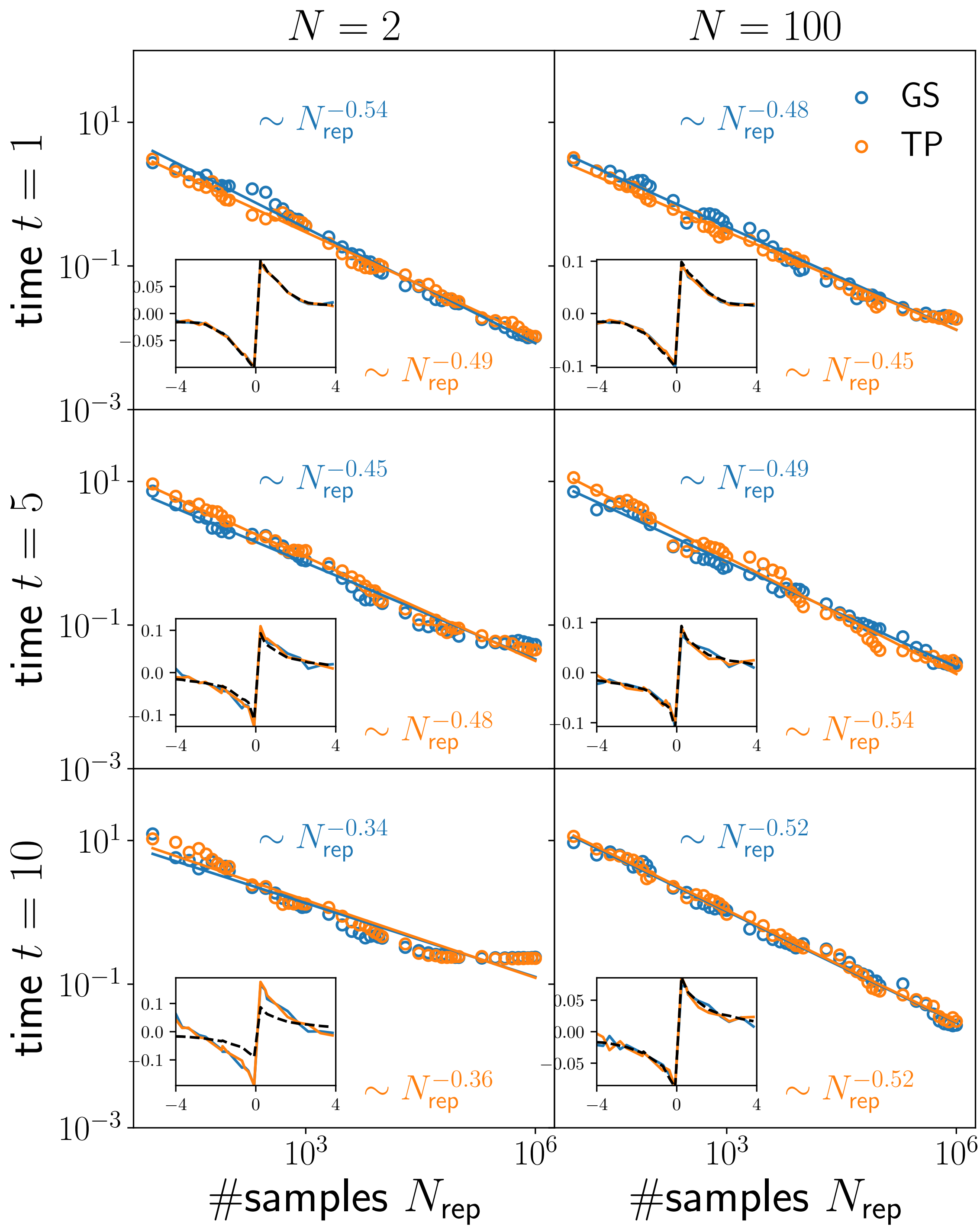

Figure A.2: Interaction quench to $U = 0.1$ in a system with 11×11 lattice sites at half filling ($N_p = 61$ electrons)

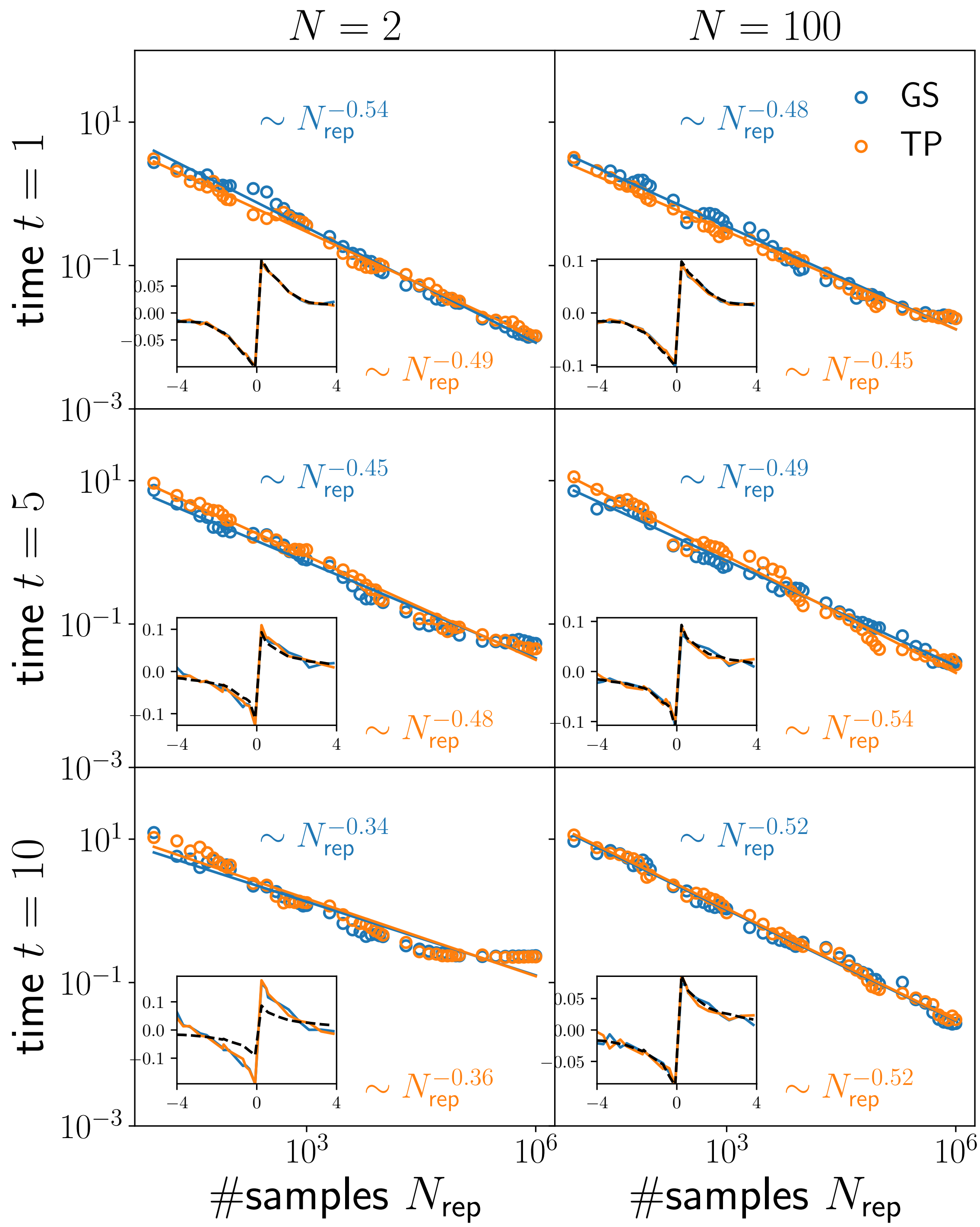

Figure A.3: Interaction quench to $U = 0.5$ in a system with 11×11 lattice sites at half filling ($N_p = 61$ electrons)

Appendix B

Review of the derivation of the Boltzmann equation

In this Appendix we review the derivation of the quantum Boltzmann equation for the Hubbard model. We follow mostly the derivation presented in [298] and [299, 300]. The starting point is the equation of motion for the mode occupations:

$$\begin{aligned} i\partial_t n_{k\sigma}(t) &= \frac{U}{V}\sum_{pp'q}\left\langle\left[\hat{n}_{k\sigma}, c^\dagger_{(p+q)\sigma}c^\dagger_{(p'-q)\bar{\sigma}}c_{p'\bar{\sigma}}c_{p\sigma}\right]\right\rangle_t \\ &= \frac{U}{V}\sum_{pp'q}\left(\delta_{k,p+q}-\delta_{k,p}\right)\left\langle c^\dagger_{(p+q)\sigma}c^\dagger_{(p'-q)\bar{\sigma}}c_{p'\bar{\sigma}}c_{p\sigma}\right\rangle_t \\ &=: \frac{U}{V}\sum_{pp'q}C_{pp'q}(t). \end{aligned} \tag{B.1}$$

The equation of motion for the above introduced object $C_{pp'q}(t)$ reads

$$\begin{aligned} i\partial_t C_{pp'q}(t) &= \frac{U}{V}\sum_{pp'q}\left\langle\left[c^\dagger_{(p+q)\sigma}c^\dagger_{(p'-q)\bar{\sigma}}c_{p'\bar{\sigma}}c_{p\sigma}, H_0+H_U\right]\right\rangle_t \\ &= -\left(\delta_{k,p+q}-\delta_{k,p}\right)\left(\epsilon_{p+q}+\epsilon_{p'-q}-\epsilon_{p'}-\epsilon_p\right)\left\langle c^\dagger_{(p+q)\sigma}c^\dagger_{(p'-q)\bar{\sigma}}c_{p'\bar{\sigma}}c_{p\sigma}\right\rangle_t \\ &\quad+\frac{U}{V}\sum_{ll'q'}\left(\delta_{k,p+q}-\delta_{k,p}\right)\left\langle\left[\hat{c}^\dagger_{(p+q)\sigma}c^\dagger_{(p'-q)\bar{\sigma}}c_{p'\bar{\sigma}}c_{p\sigma}, c^\dagger_{(l+q')\sigma}c^\dagger_{(l'-q')\bar{\sigma}}c_{l'\bar{\sigma}}c_{l\sigma}\right]\right\rangle_t \\ &=: -\Delta\epsilon_{p'p(p'-q)}C_{pp'q}(t)+S_{pp'q}(t) \end{aligned} \tag{B.2}$$

The last line of the above equation suggests a solution using the method of the variation of the constant:

$$C_{pp'q}(t) = C_{pp'q}(0)\mathrm{e}^{i\Delta\epsilon_{p'p(p'-q)}t} - i\int_0^t \mathrm{d}t'\, S_{pp'q}(t')\mathrm{e}^{i\Delta\epsilon_{p'p(p'-q)}(t-t')}. \tag{B.3}$$

Usually, $\langle c^\dagger_{(p+q)\sigma}c^\dagger_{(p'-q)\bar{\sigma}}c_{p'\bar{\sigma}}c_{p\sigma}\rangle_{t=0}\sim\delta_{q,0}$ and hence $C_{pp'q}(0)=0$.

The commutator expression in (B.2) can be simplified further:

$$\begin{aligned}
S_{pp'q}(t) &= \frac{U}{V}\sum_{ll'q'}\left(\delta_{k,p+q}-\delta_{k,p}\right)\left\langle\left[c^\dagger_{(p+q)\sigma}c^\dagger_{(p'-q)\bar\sigma}c_{p'\bar\sigma}c_{p\sigma},\,c^\dagger_{(l+q')\sigma}c^\dagger_{(l'-q')\bar\sigma}c_{l'\bar\sigma}c_{l\sigma}\right]\right\rangle_t\\
&= \frac{U}{V}\left(\delta_{k,p+q}-\delta_{k,p}\right)\sum_{ll'q'}\left\langle c^\dagger_{(p+q)\sigma}c^\dagger_{(p'-q)\bar\sigma}\left[c_{p'\bar\sigma}c_{p\sigma},\,c^\dagger_{(l+q')\sigma}c^\dagger_{(l'-q')\bar\sigma}\right]c_{l'\bar\sigma}c_{l\sigma}+\right.\\
&\qquad\left.+\,c^\dagger_{(l+q')\sigma}c^\dagger_{(l'-q')\bar\sigma}\left[c^\dagger_{(p+q)\sigma}c^\dagger_{(p'-q)\bar\sigma},\,c_{l'\bar\sigma}c_{l\sigma}\right]c_{p'\bar\sigma}c_{p\sigma}\right\rangle_t\\
&= \frac{U}{V}\left(\delta_{k,p+q}-\delta_{k,p}\right)\sum_{ll'q'}\left\langle c^\dagger_{(p+q)\sigma}c^\dagger_{(p'-q)\bar\sigma}\left(c_{p'\bar\sigma}c^\dagger_{(l'-q')\bar\sigma}\delta_{(l+q'),p}-c^\dagger_{(l+q')\sigma}c_{p\sigma}\delta_{(l'-q'),p'}\right)c_{l'\bar\sigma}c_{l\sigma}+\right.\\
&\qquad\left.+\,c^\dagger_{(l+q')\sigma}c^\dagger_{(l'-q')\bar\sigma}\left(c^\dagger_{(p+q)\sigma}c_{l\sigma}\delta_{(p'-q),l'}-c_{l'\bar\sigma}c^\dagger_{(p'-q)\bar\sigma}\delta_{(p+q),l}\right)c_{p'\bar\sigma}c_{p\sigma}\right\rangle_t
\end{aligned}\tag{B.4}$$

Omitting the contribution $C_{pp'q}(0)$, we may write

$$i\partial_t n_{k\sigma}(t) = -i\frac{U}{V}\int_0^t \mathrm{d}t'\sum_{pp'q}S_{pp'q}(t')\mathrm{e}^{i\Delta\epsilon_{p'p(p'-q)}(t-t')}\tag{B.5}$$

By insertion of the last line of (B.4) into the formula one can show that the second summand is the complex conjugate of the first and hence

$$\begin{aligned}
\partial_t n_{k\sigma}(t) &= -2\left(\frac{U}{V}\right)^2\int_0^t \mathrm{d}t'\sum_{pp'q}\sum_{ll'q'}\left(\delta_{k,p+q}-\delta_{k,p}\right)\cdot\\
&\quad\cdot\mathrm{Re}\left\langle c^\dagger_{(p+q)\sigma}c^\dagger_{(p'-q)\bar\sigma}\left(c_{p'\bar\sigma}c^\dagger_{(l'-q')\bar\sigma}\delta_{(l+q'),p}-c^\dagger_{(l+q')\sigma}c_{p\sigma}\delta_{(l'-q'),p'}\right)c_{l'\bar\sigma}c_{l\sigma}\right\rangle_{t'}\mathrm{e}^{i\Delta\epsilon_{p'p(p'-q)}(t-t')}\\
&= -2\left(\frac{U}{V}\right)^2\int_0^t \mathrm{d}t'\sum_{pp'll'q}\left(\delta_{k,p+q}-\delta_{k,p}\right)\cdot\\
&\quad\cdot\mathrm{Re}\left\langle c^\dagger_{(p+q)\sigma}c^\dagger_{(p'-q)\bar\sigma}\left(\delta_{(l+l'-p),p'}-c^\dagger_{(l+l'-p)\bar\sigma}c_{p'\bar\sigma}-c^\dagger_{(l+l'-p')\sigma}c_{p\sigma}\right)c_{l'\bar\sigma}c_{l\sigma}\right\rangle_{t'}\mathrm{e}^{i\Delta\epsilon_{p'p(p'-q)}(t-t')}
\end{aligned}\tag{B.6}$$

This expression is still exact and does not explicitly assume $n_{k\sigma}(t)=n_{k\bar\sigma}(t)$. Two approximations are now commonly applied:

1. “restricted quasifreeness” [298]/applicability of the Wick theorem [223], in combination with the assumptions of spatial homogeneity and spin diagonality:

$$\langle c^\dagger_{(p+q)\sigma}c_{p\tau}\rangle \sim \delta_{q,0}\delta_{\sigma\tau}\tag{B.7}$$

This yields:

$$\begin{aligned}
&\left\langle c^\dagger_{(p+q)\sigma} c^\dagger_{(p'-q)\bar\sigma} \left(\delta_{(l+l'-p),p'} - c^\dagger_{(l+l'-p)\bar\sigma} c_{p'\bar\sigma} - c^\dagger_{(l+l'-p')\sigma} c_{p\sigma} \right) c_{l'\bar\sigma} c_{l\sigma} \right\rangle_t \\
&= \delta_{(l+l'-p),p'} \left\langle c^\dagger_{(p+q)\sigma} c_{l\sigma} \right\rangle_t \left\langle c^\dagger_{(p'-q)\bar\sigma} c_{l'\bar\sigma} \right\rangle_t \\
&\quad - \left\langle c^\dagger_{(p+q)\sigma} c_{l\sigma} \right\rangle_t \left(\left\langle c^\dagger_{(p'-q)\bar\sigma} c_{l'\bar\sigma} \right\rangle_t \left\langle c^\dagger_{(l+l'-p)\bar\sigma} c_{p'\bar\sigma} \right\rangle_t - \left\langle c^\dagger_{(p'-q)\bar\sigma} c_{p'\bar\sigma} \right\rangle_t \left\langle c^\dagger_{(l+l'-p)\bar\sigma} c_{l'\bar\sigma} \right\rangle_t \right) \\
&\quad - \left\langle c^\dagger_{(p'-q)\bar\sigma} c_{l'\bar\sigma} \right\rangle_t \left(\left\langle c^\dagger_{(p+q)\sigma} c_{l\sigma} \right\rangle_t \left\langle c^\dagger_{(l+l'-p')\sigma} c_{p\sigma} \right\rangle_t - \left\langle c^\dagger_{(p+q)\sigma} c_{p\sigma} \right\rangle_t \left\langle c^\dagger_{(l+l'-p')\sigma} c_{l\sigma} \right\rangle_t \right)
\end{aligned} \tag{B.8}$$

Further simplifications after the summation:

$$\begin{aligned}
&\sum_{pp'q} \sum_{ll'} \left(\delta_{k,p+q} - \delta_{k,p} \right) \left\langle \dots \right\rangle_t \\
&= \sum_{pp'q} \left(\delta_{k,p+q} - \delta_{k,p} \right) n_{(p+q)\sigma} n_{(p'-q)\bar\sigma} \left(1 - n_{p\sigma} - n_{p'\bar\sigma} \right) \\
&= \sum_{pp'q} \left(\delta_{k,p+q} - \delta_{k,p} \right) n_{(p+q)\sigma} n_{(p'-q)\bar\sigma} \left(\left(1 - n_{p\sigma}\right) \left(1 - n_{p'\bar\sigma}\right) - n_{p\sigma} n_{p'\bar\sigma} \right)
\end{aligned} \tag{B.9}$$

To turn the subtraction of the two delta functions into one delta, we need to perform index shifts in the summation that are compatible with the exponential $\mathrm{e}^{i\Delta\epsilon_{p'p(p'-q)}(t-t')}$. By shifting $p \mapsto p-q, p' \mapsto p'+q, q \mapsto -q$ in the first sum we arrive at $\Delta\epsilon_{(p'-q)(p+q)p'} = -\Delta\epsilon_{p'p(p'-q)}$. Since only the real part of the expression matters, we may unite the deltas:

$$\begin{aligned}
\partial_t n_{k\sigma}(t) = -2 \left(\frac{U}{V} \right)^2 \mathrm{Re} \int_0^t \mathrm{d}t' \cdot \\
\cdot \sum_{pq} \Big(n_{k\sigma}(t') n_{p\bar\sigma}(t') \left(1 - n_{(k+q)\sigma}(t')\right) \left(1 - n_{(p-q)\bar\sigma}(t')\right) \\
- \left(k, p \longleftrightarrow k+q, p-q \right) \Big) \mathrm{e}^{i\Delta\epsilon_{pk(p-q)}(t-t')} \\
=: -2 \left(\frac{U}{V} \right)^2 \mathrm{Re} \int_0^t \mathrm{d}t' \sum_{pq} \tilde{S}_{kpq}(t') \mathrm{e}^{i\Delta\epsilon_{pk(p-q)}(t-t')}
\end{aligned} \tag{B.10}$$

2. local time [298]/Markov approximation [299, 300]: In a mathematically more rigorous manner one can study the limit of the integrand with respect to rescaled time in the limit $U \to 0$. This would correspond to the limit $t \to \infty$. Physically this is identical to the assumption of slow variance (Markov approximation in open systems) $S_{kpq}(t') \approx S_{kpq}(t)$. Transforming the integral and evaluating the real part yields

$$\partial_t n_{k\sigma}(t) = -2 \left(\frac{U}{V} \right)^2 \int_0^\infty \mathrm{d}t' \sum_{pq} \tilde{S}_{kpq}(t-t') \cos(\Delta\epsilon_{pk(p-q)} t). \tag{B.11}$$

Using the Markov approximation, the symmetry of the cosine with respect to t and the fact that in a distributional sense $\int_{-\infty}^{\infty} \mathrm{d}t \, \cos(at) = 2\pi\delta(a)$ the equation reduces to the Quantum Boltzmann equation:

$$\begin{aligned}\partial_t n_{k\sigma}(t) = -2\pi \left(\frac{U}{V}\right)^2 \sum_{pq} \delta(\epsilon_{pk(p-q)}) \Big(\\ n_{k\sigma}(t') n_{p\bar{\sigma}}(t') \big(1 - n_{(k+q)\sigma}(t')\big) \big(1 - n_{(p-q)\bar{\sigma}}(t')\big) - \big(\leftrightarrow \big) \Big)\end{aligned} \tag{B.12}$$

Bibliography

[1] Alexander Osterkorn and Stefan Kehrein. “Systematic Large Flavor fTWA Approach to Interaction Quenches in the Hubbard Model”. July 9, 2020.

[2] Alexander Osterkorn and Stefan Kehrein. “Photoinduced prethermal order parameter dynamics in the two-dimensional large-N Hubbard-Heisenberg model”. In: *Physical Review B* 106.21 (2022), p. 214318.

[3] Marius Keunecke et al. “Electromagnetic Dressing of the Electron Energy Spectrum of Au(111) at High Momenta”. In: *Physical Review B* 102.16 (Oct. 15, 2020), p. 161403. DOI: 10.1103/PhysRevB.102.161403.

[4] Alexander Osterkorn, Constantin Meyer, and Salvatore R Manmana. “In-gap band formation in a periodically driven charge density wave insulator”. In: *Communications Physics* 6.1 (2023), p. 245.

[5] S. Paeckel et al. “Detecting Superconductivity out of Equilibrium”. In: *Physical Review B* 101.18 (May 14, 2020), p. 180507. DOI: 10.1103/PhysRevB.101.180507.

[6] W. Heisenberg. “Über quantentheoretische Umdeutung kinematischer und mechanischer Beziehungen.” In: *Zeitschrift für Physik* 33.1 (Dec. 1, 1925), pp. 879–893. ISSN: 0044-3328. DOI: 10.1007/BF01328377.

[7] Neil W. Ashcroft and N. David Mermin. *Solid State Physics*. Holt, Rinehart and Winston, 1976. 868 pp. ISBN: 978-0-03-083993-1.

[8] J. Bardeen, L. N. Cooper, and J. R. Schrieffer. “Theory of Superconductivity”. In: *Physical Review* 108.5 (Dec. 1, 1957), pp. 1175–1204. ISSN: 0031-899X. DOI: 10.1103/PhysRev.108.1175.

[9] Gordon Baym and Christopher Pethick. *Landau Fermi-Liquid Theory: Concepts and Applications*. John Wiley & Sons, Sept. 26, 2008. 215 pp. ISBN: 978-3-527-61716-6.

[10] Elbio Dagotto. “Correlated Electrons in High-Temperature Superconductors”. In: *Reviews of Modern Physics* 66.3 (July 1, 1994), pp. 763–840. ISSN: 0034-6861, 1539-0756. DOI: 10.1103/RevModPhys.66.763.

[11] B. Keimer et al. “From Quantum Matter to High-Temperature Superconductivity in Copper Oxides”. In: *Nature* 518.7538 (7538 Feb. 2015), pp. 179–186. ISSN: 1476-4687. DOI: 10.1038/nature14165.

[12] Emilia Morosan et al. “Strongly Correlated Materials”. In: *Advanced Materials* 24.36 (2012), pp. 4896–4923. ISSN: 1521-4095. DOI: 10.1002/adma.201202018.

[13] Elbio Dagotto. “Complexity in Strongly Correlated Electronic Systems”. In: *Science* 309.5732 (July 8, 2005), pp. 257–262. DOI: 10.1126/science.1107559.

[14] Gabriel Kotliar and Dieter Vollhardt. “Strongly Correlated Materials: Insights From Dynamical Mean-Field Theory”. In: *Physics Today* 57.3 (Mar. 2004), pp. 53–59. ISSN: 0031-9228. DOI: 10.1063/1.1712502.

[15] Florian Gebhard. “Metal—Insulator Transitions”. In: *The Mott Metal-Insulator Transition: Models and Methods*. Ed. by Florian Gebhard. Springer Tracts in Modern Physics. Berlin, Heidelberg: Springer, 1997, pp. 1–48. ISBN: 978-3-540-14858-6. DOI: 10.1007/3-540-14858-2_1.

[16] Martin C. Gutzwiller. “Effect of Correlation on the Ferromagnetism of Transition Metals”. In: *Physical Review Letters* 10.5 (Mar. 1, 1963), pp. 159–162. ISSN: 0031-9007. DOI: 10.1103/PhysRevLett.10.159.

[17] Junjiro Kanamori. “Electron Correlation and Ferromagnetism of Transition Metals”. In: *Progress of Theoretical Physics* 30.3 (Sept. 1, 1963), pp. 275–289. ISSN: 0033-068X. DOI: 10.1143/PTP.30.275.

[18] J. Hubbard and Brian Hilton Flowers. “Electron Correlations in Narrow Energy Bands III. An Improved Solution”. In: *Proceedings of the Royal Society of London. Series A. Mathematical and Physical Sciences* 281.1386 (Sept. 22, 1964), pp. 401–419. DOI: 10.1098/rspa.1964.0190.

[19] Daniel P. Arovas et al. “The Hubbard Model”. Mar. 22, 2021.

[20] Fabian H. L. Essler et al. *The One-Dimensional Hubbard Model*. Cambridge University Press, Feb. 7, 2005. 692 pp. ISBN: 978-1-139-44158-2.

[21] Walter Metzner and Dieter Vollhardt. “Correlated Lattice Fermions in d = ∞ Dimensions”. In: *Physical Review Letters* 62.3 (Jan. 16, 1989), pp. 324–327. ISSN: 0031-9007. DOI: 10.1103/PhysRevLett.62.324.

[22] X. Y. Zhang, M. J. Rozenberg, and G. Kotliar. “Mott Transition in the d $=\infty$ Hubbard Model at Zero Temperature”. In: *Physical Review Letters* 70.11 (Mar. 15, 1993), pp. 1666–1669. ISSN: 0031-9007. DOI: 10.1103/PhysRevLett.70.1666.

[23] Stefan Kehrein. “Density of States near the Mott-Hubbard Transition in the Limit of Large Dimensions”. In: *Physical Review Letters* 81.18 (Nov. 2, 1998), pp. 3912–3915. ISSN: 0031-9007, 1079-7114. DOI: 10.1103/PhysRevLett.81.3912.

[24] J. P. F. LeBlanc et al. “Solutions of the Two-Dimensional Hubbard Model: Benchmarks and Results from a Wide Range of Numerical Algorithms”. In: *Physical Review X* 5.4 (Dec. 14, 2015), p. 041041. ISSN: 2160-3308. DOI: 10.1103/PhysRevX.5.041041.

[25] Kenneth G. Wilson. “The Renormalization Group and Critical Phenomena”. In: *Reviews of Modern Physics* 55.3 (July 1, 1983), pp. 583–600. ISSN: 0034-6861. DOI: 10.1103/RevModPhys.55.583.

[26] Steven R. White. “Density Matrix Formulation for Quantum Renormalization Groups”. In: *Physical Review Letters* 69.19 (Nov. 9, 1992), pp. 2863–2866. DOI: 10.1103/PhysRevLett.69.2863.

[27] Ulrich Schollwöck. “The Density-Matrix Renormalization Group in the Age of Matrix Product States”. In: *Annals of Physics*. January 2011 Special Issue 326.1 (Jan. 1, 2011), pp. 96–192. ISSN: 0003-4916. DOI: `10.1016/j.aop.2010.09.012`.

[28] Walter Metzner et al. “Functional Renormalization Group Approach to Correlated Fermion Systems”. In: *Reviews of Modern Physics* 84.1 (Mar. 12, 2012), pp. 299–352. ISSN: 0034-6861, 1539-0756. DOI: `10.1103/RevModPhys.84.299`.

[29] Sajedeh Manzeli et al. “2D Transition Metal Dichalcogenides”. In: *Nature Reviews Materials* 2.8 (8 June 13, 2017), pp. 1–15. ISSN: 2058-8437. DOI: `10.1038/natrevmats.2017.33`.

[30] Yuan Cao et al. “Unconventional Superconductivity in Magic-Angle Graphene Superlattices”. In: *Nature* 556.7699 (7699 Apr. 2018), pp. 43–50. ISSN: 1476-4687. DOI: `10.1038/nature26160`.

[31] Fabian R. Geisenhof et al. “Quantum Anomalous Hall Octet Driven by Orbital Magnetism in Bilayer Graphene”. In: *Nature* 598.7879 (7879 Oct. 2021), pp. 53–58. ISSN: 1476-4687. DOI: `10.1038/s41586-021-03849-w`.

[32] Anatoli Polkovnikov et al. “Colloquium: Nonequilibrium Dynamics of Closed Interacting Quantum Systems”. In: *Reviews of Modern Physics* 83.3 (Aug. 15, 2011), pp. 863–883. DOI: `10.1103/RevModPhys.83.863`.

[33] J. Eisert, M. Friesdorf, and C. Gogolin. “Quantum Many-Body Systems out of Equilibrium”. In: *Nature Physics* 11.2 (2 Feb. 2015), pp. 124–130. ISSN: 1745-2481. DOI: `10.1038/nphys3215`.

[34] Alberto de la Torre et al. “Colloquium: Nonthermal Pathways to Ultrafast Control in Quantum Materials”. In: *Reviews of Modern Physics* 93.4 (Oct. 14, 2021), p. 041002. DOI: `10.1103/RevModPhys.93.041002`.

[35] Christian Gross and Immanuel Bloch. “Quantum Simulations with Ultracold Atoms in Optical Lattices”. In: *Science* 357.6355 (Sept. 8, 2017), pp. 995–1001. ISSN: 0036-8075, 1095-9203. DOI: `10.1126/science.aal3837`.

[36] Seth Lloyd. “Universal Quantum Simulators”. In: *Science* 273.5278 (Aug. 23, 1996), pp. 1073–1078. ISSN: 0036-8075, 1095-9203. DOI: `10.1126/science.273.5278.1073`.

[37] Immanuel Bloch, Jean Dalibard, and Sylvain Nascimbène. “Quantum Simulations with Ultracold Quantum Gases”. In: *Nature Physics* 8.4 (4 Apr. 2012), pp. 267–276. ISSN: 1745-2481. DOI: `10.1038/nphys2259`.

[38] Péter Dombi et al. “Strong-Field Nano-Optics”. In: *Reviews of Modern Physics* 92.2 (June 9, 2020), p. 025003. DOI: `10.1103/RevModPhys.92.025003`.

[39] F. Schlawin, D. M. Kennes, and M. A. Sentef. “Cavity Quantum Materials”. In: *Applied Physics Reviews* 9.1 (Mar. 2022), p. 011312. DOI: `10.1063/5.0083825`.

[40] D. E. Chang et al. “*Colloquium* : Quantum Matter Built from Nanoscopic Lattices of Atoms and Photons”. In: *Reviews of Modern Physics* 90.3 (Aug. 1, 2018), p. 031002. ISSN: 0034-6861, 1539-0756. DOI: `10.1103/RevModPhys.90.031002`.

[41] Christopher L. Smallwood, Robert A. Kaindl, and Alessandra Lanzara. “Ultrafast Angle-Resolved Photoemission Spectroscopy of Quantum Materials”. In: *EPL (Europhysics Letters)* 115.2 (July 1, 2016), p. 27001. ISSN: 0295-5075, 1286-4854. DOI: 10.1209/0295-5075/115/27001.

[42] A. Miller, D. T. Reid, and D. M. Finlayson. *Ultrafast Photonics.* CRC Press, Aug. 22, 2019. 382 pp. ISBN: 978-1-4200-3321-2.

[43] Jonathan A. Sobota, Yu He, and Zhi-Xun Shen. “Angle-Resolved Photoemission Studies of Quantum Materials”. In: *Reviews of Modern Physics* 93.2 (May 26, 2021), p. 025006. ISSN: 0034-6861, 1539-0756. DOI: 10.1103/RevModPhys.93.025006.

[44] M. Zonno, F. Boschini, and A. Damascelli. “Time-Resolved ARPES on Cuprates: Tracking the Low-Energy Electrodynamics in the Time Domain”. In: *Journal of Electron Spectroscopy and Related Phenomena* 251 (Aug. 1, 2021), p. 147091. ISSN: 0368-2048. DOI: 10.1016/j.elspec.2021.147091.

[45] Timm Rohwer et al. “Collapse of Long-Range Charge Order Tracked by Time-Resolved Photoemission at High Momenta”. In: *Nature* 471.7339 (7339 Mar. 2011), pp. 490–493. ISSN: 1476-4687. DOI: 10.1038/nature09829.

[46] Y. H. Wang et al. “Observation of Floquet-Bloch States on the Surface of a Topological Insulator”. In: *Science* 342.6157 (Oct. 25, 2013), pp. 453–457. ISSN: 0036-8075, 1095-9203. DOI: 10.1126/science.1239834.

[47] Fahad Mahmood et al. “Selective Scattering between Floquet–Bloch and Volkov States in a Topological Insulator”. In: *Nature Physics* 12.4 (Apr. 2016), pp. 306–310. ISSN: 1745-2481. DOI: 10.1038/nphys3609.

[48] Andrei Kirilyuk, Alexey V. Kimel, and Theo Rasing. “Ultrafast Optical Manipulation of Magnetic Order”. In: *Reviews of Modern Physics* 82.3 (Sept. 22, 2010), pp. 2731–2784. DOI: 10.1103/RevModPhys.82.2731.

[49] D. Fausti et al. “Light-Induced Superconductivity in a Stripe-Ordered Cuprate”. In: *Science* 331.6014 (Jan. 14, 2011), pp. 189–191. DOI: 10.1126/science.1197294.

[50] M. Mitrano et al. “Possible Light-Induced Superconductivity in K3C60 at High Temperature”. In: *Nature* 530.7591 (7591 Feb. 2016), pp. 461–464. ISSN: 1476-4687. DOI: 10.1038/nature16522.

[51] J. K. Freericks, H. R. Krishnamurthy, and Th. Pruschke. “Theoretical Description of Time-Resolved Photoemission Spectroscopy: Application to Pump-Probe Experiments”. In: *Physical Review Letters* 102.13 (Mar. 30, 2009), p. 136401. DOI: 10.1103/PhysRevLett.102.136401.

[52] J. K. Freericks et al. “Gauge Invariance in the Theoretical Description of Time-Resolved Angle-Resolved Pump/Probe Photoemission Spectroscopy”. In: *Physica Scripta* T165 (Oct. 2015), p. 014012. ISSN: 1402-4896. DOI: 10.1088/0031-8949/2015/T165/014012.

[53] M. Eckstein et al. “New Theoretical Approaches for Correlated Systems in Nonequilibrium”. In: *The European Physical Journal Special Topics* 180.1 (Dec. 1, 2009), pp. 217–235. ISSN: 1951-6401. DOI: 10.1140/epjst/e2010-01219-x.

[54] Pavel E. Dolgirev et al. “Self-Similar Dynamics of Order Parameter Fluctuations in Pump-Probe Experiments”. In: *Physical Review B* 101.17 (May 8, 2020), p. 174306. DOI: `10.1103/PhysRevB.101.174306`.

[55] Zhiyuan Sun and Andrew J. Millis. “Transient Trapping into Metastable States in Systems with Competing Orders”. In: *Physical Review X* 10.2 (May 5, 2020), p. 021028. DOI: `10.1103/PhysRevX.10.021028`.

[56] Alfred Zong et al. “Role of Equilibrium Fluctuations in Light-Induced Order”. In: *Physical Review Letters* 127.22 (Nov. 24, 2021), p. 227401. DOI: `10.1103/PhysRevLett.127.227401`.

[57] Hideo Aoki et al. “Nonequilibrium Dynamical Mean-Field Theory and Its Applications”. In: *Reviews of Modern Physics* 86.2 (June 24, 2014), pp. 779–837. DOI: `10.1103/RevModPhys.86.779`.

[58] Sebastian Paeckel et al. “Time-Evolution Methods for Matrix-Product States”. In: *Annals of Physics* 411 (Dec. 1, 2019), p. 167998. ISSN: 0003-4916. DOI: `10.1016/j.aop.2019.167998`.

[59] E.M. Stoudenmire and Steven R. White. “Studying Two-Dimensional Systems with the Density Matrix Renormalization Group”. In: *Annual Review of Condensed Matter Physics* 3.1 (2012), pp. 111–128. DOI: `10.1146/annurev-conmatphys-020911-125018`.

[60] Johannes Hauschild, Frank Pollmann, and Fabian Heidrich-Meisner. “Sudden Expansion and Domain-Wall Melting of Strongly Interacting Bosons in Two-Dimensional Optical Lattices and on Multileg Ladders”. In: *Physical Review A* 92.5 (Nov. 30, 2015), p. 053629. ISSN: 1050-2947, 1094-1622. DOI: `10.1103/PhysRevA.92.053629`.

[61] Fabian H L Essler and Maurizio Fagotti. “Quench Dynamics and Relaxation in Isolated Integrable Quantum Spin Chains”. In: *Journal of Statistical Mechanics: Theory and Experiment* 2016.6 (June 27, 2016), p. 064002. ISSN: 1742-5468. DOI: `10.1088/1742-5468/2016/06/064002`.

[62] Aditi Mitra. “Quantum Quench Dynamics”. In: *Annual Review of Condensed Matter Physics* 9.1 (Mar. 10, 2018), pp. 245–259. ISSN: 1947-5454, 1947-5462. DOI: `10.1146/annurev-conmatphys-031016-025451`.

[63] Immanuel Bloch, Jean Dalibard, and Wilhelm Zwerger. “Many-Body Physics with Ultracold Gases”. In: *Reviews of Modern Physics* 80.3 (July 18, 2008), pp. 885–964. ISSN: 0034-6861, 1539-0756. DOI: `10.1103/RevModPhys.80.885`.

[64] Xie Chen, Zheng-Cheng Gu, and Xiao-Gang Wen. “Classification of Gapped Symmetric Phases in One-Dimensional Spin Systems”. In: *Physical Review B* 83.3 (Jan. 13, 2011), p. 035107. DOI: `10.1103/PhysRevB.83.035107`.

[65] F. Meinert et al. “Quantum Quench in an Atomic One-Dimensional Ising Chain”. In: *Physical Review Letters* 111.5 (July 31, 2013), p. 053003. ISSN: 0031-9007, 1079-7114. DOI: `10.1103/PhysRevLett.111.053003`.

[66] Tim Langen, Remi Geiger, and Jörg Schmiedmayer. "Ultracold Atoms Out of Equilibrium". In: *Annual Review of Condensed Matter Physics* 6.1 (Mar. 1, 2015), pp. 201–217. ISSN: 1947-5454, 1947-5462. DOI: `10.1146/annurev-conmatphys-031214-014548`.

[67] Wei Sun et al. "Uncover Topology by Quantum Quench Dynamics". In: *Physical Review Letters* 121.25 (Dec. 18, 2018), p. 250403. ISSN: 0031-9007, 1079-7114. DOI: `10.1103/PhysRevLett.121.250403`.

[68] Michele Buzzi et al. "Higgs-Mediated Optical Amplification in a Nonequilibrium Superconductor". In: *Physical Review X* 11.1 (Mar. 17, 2021), p. 011055. ISSN: 2160-3308. DOI: `10.1103/PhysRevX.11.011055`.

[69] Marcus Kollar, F. Alexander Wolf, and Martin Eckstein. "Generalized Gibbs Ensemble Prediction of Prethermalization Plateaus and Their Relation to Nonthermal Steady States in Integrable Systems". In: *Physical Review B* 84.5 (Aug. 11, 2011), p. 054304. ISSN: 1098-0121, 1550-235X. DOI: `10.1103/PhysRevB.84.054304`.

[70] Jean-Sébastien Caux and Jorn Mossel. "Remarks on the Notion of Quantum Integrability". In: *Journal of Statistical Mechanics: Theory and Experiment* 2011.02 (Feb. 10, 2011), P02023. ISSN: 1742-5468. DOI: `10.1088/1742-5468/2011/02/P02023`.

[71] Pasquale Calabrese, Fabian H. L. Essler, and Maurizio Fagotti. "Quantum Quench in the Transverse-Field Ising Chain". In: *Physical Review Letters* 106.22 (June 2, 2011), p. 227203. DOI: `10.1103/PhysRevLett.106.227203`.

[72] S. R. Manmana et al. "Strongly Correlated Fermions after a Quantum Quench". In: *Physical Review Letters* 98.21 (May 25, 2007), p. 210405. ISSN: 0031-9007, 1079-7114. DOI: `10.1103/PhysRevLett.98.210405`.

[73] Michael Moeckel and Stefan Kehrein. "Interaction Quench in the Hubbard Model". In: *Physical Review Letters* 100.17 (May 2, 2008), p. 175702. DOI: `10.1103/PhysRevLett.100.175702`.

[74] Lennart Dabelow and Peter Reimann. "Relaxation Theory for Perturbed Many-Body Quantum Systems versus Numerics and Experiment". In: *Physical Review Letters* 124.12 (Mar. 23, 2020), p. 120602. DOI: `10.1103/PhysRevLett.124.120602`.

[75] Martin Eckstein, Marcus Kollar, and Philipp Werner. "Thermalization after an Interaction Quench in the Hubbard Model". In: *Physical Review Letters* 103.5 (July 29, 2009), p. 056403. DOI: `10.1103/PhysRevLett.103.056403`.

[76] Marcos Rigol, Vanja Dunjko, and Maxim Olshanii. "Thermalization and Its Mechanism for Generic Isolated Quantum Systems". In: *Nature* 452.7189 (7189 Apr. 2008), pp. 854–858. ISSN: 1476-4687. DOI: `10.1038/nature06838`.

[77] Dmitry A. Abanin et al. "*Colloquium* : Many-body Localization, Thermalization, and Entanglement". In: *Reviews of Modern Physics* 91.2 (May 22, 2019), p. 021001. ISSN: 0034-6861, 1539-0756. DOI: `10.1103/RevModPhys.91.021001`.

[78] Marton Kormos et al. “Real-Time Confinement Following a Quantum Quench to a Non-Integrable Model”. In: *Nature Physics* 13.3 (3 Mar. 2017), pp. 246–249. ISSN: 1745-2481. DOI: 10.1038/nphys3934.

[79] Pasquale Calabrese and John Cardy. “Evolution of Entanglement Entropy in One-Dimensional Systems”. In: *Journal of Statistical Mechanics: Theory and Experiment* 2005.04 (Apr. 21, 2005), P04010. ISSN: 1742-5468. DOI: 10.1088/1742-5468/2005/04/P04010.

[80] Pasquale Calabrese and John Cardy. “Time Dependence of Correlation Functions Following a Quantum Quench”. In: *Physical Review Letters* 96.13 (Apr. 3, 2006), p. 136801. ISSN: 0031-9007, 1079-7114. DOI: 10.1103/PhysRevLett.96.136801.

[81] Pasquale Calabrese and John Cardy. “Quantum Quenches in Extended Systems”. In: *Journal of Statistical Mechanics: Theory and Experiment* 2007.06 (June 11, 2007), P06008–P06008. ISSN: 1742-5468. DOI: 10.1088/1742-5468/2007/06/P06008.

[82] Marin Bukov, Luca D’Alessio, and Anatoli Polkovnikov. “Universal High-Frequency Behavior of Periodically Driven Systems: From Dynamical Stabilization to Floquet Engineering”. In: *Advances in Physics* 64.2 (Mar. 4, 2015), pp. 139–226. ISSN: 0001-8732. DOI: 10.1080/00018732.2015.1055918.

[83] Umberto De Giovannini, Hannes Hübener, and Angel Rubio. “Monitoring Electron-Photon Dressing in WSe2”. In: *Nano Letters* 16.12 (Dec. 14, 2016), pp. 7993–7998. ISSN: 1530-6984. DOI: 10.1021/acs.nanolett.6b04419.

[84] Takashi Oka and Sota Kitamura. “Floquet Engineering of Quantum Materials”. In: *Annual Review of Condensed Matter Physics* 10.1 (2019), pp. 387–408. DOI: 10.1146/annurev-conmatphys-031218-013423.

[85] Martin Rodriguez-Vega, Michael Vogl, and Gregory A. Fiete. “Low-Frequency and Moiré–Floquet Engineering: A Review”. In: *Annals of Physics*. Special Issue on Philip W. Anderson 435 (Dec. 1, 2021), p. 168434. ISSN: 0003-4916. DOI: 10.1016/j.aop.2021.168434.

[86] D. M. Kennes et al. “Floquet Engineering in Quantum Chains”. In: *Physical Review Letters* 120.12 (Mar. 23, 2018), p. 127601. DOI: 10.1103/PhysRevLett.120.127601.

[87] Gregor Jotzu et al. “Experimental Realization of the Topological Haldane Model with Ultracold Fermions”. In: *Nature* 515.7526 (7526 Nov. 2014), pp. 237–240. ISSN: 1476-4687. DOI: 10.1038/nature13915.

[88] Qingqing Cheng et al. “Observation of Anomalous π Modes in Photonic Floquet Engineering”. In: *Physical Review Letters* 122.17 (May 3, 2019), p. 173901. ISSN: 0031-9007, 1079-7114. DOI: 10.1103/PhysRevLett.122.173901.

[89] Christof Weitenberg and Juliette Simonet. “Tailoring Quantum Gases by Floquet Engineering”. In: *Nature Physics* 17.12 (12 Dec. 2021), pp. 1342–1348. ISSN: 1745-2481. DOI: 10.1038/s41567-021-01316-x.

[90] R. Moessner and S. L. Sondhi. “Equilibration and Order in Quantum Floquet Matter”. In: *Nature Physics* 13.5 (5 May 2017), pp. 424–428. ISSN: 1745-2481. DOI: 10.1038/nphys4106.

[91] Dmitry A. Abanin, Wojciech De Roeck, and François Huveneers. “Exponentially Slow Heating in Periodically Driven Many-Body Systems”. In: *Physical Review Letters* 115.25 (Dec. 15, 2015), p. 256803. ISSN: 0031-9007, 1079-7114. DOI: 10.1103/PhysRevLett.115.256803.

[92] Marin Bukov et al. “Prethermal Floquet Steady States and Instabilities in the Periodically Driven, Weakly Interacting Bose-Hubbard Model”. In: *Physical Review Letters* 115.20 (Nov. 11, 2015), p. 205301. ISSN: 0031-9007, 1079-7114. DOI: 10.1103/PhysRevLett.115.205301.

[93] Tatsuhiko N. Ikeda and Anatoli Polkovnikov. “Fermi’s Golden Rule for Heating in Strongly Driven Floquet Systems”. In: *Physical Review B* 104.13 (Oct. 15, 2021), p. 134308. DOI: 10.1103/PhysRevB.104.134308.

[94] Aron Beekman, Louk Rademaker, and Jasper van Wezel. “An Introduction to Spontaneous Symmetry Breaking”. In: *SciPost Physics Lecture Notes* (Dec. 4, 2019), p. 011. ISSN: 2590-1990. DOI: 10.21468/SciPostPhysLectNotes.11.

[95] Assa Auerbach. *Interacting Electrons and Quantum Magnetism*. Springer Science & Business Media, Dec. 6, 2012. 249 pp. ISBN: 978-1-4612-0869-3.

[96] C. N. Yang. “Concept of Off-Diagonal Long-Range Order and the Quantum Phases of Liquid He and of Superconductors”. In: *Reviews of Modern Physics* 34.4 (Oct. 1, 1962), pp. 694–704. DOI: 10.1103/RevModPhys.34.694.

[97] Jing Wang and Shou-Cheng Zhang. “Topological States of Condensed Matter”. In: *Nature Materials* 16.11 (11 Nov. 2017), pp. 1062–1067. ISSN: 1476-4660. DOI: 10.1038/nmat5012.

[98] Subir Sachdev. “Quantum Criticality: Competing Ground States in Low Dimensions”. In: *Science* 288.5465 (Apr. 21, 2000), pp. 475–480. ISSN: 0036-8075, 1095-9203. DOI: 10.1126/science.288.5465.475.

[99] G. Grüner. “The Dynamics of Charge-Density Waves”. In: *Reviews of Modern Physics* 60.4 (Oct. 1, 1988), pp. 1129–1181. DOI: 10.1103/RevModPhys.60.1129.

[100] Chen Ning Yang. “η Pairing and Off-Diagonal Long-Range Order in a Hubbard Model”. In: *Physical Review Letters* 63.19 (Nov. 6, 1989), pp. 2144–2147. ISSN: 0031-9007. DOI: 10.1103/PhysRevLett.63.2144.

[101] Tatsuya Kaneko et al. “Photoinduced $\ensuremath{\eta}$ Pairing in the Hubbard Model”. In: *Physical Review Letters* 122.7 (Feb. 22, 2019), p. 077002. DOI: 10.1103/PhysRevLett.122.077002.

[102] Satoshi Ejima, Florian Lange, and Holger Fehske. “Nonequilibrium Dynamics in Pumped Mott Insulators”. In: *Physical Review Research* 4.1 (Feb. 9, 2022), p. L012012. DOI: 10.1103/PhysRevResearch.4.L012012.

[103] G. I. Japaridze et al. “η -Pairing Superconductivity in the Hubbard Chain with Pair Hopping”. In: *Physical Review B* 65.1 (Dec. 13, 2001), p. 014518. ISSN: 0163-1829, 1095-3795. DOI: 10.1103/PhysRevB.65.014518.

[104] Lucile Savary and Leon Balents. “Quantum Spin Liquids: A Review”. In: *Reports on Progress in Physics* 80.1 (Nov. 2016), p. 016502. ISSN: 0034-4885. DOI: 10.1088/0034-4885/80/1/016502.

[105] Subir Sachdev. “*Colloquium:* Order and Quantum Phase Transitions in the Cuprate Superconductors”. In: *Reviews of Modern Physics* 75.3 (July 16, 2003), pp. 913–932. ISSN: 0034-6861, 1539-0756. DOI: 10.1103/RevModPhys.75.913.

[106] Eduardo Fradkin, Steven A. Kivelson, and John M. Tranquada. “*Colloquium* : Theory of Intertwined Orders in High Temperature Superconductors”. In: *Reviews of Modern Physics* 87.2 (May 26, 2015), pp. 457–482. ISSN: 0034-6861, 1539-0756. DOI: 10.1103/RevModPhys.87.457.

[107] R. B. Laughlin. “Hartree-Fock Computation of the High-${T}_{c}$ Cuprate Phase Diagram”. In: *Physical Review B* 89.3 (Jan. 22, 2014), p. 035134. DOI: 10.1103/PhysRevB.89.035134.

[108] I. Grote, E. Körding, and F. Wegner. “Stability Analysis of the Hubbard Model”. In: *Journal of Low Temperature Physics* 126.3 (Feb. 1, 2002), pp. 1385–1409. ISSN: 1573-7357. DOI: 10.1023/A:1013804405357.

[109] Zhiyuan Sun and Andrew J. Millis. “Pump-Induced Motion of an Interface between Competing Orders”. In: *Physical Review B* 101.22 (June 22, 2020), p. 224305. DOI: 10.1103/PhysRevB.101.224305.

[110] Alfred Zong et al. “Dynamical Slowing-Down in an Ultrafast Photoinduced Phase Transition”. In: *Physical Review Letters* 123.9 (Aug. 29, 2019), p. 097601. DOI: 10.1103/PhysRevLett.123.097601.

[111] M. A. Sentef et al. “Theory of Laser-Controlled Competing Superconducting and Charge Orders”. In: *Physical Review Letters* 118.8 (Feb. 21, 2017), p. 087002. DOI: 10.1103/PhysRevLett.118.087002.

[112] Shainen M. Davidson, Dries Sels, and Anatoli Polkovnikov. “Semiclassical Approach to Dynamics of Interacting Fermions”. In: *Annals of Physics* 384 (Sept. 1, 2017), pp. 128–141. ISSN: 0003-4916. DOI: 10.1016/j.aop.2017.07.003.

[113] Gianluca Stefanucci and Robert van Leeuwen. *Nonequilibrium Many-Body Theory of Quantum Systems: A Modern Introduction*. Cambridge University Press, Mar. 7, 2013. 620 pp. ISBN: 978-0-521-76617-3.

[114] Mona H. Kalthoff, Götz S. Uhrig, and J. K. Freericks. “Emergence of Floquet Behavior for Lattice Fermions Driven by Light Pulses”. In: *Physical Review B* 98.3 (July 23, 2018), p. 035138. DOI: 10.1103/PhysRevB.98.035138.

[115] J. K. Freericks and Alexander F. Kemper. “What Do the Two Times in Two-Time Correlation Functions Mean for Interpreting Tr-ARPES?” In: *Journal of Electron Spectroscopy and Related Phenomena* 251 (Aug. 1, 2021), p. 147104. ISSN: 0368-2048. DOI: 10.1016/j.elspec.2021.147104.

[116] Götz S. Uhrig, Mona H. Kalthoff, and James K. Freericks. “Positivity of the Spectral Densities of Retarded Floquet Green Functions”. In: *Physical Review Letters* 122.13 (Apr. 5, 2019), p. 130604. DOI: 10.1103/PhysRevLett.122.130604.

[117] John David Jackson. *Classical Electrodynamics*. John Wiley & Sons, May 13, 2021. 835 pp. ISBN: 978-1-119-77076-3.

[118] R. Peierls. “Zur Theorie des Diamagnetismus von Leitungselektronen”. In: *Zeitschrift für Physik* 80.11 (Nov. 1, 1933), pp. 763–791. ISSN: 0044-3328. DOI: `10.1007/BF01342591`.

[119] J. M. Luttinger. “The Effect of a Magnetic Field on Electrons in a Periodic Potential”. In: *Physical Review* 84.4 (Nov. 15, 1951), pp. 814–817. ISSN: 0031-899X. DOI: `10.1103/PhysRev.84.814`.

[120] Jiajun Li et al. “Electromagnetic Coupling in Tight-Binding Models for Strongly Correlated Light and Matter”. In: *Physical Review B* 101.20 (May 21, 2020), p. 205140. DOI: `10.1103/PhysRevB.101.205140`.

[121] N. Goldman et al. “Light-Induced Gauge Fields for Ultracold Atoms”. In: *Reports on Progress in Physics* 77.12 (Nov. 2014), p. 126401. ISSN: 0034-4885. DOI: `10.1088/0034-4885/77/12/126401`.

[122] Lars Bojer Madsen. “Strong-Field Approximation in Laser-Assisted Dynamics”. In: *American Journal of Physics* 73.1 (Dec. 13, 2004), pp. 57–62. ISSN: 0002-9505. DOI: `10.1119/1.1796791`.

[123] J. C. Baggesen and L. B. Madsen. “Theory for Time-Resolved Measurements of Laser-Induced Electron Emission from Metal Surfaces”. In: *Physical Review A* 78.3 (Sept. 16, 2008), p. 032903. DOI: `10.1103/PhysRevA.78.032903`.

[124] Sang Tae Park. “Interference in Floquet-Volkov Transitions”. In: *Physical Review A* 90.1 (July 28, 2014), p. 013420. DOI: `10.1103/PhysRevA.90.013420`.

[125] M. Keunecke et al. “Time-Resolved Momentum Microscopy with a 1 MHz High-Harmonic Extreme Ultraviolet Beamline”. Mar. 3, 2020.

[126] Stefan Hüfner. *Photoelectron Spectroscopy*. Red. by Manuel Cardona et al. Vol. 82. Springer Series in Solid-State Sciences. Berlin, Heidelberg: Springer, 1996. ISBN: 978-3-662-03211-4 978-3-662-03209-1. DOI: `10.1007/978-3-662-03209-1`.

[127] Eva Pavarini et al. *DMFT at 25: Infinite Dimensions*. Schriften Des Forschungszentrums Jülich. Modeling and Simulation 4. Jülich: Forschungszentrum Jülich Zentralbibliothek, Verlag, 2014. 450 pp. ISBN: 978-3-89336-953-9.

[128] J. K. Freericks, H. R. Krishnamurthy, and Th. Pruschke. “Erratum: Theoretical Description of Time-Resolved Photoemission Spectroscopy: Application to Pump-Probe Experiments [Phys. Rev. Lett. 102, 136401 (2009)]”. In: *Physical Review Letters* 119.18 (Nov. 2, 2017), p. 189903. DOI: `10.1103/PhysRevLett.119.189903`.

[129] G. C. Wick. “The Evaluation of the Collision Matrix”. In: *Physical Review* 80.2 (Oct. 15, 1950), pp. 268–272. ISSN: 0031-899X. DOI: `10.1103/PhysRev.80.268`.

[130] Luca Guido Molinari. *Notes on Wick’s Theorem in Many-Body Theory*. Oct. 25, 2017. DOI: `10.48550/arXiv.1710.09248`.

[131] H. J. Lipkin, N. Meshkov, and A. J. Glick. “Validity of Many-Body Approximation Methods for a Solvable Model: (I). Exact Solutions and Perturbation Theory”. In: *Nuclear Physics* 62.2 (Feb. 1, 1965), pp. 188–198. ISSN: 0029-5582. DOI: `10.1016/0029-5582(65)90862-X`.

[132] Bruno Sciolla and Giulio Biroli. “Dynamical Transitions and Quantum Quenches in Mean-Field Models”. In: *Journal of Statistical Mechanics: Theory and Experiment* 2011.11 (Nov. 2, 2011), P11003. ISSN: 1742-5468. DOI: `10.1088/1742-5468/2011/11/P11003`.

[133] Angelo Russomanno, Rosario Fazio, and Giuseppe E. Santoro. “Thermalization in a Periodically Driven Fully Connected Quantum Ising Ferromagnet”. In: *EPL (Europhysics Letters)* 110.3 (May 1, 2015), p. 37005. ISSN: 0295-5075, 1286-4854. DOI: `10.1209/0295-5075/110/37005`.

[134] Silvia Pappalardi et al. “Scrambling and Entanglement Spreading in Long-Range Spin Chains”. In: *Physical Review B* 98.13 (Oct. 8, 2018), p. 134303. ISSN: 2469-9950, 2469-9969. DOI: `10.1103/PhysRevB.98.134303`.

[135] Rodney J. Baxter. *Exactly Solved Models in Statistical Mechanics*. Elsevier, June 12, 2016. 499 pp. ISBN: 978-1-4832-6594-0.

[136] E. Müller-Hartmann. “Correlated Fermions on a Lattice in High Dimensions”. In: *Zeitschrift für Physik B Condensed Matter* 74.4 (Dec. 1, 1989), pp. 507–512. ISSN: 1431-584X. DOI: `10.1007/BF01311397`.

[137] Antoine Georges et al. “Dynamical Mean-Field Theory of Strongly Correlated Fermion Systems and the Limit of Infinite Dimensions”. In: *Reviews of Modern Physics* 68.1 (Jan. 1, 1996), pp. 13–125. DOI: `10.1103/RevModPhys.68.13`.

[138] Roberto Franzosi, Vittorio Penna, and Riccardo Zecchina. “Quantum Dynamics of Coupled Bosonic Wells within the Bose–Hubbard Picture”. In: *International Journal of Modern Physics B* 14.09 (Apr. 10, 2000), pp. 943–961. ISSN: 0217-9792. DOI: `10.1142/S0217979200001011`.

[139] Anatoli Polkovnikov, Subir Sachdev, and S. M. Girvin. “Nonequilibrium Gross-Pitaevskii Dynamics of Boson Lattice Models”. In: *Physical Review A* 66.5 (Nov. 12, 2002), p. 053607. DOI: `10.1103/PhysRevA.66.053607`.

[140] F. F. Assaad. “Phase Diagram of the Half-Filled Two-Dimensional $\mathrm{SU}(N)$ Hubbard-Heisenberg Model: A Quantum Monte Carlo Study”. In: *Physical Review B* 71.7 (Feb. 4, 2005), p. 075103. DOI: `10.1103/PhysRevB.71.075103`.

[141] Ian Affleck and J. Brad Marston. “Large-n Limit of the Heisenberg-Hubbard Model: Implications for High-T_c Superconductors”. In: *Physical Review B* 37.7 (Mar. 1, 1988), pp. 3774–3777. DOI: `10.1103/PhysRevB.37.3774`.

[142] J. Brad Marston and Ian Affleck. “Large-n Limit of the Hubbard-Heisenberg Model”. In: *Physical Review B* 39.16 (June 1, 1989), pp. 11538–11558. DOI: `10.1103/PhysRevB.39.11538`.

[143] Pauli Virtanen et al. “SciPy 1.0: Fundamental Algorithms for Scientific Computing in Python”. In: *Nature Methods* 17.3 (3 Mar. 2020), pp. 261–272. ISSN: 1548-7105. DOI: `10.1038/s41592-019-0686-2`.

[144] Michele Fabrizio. *A Course in Quantum Many-Body Theory: From Conventional Fermi Liquids to Strongly Correlated Systems*. Graduate Texts in Physics. Cham: Springer International Publishing, 2022. ISBN: 978-3-031-16304-3 978-3-031-16305-0. DOI: `10.1007/978-3-031-16305-0`.

[145] Michael Bonitz. *Quantum Kinetic Theory*. Cham: Springer International Publishing, 2016. ISBN: 978-3-319-24119-7 978-3-319-24121-0. DOI: `10.1007/978-3-319-24121-0`.

[146] Cosmas Zachos. “Deformation Quantization: Quantum Mechanics Lives and Works in Phase-Space”. In: *International Journal of Modern Physics A* 17.03 (Jan. 30, 2002), pp. 297–316. ISSN: 0217-751X. DOI: `10.1142/S0217751X02006079`.

[147] Hilbrand Johannes Groenewold. “On the Principles of Elementary Quantum Mechanics”. In: *On the Principles of Elementary Quantum Mechanics*. Ed. by Hilbrand Johannes Groenewold. Dordrecht: Springer Netherlands, 1946, pp. 1–56. ISBN: 978-94-017-6065-2. DOI: `10.1007/978-94-017-6065-2_1`.

[148] Léon van Hove. “Sur Certaines Représentations Unitaires d’un Groupe Infini de Transformations”. In: *Proc. R. Acad. Sci. Belgium* 26 (1951), pp. 1–102.

[149] Mark J. Gotay. “On the Groenewold–Van Hove Problem for R2n”. In: *Journal of Mathematical Physics* 40.4 (Apr. 1999), pp. 2107–2116. ISSN: 0022-2488. DOI: `10.1063/1.532854`.

[150] Anatoli Polkovnikov. “Phase Space Representation of Quantum Dynamics”. In: *Annals of Physics* 325.8 (Aug. 1, 2010), pp. 1790–1852. ISSN: 0003-4916. DOI: `10.1016/j.aop.2010.02.006`.

[151] Anatoli Polkovnikov. “Quantum Corrections to the Dynamics of Interacting Bosons: Beyond the Truncated Wigner Approximation”. In: *Physical Review A* 68.5 (Nov. 4, 2003), p. 053604. DOI: `10.1103/PhysRevA.68.053604`.

[152] Shainen M. Davidson and Anatoli Polkovnikov. “$SU(3)$ Semiclassical Representation of Quantum Dynamics of Interacting Spins”. In: *Physical Review Letters* 114.4 (Jan. 29, 2015), p. 045701. DOI: `10.1103/PhysRevLett.114.045701`.

[153] Jonathan Wurtz, Anatoli Polkovnikov, and Dries Sels. “Cluster Truncated Wigner Approximation in Strongly Interacting Systems”. In: *Annals of Physics* 395 (Aug. 2018), pp. 341–365. ISSN: 00034916. DOI: `10.1016/j.aop.2018.06.001`.

[154] Jonathan Wurtz and Anatoli Polkovnikov. “Quantum Diffusion in Spin Chains with Phase Space Methods”. In: *Physical Review E* 101.5 (May 15, 2020), p. 052120. DOI: `10.1103/PhysRevE.101.052120`.

[155] J. Schachenmayer, A. Pikovski, and A. M. Rey. “Many-Body Quantum Spin Dynamics with Monte Carlo Trajectories on a Discrete Phase Space”. In: *Physical Review X* 5.1 (Feb. 25, 2015), p. 011022. DOI: `10.1103/PhysRevX.5.011022`.

[156] Markus Schmitt et al. “Semiclassical Echo Dynamics in the Sachdev-Ye-Kitaev Model”. In: *Physical Review B* 99.13 (Apr. 8, 2019), p. 134301. DOI: `10.1103/PhysRevB.99.134301`.

[157] Adam S. Sajna and Anatoli Polkovnikov. “Semiclassical Dynamics of a Disordered Two-Dimensional Hubbard Model with Long-Range Interactions”. In: *Physical Review A* 102.3 (Sept. 28, 2020), p. 033338. DOI: `10.1103/PhysRevA.102.033338`.

[158] Łukasz Iwanek et al. *Semiclassical Bounds on Dynamics of Two-Dimensional Interacting Disordered Fermions*. Oct. 27, 2022. DOI: `10.48550/arXiv.2209.15062`.

[159] Aleksander Kaczmarek and Adam S. Sajna. *Slow Semiclassical Dynamics of a Two-Dimensional Hubbard Model in Disorder-Free Potentials*. Oct. 17, 2022. DOI: `10.48550/arXiv.2210.01082`.

[160] Sakir Ayik. “A Stochastic Mean-Field Approach for Nuclear Dynamics”. In: *Physics Letters B* 658.4 (Jan. 3, 2008), pp. 174–179. ISSN: 0370-2693. DOI: `10.1016/j.physletb.2007.09.072`.

[161] Denis Lacroix, Sakir Ayik, and Bulent Yilmaz. “Symmetry Breaking and Fluctuations within Stochastic Mean-Field Dynamics: Importance of Initial Quantum Fluctuations”. In: *Physical Review C* 85.4 (Apr. 19, 2012), p. 041602. ISSN: 0556-2813, 1089-490X. DOI: `10.1103/PhysRevC.85.041602`.

[162] Denis Lacroix, Danilo Gambacurta, and Sakir Ayik. “Quantal Corrections to Mean-Field Dynamics Including Pairing”. In: *Physical Review C* 87.6 (June 28, 2013), p. 061302. DOI: `10.1103/PhysRevC.87.061302`.

[163] Denis Lacroix et al. “Ultrafast Dynamics of Finite Hubbard Clusters: A Stochastic Mean-Field Approach”. In: *Physical Review B* 90.12 (Sept. 5, 2014), p. 125112. DOI: `10.1103/PhysRevB.90.125112`.

[164] Denis Lacroix et al. “A Simplified BBGKY Hierarchy for Correlated Fermions from a Stochastic Mean-Field Approach”. In: *The European Physical Journal A* 52.4 (Apr. 19, 2016), p. 94. ISSN: 1434-601X. DOI: `10.1140/epja/i2016-16094-1`.

[165] Ibrahim Ulgen, Bulent Yilmaz, and Denis Lacroix. “Impact of Initial Fluctuations on the Dissipative Dynamics of Interacting Fermi Systems: A Model Case Study”. In: *Physical Review C* 100.5 (Nov. 6, 2019), p. 054603. DOI: `10.1103/PhysRevC.100.054603`.

[166] Thomas Czuba et al. “Combining Phase-Space and Time-Dependent Reduced Density Matrix Approach to Describe the Dynamics of Interacting Fermions”. In: *The European Physical Journal A* 56.4 (Apr. 8, 2020), p. 111. ISSN: 1434-601X. DOI: `10.1140/epja/s10050-020-00119-7`.

[167] Lorenzo Pucci, Analabha Roy, and Michael Kastner. “Simulation of Quantum Spin Dynamics by Phase Space Sampling of Bogoliubov-Born-Green-Kirkwood-Yvon Trajectories”. In: *Physical Review B* 93.17 (May 4, 2016), p. 174302. DOI: `10.1103/PhysRevB.93.174302`.

[168] Asier Piñeiro Orioli et al. “Nonequilibrium Dynamics of Spin-Boson Models from Phase-Space Methods”. In: *Physical Review A* 96.3 (Sept. 5, 2017), p. 033607. DOI: `10.1103/PhysRevA.96.033607`.

[169] Karsten Ahnert and Mario Mulansky. “Odeint – Solving Ordinary Differential Equations in C++”. In: *AIP Conference Proceedings* 1389.1 (Sept. 14, 2011), pp. 1586–1589. ISSN: 0094-243X. DOI: `10.1063/1.3637934`.

[170] Erwin Fehlberg. “Eine Methode zur Fehlerverkleinerung beim Runge-Kutta-Verfahren”. In: *ZAMM - Journal of Applied Mathematics and Mechanics / Zeitschrift für Angewandte Mathematik und Mechanik* 38.11-12 (1958), pp. 421–426. ISSN: 1521-4001. DOI: `10.1002/zamm.19580381102`.

[171] J. R. Cash and Alan H. Karp. “A Variable Order Runge-Kutta Method for Initial Value Problems with Rapidly Varying Right-Hand Sides”. In: *ACM Transactions on Mathematical Software* 16.3 (Sept. 1, 1990), pp. 201–222. ISSN: 0098-3500. DOI: `10.1145/79505.79507`.

[172] William Feller. *An Introduction to Probability Theory and Its Applications, Volume 2*. John Wiley & Sons, Jan. 8, 1991. 709 pp. ISBN: 978-0-471-25709-7.

[173] Erich Schubert and Michael Gertz. “Numerically Stable Parallel Computation of (Co-)Variance”. In: *Proceedings of the 30th International Conference on Scientific and Statistical Database Management*. SSDBM ’18. Bozen-Bolzano, Italy: Association for Computing Machinery, July 9, 2018, pp. 1–12. ISBN: 978-1-4503-6505-5. DOI: `10.1145/3221269.3223036`.

[174] André Eckardt. “Colloquium: Atomic Quantum Gases in Periodically Driven Optical Lattices”. In: *Reviews of Modern Physics* 89.1 (Mar. 31, 2017), p. 011004. DOI: `10.1103/RevModPhys.89.011004`.

[175] André Eckardt and Egidijus Anisimovas. “High-Frequency Approximation for Periodically Driven Quantum Systems from a Floquet-space Perspective”. In: *New Journal of Physics* 17.9 (Sept. 2015), p. 093039. ISSN: 1367-2630. DOI: `10.1088/1367-2630/17/9/093039`.

[176] B. Rethfeld et al. “Ultrafast Dynamics of Nonequilibrium Electrons in Metals under Femtosecond Laser Irradiation”. In: *Physical Review B* 65.21 (May 22, 2002), p. 214303. DOI: `10.1103/PhysRevB.65.214303`.

[177] B. Y. Mueller and B. Rethfeld. “Relaxation Dynamics in Laser-Excited Metals under Nonequilibrium Conditions”. In: *Physical Review B* 87.3 (Jan. 30, 2013), p. 035139. DOI: `10.1103/PhysRevB.87.035139`.

[178] B. Koopmans et al. “Explaining the Paradoxical Diversity of Ultrafast Laser-Induced Demagnetization”. In: *Nature Materials* 9.3 (3 Mar. 2010), pp. 259–265. ISSN: 1476-4660. DOI: `10.1038/nmat2593`.

[179] L. Stojchevska et al. “Ultrafast Switching to a Stable Hidden Quantum State in an Electronic Crystal”. In: *Science* 344.6180 (Apr. 11, 2014), pp. 177–180. DOI: `10.1126/science.1241591`.

[180] Michael A. Sentef et al. “Quantum to Classical Crossover of Floquet Engineering in Correlated Quantum Systems”. In: *Physical Review Research* 2.3 (July 7, 2020), p. 033033. ISSN: 2643-1564. DOI: `10.1103/PhysRevResearch.2.033033`.

[181] F. L. Moore et al. “Observation of Dynamical Localization in Atomic Momentum Transfer: A New Testing Ground for Quantum Chaos”. In: *Physical Review Letters* 73.22 (Nov. 28, 1994), pp. 2974–2977. ISSN: 0031-9007. DOI: `10.1103/PhysRevLett.73.2974`.

[182] Luca D’Alessio and Marcos Rigol. “Long-Time Behavior of Isolated Periodically Driven Interacting Lattice Systems”. In: *Physical Review X* 4.4 (Dec. 19, 2014), p. 041048. DOI: `10.1103/PhysRevX.4.041048`.

[183] Vedika Khemani, Roderich Moessner, and S. L. Sondhi. “A Brief History of Time Crystals”. Oct. 23, 2019.

[184] Simon A. Weidinger and Michael Knap. “Floquet Prethermalization and Regimes of Heating in a Periodically Driven, Interacting Quantum System”. In: *Scientific Reports* 7.1 (1 Apr. 3, 2017), p. 45382. ISSN: 2045-2322. DOI: `10.1038/srep45382`.

[185] Mark S. Rudner and Netanel H. Lindner. “Band Structure Engineering and Non-Equilibrium Dynamics in Floquet Topological Insulators”. In: *Nature Reviews Physics* 2.5 (5 May 2020), pp. 229–244. ISSN: 2522-5820. DOI: `10.1038/s42254-020-0170-z`.

[186] T. E. Glover et al. “Observation of Laser Assisted Photoelectric Effect and Femtosecond High Order Harmonic Radiation”. In: *Physical Review Letters* 76.14 (Apr. 1, 1996), pp. 2468–2471. DOI: `10.1103/PhysRevLett.76.2468`.

[187] L. Miaja-Avila et al. “Laser-Assisted Photoelectric Effect from Surfaces”. In: *Physical Review Letters* 97.11 (Sept. 14, 2006), p. 113604. DOI: `10.1103/PhysRevLett.97.113604`.

[188] G. Saathoff et al. “Laser-Assisted Photoemission from Surfaces”. In: *Physical Review A* 77.2 (Feb. 29, 2008), p. 022903. DOI: `10.1103/PhysRevA.77.022903`.

[189] L. Miaja-Avila et al. “Ultrafast Studies of Electronic Processes at Surfaces Using the Laser-Assisted Photoelectric Effect with Long-Wavelength Dressing Light”. In: *Physical Review A* 79.3 (Mar. 30, 2009), p. 030901. DOI: `10.1103/PhysRevA.79.030901`.

[190] James K. Freericks and H. R. Krishnamurthy. “Constant Matrix Element Approximation to Time-Resolved Angle-Resolved Photoemission Spectroscopy”. In: *Photonics* 3.4 (4 Dec. 2016), p. 58. DOI: `10.3390/photonics3040058`.

[191] A. K. Geim and K. S. Novoselov. “The Rise of Graphene”. In: *Nature Materials* 6.3 (3 Mar. 2007), pp. 183–191. ISSN: 1476-4660. DOI: `10.1038/nmat1849`.

[192] M. A. Sentef et al. “Theory of Floquet Band Formation and Local Pseudospin Textures in Pump-Probe Photoemission of Graphene”. In: *Nature Communications* 6.1 (May 11, 2015), pp. 1–8. ISSN: 2041-1723. DOI: `10.1038/ncomms8047`.

[193] Sven Aeschlimann et al. “Survival of Floquet–Bloch States in the Presence of Scattering”. In: *Nano Letters* 21.12 (June 23, 2021), pp. 5028–5035. ISSN: 1530-6984. DOI: `10.1021/acs.nanolett.1c00801`.

[194] Lukas Broers and Ludwig Mathey. “Detecting Light-Induced Floquet Band Gaps of Graphene via trARPES”. In: *Physical Review Research* 4.1 (Jan. 28, 2022), p. 013057. DOI: `10.1103/PhysRevResearch.4.013057`.

[195] M. N. Faraggi, M. S. Gravielle, and D. M. Mitnik. “Interaction of Ultrashort Laser Pulses with Metal Surfaces: Impulsive Jellium-Volkov Approximation versus the Solution of the Time-Dependent Schr\”odinger Equation”. In: *Physical Review A* 76.1 (July 25, 2007), p. 012903. DOI: 10.1103/PhysRevA.76.012903.

[196] D. M. Wolkow. “Über eine Klasse von Lösungen der Diracschen Gleichung”. In: *Zeitschrift für Physik* 94.3 (Mar. 1, 1935), pp. 250–260. ISSN: 0044-3328. DOI: 10.1007/BF01331022.

[197] T. Rangel et al. “Band Structure of Gold from Many-Body Perturbation Theory”. In: *Physical Review B* 86.12 (Sept. 17, 2012), p. 125125. DOI: 10.1103/PhysRevB.86.125125.

[198] F. Roth et al. “Angle Resolved Photoemission from Ag and Au Single Crystals: Final State Lifetimes in the Attosecond Range”. In: *Journal of Electron Spectroscopy and Related Phenomena* 224 (Apr. 1, 2018), pp. 84–92. ISSN: 0368-2048. DOI: 10.1016/j.elspec.2017.05.008.

[199] F. Reinert et al. “Direct Measurements of the L-gap Surface States on the (111) Face of Noble Metals by Photoelectron Spectroscopy”. In: *Physical Review B* 63.11 (Mar. 1, 2001), p. 115415. DOI: 10.1103/PhysRevB.63.115415.

[200] Marius Keunecke. “Ultrafast Electron Dynamics Measured with a Novel Time-Resolved High-Repetition Rate Momentum Microscopy Setup”. doctoralThesis. Mar. 25, 2021. ISBN: 9781752572533. DOI: 10.53846/goediss-8515.

[201] Peter J. Feibelman. “Comment on Recent Theories of Photoemission”. In: *Surface Science* 46.2 (Dec. 1, 1974), pp. 558–566. ISSN: 0039-6028. DOI: 10.1016/0039-6028(74)90324-0.

[202] M A B Whitaker. “Use of the Fresnel Equations in the Theory of Angle-Resolved Photoemission”. In: *Journal of Physics C: Solid State Physics* 11.4 (Feb. 28, 1978), pp. L151–L156. ISSN: 0022-3719. DOI: 10.1088/0022-3719/11/4/007.

[203] Robert L. Olmon et al. “Optical Dielectric Function of Gold”. In: *Physical Review B* 86.23 (Dec. 28, 2012), p. 235147. ISSN: 1098-0121, 1550-235X. DOI: 10.1103/PhysRevB.86.235147.

[204] Piers Coleman. *Introduction to Many-Body Physics*. Cambridge University Press, Nov. 26, 2015. 815 pp. ISBN: 978-0-521-86488-6.

[205] Jacques Des Cloizeaux and Michel Gaudin. “Anisotropic Linear Magnetic Chain”. In: *Journal of Mathematical Physics* 7.8 (Aug. 1966), pp. 1384–1400. ISSN: 0022-2488. DOI: 10.1063/1.1705048.

[206] J Michael Kosterlitz. “Kosterlitz–Thouless Physics: A Review of Key Issues”. In: *Reports on Progress in Physics* 79.2 (Feb. 1, 2016), p. 026001. ISSN: 0034-4885, 1361-6633. DOI: 10.1088/0034-4885/79/2/026001.

[207] Thierry Giamarchi. *Quantum Physics in One Dimension*. Clarendon Press, Dec. 18, 2003. 441 pp. ISBN: 978-0-19-152345-8.

[208] Mona H. Kalthoff, Dante M. Kennes, and Michael A. Sentef. “Floquet-Engineered Light-Cone Spreading of Correlations in a Driven Quantum Chain”. In: *Physical Review B* 100.16 (Oct. 16, 2019), p. 165125. DOI: 10.1103/PhysRevB.100.165125.

[209] Denitsa R. Baykusheva et al. *Witnessing Nonequilibrium Entanglement Dynamics in a Strongly Correlated Fermionic Chain.* Sept. 5, 2022.

[210] Marin Bukov, Michael Kolodrubetz, and Anatoli Polkovnikov. “Schrieffer-Wolff Transformation for Periodically Driven Systems: Strongly Correlated Systems with Artificial Gauge Fields”. In: *Physical Review Letters* 116.12 (Mar. 21, 2016), p. 125301. DOI: `10.1103/PhysRevLett.116.125301`.

[211] Andreas Herrmann et al. “Floquet Prethermalization in the Resonantly Driven Hubbard Model”. In: *EPL (Europhysics Letters)* 120.5 (Dec. 2017), p. 57001. ISSN: 0295-5075. DOI: `10.1209/0295-5075/120/57001`.

[212] Constantin Meyer. “Matrix Product State Approaches to Non-equilibrium Spectral Quantities of Strongly Correlated Fermions in One Dimension”. doctoralThesis. June 9, 2022. ISBN: 9781806813384. DOI: `10.53846/goediss-9286`.

[213] U. Busch and K. A. Penson. “Tight-Binding Electrons on Open Chains: Density Distribution and Correlations”. In: *Physical Review B* 36.17 (Dec. 15, 1987), pp. 9271–9274. DOI: `10.1103/PhysRevB.36.9271`.

[214] Wen Shen et al. “Nonequilibrium “Melting” of a Charge Density Wave Insulator via an Ultrafast Laser Pulse”. In: *Physical Review Letters* 112.17 (May 2, 2014), p. 176404. DOI: `10.1103/PhysRevLett.112.176404`.

[215] W. Shen, T. P. Devereaux, and J. K. Freericks. “Exact Solution for Bloch Oscillations of a Simple Charge-Density-Wave Insulator”. In: *Physical Review B* 89.23 (June 24, 2014), p. 235129. DOI: `10.1103/PhysRevB.89.235129`.

[216] Michael Moeckel and Stefan Kehrein. “Real-Time Evolution for Weak Interaction Quenches in Quantum Systems”. In: *Annals of Physics* 324.10 (Oct. 1, 2009), pp. 2146–2178. ISSN: 0003-4916. DOI: `10.1016/j.aop.2009.03.009`.

[217] Michael Moeckel and Stefan Kehrein. “Crossover from Adiabatic to Sudden Interaction Quenches in the Hubbard Model: Prethermalization and Non-Equilibrium Dynamics”. In: *New Journal of Physics* 12.5 (May 2010), p. 055016. ISSN: 1367-2630. DOI: `10.1088/1367-2630/12/5/055016`.

[218] A. Hackl and S. Kehrein. “Real Time Evolution in Quantum Many-Body Systems with Unitary Perturbation Theory”. In: *Physical Review B* 78.9 (Sept. 17, 2008), p. 092303. DOI: `10.1103/PhysRevB.78.092303`.

[219] Franz Wegner. “Flow-Equations for Hamiltonians”. In: *Annalen der Physik* 506.2 (1994), pp. 77–91. ISSN: 1521-3889. DOI: `10.1002/andp.19945060203`.

[220] Stefan Kehrein. *The Flow Equation Approach to Many-Particle Systems.* Springer, Jan. 9, 2007. 179 pp. ISBN: 978-3-540-34068-3.

[221] Manuel Kreye. “A Unitary Perturbation Theory Approach to Real-Time Evolution in the Hubbard Model”. doctoralThesis. Oct. 29, 2019. ISBN: 9781680682922. DOI: `10.53846/goediss-7704`.

[222] Manuel Kreye and Stefan Kehrein. *Prethermalization of Density-Density Correlations after an Interaction Quench in the Hubbard Model.* Aug. 28, 2019. DOI: `10.48550/arXiv.1908.10685`.

[223] Michael Stark and Marcus Kollar. “Kinetic Description of Thermalization Dynamics in Weakly Interacting Quantum Systems”. Aug. 25, 2013.

[224] Jürgen Berges. “Introduction to Nonequilibrium Quantum Field Theory”. In: *AIP Conference Proceedings* 739.1 (Dec. 2, 2004), pp. 3–62. ISSN: 0094-243X. DOI: 10.1063/1.1843591.

[225] Martin Eckstein, Marcus Kollar, and Philipp Werner. “Interaction Quench in the Hubbard Model: Relaxation of the Spectral Function and the Optical Conductivity”. In: *Physical Review B* 81.11 (Mar. 22, 2010), p. 115131. ISSN: 1098-0121, 1550-235X. DOI: 10.1103/PhysRevB.81.115131.

[226] Peter Reimann and Lennart Dabelow. “Typicality of Prethermalization”. In: *Physical Review Letters* 122.8 (Mar. 1, 2019), p. 080603. DOI: 10.1103/PhysRevLett.122.080603.

[227] Krishnanand Mallayya, Marcos Rigol, and Wojciech De Roeck. “Prethermalization and Thermalization in Isolated Quantum Systems”. In: *Physical Review X* 9.2 (May 9, 2019), p. 021027. ISSN: 2160-3308. DOI: 10.1103/PhysRevX.9.021027.

[228] Jamir Marino et al. “Dynamical Phase Transitions in the Collisionless Pre-Thermal Statesof Isolated Quantum Systems: Theory and Experiments”. In: *Reports on Progress in Physics* (2022). ISSN: 0034-4885. DOI: 10.1088/1361-6633/ac906c.

[229] Simone A. Hamerla and Götz S. Uhrig. “Interaction Quenches in the Two-Dimensional Fermionic Hubbard Model”. In: *Physical Review B* 89.10 (Mar. 13, 2014), p. 104301. DOI: 10.1103/PhysRevB.89.104301.

[230] Marc Alexander and Marcus Kollar. “Photoinduced Prethermalization Phenomena in Correlated Metals”. In: *physica status solidi (b)* n/a.n/a (2022), p. 2100280. ISSN: 1521-3951. DOI: 10.1002/pssb.202100280.

[231] Conrad Sanderson and Ryan Curtin. “Armadillo: A Template-Based C++ Library for Linear Algebra”. In: *The Journal of Open Source Software* 1 (June 1, 2016), p. 26. DOI: 10.21105/joss.00026.

[232] Conrad Sanderson and Ryan R. Curtin. “A User-Friendly Hybrid Sparse Matrix Class in C++”. In: *ICMS*. 2018. DOI: 10.1007/978-3-319-96418-8_50.

[233] J. G. Bednorz and K. A. Müller. “Possible HighT_c Superconductivity in the Ba-La-Cu-O System”. In: *Zeitschrift für Physik B Condensed Matter* 64.2 (June 1, 1986), pp. 189–193. ISSN: 1431-584X. DOI: 10.1007/BF01303701.

[234] F. C. Zhang and T. M. Rice. “Effective Hamiltonian for the Superconducting Cu Oxides”. In: *Physical Review B* 37.7 (Mar. 1, 1988), pp. 3759–3761. DOI: 10.1103/PhysRevB.37.3759.

[235] D. M. Newns et al. “Theory of High- T c Superconductors within a Realistic Anderson Lattice Model”. In: *Physical Review B* 38.10 (Oct. 1, 1988), pp. 7033–7036. ISSN: 0163-1829. DOI: 10.1103/PhysRevB.38.7033.

[236] V. Emery. *Correlated Electron Systems - Proceedings Of The 9th Jerusalem Winter School For Theoretical Physics*. World Scientific, Aug. 30, 1993. 364 pp. ISBN: 978-981-4553-69-8.

[237] N. Read and Subir Sachdev. “Large-N Expansion for Frustrated Quantum Antiferromagnets”. In: *Physical Review Letters* 66.13 (Apr. 1, 1991), pp. 1773–1776. DOI: `10.1103/PhysRevLett.66.1773`.

[238] Subir Sachdev and N. Read. “Large n Expansion for Frustrated and Doped Quantum Antiferromagnets”. In: *International Journal of Modern Physics B* 05 (01n02 Jan. 1, 1991), pp. 219–249. ISSN: 0217-9792. DOI: `10.1142/S0217979291000158`.

[239] Piers Coleman. “New Approach to the Mixed-Valence Problem”. In: *Physical Review B* 29.6 (Mar. 15, 1984), pp. 3035–3044. ISSN: 0163-1829. DOI: `10.1103/PhysRevB.29.3035`.

[240] D. M. Newns and N. Read. “Mean-Field Theory of Intermediate Valence/Heavy Fermion Systems”. In: *Advances in Physics* 36.6 (Jan. 1, 1987), pp. 799–849. ISSN: 0001-8732. DOI: `10.1080/00018738700101082`.

[241] P. C. Pattnaik and D. M. Newns. “Evidence for the Heavy-Fermion Normal State of High-Temperature Superconductors from the Theory of Spectroscopy”. In: *Physical Review B* 41.1 (Jan. 1, 1990), pp. 880–883. ISSN: 0163-1829, 1095-3795. DOI: `10.1103/PhysRevB.41.880`.

[242] N. Read and Subir Sachdev. “Valence-Bond and Spin-Peierls Ground States of Low-Dimensional Quantum Antiferromagnets”. In: *Physical Review Letters* 62.14 (Apr. 3, 1989), pp. 1694–1697. ISSN: 0031-9007. DOI: `10.1103/PhysRevLett.62.1694`.

[243] Daniel P. Arovas and Assa Auerbach. “Functional Integral Theories of Low-Dimensional Quantum Heisenberg Models”. In: *Physical Review B* 38.1 (July 1, 1988), pp. 316–332. DOI: `10.1103/PhysRevB.38.316`.

[244] Serge Florens and Antoine Georges. “Quantum Impurity Solvers Using a Slave Rotor Representation”. In: *Physical Review B* 66.16 (Oct. 29, 2002), p. 165111. ISSN: 0163-1829, 1095-3795. DOI: `10.1103/PhysRevB.66.165111`.

[245] Serge Florens and Antoine Georges. “Slave-Rotor Mean-Field Theories of Strongly Correlated Systems and the Mott Transition in Finite Dimensions”. In: *Physical Review B* 70.3 (July 27, 2004), p. 035114. DOI: `10.1103/PhysRevB.70.035114`.

[246] P. W. Anderson. “The Resonating Valence Bond State in La $_2$ CuO $_4$ and Superconductivity”. In: *Science* 235.4793 (Mar. 6, 1987), pp. 1196–1198. ISSN: 0036-8075, 1095-9203. DOI: `10.1126/science.235.4793.1196`.

[247] N. Read and Subir Sachdev. “Some Features of the Phase Diagram of the Square Lattice SU(N) Antiferromagnet”. In: *Nuclear Physics B* 316.3 (Apr. 17, 1989), pp. 609–640. ISSN: 0550-3213. DOI: `10.1016/0550-3213(89)90061-8`.

[248] N. Read and Subir Sachdev. “Spin-Peierls, Valence-Bond Solid, and Néel Ground States of Low-Dimensional Quantum Antiferromagnets”. In: *Physical Review B* 42.7 (Sept. 1, 1990), pp. 4568–4589. ISSN: 0163-1829, 1095-3795. DOI: `10.1103/PhysRevB.42.4568`.

[249] Michael Hermele and Victor Gurarie. “Topological Liquids and Valence Cluster States in Two-Dimensional SU (N) Magnets”. In: *Physical Review B* 84.17 (Nov. 30, 2011), p. 174441. ISSN: 1098-0121, 1550-235X. DOI: `10.1103/PhysRevB.84.174441`.

[250] T. C. Hsu, J. B. Marston, and I. Affleck. “Two Observable Features of the Staggered-Flux Phase at Nonzero Doping”. In: *Physical Review B* 43.4 (Feb. 1, 1991), pp. 2866–2877. ISSN: 0163-1829, 1095-3795. DOI: `10.1103/PhysRevB.43.2866`.

[251] Menke U. Ubbens and Patrick A. Lee. “Flux Phases in the t - J Model”. In: *Physical Review B* 46.13 (Oct. 1, 1992), pp. 8434–8439. ISSN: 0163-1829, 1095-3795. DOI: `10.1103/PhysRevB.46.8434`.

[252] J. B. Marston, J. O. Fjærestad, and A. Sudbø. “Staggered Flux Phase in a Model of Strongly Correlated Electrons”. In: *Physical Review Letters* 89.5 (July 15, 2002), p. 056404. ISSN: 0031-9007, 1079-7114. DOI: `10.1103/PhysRevLett.89.056404`.

[253] U. Schollwöck et al. “Broken Time-Reversal Symmetry in Strongly Correlated Ladder Structures”. In: *Physical Review Letters* 90.18 (May 5, 2003), p. 186401. DOI: `10.1103/PhysRevLett.90.186401`.

[254] C. H. Chung, J. B. Marston, and Ross H. McKenzie. “Large-Nsolutions of the Heisenberg and Hubbard-Heisenberg Models on the Anisotropic Triangular Lattice: Application to Cs2CuCl4and to the Layered Organic Superconductors $\upkappa$-(BEDT-TTF)2X (BEDT-TTF$\equiv$bis(Ethylene-Dithio)Tetrathiafulvalene)$\ X$\equiv$anion)”. In: *Journal of Physics: Condensed Matter* 13.22 (May 2001), pp. 5159–5181. ISSN: 0953-8984. DOI: `10.1088/0953-8984/13/22/311`.

[255] A. V. Gorshkov et al. “Two-Orbital SU(N) Magnetism with Ultracold Alkaline-Earth Atoms”. In: *Nature Physics* 6.4 (Apr. 2010), pp. 289–295. ISSN: 1745-2481. DOI: `10.1038/nphys1535`.

[256] Miguel A Cazalilla and Ana Maria Rey. “Ultracold Fermi Gases with Emergent SU($\boldsymbol{N}$) Symmetry”. In: *Reports on Progress in Physics* 77.12 (Dec. 1, 2014), p. 124401. ISSN: 0034-4885, 1361-6633. DOI: `10.1088/0034-4885/77/12/124401`.

[257] Sayan Choudhury et al. “Collective Modes of Ultracold Fermionic Alkaline-Earth-Metal Gases with SU(N) Symmetry”. In: *Physical Review A* 101.5 (May 7, 2020), p. 053612. DOI: `10.1103/PhysRevA.101.053612`.

[258] Takeshi Fukuhara et al. “Degenerate Fermi Gases of Ytterbium”. In: *Physical Review Letters* 98.3 (Jan. 17, 2007), p. 030401. ISSN: 0031-9007, 1079-7114. DOI: `10.1103/PhysRevLett.98.030401`.

[259] M A Cazalilla, A F Ho, and M Ueda. “Ultracold Gases of Ytterbium: Ferromagnetism and Mott States in an SU(6) Fermi System”. In: *New Journal of Physics* 11.10 (Oct. 21, 2009), p. 103033. ISSN: 1367-2630. DOI: `10.1088/1367-2630/11/10/103033`.

[260] G. K. Campbell et al. “Probing Interactions Between Ultracold Fermions”. In: *Science* 324.5925 (Apr. 17, 2009), pp. 360–363. DOI: `10.1126/science.1169724`.

[261] Carsten Honerkamp and Walter Hofstetter. “Ultracold Fermions and the $\mathrm{SU}(N)$ Hubbard Model”. In: *Physical Review Letters* 92.17 (Apr. 30, 2004), p. 170403. DOI: `10.1103/PhysRevLett.92.170403`.

[262] Lih-King Lim, Andreas Hemmerich, and C. Morais Smith. "Artificial Staggered Magnetic Field for Ultracold Atoms in Optical Lattices". In: *Physical Review A* 81.2 (Feb. 4, 2010), p. 023404. ISSN: 1050-2947, 1094-1622. DOI: `10.1103/PhysRevA.81.023404`.

[263] K. Buchta et al. "Mott Transition and Dimerization in the One-Dimensional \$\mathrm{SU}(n)\$ Hubbard Model". In: *Physical Review B* 75.15 (Apr. 19, 2007), p. 155108. DOI: `10.1103/PhysRevB.75.155108`.

[264] Pierre Nataf and Frédéric Mila. "Exact Diagonalization of Heisenberg SU (N) Chains in the Fully Symmetric and Antisymmetric Representations". In: *Physical Review B* 93.15 (Apr. 18, 2016), p. 155134. ISSN: 2469-9950, 2469-9969. DOI: `10.1103/PhysRevB.93.155134`.

[265] Pierre Nataf and Frédéric Mila. "Density Matrix Renormalization Group Simulations of SU(N) Heisenberg Chains Using Standard Young Tableaus: Fundamental Representation and Comparison with a Finite-Size Bethe Ansatz". In: *Physical Review B* 97.13 (Apr. 20, 2018), p. 134420. ISSN: 2469-9950, 2469-9969. DOI: `10.1103/PhysRevB.97.134420`.

[266] A. Weichselbaum et al. "Unified Phase Diagram of Antiferromagnetic SU(N) Spin Ladders". In: *Physical Review B* 98.8 (Aug. 3, 2018), p. 085104. ISSN: 2469-9950, 2469-9969. DOI: `10.1103/PhysRevB.98.085104`.

[267] Olivier Parcollet et al. "Overscreened Multichannel SU (N) Kondo Model: Large- N Solution and Conformal Field Theory". In: *Physical Review B* 58.7 (Aug. 15, 1998), pp. 3794–3813. ISSN: 0163-1829, 1095-3795. DOI: `10.1103/PhysRevB.58.3794`.

[268] Christophe Mora et al. "Theory of Nonequilibrium Transport in the SU (N) Kondo Regime". In: *Physical Review B* 80.15 (Oct. 23, 2009), p. 155322. ISSN: 1098-0121, 1550-235X. DOI: `10.1103/PhysRevB.80.155322`.

[269] Fred Cooper and Emil Mottola. "Initial-Value Problems in Quantum Field Theory in the Large-N Approximation". In: *Physical Review D* 36.10 (Nov. 15, 1987), pp. 3114–3127. DOI: `10.1103/PhysRevD.36.3114`.

[270] Jürgen Berges. "Controlled Nonperturbative Dynamics of Quantum Fields out of Equilibrium". In: *Nuclear Physics A* 699.3 (Mar. 11, 2002), pp. 847–886. ISSN: 0375-9474. DOI: `10.1016/S0375-9474(01)01295-7`.

[271] Sumit R. Das and Krishnendu Sengupta. "Non-Equilibrium Dynamics of O(N) Nonlinear Sigma Models: A Large-N Approach". In: *Journal of High Energy Physics* 2012.9 (Sept. 2012), p. 72. ISSN: 1029-8479. DOI: `10.1007/JHEP09(2012)072`.

[272] R. Walz, K. Boguslavski, and J. Berges. "Large-\$N\$ Kinetic Theory for Highly Occupied Systems". In: *Physical Review D* 97.11 (June 12, 2018), p. 116011. DOI: `10.1103/PhysRevD.97.116011`.

[273] M. Kronenwett and T. Gasenzer. "Far-from-Equilibrium Dynamics of an Ultracold Fermi Gas". In: *Applied Physics B* 102.3 (Mar. 1, 2011), pp. 469–488. ISSN: 1432-0649. DOI: `10.1007/s00340-011-4426-2`.

[274] Yonah Lemonik and Aditi Mitra. “Time-Resolved Spectral Density of Interacting Fermions Following a Quench to a Superconducting Critical Point”. In: *Physical Review B* 96.10 (Sept. 13, 2017), p. 104506. DOI: `10.1103/PhysRevB.96.104506`.

[275] Mikhail Mamaev et al. “Resonant Dynamics of Strongly Interacting SU(n) Fermionic Atoms in a Synthetic Flux Ladder”. In: *PRX Quantum* 3.3 (Aug. 26, 2022), p. 030328. ISSN: 2691-3399. DOI: `10.1103/PRXQuantum.3.030328`.

[276] Masakatsu Watanabe and William P. Reinhardt. “Direct Dynamical Calculation of Entropy and Free Energy by Adiabatic Switching”. In: *Physical Review Letters* 65.26 (Dec. 24, 1990), pp. 3301–3304. DOI: `10.1103/PhysRevLett.65.3301`.

[277] R. A. Barankov and L. S. Levitov. “Synchronization in the BCS Pairing Dynamics as a Critical Phenomenon”. In: *Physical Review Letters* 96.23 (June 16, 2006), p. 230403. DOI: `10.1103/PhysRevLett.96.230403`.

[278] Emil A. Yuzbashyan and Maxim Dzero. “Dynamical Vanishing of the Order Parameter in a Fermionic Condensate”. In: *Physical Review Letters* 96.23 (June 16, 2006), p. 230404. DOI: `10.1103/PhysRevLett.96.230404`.

[279] Emil A. Yuzbashyan, Oleksandr Tsyplyatyev, and Boris L. Altshuler. “Relaxation and Persistent Oscillations of the Order Parameter in Fermionic Condensates”. In: *Physical Review Letters* 96.9 (Mar. 8, 2006), p. 097005. DOI: `10.1103/PhysRevLett.96.097005`.

[280] Takashi Oka, Ryotaro Arita, and Hideo Aoki. “Breakdown of a Mott Insulator: A Nonadiabatic Tunneling Mechanism”. In: *Physical Review Letters* 91.6 (Aug. 5, 2003), p. 066406. ISSN: 0031-9007, 1079-7114. DOI: `10.1103/PhysRevLett.91.066406`.

[281] Martin Eckstein, Takashi Oka, and Philipp Werner. “Dielectric Breakdown of Mott Insulators in Dynamical Mean-Field Theory”. In: *Physical Review Letters* 105.14 (Sept. 28, 2010), p. 146404. ISSN: 0031-9007, 1079-7114. DOI: `10.1103/PhysRevLett.105.146404`.

[282] Takashi Oka and Hideo Aoki. “Ground-State Decay Rate for the Zener Breakdown in Band and Mott Insulators”. In: *Physical Review Letters* 95.13 (Sept. 21, 2005), p. 137601. ISSN: 0031-9007, 1079-7114. DOI: `10.1103/PhysRevLett.95.137601`.

[283] F. Heidrich-Meisner et al. “Nonequilibrium Electronic Transport in a One-Dimensional Mott Insulator”. In: *Physical Review B* 82.20 (Nov. 10, 2010), p. 205110. ISSN: 1098-0121, 1550-235X. DOI: `10.1103/PhysRevB.82.205110`.

[284] Takashi Oka. “Nonlinear Doublon Production in a Mott Insulator: Landau-Dykhne Method Applied to an Integrable Model”. In: *Physical Review B* 86.7 (Aug. 27, 2012), p. 075148. ISSN: 1098-0121, 1550-235X. DOI: `10.1103/PhysRevB.86.075148`.

[285] Wen Shen, T. P. Devereaux, and J. K. Freericks. “Beyond Planck-Einstein Quanta: Amplitude-driven Quantum Excitation”. In: *Physical Review B* 90.19 (Nov. 4, 2014), p. 195104. DOI: `10.1103/PhysRevB.90.195104`.

[286] Simon Wall et al. "Ultrafast Disordering of Vanadium Dimers in Photoexcited VO2". In: *Science* 362.6414 (Nov. 2, 2018), pp. 572–576. DOI: 10.1126/science.aau3873.

[287] Daniel Perez-Salinas et al. "Multi-Mode Excitation Drives Disorder during the Ultrafast Melting of a C4-symmetry-broken Phase". In: *Nature Communications* 13.1 (1 Jan. 11, 2022), p. 238. ISSN: 2041-1723. DOI: 10.1038/s41467-021-27819-y.

[288] Antonio Picano, Francesco Grandi, and Martin Eckstein. *Inhomogeneous Disordering at a Photo-Induced Charge Density Wave Transition*. Dec. 31, 2021. DOI: 10.48550/arXiv.2112.15323.

[289] Antonio Picano et al. *Stochastic Semiclassical Theory for Non-Equilibrium Electron-Phonon Coupled Systems*. Sept. 1, 2022. DOI: 10.48550/arXiv.2209.00428.

[290] Hiroshi Kano. "Excitation of Surface Plasmon Polaritons by a Focused Laser Beam". In: *Near-Field Optics and Surface Plasmon Polaritons*. Ed. by Satoshi Kawata. Topics in Applied Physics. Berlin, Heidelberg: Springer, 2001, pp. 189–206. ISBN: 978-3-540-44552-4. DOI: 10.1007/3-540-44552-8_10.

[291] C. Karrasch, J. E. Moore, and F. Heidrich-Meisner. "Real-Time and Real-Space Spin and Energy Dynamics in One-Dimensional Spin- 1 2 Systems Induced by Local Quantum Quenches at Finite Temperatures". In: *Physical Review B* 89.7 (Feb. 28, 2014), p. 075139. ISSN: 1098-0121, 1550-235X. DOI: 10.1103/PhysRevB.89.075139.

[292] F. Dorfner et al. "Real-Time Decay of a Highly Excited Charge Carrier in the One-Dimensional Holstein Model". In: *Physical Review B* 91.10 (Mar. 3, 2015), p. 104302. ISSN: 1098-0121, 1550-235X. DOI: 10.1103/PhysRevB.91.104302.

[293] Fabian R. A. Biebl and Stefan Kehrein. "Thermalization Rates in the One-Dimensional Hubbard Model with next-to-Nearest Neighbor Hopping". In: *Physical Review B* 95.10 (Mar. 17, 2017), p. 104304. DOI: 10.1103/PhysRevB.95.104304.

[294] Mohsen Jemaï et al. "Self-Consistent Random Phase Approximation: Application to the Hubbard Model for Finite Number of Sites". In: *Physical Review B* 71.8 (Feb. 22, 2005), p. 085115. DOI: 10.1103/PhysRevB.71.085115.

[295] Francisco H. Kim et al. "Linear Flavor-Wave Theory for Fully Antisymmetric SU(N) Irreducible Representations". In: *Physical Review B* 96.20 (Nov. 22, 2017), p. 205142. DOI: 10.1103/PhysRevB.96.205142.

[296] Fakher Assaad et al. "The ALF (Algorithms for Lattice Fermions) Project Release 2.0. Documentation for the Auxiliary-Field Quantum Monte Carlo Code". In: *SciPost Physics Codebases* (Aug. 22, 2022), p. 001. DOI: 10.21468/SciPostPhysCodeb.1.

[297] M. ten Brink et al. "Real-Time Non-Adiabatic Dynamics in the One-Dimensional Holstein Model: Trajectory-based vs Exact Methods". In: *The Journal of Chemical Physics* 156.23 (June 21, 2022), p. 234109. ISSN: 0021-9606. DOI: 10.1063/5.0092063.

[298] László Erdős, Manfred Salmhofer, and Horng-Tzer Yau. “On the Quantum Boltzmann Equation”. In: *Journal of Statistical Physics* 116.1 (Aug. 1, 2004), pp. 367–380. ISSN: 1572-9613. DOI: `10.1023/B:JOSS.0000037224.56191.ed`.

[299] Friedemann Queisser et al. “Boltzmann Relaxation Dynamics of Strongly Interacting Spinless Fermions on a Lattice”. In: *Physical Review B* 100.24 (Dec. 5, 2019), p. 245110. DOI: `10.1103/PhysRevB.100.245110`.

[300] Friedemann Queisser and Ralf Schützhold. “Boltzmann Relaxation Dynamics in the Strongly Interacting Fermi-Hubbard Model”. In: *Physical Review A* 100.5 (Nov. 19, 2019), p. 053617. DOI: `10.1103/PhysRevA.100.053617`.

Acknowledgements

I would like to thank Stefan Kehrein for being my academic supervisor, from whom I learned a lot about non-equilibrium physics, and also for allowing me the freedom to work on a number of different topics during my PhD time. In addition, I would like to thank him especially also for his support of my research stay at Boston University.

Further thanks go to Salvatore Manmana, with whom I had many discussions about physics and the world, which I all enjoyed a lot. I (and I think the whole condensed matter theory group) profit a lot from your open door policy, thank you very much!

I thank Stefan Mathias for being my second supervisor and especially for organizing the paper discussion club in his office – truely a scientific highlight of the PhD time.

I would like to thank all the other members of the condensed matter theory group for offering a very friendly working environment! I want to say thank you especially to Niklas Bölter for being my office mate and for proving helpful feedback on this dissertation.

I am grateful also to the members of my examination board, Fabian Heidrich-Meisner, Stefan Mathias, Claus Ropers and Matthias Krüger for volunteering to do so.

I thank Anatoli Polkovnikov for our discussions and for all the new insights he gave me into TWA methods and many other topics in physics.

I acknowledge financial support by the SFB 1073 for providing me the funding for my PhD as well as the DAAD for granting me a stipend to visit BU in 2021.

Finally, I do want to say thank you to my family, my friends and, in particular, to Lotta.

Research Data Management

The data associated to the t_h-V chain project is currently stored in the repository
`ssh://git@projects.gwdg.de/floquet-graphene-stripes.git`
(A. Osterkorn, C. Meyer and S.R. Manmana have access)
and will be migrated to
`https://gitlab.gwdg.de/meyer349/paper_floquet`
(same people have access)

The code and data associated with the fTWA projects is currently stored in the repository
`https://gitlab.gwdg.de/osterkorn/phd_data`
(only Alexander Osterkorn has access)
Before the publication of this thesis, the data will be moved to
`https://gitlab.gwdg.de/stefan-kehrein-condensed-matter-theory/alexander-osterkorn/phd_data`
(all members of the Kehrein group, in particular Stefan Kehrein, have access)

Similarly, the fTWA code will be copied to
`https://gitlab.gwdg.de/stefan-kehrein-condensed-matter-theory/alexander-osterkorn/ftwa_code`
and made publicly available.

Moreover, before leaving the institute, all important data will be stored on tape in the 10- Years-Archive provided by the IT of the Institut für Theoretische Physik, Georg-August-Universität Göttingen.